Electrode surface modification using metallophthalocyanines and metal nanoparticles: Electrocatalytic activity

A thesis submitted in fulfilment of the requirements for the degree of

Doctor of Philosophy

of

Rhodes University

by

Audacity Maringa

Supervisor: Dist. Prof. T. Nyokong

October 2014

DEDICATIONS

To my beloved wife, Josphine and daughter, Audrey.

"...perfect love cast out fear..."

ABSTRACT

Metallophthalocyanines and metal nanoparticles were successfully synthesized and applied for the electrooxidation of amitrole, nitrite and hydrazine individually or when employed together. The synthesized materials were characterized using the following techniques: predominantly scanning electron microscopy (SEM), X-ray photoelectron spectroscopy (XPS), electrochemistry and scanning electrochemical microscopy (SECM).

Different electrode modification methods were used to modify the glassy carbon substrates. The methods include adsorption, electrodeposition, electropolymerization and click chemistry. Modifying the glassy carbon substrate with MPc (electropolymerization) followed by metal nanoparticles (electrodeposition) or vice versa, made a hybrid modified surface that had efficient electron transfer. This was confirmed by electrochemical impedance studies with voltammetry measurements having lower detection potentials for the analytes.

This work also describes for the first time the micropatterning of the glassy carbon substrate using the SECM tip. The substrate was electrografted with 4-azidobenzenediazonium salt and then the click reaction was performed using ethynylferrocene facilitated by Cu^{+} produced at the SECM tip. The SECM imaging was then used to show the clicked spot.

ACKNOWLEDGEMENTS

I would like to thank the following people and organizations for their support and assistance towards the success of this project:

- Distinguished Professor Tebello Nyokong for her outstanding supervision during the course of this study.
- Dr Edith Antunes and Dr Philani Mashazi for assistance with instruments especially X-ray photoelectron spectroscopy.
- Dr Fethi Bedioui and Dr Sophie Griveau for their hospitality while I was working in their lab in Paris.
- S22 group for company and support that you provided.
- Rhodes University and National Research Foundation (NRF) for the financial support.
- My family, my father, Mr D. Maringa, my mother, Mrs A. Maringa and my siblings, Alice, Nyaradzo, Polite and Peter for their love, support and motivation.
- My beloved wife, Josphine and child, Audrey, for their love, patience and understanding throughout my studies.
- Finally I thank Jehovah for making it possible.

TABLE OF CONTENTS

LIST OF ABBREVIATIONS

ACN	Acetonitrile
AFM	Atomic force microscopy
a.u	Arbitrary unit
AuNPs	Gold nanoparticles
BDCA	Benzene-1,4-dicarbaldehyde
CA	Chronoamperometry
CE	Counter electrode
CME	Chemically modified electrode
CNT	Carbon nanotube
CV	Cyclic voltammetry/voltammograms
DMF	Dimethylformamide
EDS	Energy dispersion X-ray spectroscopy
EIS	Electrochemical impedance spectroscopy
FeTCPc	Iron tetracarboxyphthalocyanine
GCE	Glassy carbon electrode
HOMO	Highest occupied molecular orbital
ITO	Indium tin oxide
LoD	Limit of detection
LUMO	Lowest unoccupied molecular orbital
MNP	Metal nanoparticles
MPc(s)	Metallophthalocyanine(s)
MWCNT	Multi-walled carbon nanotubes
NP(s)	Nanoparticle(s)

OPG	Ordered pyrolytic graphite
PANI	Polyaniline
Pc	Phthalocyanine
PdNPs	Palladium nanoparticles
PEDOP	Poly-ethylenedioxy pyrrole
Poly-CoTAPc	Polymer of cobalt tetraaminophthalocyanine
RDS	Rate determining step
RE	Reference electrode
Redox	Reduction/oxidation
SAM	Self-assembled monolayer
SEEC	Simultaneous electropolymerization and electro-click
SECM	Scanning electrochemical microscopy
SEM	Scanning electron microscopy
SPAuE	Screen-printed gold electrode
SWCNT	Single-walled carbon nanotubes
SWV	Square wave voltammetry
TAPc	Tetraaminophthalocyanine
$TBABF_4$	Tetrabutylammonium tetrafluoroborate
TEM	Transmission electron microscopy
TSPc	Tetrasulfonated phthalocyanine
UME	Ultramicroelectrode
UV-Vis	Ultraviolet-visible
WE	Working electrode
WHO	World health organization
XPS	X-ray photoelectron spectroscopy

LIST OF SYMBOLS

A_{eff}	Effective surface area
α	Electron transfer coefficient
Γ	Surface coverage
λ	Wavelength
Ω	Ohm
a	Radius
C	Concentration
C_{dl}	Double layer capacitance
d	Distance
e^-	Electron
ΔE	Peak to Peak potential separation
E_p	Peak potential
$E_{p1/2}$	Half wave potential
f	Frequency
F	Faraday's constant
I	Current
I_{buf}	Current produced in a buffer
I_{cat}	Catalytic current
I_{lim}	Limiting current
I_p	Peak current
k_{app}	Apparent electron-transfer rate constant
M	Molar concentration
n	Number of electrons transferred
Q	Charge

R	Universal gas constant
R_{ct}	Charge transfer resistance
R_s	Solution resistance
t	time
T	Temperature
υ	Scan rate
V	Volts
$Z_{imaginary}$	Imaginary impedance component
Z_{real}	Real impedance component
Z_w	Warburg impedance

LIST OF FIGURES

LIST OF SCHEMES

LIST OF TABLES

CHAPTER 1

INTRODUCTION

1.1. Metallophthalocyanine (MPc)

MPcs are used to modify electrodes in the presence of metal nanoparticles (Au, Pd and Ni). The aim of this work is to use MPc and metal nanoparticles to develop novel electrochemical sensors for various electrocatalytic reactions.

1.1.1. Discovery and general applications

The discovery of phthalocyanines (Pcs) dates back to 1907 when they were made accidentally during o-cyanobenzamide synthesis [1]. In 1929, Scottish Dyes obtained a patent for the preparation of Pcs from phthalic anhydride, a metal salt and ammonia [2]. In 1934, Linstead and co-workers deduced the structure of this macrocycle and coined the name phthalocyanine (phthalo from naphtha and cyanine meaning blue) [3]. Pcs are stable blue or green pigments which exhibit intriguing physical and chemical properties. These properties render them useful in many applications including as dyes and pigments, in organic semiconductors, as photosensitizer in photodynamic therapy, in nonlinear optical materials, as catalysts for photo oxidation, in optical recording materials and in gas sensing [4]. Fig. 1.1 shows the typical structures of unsubstituted and tetrasubstituted metallophthalocyanine.

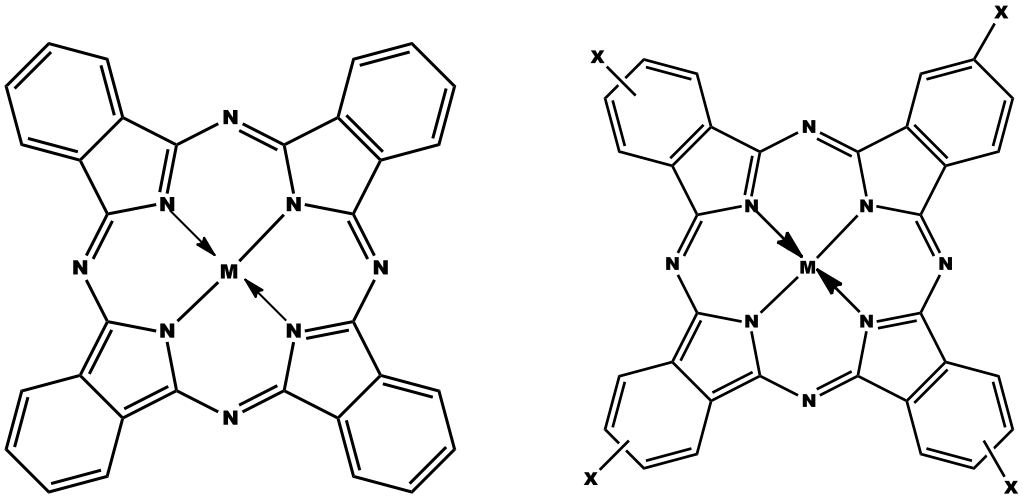

Fig. 1.1. Unsubstituted and tetrasubstituted Pcs. Where M can be Ni, Co, Fe; X can be COOH, NH_2, SO_3.

1.1.2. Electronic absorption spectra of metallophthalocyanine

The absorption spectra of metallophthalocyanines (MPcs) are characterized by two bands namely the Q band (between 600 and 700 nm) and Soret or B band (between 300 and 400 nm) [5]. Fig. 1.2 shows an example of the absorption spectra of MPcs [6]. Both bands are a result of $\pi \rightarrow \pi^*$ transitions. There are various factors which affect the position of the Q band. These include central metal, solvents, axial ligation, peripheral and nonperipheral substitutions. It can be seen from Fig. 1.2 that when the central atom change, the position of the Q band and the B band also changes [6].

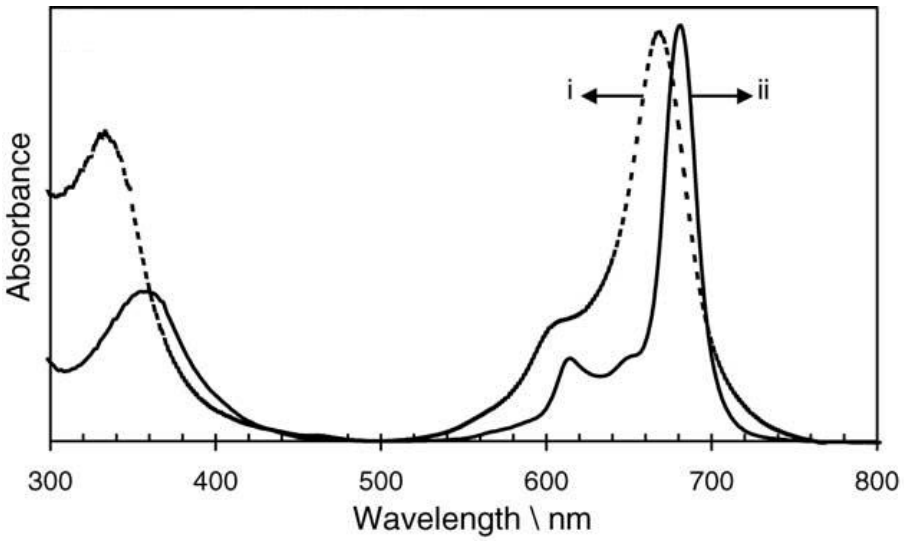

Fig. 1.2. Absorption spectra of CoTMPyrPc (i) and ZnTMPyrPc (ii) in DMF. TMPyrPc: tetramercaptopyrimidine phthalocyanines [6].

1.1.3. Metallophthalocyanine (MPc) synthesis

1.1.3.1. General synthesis of metallophthalocyanine

The synthesis of MPc involves the reaction of precursors (e.g. phthalic anhydride [5, 7], phthalimide [8], diiminoisoindoline [5], phthalonitrile [5, 7], o-cyanobenzamide [5] or phthalic acid [9]) with a metal salt and a catalyst. Scheme 1.1 shows the various synthetic routes for the synthesis of MPc.

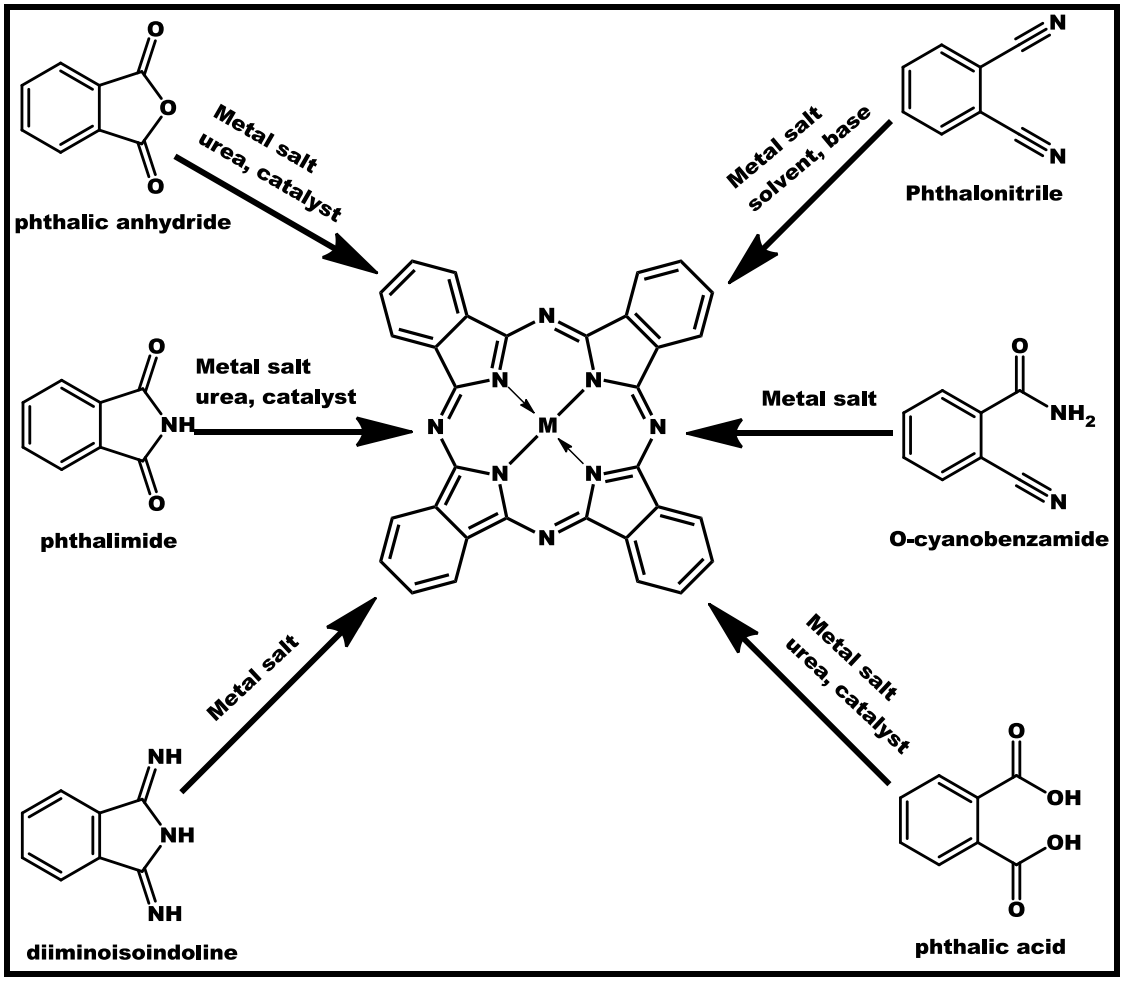

Scheme 1.1. General synthesis of metallophthalocyanine

1.1.3.2. Synthesis of tetrasubstituted metallophthalocyanine

Laboratory synthesis of tetrasubstituted MPc involves cyclotetramerisation of the substituted precursor in the presence of metal salt and catalyst. Scheme 1.2 shows the two routes for the synthesis of the tetrasubstituted MPc using 4-nitrophthalic acid [10] or phthalic anhydride [11]. Both methods were employed in this work. The complexes used in this work are well known and these are unsubstituted Ni phthalocyanine (NiPc), Ni

tetrasulfonated phthalocyanine (NiTSPc), Co tetraaminophthalocyanine (CoTAPc) and Fe tetracarboxyphthalocyanine (FeTCPc).

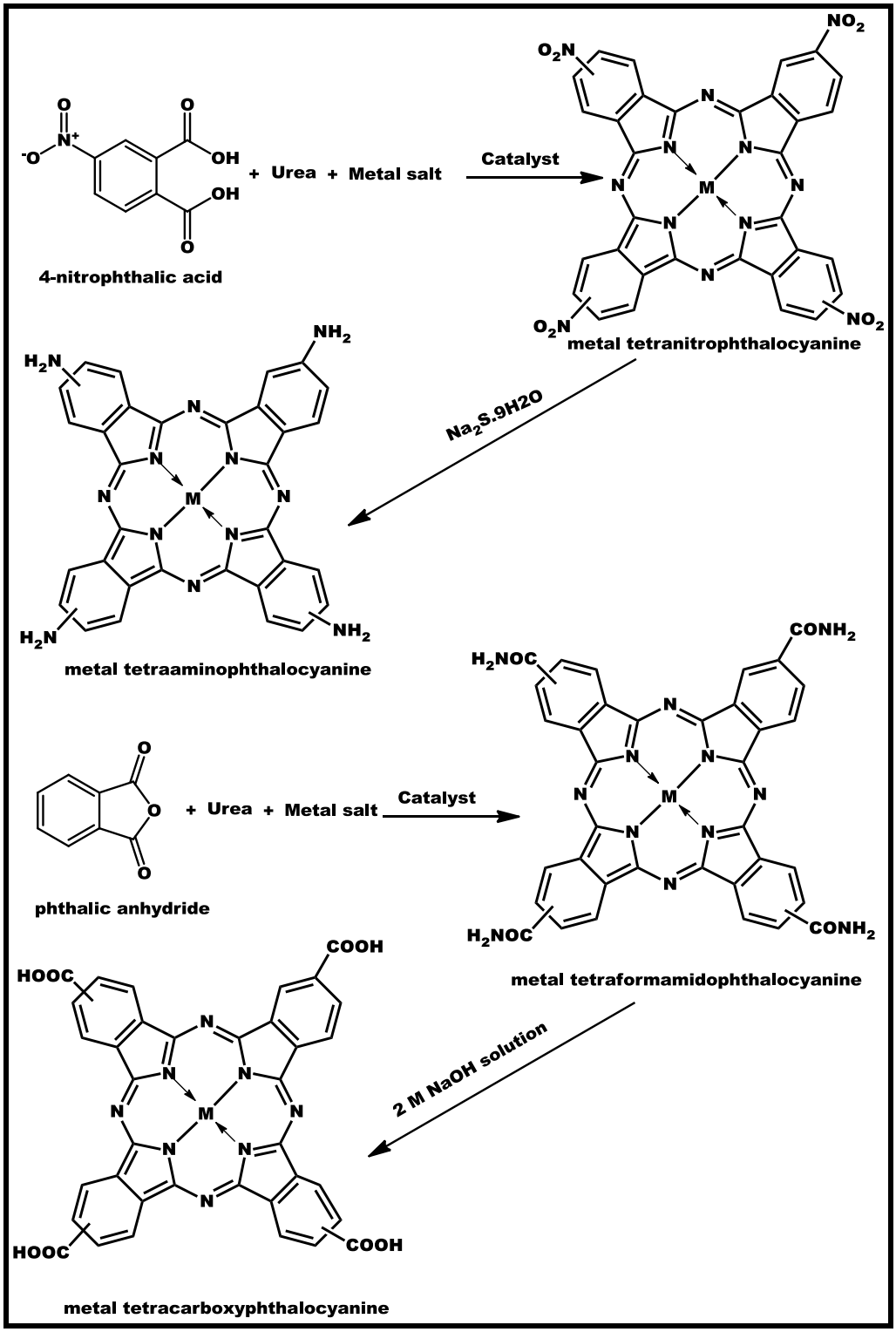

Scheme 1.2. Synthesis of tetrasubstituted phthalocyanine.

1.2. Methods of electrode modification using Pcs

Chemically modified electrodes involve attaching specific molecules to the surface of conventional electrodes [12]. This is crucial especially for electroanalysis where electrode modification provide surfaces which resist fouling, concentrates species, offers selectivity [13] and limit access of interference on a complex sample [14]. Several methods are available for modifying electrodes using MPc complexes. The methods used in this work include adsorption (drop and dry), electrodeposition, electropolymerization, electrografting and click chemistry.

1.2.1. Adsorption (drop and dry)

This is the simplest modification method. It involves dissolving the electrocatalyst (MPc) in an appropriate solvent followed by applying aliquot of the solution onto the electrode. The electrode would be left to dry in an inert environment [15, 16]. The advantage of adsorption is that it is a fast and easy method. In other words any Pc can be used without complications. However its limitation is that it is not reproducible. The drop and dry method was used in this work for attaching NiPc and NiNPs.

1.2.2. Electropolymerization

Electrochemical polymerization has been widely used to synthesize conducting polymers such as polyaniline, polypyrrole and polythiophene

[17]. It involves repetitive cyclization of the monomer at a predetermined potential. The Pc for polymerization must have a polymerizable group such as NH_2 or pyrrole. Scheme 1.3 shows the mechanism of polymer formation on an NH_2 substituted Pc [18]. The NH_2 group on the Pc undergoes oxidation to give a radical cation (Step I), followed by loss of the proton to produce radicals (Step II). The radicals produced, react together in what is termed oxidative coupling. The process repeats until a polymer is formed.

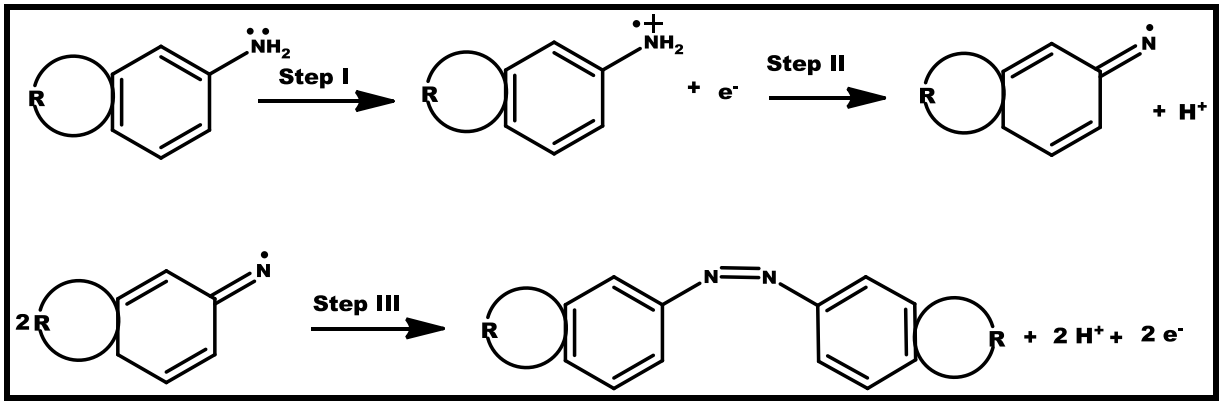

Scheme 1.3. Proposed mechanism of MTAPc complex. Step I oxidation of the amine, step II loss of proton from the radical cation and step III oxidative coupling of the monomers. R: rest of the MTAPc molecule [18].

Polymer formation is observed by difference in the successive scan and appearance of new peaks [19]. Fig. 1.3 shows polymerisation of CoTAPc in DMF [20]. As the number of cycles increase, the peak currents also increase and new peaks are formed, confirming that polymerization is taking place. The advantage of polymerization is that the thickness can be controlled by the number of polymer cycles. However, the Pc required have complicated synthetic procedures. NiPc derivatives also undergo polymerization and yield

polymers with O–Ni–O oxo bridges. Fig. 1.4 shows the transformation of ads-α-NiPc(OH)$_8$ to poly-α-Ni(O)Pc(OH)$_8$ in 0.1 M NaOH solution [21].

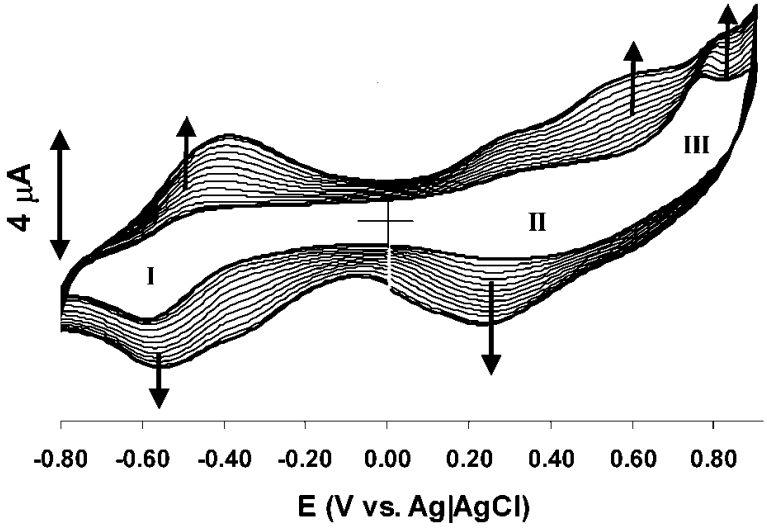

Fig. 1.3. Evolution of the cyclic voltammograms of 1 mM CoTAPc in DMF containing 0.1 M TBABF$_4$ during the formation of polymers on gold electrode [20].

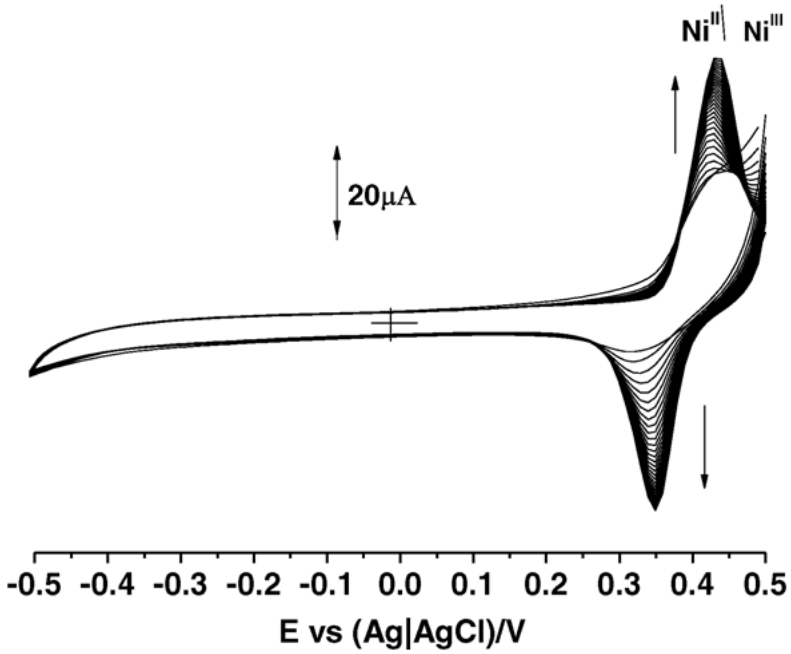

Fig. 1.4. Repetitive cyclic voltammogram of ads-α-NiPc(OH)$_8$ adsorbed on the OPG electrode in 0.1 M NaOH, forming poly-α-Ni(O)Pc(OH)$_8$. Scan rate = 100mV/s [21].

1.2.3. Electrografting

Electrografting allows the deposition of very thin organic film via very strong substrate-molecule link [22]. In general, the organic films formed are insulating, highly adherent and optically transparent [23]. Due to the covalent bond formed between the substrate and organic material, grafting has found use in sensors, protection against corrosion, soldering and lubrication [23]. For this work, aromatic diazonium salts were to modify the electrodes. The mechanism for the diazotization reaction involves the reduction of the diazonium group resulting in the formation of an aryl radical with the release of N_2 as shown in reaction Scheme 1.4 [24].

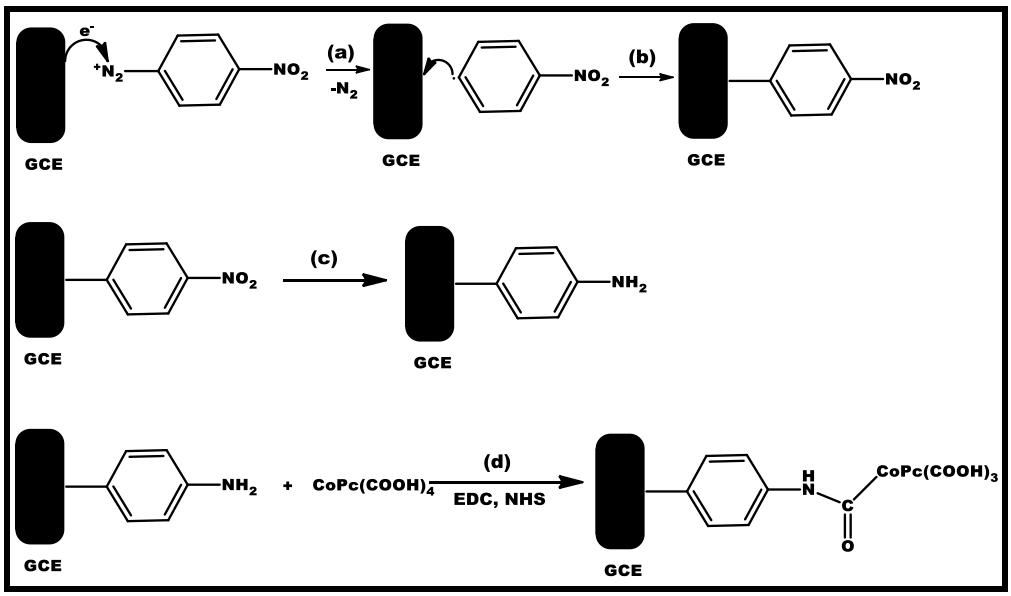

Scheme 1.4. The processes in grafting may involve as an example (a) electrochemical reduction of aryldiazonium salt, (b) grafting of aryl radical, (c) electrochemical reduction of NO_2 group and (d) attachment of Co tetracarboxyphthalocyanine (CoTCPc) using EDS and NHS coupling agents. EDC: ethyl(dimethylaminopropyl) carbodiimide, NHS: N-Hydroxysuccinimide [24].

Fig. 1.5 shows the CV for the grafting of the diazonium salt onto the glassy carbon electrode [24]. The difference between scan number 1 and scan number 2 is a typical behaviour of the successful grafting of GCE surface. The inhibition of peaks in scan number 2 is caused by blocking behaviour of nitrophenyls on the GCE surface.

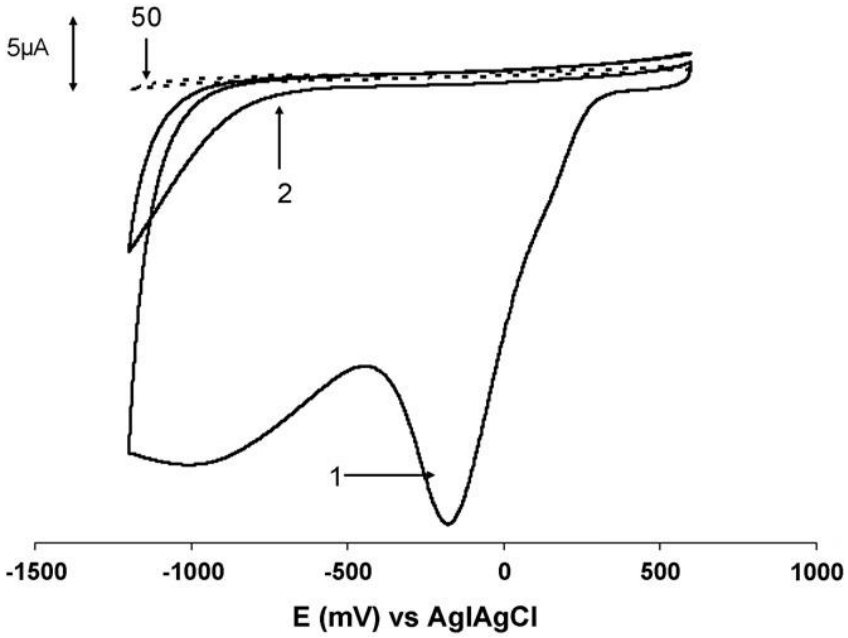

Fig. 1.5. Cyclic voltammograms of a GCE recorded in 0.01 M 4-nitrobenzenediazonium tetrafluoroborate, in ACN containing 0.1 M $TBABF_4$. Numbers refer to scan numbers. Scan rate = 200 mV/s [24].

Table 1.1. MPc linked through grafting and/or click chemistry for the modification of the electrode.

MPc	**Electrode**	**Method of attachment**	**Analytes**	**Ref**
CoTCPc	GC	Grafting followed by coupling MPc with EDS and NHS	Thiocyanate	24
BPR	ITO	Grafting and SAM	_	25
NiTSPc	GC	Electrodeposition and grafting	Nitric oxide	26
CoTAPc, MnTAPc	Au	Grafting followed by coupling MPc with BDCA	H_2O_2 and glucose	27
CoTAPc	SPAu	Grafting followed by coupling MPc with BDCA	H_2O_2	28
FePc	GC	Grafting, click chemistry and axial ligation	Hydrazine	29, 30
TA-CoPc	GC	Electropolymerization and click chemistry	Eserine	31

BPR: bis(4,4-bipyridine)(phthalocyaninato)ruthenium(II), TA-CoPc: terminal-alkynyl substituted cobalt phthalocyanine, GC: glassy carbon, ITO: indium tin oxide, SPAu: screen-printed gold, SAM: self-assembled monolayer, EDC: ethyl(dimethylaminopropyl) carbodiimide, NHS: N-Hydroxysuccinimide and BDCA: benzene-1,4-dicarbaldehyde.

Table 1.1 shows Pc that were attached onto the electrode after grafting [24-30]. The advantage of electrografting is that R group (NO_2 in Scheme 1.4) which is attached may be linked with other reactive groups. For example, if the R group is azide, click chemistry with an alkyne group can be employed to add other functional groups. The major drawback is lack of control in

terms of thickness and organization [32]. This work reports on the grafting followed by click chemistry for the first time, using GCE.

1.2.4. Click chemistry

Click chemistry was first introduced by Sharpless et al [33] to denote the development of a set of powerful, reliable and selective reactions for the rapid synthesis of useful compounds. The characteristics of click reactions are simple reaction conditions, generation of products in high yields, inoffensive by-products, stereospecificity and minimal requirements for product purifications [33]. For this work, our focus will be on the Huisgen cycloaddition of azides and alkynes [34]. The azide-alkyne cycloaddition reaction enables the unreactive (azide and alkyne groups) to react in the presence of Cu^{1} catalysts [35]. The click reaction is shown in Scheme 1.5. The click reaction requires the use of alkyne or azide functionality, copper salt (mostly $CuSO_4$) and ascorbic acid or sodium ascorbate. The copper salt is the source of Cu catalyst, ascorbic acid or sodium ascorbate function to reduce Cu^{II} to Cu^{I}. The common solvent system used is water and ethanol in the ratio of 1:1.

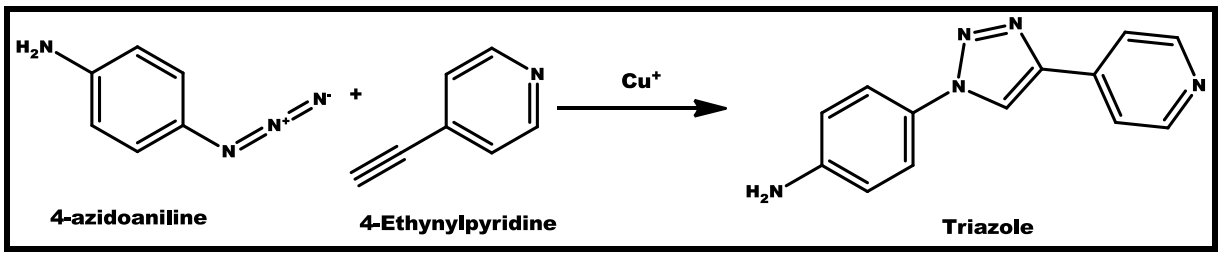

Scheme 1.5. The azide-alkyne cycloaddition reaction.

Click chemistry reaction can be performed in an electrochemical environment. This is done by reducing Cu^{II} to Cu^{I} electrochemically. This reaction has been termed electro-click. The biased potentials applied for the electro-click reactions are in the range -0.2 V to -0.5 V [36-38]. The rationale being that these potentials are roughly 300 mV negative of the $Cu^{(II/I)}$ standard potential of the catalyst, ensuring that Cu^{I} is formed at the electrode surface. The other reason is during the reduction of Cu^{II} to Cu^{0}, a small amount of Cu^{I} is produced which is enough to catalyse the click chemistry reaction [39]. For this work, electro-click has been employed as it is fast and flexible as far as immobilising molecules on the surface compared to the chemical approach.

From Table 1.1 [29-31], it can be seen clearly that not much work has been done in click chemistry using MPc. FePc and CoPc were used for analysis of hydrazine and serine respectively, Table 1.1. Coates and Nyokong, used electrografting to deposit the azide groups, perform click chemistry using ethynylpyridine and link the FePc through axial ligation [30]. The electrode modification pathway is shown in Scheme 1.6.

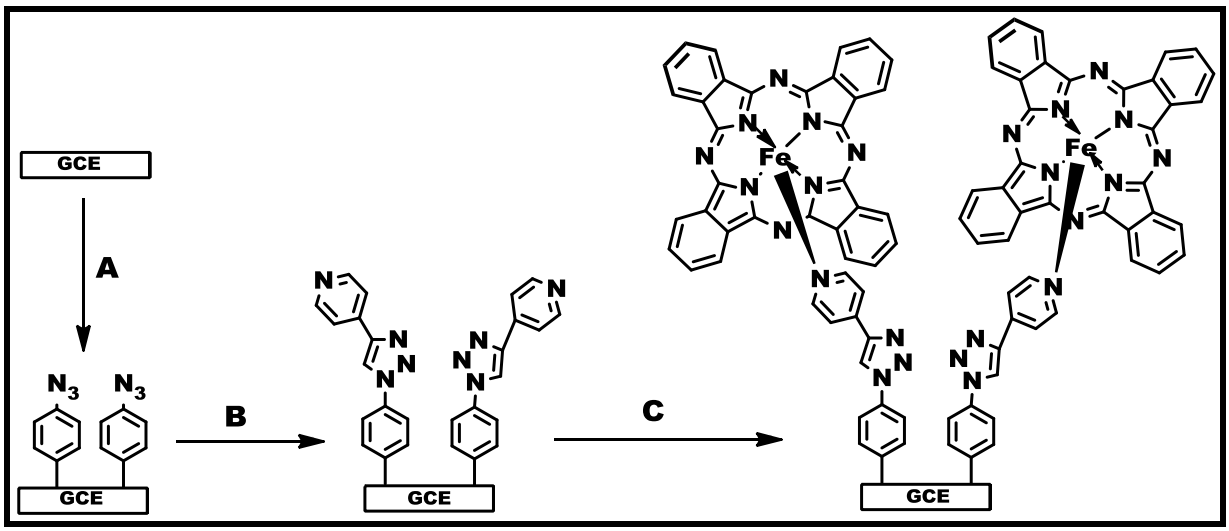

Scheme 1.6 Attachment of FePc through: (A) grafting of the bare GCE by electrochemical reduction of 4-azidodiazonium, (B) click chemistry with 4-ethynylpyridine and (C) axial ligation of FePc [30].

Ipek et al, used electropolymerization to deposit the azide group followed by either click chemistry or electro-click chemistry with terminal-alkynyl substituted cobalt phthalocyanine [31]. In this work, we used two routes. The first route involves electropolymerization to deposit the azide groups, electro-click with ethynylpyridine and link with Fe tetracarboxyphthalocyanine (FeTCPc) through axial ligation. Second route involve simultaneous electropolymerization and electro-click reaction followed by linking with FeTCPc through axial ligation. This is the first time that a substituted MPc is being linked through axial ligation and the comparison of two routes of click chemistry.

1.2.5. Characterization of chemically modified electrodes

The chemically modified electrodes in this work were characterized using cyclic voltammetry, electrochemical impedance spectroscopy (EIS) and

scanning electrochemical microscopy (SECM), scanning electron microscopy (SEM) and X-ray photoelectron spectroscopy (XPS).

1.2.5.1. Cyclic voltammetry (CV)

In order to check the conductivity of the modified electrode and to calculate surface coverage etc, the CV of the electrodes in ferricyanide solution are often recorded. Fig. 1.6 shows the CV of electrode modified through polymerization of MTAPc [20]. The behaviour of different metals can be noted, CoTAPc had an increase in the peak current while MnTAPc had a decrease in peak current compared to the bare gold electrode.

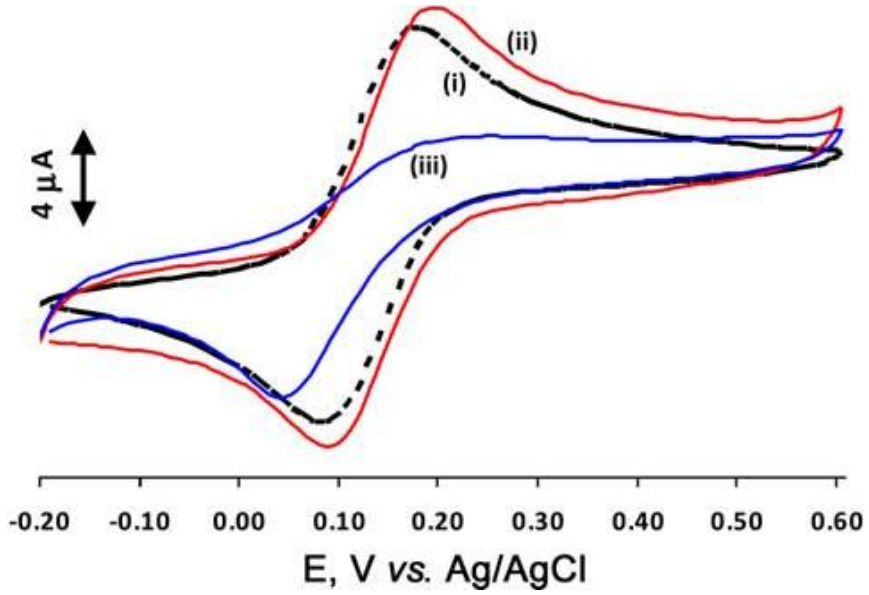

Fig. 1.6. Cyclic voltammograms of (i) bare, (ii) poly-CoTAPc and (iii) poly-MnTAPc-modified gold electrode in 1 mM $[Fe(CN)_6]^{3-/4-}$ in 0.1 M KCl [20].

The tendency to block electron transfer was observed in Fig 1.5 and further confirmation can be obtained by cycling the grafted electrode in ferricyanide. Fig. 1.7 shows the behaviour of electrodes in ferricyanide [30]. The Fe^{III}/Fe^{II}

redox couple observed in the bare electrode has disappeared showing that grafting causes blockage of electron transfer.

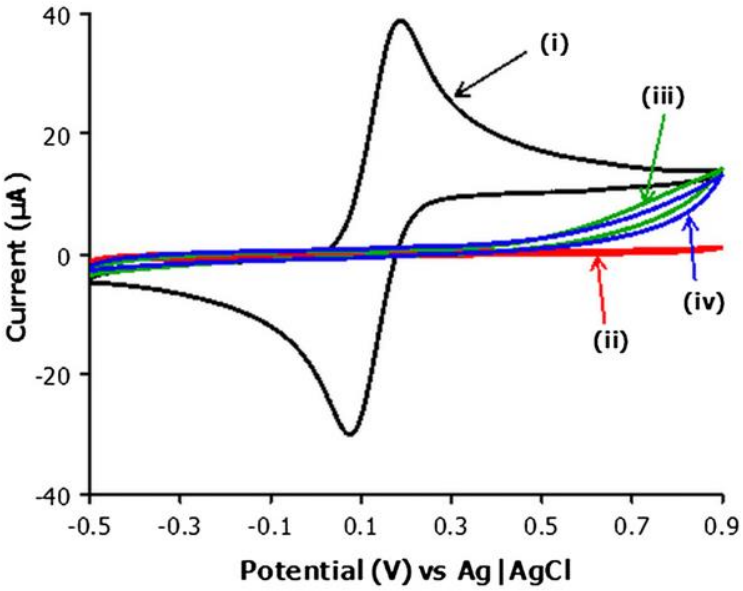

Fig. 1.7. Cyclic voltammograms of (i) bare GCE, (ii) grafted GCE, (iii) grafted GCE after click chemistry in ethynylpyridine, and (iv) grafted GCE after click chemistry in ethynylpyridine and 3 h in 1 mM FePc in DMF [30].

From Fig. 1.6, the effective surface area and surface roughness factor for the modified electrodes can be determined using $[Fe(CN)_6]^{3-/4-}$ redox system and applying Randles–Sevcik Eq. 1.1 for reversible systems [40]:

$$I_p = 2.69 \times 10^5 n^{3/2} A_{eff} C D^{1/2} v^{1/2} \qquad (1.1)$$

where I_p, n, A, C, D and v are the peak current, the number of electrons involved in the reaction, the effective surface area, the concentration of the reactant, the diffusion coefficient of the reactant species and the scan rate, respectively. From literature, the D value for $K_3[Fe(CN)_6]$ = 7.6 x 10^{-6} cm^2 s^{-1} [41] and n = 1.

The CV obtained in the buffer solution in the absence of a redox probe allows for the determination of the surface coverage. Using the effective area of the electrode, the surface coverage may be calculated using Eq. 1.2a or 1.2b [42].

$\Gamma = \frac{Q}{nFA}$ (1.2a) or $I_p = \frac{n^2F^2\,vA_{eff}\Gamma}{4RT}$ (1.2b)

where Γ is the film surface coverage, Q is the charge obtained from the peak area of interest, n is the number of transferred electrons, F is the Faraday constant and A is the effective area of the electrode area, I_p is the background corrected peak current, R is the universal gas constant and T is the temperature (298 K). Surface coverage gives a measure of how electrocatalytic the chemically modified electrode would be in an electrochemical reaction.

1.2.5.2. Electrochemical impedance spectroscopy (EIS)

EIS measures the frequency response of a system by measuring impedance (Z). This is achieved by applying a small AC signal over a range of frequencies at a potential determined by CV studies. When the frequencies change, the contribution of each element in the Randles circuit also changes. There are two main plots determined in EIS, Nyquist plots and Bode plots.

Nyquist plot also known as complex-plane impedance plot. Fig. 1.8 shows an example of the Nyquist plot [43]. Nyquist plots have the advantage that

activation-controlled processes with characteristic time-constants exhibits impedance arcs and the shape of the curves give insight into the probable reaction mechanism [44]. The semi-circles and straight line portions represent charge transfer (R_{ct}) and diffusion controlled processes, respectively. The disadvantage of the Nyquist plot is that frequency is not explicitly shown as a result, the Bode plots are employed to compliment the Nyquist plot [45].

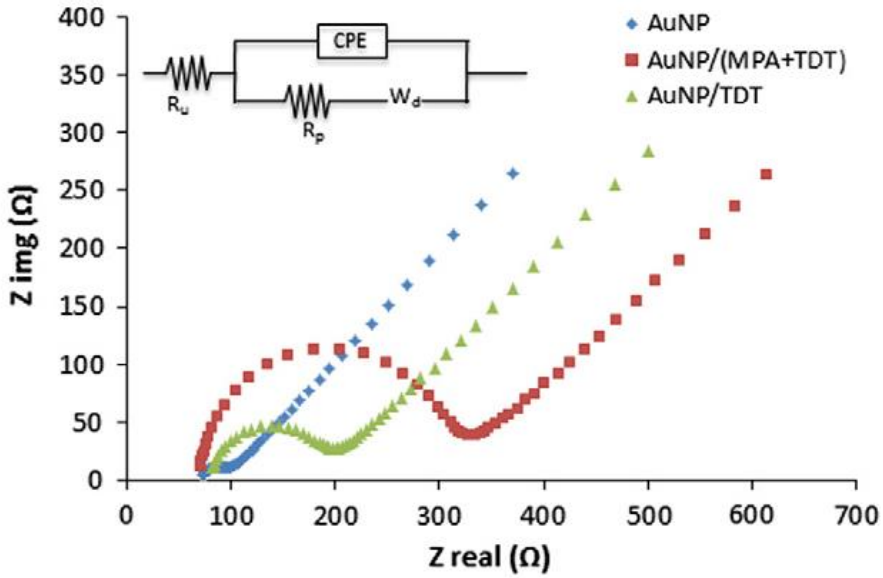

Fig. 1.8. Nyquist plots of the AuNP-modified electrodes with the binary SAMs (MPA and TDT, 1:1). Inset: The equivalent electrical circuit used to fit all the experimental results. MPA: 3-mercaptopropionic acid and TDT: 1-tetradecanethiol [43].

Fig. 1.9 shows the Bode plots of the various modified electrodes [43]. Bode plots refers to representation of the impedance magnitude and phase angle as a function of frequency. Bode plot shows the frequency-dependence of the impedance of the CME. The Bode plots confirm the structural differences

between the modified and the bare GCE. The slight changes in the phase angle and frequencies confirmed that oxidation processes were taking place at the modified surfaces rather than on the bare GCE.

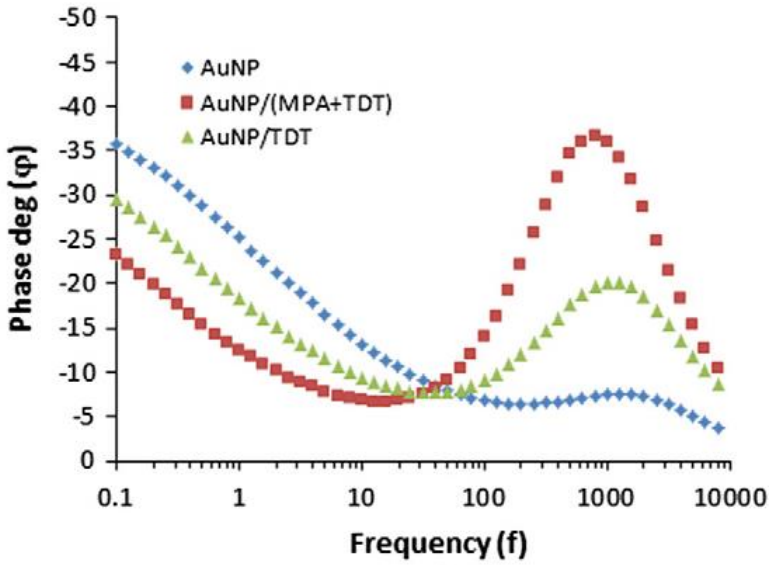

Fig. 1.9. Bode plots of the AuNP-modified electrodes with the binary SAMs (MPA and TDT, 1:1). MPA: 3-mercaptopropionic acid and TDT: 1-tetradecanethiol [43].

1.2.5.3. Scanning electrochemical microscopy (SECM)

SECM is a powerful electrochemical tool used to investigate heterogeneous electron transfer reaction at the interface [46]. SECM provides information on the electrochemical process in which the target molecules are involved, giving chemical and topographic information about the investigated surface [47]. SECM involves the measurement of current through the ultramicroelectrode (UME) when it is held or moved in a solution in the vicinity of the substrate. UME is an electrode with a radius of order of few

nm to 25 µm. UME is also known as the tip. In this work, the feedback mode was used for the operation of the SECM. In the feedback mode, the current of the tip is monitored. There are two types of feedback namely positive and negative feedbacks. The positive feedback is when the current at the tip increase due to regeneration of the oxidising species at the substrate (conducting) while negative feedback occurs when current at the tip is decreased due to blockage of diffusion by solution species at the substrate (insulating) [48]. Apart from characterizing the modified surfaces, SECM can be used as a tool for surface modification [48]. This process is described as micropatterning using electrochemical techniques. Fig. 1.10 shows the approach curves obtained by Coates et al [49]. The area where grafting was done was insulating (blocking electron transfer) and as a result the current was decreasing as the tip approaches the grafted spot (curve 1). On the other hand current was increasing on the surface where grafting was not performed (curve 2).

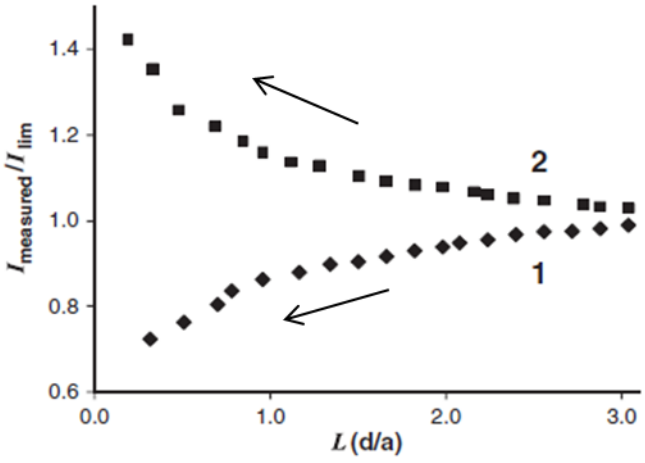

Fig. 1.10. SECM approach curves for a 12.5 µm diameter Pt in 5 mM $Ru(NH_3)_6Cl_3$ in 0.1 M KCl aqueous solution above the locally electrografted

area of the gold substrate (curve 1) and 500 µm away (curve 2). (E_{tip} = − 0.45 V vs. Ag/AgCl; I_{lim} = 9.8 nA). Adapted from [49].

In order to get topographical information about the area where the grafting was taking place, an area scan may be taken, Fig. 1.11 [49]. The grafted spot can be seen clearly, having the lowest current.

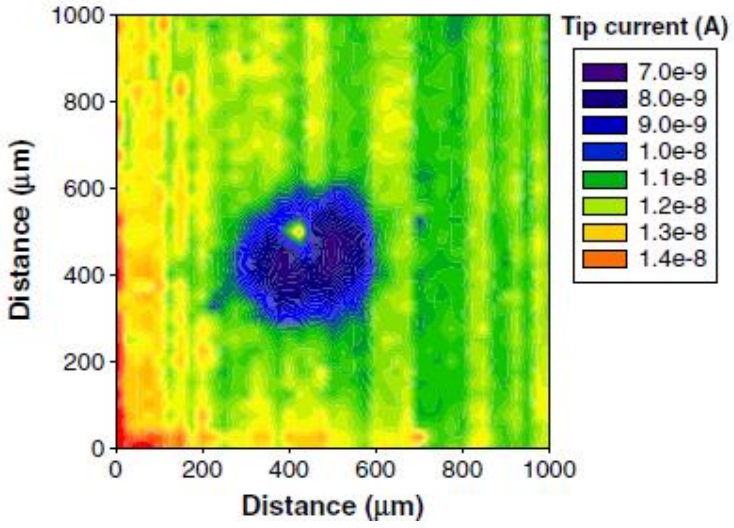

Fig. 1.11. SECM images of locally electrografted gold substrate with a Pt tip in 5 mM $Ru(NH_3)_6Cl_3$ in 0.1 M KCl aqueous solution (E_{tip}=−0.45 V vs. Ag/AgCl; I_{lim}=9.8 nA for 12.5 µm diameter). The tip was scanned at 50 µm/s. The electrografting was obtained by a Pt tip of 12.5 µm diameter positioned 1 µm above the gold surface [49].

In this work, the substrate (macroelectrode) was modified by electrografting of 4-azidobenzenediazonium. The novel micropatterning was achieved by performing the localized click reaction using ethynylferrocene, holding the tip at the potential of -0.3 V. This was the first time it was done on the glassy carbon substrate and the evidence was shown using SECM imaging.

1.2.5.4. Scanning electron microscopy (SEM)

SEM is a versatile instrument for the examination and analysis of microstructure morphology and chemical composition characterization [50]. In SEM, a fine probe of electrons is focused on a specimen and scanned along a pattern of parallel line [51]. Numerous signals are given out as a result of the impact of the incident electrons that are collected to form an image or to analyse the sample surface [51]. SEM gives information about the sample's topography and composition. Fig. 1.12 shows the SEM image of the gold nanoparticles deposited on the glassy carbon electrode [52]. The distribution, size and roughness of the gold nanoparticles can be seen clearly in Fig. 1.12. The advantage of SEM is that it has high spatial resolution, large depth of field and simple specimen preparation [50].

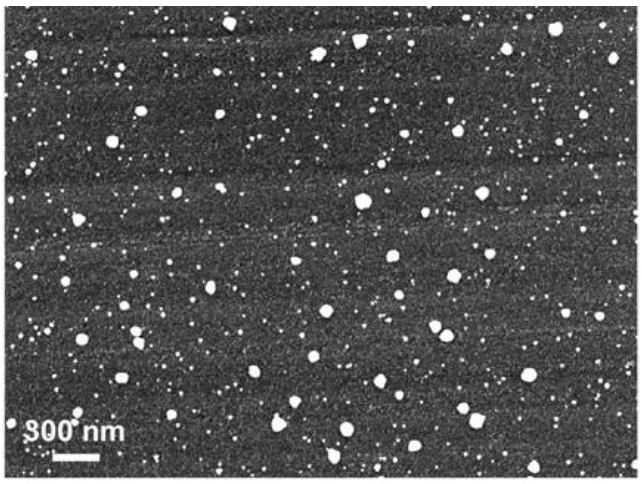

Fig. 1.12. FEG-SEM image of AuNPs–GC electrodes prepared by CV from a 0.25 mM $HAuCl_4$ solution in 0.1 M $NaNO_3$. Adapted from [52].

1.2.5.5. X-ray photoelectron spectroscopy (XPS)

XPS is also known as electron spectroscopy chemical analysis (ESCA). XPS is a widely used analytical technique for investigating the chemical composition of the solid surface [53]. XPS involves irradiation of the solid surface with X-ray and sorting the emitted electrons by energy [53]. The spectrum obtained is a plot of the number of emitted electrons versus their kinetic energy. Fig. 1.13 shows the XPS spectra of grafted GCE (i), grafted GCE following click chemistry with ethynylpyridine (ii) and grafted GCE after click chemistry in ethynylpyridine and immersion in FePc (iii). Peak heights can give quantitative data and peak position and separation allows identification of chemical state [53]. The main purpose of XPS is to determine the elements present and their oxidation states when attached to the GCE surface [30].

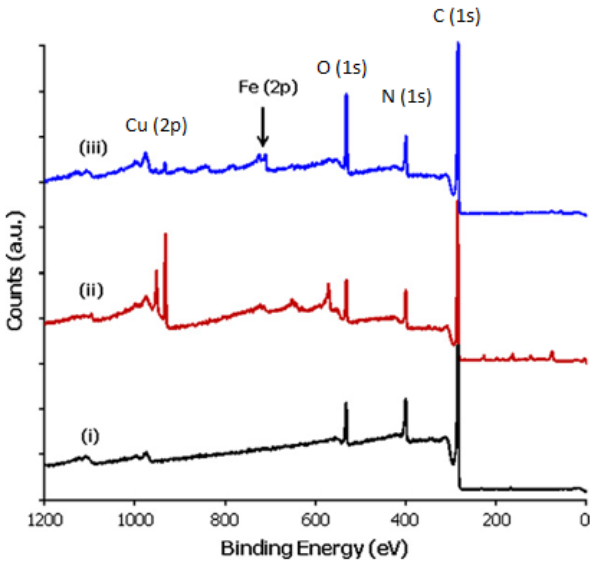

Fig. 1.13. XPS spectra for: (i) grafted GCE, (ii) grafted GCE following click chemistry with ethynylpyridine and (iii) grafted GCE after click chemistry in ethynylpyridine and immersion in FePc [30].

Atomic force microscopy can also be used to obtain the topographic information from the electrode. However, it was not used in this work.

1.3. Metal Nanoparticles

1.3.1. Properties

Metal nanoparticles are defined as particles that have at least one dimension in the nanometer size range (1-100 nm) [54]. Due to their small size, metal nanoparticles have physical, chemical and electronic properties that differ from the bulk metals [55]. Metal nanoparticles exhibit quantum size behaviour due to the existence of discrete electronic energy levels and the loss of overlapping electronic bands [56]. Metal nanoparticles have higher surface to volume ratio compared to the bulk form. This means, a larger fraction of the active atoms are on the surface. Owing to these unique properties, metal nanoparticles have applications in chemical sensors, biosensors, photovoltaic device, drug delivery, fuel cells, industrial lithography and catalysis [55].

1.3.2. Synthesis

Various methods have been employed to synthesize metal nanoparticles. The most common ones are categorized under the following titles namely physical methods, chemical methods and electrochemical methods. A physical method involves evaporation of a metal in a vacuum by laser

ablation [57]. The limitation of this method is that it is very difficult to control the size of the nanoparticles formed. Though in theory the size can be controlled be regulating the rate of evaporation and also using inert gases. Chemical methods mostly involve reduction of metal salts dissolved in appropriate solvents to produce metal nanoparticles of varying size distribution [58]. The size of nanoparticles formed maybe controlled by using protecting or capping agents. Frequently used protecting agents are surfactants (cetyltrimethylammonium bromide (CTAB)) and polymeric ligands (polyvinyl pyrrolidone (PVP)). The limitation of this method is that the nanoparticle have a tendency of making a strong bond with these ligands and therefore not very effective in a chosen application. For electrochemical applications, the nanoparticles containing these capping agents may need activation step before analysis. The electrochemical methods involve electrodepositing the metal nanoparticles on the working electrode by applying potential steps [59]. The size of metal nanoparticles can be controlled by adjusting the potential steps and deposition time.

Bimetallic nanoparticle electrocatalysts are composed of nanoparticles based on two different metals and show improved catalytic activity compared to pristine metal nanoparticles. The advantage of the bimetallic nanoparticles is that one has high performance in electroactivity and the other influences the electrocatalytic activity or prevents poisoning problem [60]. The unique electrocatalytic behaviour of bimetallic nanoparticles is attributed to their electronic structures which are quite distinct from those of the pure nanoparticles [61]. Many researchers have observed an enhanced

performance in electrocatalytic activity and attributed it to the synergetic effect of the bimetallic nanoparticles.

Electrochemical methods were employed to synthesize metal nanoparticles (over other methods) in this thesis. Electrochemical methods have been chosen because they are simple, rapid and flexible. The other advantages of this method include low cost, high growth rate at room temperature, reproducible, environmental friendliness and easier control of size and shape. For electrocatalytic activities, the electrodeposited metal nanoparticles are active and ready for use in analysis. On the other hand the metal nanoparticles made from the other methods, need to be cleaned and then put onto the electrode, which makes the process tedious.

1.4. Electrocatalysis

Electrocatalysis is a term used to describe the processes occurring at the electrode surface. Fig. 1.14 shows the response of electrode bare and modified to L-cysteine [62]. Electrocatalysis is given as the increase in currents and the lowering of the overpotential in comparison to the bare electrode. The mechanism in which electrocatalysis is achieved in MPc and in metal nanoparticles used in this study are described below.

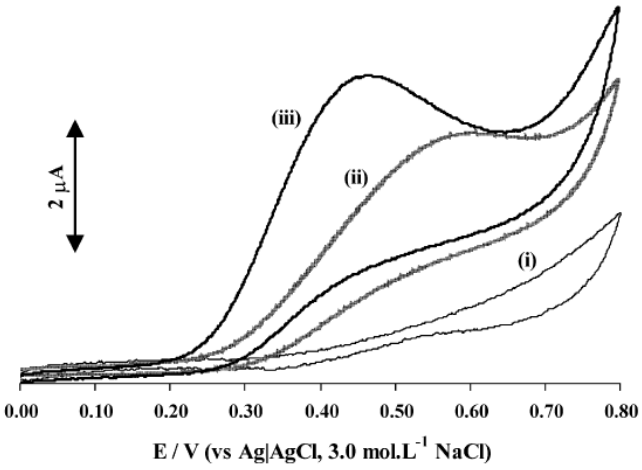

Fig. 1.14. Cyclic voltammetric responses of (i) bare gold electrode, (ii) Au-ME SAM and (iii) Au-ME-FeTCAPc SAM in pH 4 solution containing 0.1 mM L-cysteine. ME-SAM: mercaptoethanol self-assembled monolayer, TCAPc: tetra-carboxylic acid chloride phthalocyanine. Adapted from [62].

1.4.1. MPc alone

The MPcs to be employed in this work are NiPc, NiTSPc, CoTAPc and FeTCPc. When NiPc and its derivative are adsorbed on the electrodes, they exhibit the Ni^{III}/Ni^{II} redox couple in basic medium. Repetitive cyclization of NiPc and its derivatives in basic medium produces O–Ni–O oxo bridges which in turn improve the electrocatalytic performance of NiPc and their derivative. Ni^{III}/Ni^{II} redox couple is the one responsible for the electrocatalysis of many analytes. The mechanism of the electrocatalysis is shown in Eqs. 1.3 and 1.4.

$$Ni^{II}Pc \rightarrow [Ni^{III}Pc]^{+} + e^{-} \quad (1.3)$$

$$[Ni^{III}Pc]^{+} + A \rightarrow Ni^{II}Pc + P \quad (1.4)$$

where A is the analyte and P is the product.

Metallophthalocyanine with metals that have orbitals which possess energy level lying between the highest occupied molecular orbital (HOMO) and the lowest unoccupied molecular orbital (LUMO) of the Pc will exhibit redox processes on both the central metal and the ring. These metals include Cr, Mn, Co and Fe. Depending on the nature of solvents, CoPc and FePc show M^{III}/M^{II} and M^{II}/M^{I} redox potentials (where M is either Co or Fe) [63]. However, M^{III}/M^{II} is involved in oxidation reactions. The mechanism would be similar to the one shown for NiPc. When M^{II}/M^{I} redox potentials are involved in the electrocatalyzing a reduction reaction, the mechanism is given in Eqs. 1.5 and 1.6.

$$M^{II}Pc + e^{-} \rightarrow M^{I}Pc \quad (1.5)$$

$$M^{I}Pc + A \rightarrow M^{II}Pc + P \quad (1.6)$$

1.4.2. Metal nanoparticles alone

1.4.2.1. Electrocatalytic behaviour of Ni nanoparticles

Nickel nanoparticles are used as electrode modifiers for carbon electrodes because they are a suitable substitute for noble metals. They are also produced at low cost and have good electrical conductivity [64]. They have been used to electrocatalyse a number of reactions which include detection of bisphenol A [65], detection of ethanol [66], electrooxidation of propargyl alcohol [67] and oxygen reduction reactions [68]. Once the Ni nanoparticles are exposed to the alkaline medium, they react instantly to form a film of the hydrous Ni(II) oxide species, α-$Ni(OH)_2$. The α-$Ni(OH)_2$ species may dehydrate

to form β-$Ni(OH)_2$ [68]. During cyclization in alkaline medium, $Ni(OH)_2$, will react with the hydroxyl group to form a Ni^{III} species, NiOOH as shown in Eq. 1.7.

$$Ni(OH)_2 + OH^- \rightarrow NiOOH + H_2O + e^- \quad (1.7)$$

The mechanism of Ni nanoparticles electrocatalysis involve the Ni^{II} and Ni^{III} species, Eqs. 1.8 and 1.9.

$$Ni^{II} \rightarrow Ni^{III} + e^- \quad (1.8)$$

$$Ni^{III} + analyte \rightarrow Ni^{II} + products \quad (1.9)$$

Both NiPc and NiNP form Ni oxo complexes and hence the combination of the two was employed to see the effects on electrocatalysis.

1.4.2.2. Electrocatalytic behaviour of Au nanoparticles.

Gold nanoparticles offer high electrocatalytic activities towards several electrocatalytic reactions such as electrooxidation of hydrogen peroxide [69], glucose [70] and methanol [71]. This is due to their unique physical and chemical properties. Their electrocatalytic performance is dependent on size, shape and crystallographic orientations [72]. These characteristic are particularly important to AuNPs since the bulk gold is less reactive, whereas Ni can still catalyse in the bulk state. Of importance is the ease at which AuNPs can be electrodeposited on the carbon electrodes. The reaction involved in the electrodeposition is the reduction of gold(III) salt ($HAuCl_4$) to gold nanoparticles (Au^0). The mechanisms of gold electrocatalysis may proceed via adsorption of the analyte [70]. For example in glucose electrooxidation, there is formation of $(OH)_{ads}$ on the Au nanoparticles

surface. This is followed by interaction of adsorbed glucose and $(OH)_{ads}$. Eqs. 1.10 to 1.12 [73].

$$Au + H_2O \rightarrow Au(OH)_{ads} + H^+ + e^- \quad (1.10)$$

$$Au(OH)_{ads} + C_6H_{12}O_6 \rightarrow Au(C_6H_{11}O_6)_{ads} + H_2O \quad (1.11)$$

$$Au(C_6H_{11}O_6)_{ads} \rightarrow C_6H_{10}O_6 + Au + H^+ + e^- \quad (1.12)$$

1.4.2.3. Electrocatalytic behaviour of Pd nanoparticles.

Palladium nanoparticles are known to electrocatalyse a wide variety of reactions which includes electrooxidation of formic acid [74], ethanol [75] and hydrazine [76]. Pd nanoparticle has propensity to absorb hydrogen, thus it easily form hydrides on its surface [77]. This behaviour may affect positively or negatively the electrocatalytic activities, depending on the nature of reaction. In aqueous medium, Pd nanoparticles easily form PdO or PdOH as shown in Eqs. 1.13 and 1.14 [77].

$$Pd + H_2O \rightarrow PdO + 2H^+ + 2e^- \quad (1.13)$$

$$Pd + H_2O \rightarrow PdOH + H^+ + e^- \quad (1.14)$$

In electrochemical reactions, further oxidation of PdO is known and it gives rise to PdO_2. The Pd oxides can also be reduced back to Pd nanoparticles. The electrooxidation of Pd nanoparticles and reduction of its surface oxides lead to changes in the surface morphology and micro-roughness [77]. This in turn increase the electrode's real surface area through the formation of surface defects namely clusters of adatoms, vacancies and rearrangement of atoms at grain boundaries [77]. The mechanism of ethanol electrooxidation (as an example) is shown in Eqs. 1.15 to 1.17 [75].

$$Pd + OH^- \rightarrow Pd - OH_{ads} + e^- \quad (1.15)$$

$$Pd - (CH_3CH_2OH)_{ads} + 3OH^- \rightarrow Pd - (COCH_3)_{ads} + 3H_2O + 3e^- \quad (1.16)$$

$$Pd - COCH_3)_{ads} + Pd - OH_{ads} \rightarrow Pd - CH_3COOH + Pd \quad (1.17)\ \text{rds}$$

1.4.2.4. Electrocatalytic behaviour of bimetallic nanoparticles

Bimetallic nanoparticles (core-shell or alloy) exhibit remarkable electrocatalytic activities due to their enhanced properties such as selectivity, stability and electrochemical reversibility for redox reactions, which are different from their corresponding monometallic nanoparticles [78]. Of the bimetallic nanoparticles available, Au-Pd nanoparticles have been widely used for a variety of electrochemical reactions [79-82]. In the Au-Pd nanoparticle, there is stronger adsorption of analytes on the surface thus facilitating high electrocatalytic performance. The superior behaviour of Au-Pd nanoparticles can be explained by electronic effects and bi-functional mechanism [83]. The mechanism of methanol oxidation (as an example) on the Au-Pd nanoparticle surface involves adsorption of methanol followed by dehydrogenation of methanol to form CO_{ads}. CO_{ads} further oxidizes to give CO_2 according to Eqs. 1.18 and 1.19 [83].

$$CO_{ads} - Pd - Au - OH_{ads} \rightarrow Pd - CO - Au - OH$$
$$\rightarrow Pd - Au - CO - OH$$
$$\rightarrow Pd - Au - COOH \quad (1.18)$$

$$Pd - Au - COOH + OH_{ads} \rightarrow Pd - Au + CO_2 + H_2O \quad (1.19)$$

In the methanol oxidation, Pd nanoparticles act as primary sites for dehydrogenation of methanol while Au nanoparticles enhance the activity and poison tolerance of neighbouring Pd nanoparticle [83].

1.4.3. Electrocatalytic behaviour of metallophthalocyanine-metal nanoparticles (MPc-MNP) hybrids

Table 1.2. Application of MPc-MNP modified electrode

MPc-NP	**Electrodes and MPc-MNP formation**	**Modification methods**	**Analytes**	**Ref**
MWCNTs-CoPc/GR-AuNPs/CS-AuNPs	Au. Preformed AuNPs cast onto the electrode followed by casting of CoPc.	Drop and dry (adsorption)	Kanamycin	84
PAH-AuNP/NiTSPc	ITO. Preformed PAH-AuNPs was cast onto the ITO followed by immersion in NiTSPc	Drop and dry	H_2O_2	85
C-CoO_x-FePc	GC. Preformed C-CoO_x was dispersed in the FePc.	Drop and dry	O_2	86
Au-MPS-CoPc	GC. Preformed MPS-AuNPs were mixed with CoPc.	Drop and dry	O_2	87
Pd/CuTSPc-MWCNTs	GC. CuTSPc was mixed with $PdCl_2$ followed by reduction of Pd^{2+} to Pd^0 with $NaBH_4$.	Drop and dry	Formic acid	88

MPc-NP	**Electrodes and MPc-MNP formation**	**Modification methods**	**Analytes**	**Ref**
NiTAPc-AuNPs	Au. NiTAPc was mixed with $HAuCl_4$ followed by reduction of Au^{3+} to Au^0 with $NaBH_4$.	SAM	Hydrazine	89
TaPc-AuNP	Au. Preformed AuNPs are mixed with TAPc.	Drop and dry	Bisphenol A	15, 16
MPTS/NiTAPc -AuNPs	Au and ITO. NiTAPc was mixed with $HAuCl_4$ followed by reduction of Au^{3+} to Au^0 by $NaBH_4$.	SAM	L-tyrosine	90
CoTAPc capped RhNP	GC. CoTAPc was mixed with $RhCl_3$ followed by reduction of Rh^{3+} to Rh^0 with $NaBH_4$.	Drop and dry	Cytochrome C	91
CoPc@Ag/C $CoPcF_{16}$@Ag/ C	GC. Preformed AgNPs were mixed with CoPc or $CoPcF_{16}$.	Drop and dry	O_2	92
Pt/NiTSPc-graphene	GC. NiTSPc was mixed with H_2PtCl_6 followed by reduction of Pt^{4+} to Pt^0 with $NaBH_4$.	Drop and dry	Methanol	93
CoTAPc capped CuNPs	GC. CoTAPc was mixed with $CuCl_2$ followed by reduction of Cu^{2+} to Cu^0 with $NaBH_4$.	Drop and dry	O_2	94
Pt/CuTSPc-graphene	GC. CuTSPc was mixed with H_2PtCl_6 followed by reduction of Pt^{4+} to Pt^0 with $NaBH_4$	Drop and dry	Methanol	95

MPc-NP	**Electrodes and MPc-MNP formation**	**Modification methods**	**Analytes**	**Ref**
Pt/$VOPcR_4$	GC. $VOPcR_4$ was mixed with H_2PtCl_4 followed by microwave reduction of Pt^{4+} to Pt^0.	Drop and dry	O_2	96
Ag-MPS-ZnPc Au-MPS-ZnPc	GC. Preformed Ag-MPS or Au-MPS attached to GC were immersed in ZnPc.	SAM	CO_2	97

MWCNT: multiwall carbon nanotubes, NPs: nanoparticles, GR: graphene, CS: chitosan, TSPc: tetrasulfonated phthalocyanine, TAPc: tetraaminophthalocyanine, PAH: polyallylamine hydrochloride, MPS: mercaptopropyl functionalized organo silica, MPTS: mercaptopropyltriethoxysilane, $VOPcR_4$: tetrakis(thiohecyl) vanadyl-phthalocyanine, GC: glassy carbon, ITO: indium tin oxide, SAM: self-assembled monolayer.

Table 1.2 shows the MPc-MNP conjugates and mixtures that have been applied in electrocatalysis [15, 16, 84-97]. Individual metallophthalocyanine and metal nanoparticles offers high electrocatalytic activities for a variety of analytes. It is important to study the composite or hybrid of the two in order to determine whether they would be an increase in the electrocatalytic performance. It is clear from Table 1.2 that the hybrids or composite were immobilised onto the electrodes by either adsorption (drop and dry) or self-assembled monolayer (SAM). Our aim is to introduce other forms of modification and form new hybrids through these methods. The composite in this thesis were immobilised onto the electrodes using two main methods that is electrodeposition (for metal nanoparticles (MNP)) and

electropolymerization (for MPc). The immobilisation of the composite involves electrodeposition of MNPs followed by electropolymerization of MPc or vice versa. The research was motivated by the novel formation of the hybrid modified electrode with the aim of improving the electrocatalytic performance. The nanoparticles in Table 1.2 were formed first chemically and then adsorbed onto the electrode while in this thesis nanoparticles are formed in situ electrochemically. Also the majority of conjugates with Pc were formed chemically but in this thesis attachment of Pc (through electropolymerization) and then nanoparticle attachment (through electrodeposition) or vice versa.

1.5. Analytes used in this work

The use of electrochemistry for analytical purpose has found applications in environmental monitoring, industrial quality control and biomedical analysis [98]. Electroanalytical techniques have an edge over other detection methods such chromatography and spectroscopy in that, they are of low cost, easy to use, have accuracy and are reliable [99]. For this work, electrooxidation of amitrole, nitrite and hydrazine was performed to test the performance of the electrocatalysts developed.

1.5.1. Amitrole

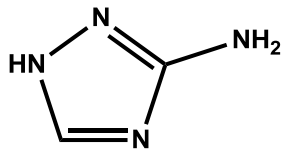

Fig. 1.15. The structure of amitrole.

The full name of amitrole is 3-amino-1,2,4-triazole. Amitrole is a terrestrial herbicide used in weed control [100]. The mechanism of action for amitrole is by inhibiting carotenoid synthesis, chlorophyll formation and limited regrowth of buds [101]. However amitrole poses danger to human health. Amitrole is mobile, persistent and may have potential to contaminate ground water. During spray application, amitrole may contaminate the surface water through spray drift [101]. Amitrole causes cancer in human beings. For this reason, it is vital to detect amitrole using electrochemical techniques. Electrochemical detection of amitrole has been done using NiTAPc in the presence of multiwalled carbon nanotubes and NiTAPc was found to perform worse than the corresponding FeTAPc, MnTAPc and CoTAPc derivatives [102]. In order to improve MPc activity, in this study, amitrole is employed as a test molecule for the electrocatalytic behaviour of the NiNPs alone or in combination with Ni phthalocyanines. This is the first time in which the NiNPs are used for the electrochemical detection of amitrole with the aim of making a better electrochemical detector for amitrole.

1.5.2. Nitrite

Nitrite plays a very important role in our society. Nitrites are known to be good corrosion inhibitors for water and can supress the corrosion of steel [103]. Nitrite is also used in meat preservation particularly sodium nitrite since it is known to inhibit bacteria growth [104]. However, nitrite poses a threat to human health. High level of nitrite in the blood has proved to promote the irreversible oxidation of haemoglobin [105]. Nitrite contamination in drinking water can cause many forms of cancer such as stomach and bladder cancer by formation of N-nitrosamines (when nitrite ions interact with amines) [106]. Therefore, it is crucial to obtain accurate methods of monitoring the level of nitrites for public health, environmental and food industries. The maximum permissible level of nitrites by the World Health Organisation is 3 mgL^{-1}. The electrochemical detection of nitrite has been performed on the electrode modified with metal nanoparticles [107] and MPc [108], since the bare electrodes requires high overpontials (>0.7 V). In this work, a combination of metal nanoparticles and MPc has been explored to modify the electrodes with the goal of lowering the overpotential as well as improve sensitivity for nitrite sensing.

1.5.3. Hydrazine

Hydrazine (N_2H_4) is used in agricultural chemicals, chemical blowing agents, pharmaceutical intermediates, photography chemicals, boiler water treatment for corrosion protection and as fuel for rockets and spacecraft

[109]. However, hydrazine is both toxic and corrosive and has to be handled with care. Apart from safety concern, hydrazine poses a threat to human health. Hydrazine has been recognised as a carcinogenic and hepatotoxic substance which affects the liver and the brain glutathione [110]. For this reason it is imperative to detect hydrazine. Metal nanoparticles have been used for the electrooxidation of hydrazine [111-113]. Of interest is the use of palladium nanoparticles for the electrochemical detection of hydrazine. PdNPs has been supported on carbon black and multiwall carbon nanotubes for hydrazine detection [111-113]. The results showed better electrocatalytic activity compared to the bare electrode. MPc were also used for the electrooxidation of hydrazine [114-116]. These include FePc and CoPc. For this work, PdNPs, AuNPs, Au-Pd, CoTAPc and a combination of nanoparticle and MPc has been explored with the goal of obtaining a better electrocatalyst for the electrooxidation of hydrazine. Of interest was the use of FeTCPc in the electrochemical detection of hydrazine. The hydrazine electrooxidation was carried out using FeTCPc modified ordinary pyrolytic graphite (OPG) [117]. This work present for the first time the use of FeTCPc modified glassy carbon electrode for hydrazine electrooxidation. The advantages of the GCE are its wide range usable potential, its relatively reproducible performance and mechanical durability than the graphite electrode.

1.6. Summary of the aims of the thesis

Considering that metal nanoparticles and MPc exhibit good electron transfer, combining the two could produce a hybrid with superior properties for the electrocatalytic activities. From literature, the combination of metal nanoparticles and MPc has been carried out. However the reports were limited to chemical linking of the metal nanoparticle and MPc and use either adsorption or SAM to modify the bare electrode. In this work we explore the use of adsorption, electropolymerization, electrodeposition and click chemistry as a means to modify the bare electrodes with metal nanoparticles and MPc. Therefore the aims of this work are as follows:

1) Synthesis of nickel phthalocyanine (NiPc), cobalt tetraaminophthalocyanine (CoTAPc) and iron tetracarboxyphthalocyanine (FeTCPc).
2) Synthesis of nickel nanoparticles using chemical reduction method.
3) Electrosynthesis (electrodeposition) of Au, Pd, Au-Pd nanoparticles.
4) Characterization of the MPcs and metal nanoparticles.
5) Combining the MPc and metal nanoparticle and characterize them.
6) Application of scanning electrochemical microscopy (SECM) for micropatterning of the glass carbon substrate.
7) Applications for the MPc and metal nanoparticles for the electrochemical detection of amitrole, nitrite and hydrazine.

CHAPTER 2

EXPERIMENTAL

2.1. Materials

The following chemicals were purchased from Sigma-Aldrich: gold salt ($HAuCl_4$), palladium (II) chloride, hydrazine sulphate, ethylene glycol, nickel tetrasulfonated phthalocyanine tetrasodium salt (NiTSPc), ethynylferrocene, 4-ethynylpyridine hydrochloride, 4-azidoaniline hydrochloride, HBF_4, sodium borohydride, sodium nitrite and sodium nitrate. Saarchem supplied the following: Acetone, ethanol, methanol, $K_3Fe(CN)_6$, $CuSO_4$, KH_2PO_4 and K_2HPO_4. Merck provided potassium chloride, acetonitrile, dimethyl formamide (DMF), $NiCl_2.6H_2O$, sodium carbonate, and tetrabutylammonium fluoroborate ($TBAFB_4$). Fluka supplied pH 4 and pH 9.2 tablets. Aqueous solutions were prepared using Millipore water from Milli-Q-Water Systems (Millipore Corp., Bedford, MA, USA). A stock solution of 1 mM amitrole was preared by pre-dissolving the pesticide in methanol (5 mL) and making up the volume to 100 mL with pH 9.2 buffer solution. Stock solutions of 1 mM hydrazine, 1 mM nitrite were prepared in pH 8 or pH 4 buffer solution. A pH 8 buffer solution was prepared from KH_2PO_4 and K_2HPO_4.

2.2. Equipment

1. Absorption spectra were recorded using Shimadzu UV-2550 spectrophotometer with a range from 200-800 nm.
2. Powder x-ray diffraction (XRD) was performed on a Bruker D8 Discover X-ray diffractometer with CuK_α (λ= 1.5405 Å) radiation. Samples were placed on a holder with a zero background silicon wafer

and data recorded within the range from $2\theta = 0^{o}$ to 100^{o}. X-ray diffraction data were fitted using software called Eva and the analysis of data was performed using International Center Diffraction Data (ICDD) database.

3. Scanning electron microscope (SEM) images were obtained using a JOEL JSM 840 scanning electron microscope. Glassy carbon plates (GCP, Goodfellow, UK) of 1×1 cm and 2 mm thick were used as substrates for SEM.
4. Energy dispersive X-ray (EDX) spectroscopy was done on an INCA PENTA FET coupled to the VAGA TESCAM using 20 kV accelerating voltage.
5. Transmission electron microscopy (TEM) images were obtained using a JEOL JEM 1210 TEM model operated at 100 kV.
6. Electron paramagnetic resonance (EPR) measurements were carried out using a Bruker EMX Plus EPR spectrometer, model number: EMP-9.5/12B/P. EPR settings were 0.632 mW for the microwave power, frequency 9.8 GHz, resolution 1024 points, centre field 3455 G and 100 G for the sweep width.
7. X-ray photoelectron spectroscopy (XPS) analysis was done using an AXIS Ultra DLD, with Al (monochromatic) anode equipped with a charge neutraliser, supplied by Kratos Analytical. The following parameters were used: the emission was 10 mA, the anode (HT) was 15 kV and the operating pressure below 5×10^{-9} torr. A hybrid lens was used and resolution to acquire scans was at 160 eV pass energy in slot mode. The centre used for the scans was at 520 eV with a

width of 1205 eV, with steps at 1 eV and dwell time at 100 ms. High resolution scans were done using 40 eV and 80 eV pass energy.

8. All electrochemical experiments were performed using Autolab potentiostat PGSTAT 302 (Eco Chemie, Utrecht, The Netherlands) driven by the general purpose electrochemical system data processing software (GPES, software version 4.9). A three electrode electrochemical cell comprising a glassy carbon electrode (GCE) as working, platinum wire (Pt) as counter and (Ag|AgCl, 3M KCl) reference electrodes was employed.
9. Electrochemical impedance spectroscopy (EIS) measurements were performed using Autolab FRA software, between 0.1 Hz and 10 kHz, with signal amplitude of 10 mV. A nonlinear least squares (NNLS) method based on the EQUIVCRT programme was used for automatic fitting of the obtained EIS data
10. Scanning electrochemical microscopy (SECM) experiments were carried out using Uniscan Model 370 equipment and ultramicroelectrodes (25, 15 or 12.5 μm Pt microelectrode from Uniscan) as the tip. SECM approach curves were done using the Pt microelectrode with a Pt counter electrode and Ag|AgCl wire as the pseudo-reference electrode. Images were obtained by maintaining the tip at a constant Z position and scanning in the X–Y plane over the desired area (constant-height mode of SECM) and monitoring changes in the steady-state current of $K_3[Fe(CN)_6]$ oxidation at -0.1 V vs. Ag|AgCl as the tip travels. Glassy carbon plates (Goodfellow, UK) of 1×1 cm and 2 mm thick were used as substrates for SECM.

2.3. Synthesis

2.3.1. Synthesis of metallophthalocyanine (MPc)

The MPc used in this work were not new, therefore details for their synthesis is not given. They were synthesized according to literature methods, NiPc [118], NiTSPc (Aldrich), CoTAPc [10] and FeTCPc [11].

2.3.2. Synthesis of nickel nanoparticles (NiNPs)

The synthesis of nickel nanoparticles (NiNPs) was as reported before [119] with slight modifications. Fig. 2.1 represents the synthesis of NiNPs. In a typical synthesis, $NiCl_2.6H_2O$ (52 mg) was dissolved in the ethylene glycol (20 mL) in a 100 mL round bottom flask and heated to 150 ^oC. A reducing agent, sodium borohydride (90 mg) was added and the green solution changed immediately to a black colour. The reaction was allowed to continue for 3 h and subsequently the heating was turned off. A colloidal dispersion was formed and precipitated with acetone. The precipitate was filtered and washed with acetone and ethanol and dried at 100 ^oC.

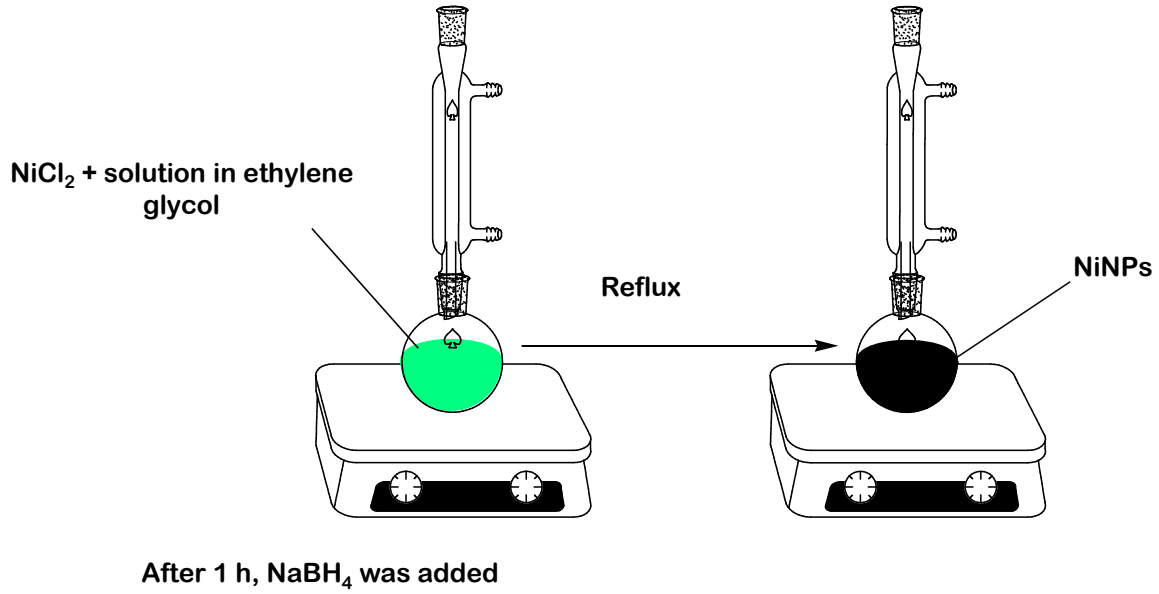

Fig. 2.1. Synthesis of NiNPs.

2.3.3. Synthesis of 4-azidobenzenediazonium tetrafluoroborate

The synthesis of 4-azidobenzenediazonium tetrafluoroborate was as reported before [120] with slight modifications. Briefly, $NaNO_2$ (0.65 mmol) was dissolved in Millipore to make a solution of 0.25 ml. It was then cooled in a refrigerator. Azidoaniline hydrochloride (0.59 mmol), was dissolved in HBF_4 (1 ml) and placed in an ice bath to maintain a temperature of 4 ^oC. The cold solution of $NaNO_2$ was then added slowly to the cold azidoaniline and the reaction allowed to continue for 1 h. The off-white precipitate was filtered and rinsed with cold ether (10 ml). The crude product was purified by recrystallization from acetonitrile in the presence of an excess of diethyl ether. The solid was dried and stored in a deep freezer.

2.4. Electrode modification

The glassy carbon electrode (GCE) surface was polished using silicon carbide grinding paper (grit 1200) followed by polishing on a Buehler-felt pad using alumina (0.05 μm). Between each polishing step, absolute ethanol was used to remove any impurity by sonicating for 5 min. The electrode was then rinsed with Millipore water and dried under a N_2 stream. This was done to ensure that there are no contaminates on the electrode surface before the electrochemical measurements. A summary of modified electrodes is presented in Table 4.1.

2.4.1. Adsorption (drop and dry)

The process involved dispersing NiNPs, NiPc and NiNPs/NiPc (mix) in dimethylformamide (DMF) through sonication for 1 h. NiNPs/NiPc (mix) was obtained by mixing 1:1, 1 mM NiNPs and 1 mM NiPc in DMF. The drop and dry method was used to introduce 5 μL of the various modifiers onto the GCE surface and then allowing the electrode to dry in an atmosphere of nitrogen. The modified electrode was then rinsed in pH 9.2 buffer solution before analysis. Regeneration of the modified electrode after use was achieved by either shaking it in pH 9.2 buffer solution or in methanol, followed by repetitive scanning in pH 9.2 buffer until stable voltammetric currents were obtained. The GCE was modified with NiNPs, NiPc and NiNP/NiPc (mix) are represented as NiNP-GCE, NiPc-GCE and NiNP/NiPc mix-GCE, respectively.

2.4.2. Electropolymerization

Co tetraaminophthalocyanine (CoTAPc) was electropolymerized on the GCE by continuous cyclic voltammetry of the CoTAPc monomer (1mM) in DMF containing 0.1 M $TBAFB_4$ as an electrolyte from −1.2 V to +1.3 V (versus Ag|AgCl) at 100 mV/s or 200 mV/s for 25 or 50 cycles, as reported in literature [121-123]. The electrode is denoted poly-CoTAPc-GCE.

Electropolymerization of nickel tetrasulfonated phthalocyanine (NiTSPc) was carried out by continuous cyclic voltammetry [124] in a solution containing 1 mM NiTSPc in 0.1 M NaOH within a potential range of −0.2 V to +0.84 V (versus Ag|AgCl) at 10 mV/s for 20 cycles. The electrode is denoted as poly-NiTSPc-GCE.

Electropolymerization of 4-azidoaniline (10 mM) was performed by cycling from -0.6 V to 0.9 V at a scan rate of 50 mV/s (vs Ag|AgCl) in a water/ethanol solution using 0.5 M H_2SO_4 as an electrolyte. The number of cycles performed was 50.

2.4.3. Electrodeposition

Electrodeposition was the method used to deposit AuNPs, PdNPs and bimetallic (core shell and alloy) of gold and palladium nanoparticles.

2.4.3.1. Electrodeposition of gold nanoparticles

The gold nanoparticles modification of GCE was done using cyclic voltammetry and a method proposed by Hezard et al [52]. A deaerated solution of 1 mM $HAuCl_4$ in 0.1 M $NaNO_3$ was cycled at a scan rate of 50 mV/s for 10 scans from 1 V to 0 V or 0.4 V to 1.2 V [125]. The modified electrode is denoted as Au-GCE.

2.4.3.2. Electrodeposition of palladium nanoparticles

Palladium nanoparticles were electrodeposited on to the GCE using cyclic voltammetry scanning from -0.4 V to 0.6 V in a deaerated solution containing 1 mM $PdCl_2$ (0.1 M HCl) at a scan rate of 50 mV/s for 10 scans, using modified literature procedure [125]. The modified electrode is denoted as Pd-GCE.

2.4.3.3. Electrodeposition of bimetallic nanoparticles

Au-Pd (co-deposited) nanoparticles were co-electrodeposited on to the GCE using cyclic voltammetry scanning from -0.4 V to 1.2 V in a deaerated solution containing 1 mM $HAuCl_4$ and 1 mM $PdCl_2$ (0.1 M HCl) at a scan rate of 50 mV/s for 10 scans, using modified literature procedure [125]. The electrode is denoted Au-Pd (co-deposited)-GCE.

Using the same concentrations of $HAuCl_4$ or $PdCl_2$ as used for co-electrodeposition, electrodes where Pd and Au were deposited sequentially on GCE were also studies and are represented as Au/Pd-GCE (for PdNPs deposited first) or Pd/Au-GCE (for AuNPs deposited first).

2.4.4. Combining electropolymerization and electrodeposition

Electrodes where MPc (NiTSPc and CoTAPc) was first electropolymerized onto the electrode followed by electrodeposition of metal nanoparticles were also prepared. The electrodes were denoted Au/poly-CoTAPc-GCE, Pd/poly-CoTAPc-GCE, Au/Pd-poly-CoTAPc-GCE, Pd/Au-poly-CoTAPc-GCE and Au-Pd (co-deposited/poly-CoTAPc-GCE.

Electrodes where metal nanoparticles were first electrodeposited onto the electrode followed by electropolymerization of MPc were also prepared. These were denoted poly-NiTSPc/Au-GCE and poly-CoTAPc/Au-GCE.

2.4.5. Electrografting

Electrografting was achieved by scanning a solution of 1 mM 4-azidobenzenediazonium tetrafluoroborate containing 0.1 M $TBABF_4$ in de-aerated acetonitrile at the potential range of 0.4 V to -0.3 V. Alternatively, the electrografting of the GCE surface with azidoaryl groups was achieved by chonoamperometry at −0.9 V *vs* Ag/AgCl for 60 s, at room temperature and

without deaerating the aqueous solution containing 1 mM 4-azidobenzenediazonium and 100 mM HCl.

2.4.6. Click chemistry

The GCE was modified using simultaneous electropolymerization and electro-click (SEEC) functionalization process following literature methods [126]. This was achieved by scanning a solution containing 10 mM 4-azidoaniline, 10 mM 4-ethynylpyridine and 10 mM copper sulphate in a water/ethanol with 0.5 M H_2SO_4 as an electrolyte, within a potential window from -0.6 V to 0.9 V at a scan rate of 50 mV/s (using a pseudo Ag/AgCl reference electrode). The number of cycles performed was 50. Adsorbed species were removed by thorough rinsing in ethanol and water.

In another approach electropolymerization of azidoaniline was done first followed by the attachment of 4-ethynylpyridine using electro-click reaction. Electro-click reaction was carried out at a constant potential of -0.2 V in 10 mM 4-ethynylpyridine and 10 mM copper sulphate in a water/ethanol solution with 0.5 M H_2SO_4 as an electrolyte. Electropolymerization followed by click chemistry was termed step by step route.

2.4.7. Axial ligation

FeTCPc was introduced to both electrodes (SEEC or step by step) by immersion of the electrode into a solution of 1 mM FeTCPc in DMF for 1 h.

The pyridinic nitrogen from 4-ethynylpyridine form an axial bond with Fe in FeTCPc.

2.4.8. Micropatterning on the glassy carbon substrate

Glassy carbon plates (Goodfellow, UK) of 1 x 1 cm and 2 mm thick were used as the substrate in the SECM experiments. Each substrate was manually polished before each experiment with liquid diamond (Biodiamant, Lamplan, France) of 1 μm and ¼ μm. The substrate was then thoroughly rinsed with ultra-pure water (Millipore System). Scheme 4.3 shows the micropatterning of the glass carbon substrate using the SECM tip. The SECM tip was positioned ≈10 μm above the surface of the azido-modified substrate, and Cu^{+} ions were produced at the tip. This is aimed at locally triggering the copper (I) catalyzed azide-alkyne 1,3-dipolar Huisgen cycloaddition (CuAAC) reaction between azido moieties on the surface and ethynylferrocene in solution. A potential of −0.3 V was applied on the tip for the local click procedure. Although this process probably corresponds to the reduction of Cu^{2+} to Cu^{0}, a small amount of Cu^{+} is also present and this small amount can be enough to catalyze the click chemistry reaction.

RESULTS AND DISCUSSION

This section has been split into three chapters:

Chapter 3: Characterization of phthalocyanines and nanoparticles

Chapter 4: Electrode modification

Chapter 5: Electrocatalytic studies

PUBLICATIONS

The work presented in the following chapters has been published or submitted to peer-reviewed journals:

1) Damien Quinton, Audacity Maringa, Sophie Griveau, Tebello Nyokong and Fethi Bedioui, Surface patterning using scanning electrochemical microscopy to trigger a "click" chemistry reaction. *Electrochem. Commun.* **31** (2013) 112-115.
2) Audacity Maringa, Tawanda Mugadza, Edith Antunes and Tebello Nyokong, Characterization and electrocatalytic behaviour of glassy carbon electrode modified with nickel nanoparticles towards amitrole detection, *J. Electroanal. Chem.* **700** (2013) 86-92.
3) Audacity Maringa, Edith Antunes and Tebello Nyokong, Electrochemical behaviour of gold nanoparticles and Co tetraaminophthalocyanine on glassy carbon electrode, *Electrochim. Acta.* **121** (2014) 93-101.
4) Audacity Maringa and Tebello Nyokong, Behaviour of palladium nanoparticles in the absence or presence of Co tetraaminopthalocyanine, *Electroanalysis.* **26** (2014) 1068-1077.
5) Audacity Maringa and Tebello Nyokong, The influence of gold nanoparticles on the electroactivity of Ni tetrasulfonated phthalocyanine, *J. Porphyrins Phthalocyanines* **18** (2014) 1-10.
6) Audacity Maringa, Philani Mashazi and Tebello Nyokong, Characterization of electrodes modified by electro-click reaction and

axial ligation of iron tetracarboxyphthalocyanine: comparison of one pot click with step by step, *Electrochim. Acta* **145** (2014) 237-244.

7) Audacity Maringa, Philani Mashazi and Tebello Nyokong, Electrocatalytic activity of bimetallic Au-Pd nanoparticles in the presence of cobalt tetraaminophthalocyanine, *J. Colloids Interfacial Sci. accepted with revision.*

CHAPTER 3

CHARACTERIZATION OF PHTHALOCYANINES AND NANOPARTICLES

Table 3.1. List of metallophthalocyanines (MPcs) used in this work.

MPcs complexes	Abbreviations	Q band (nm)
Nickel (II) phthalocyanine	NiPc	676, 621
Nickel (II) tetrasulfonated phthalocyanine	NiTSPc	660, 607
Cobalt (II) tetraaminophthalocyanine	CoTAPc	710
Iron (II) tetracarboxyphthalocyanine	FeTCPc	642

3.1. UV-Vis spectra of MPcs

3.1.1. UV-Vis spectrum of NiPc

Fig. 3.1 shows the UV-Vis spectrum of NiPc dissolved in pyridine. It has a two Q bands at 676 nm and 621 nm. The peak at 676 nm is a characteristic peak of monomeric NiPc while the peak at 621 nm shows aggregation of the NiPc [127]. The Soret band is seen at 335 nm.

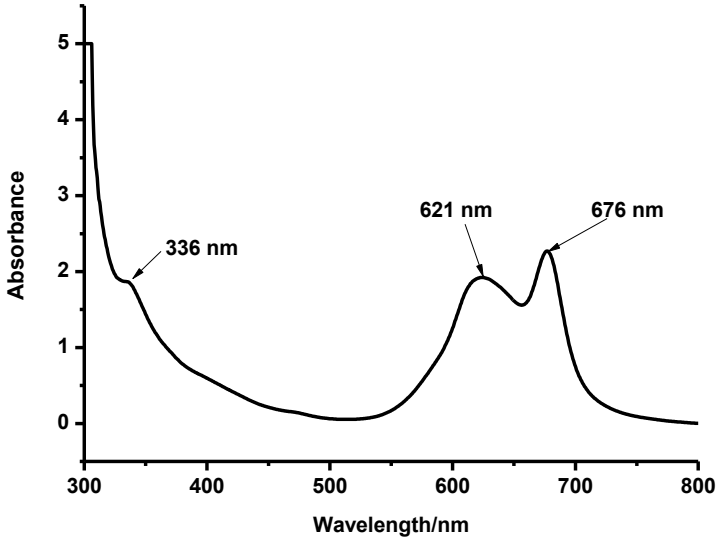

Fig. 3.1. UV-Vis absorption spectra of NiPc in pyridine (concentration ~ 1 $\times 10^{-5}$ M)

3.1.2. UV-Vis spectrum of NiTSPc

The UV-Vis spectrum of NiTSPc in 0.1 M NaOH exhibits a Soret band at 333 nm and a Q band at 607 nm, Fig. 3.2. This is a typical absorption spectrum of NiTSPc. These results are closely related to those obtained by Ureta-Zanartu et al [128]. The spectrum shows extensive aggregation with the band due to the aggregate at 607 nm and the monomer as a shoulder near 660 nm [129].

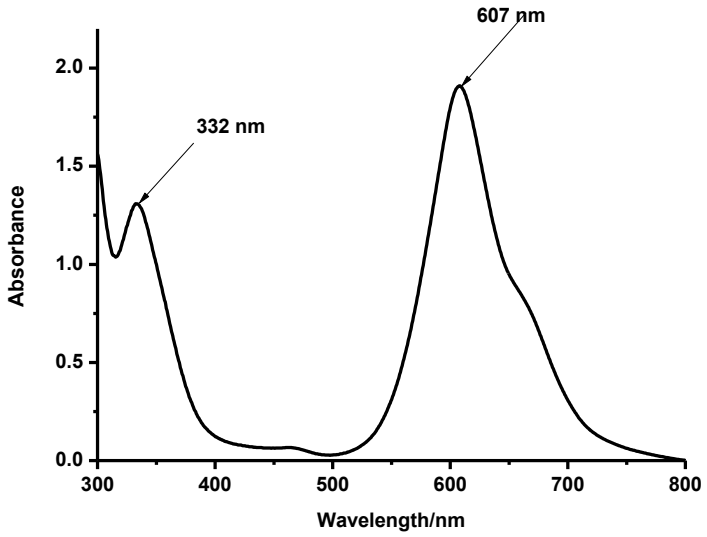

Fig. 3.2. Absorption spectrum of NiTSPc in 0.1 M NaOH.

3.1.3. UV-Vis spectrum of CoTAPc

The UV-Vis spectrum of CoTAPc in DMF exhibits a Soret band at 420 nm and a Q band at 710 nm, Fig. 3.3. This is a typical absorption spectrum of CoTAPc. Similar spectra were observed in literature [20, 121].

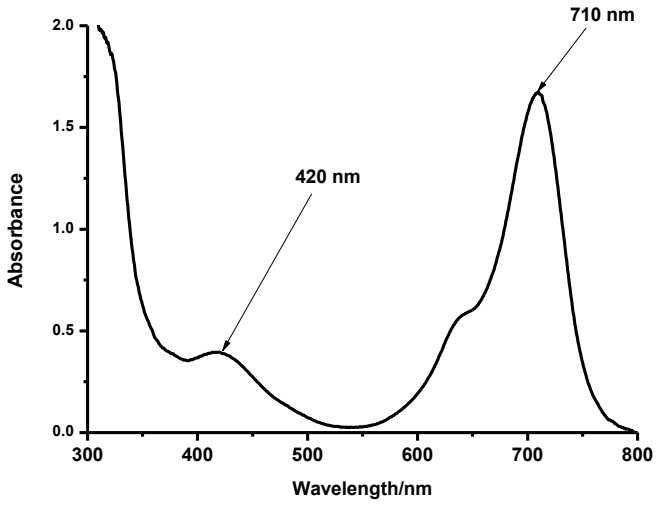

Fig. 3.3. Absorption spectrum of CoTAPc in DMF.

3.1.4. UV-Vis spectrum of FeTCPc

Fig. 3.4 shows the UV-Vis absorption spectrum of FeTCPc. FeTCPc gives a characteristic Q band of non-aggregated carboxyphthalocyanine at 640 nm. Zhang et al obtained similar results in which the peak of non-aggregated FeTCPc peak occurred at 642 nm [130].

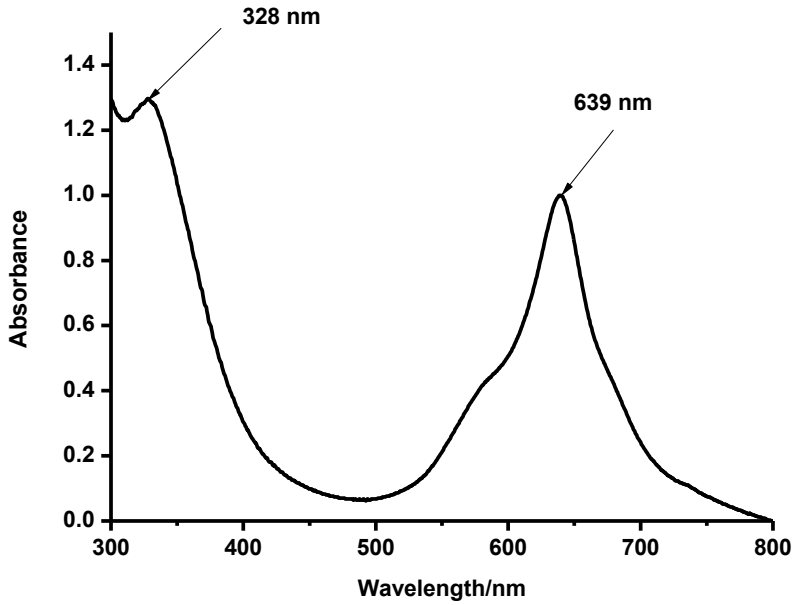

Fig. 3.4. Absorption spectrum of FeTCPc in DMF.

3.2. Characterization of nickel nanoparticles (NiNPs)

The discussion in this section will be of NiNPs as the other nanoparticles were made electrochemically. Therefore they will be discussed under electrode modification.

3.2.1. UV-Vis spectra of NiNPs

When $NiCl_2.6H_2O$ was dissolved in ethylene glycol, a green solution was formed. Fig. 3.5 shows the UV-Vis spectrum of the Ni^{2+} solution with a strong band at 394 nm and weak ones between 600-800 nm as reported before [131]. The addition of sodium borohydride caused colour a change from green to black, where the Ni nanoparticles are black in colour. The UV-Vis absorption spectrum was taken at the end of the reaction and it showed the disappearance of the peaks at 394 nm and 600-800 nm as shown in Fig 3.5. This indicates that Ni^{2+} has been reduced to Ni^0.

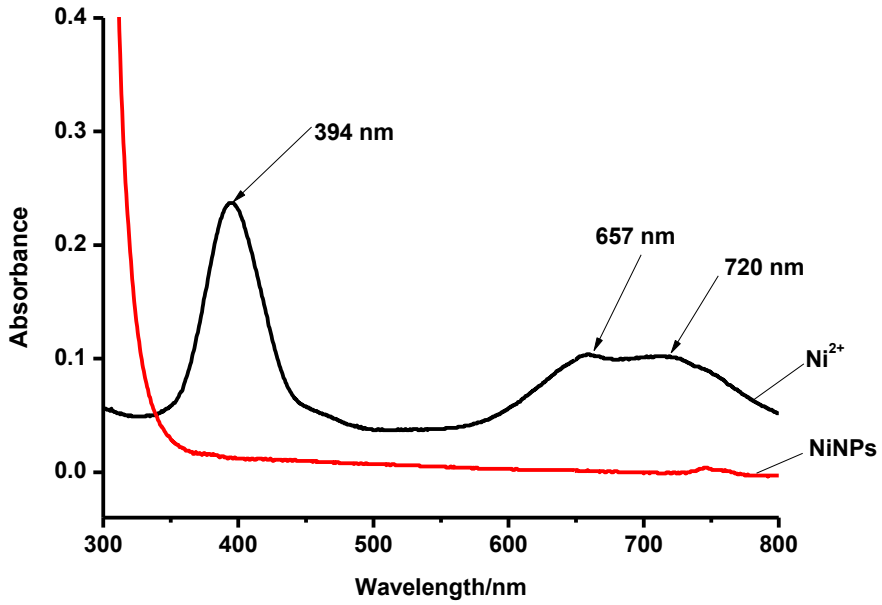

Fig. 3.5. Absorption spectra of Ni^{2+} and NiNPs in ethylene glycol.

3.2.2. Transmission electron microscopy (TEM) images of NiNPs

The Ni nanoparticles obtained were characterized using TEM. Fig. 3.6 shows the TEM micrographs of uncapped Ni nanoparticles. It can be seen from the TEM image that the Ni nanoparticles are well dispersed. Due to the large surface to volume ratio and strong magnetic forces, the Ni nanoparticles tend to aggregate in order to minimise the total surface energy of the system [132]. Singh and co-workers [133] showed that Ni nanoparticles capped with polyvinyl pyrrolidone (PVP) were smaller and well dispersed compared to NiNPs shown in Fig. 3.6. Though their NiNPs were observed as small spheres surrounded by PVP capping, this may affect the electrocatalytic activity of the NiNPs. The average particle size was estimate by ImageJ software and was found to be 16 nm. The formation of agglomerates was controlled due to the presence of ethylene glycol which act as a capping agent. The uncapped NiNPs were however employed in this work since the capped ones did not show good electrocatalytic behaviour.

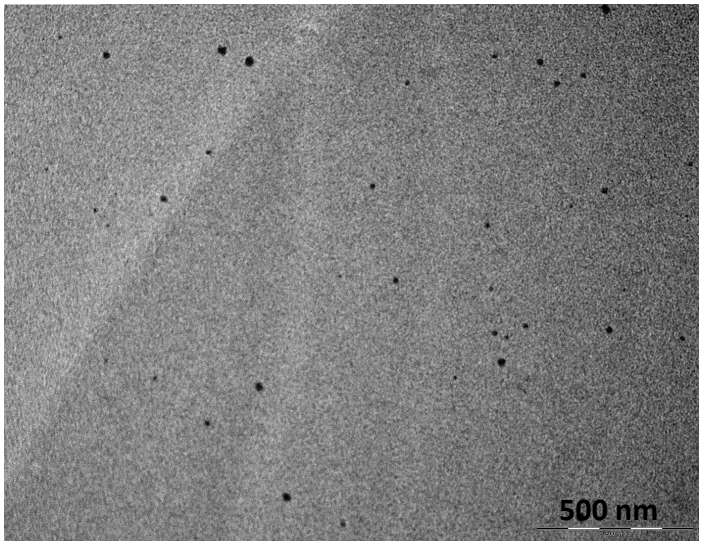

Fig. 3.6. TEM image with NiNPs.

3.2.3. Powder X-ray diffraction (XRD) pattern of NiNPs

The crystalline size of the NiNPs was determined by XRD. Fig. 3.7 shows the XRD pattern of uncapped Ni nanoparticles prepared. The peaks are sharp which is indicative of the crystallinity of the nanoparticles. The XRD standard pattern for Ni nanoparticles gave 2θ values at: 44°, 51°, 75°, 91° and 97°, they were also observed in the literature [134] and were indexed as the (111), (200), (220), (311) and (222) planes of the face centered-cubic (fcc) nickel, respectively. No impurity diffraction peaks, such as nickel oxides or nickel hydroxides, were detected, indicating that the NiNP were pure. The crystalline (particle) size of the Ni nanoparticles was calculated using the Scherrer equations. The Scherrer Eq. 3.1 [133]:

$$L = \frac{0.9\lambda}{BCos\theta} \qquad (3.1)$$

where L is the average particle size, λ is the wavelength (1.5405Å) of the X-ray source, B is the full width at half maximum of the peak position and θ is the angle at which the diffraction peak occurs. The average size of these uncapped NiNP was 14 nm. The value is close to the one obtained using TEM which is 16 nm.

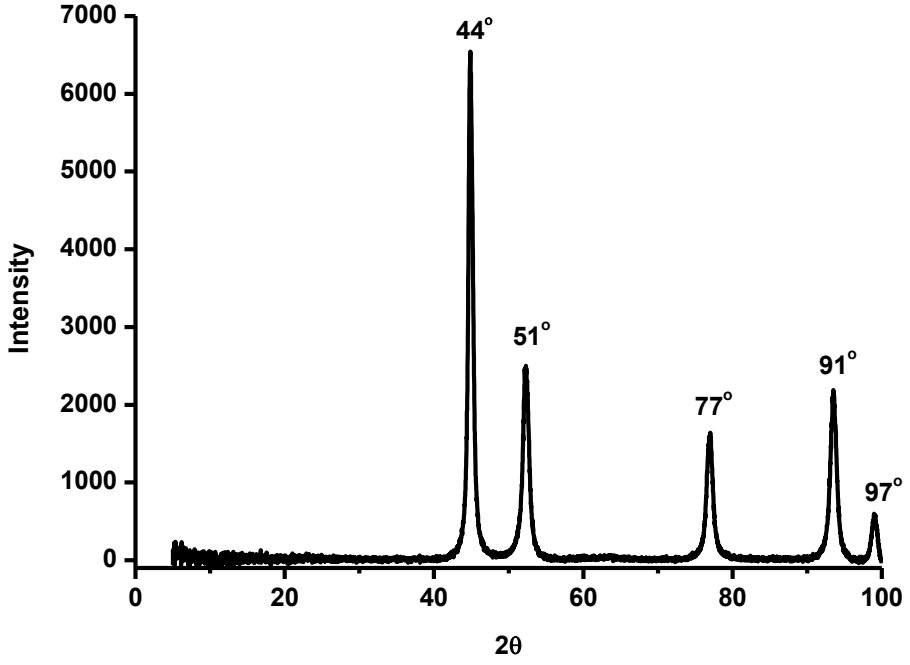

Fig. 3.7. XRD pattern of NiNPs.

3.2.4. Electron paramagnetic resonance (EPR) spectrum of NiNPs

The presence of paramagnetism in the NiNPs and NiPc was determined by EPR. Fig. 3.8 shows the EPR spectrum of NiNPs. NiPc did not show the EPR spectrum because of its diamagnetism. The line width is large and shape is distorted for uncapped NiNPs in Fig. 3.8. The line width in the EPR spectrum of NPs is known to increase with increase in the size and distribution of nanoparticles [135]. Thus the large line width observed for NiNPs suggests a large size distribution. The large size distribution could be due the presence of different extends of aggregation in addition to some of the NiNPs not being aggregated. Thus EPR supports TEM and XRD in terms of the aggregated nature of the NiNPs.

The effective *g* factor was experimentally determined using $h\upsilon/\mu_B H$, where υ is the microwave frequency, H is the magnetic field at which the resonance maximum occurs, h is the Planck's constant, and μ_B is the Bohr magneton. The effective *g* factor was found to be 2.26 for these uncapped NiNPs. The value of the *g* factor is typical of ferromagnetic substances [136] and thus confirms the magnetic status of the NiNPs.

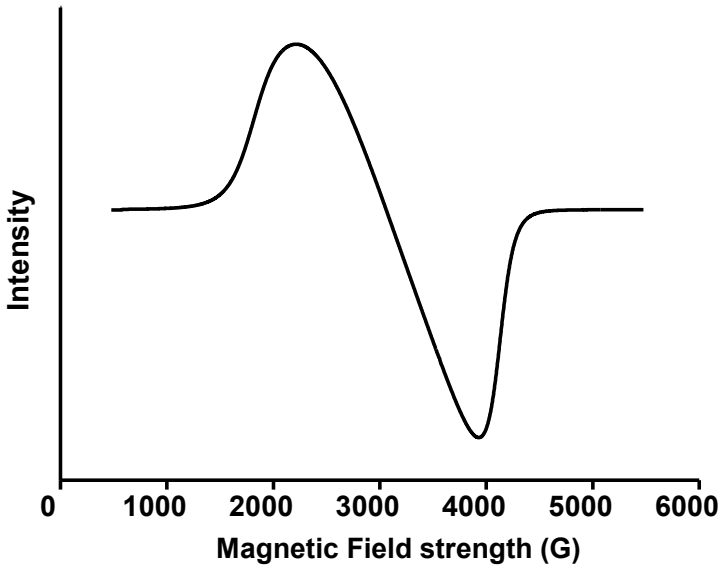

Fig. 3.8. EPR spectrum of NiNPs.

CHAPTER 4

ELECTRODE MODIFICATION

Various methods were used to modify the glassy carbon substrate (electrodes or plates). These methods include adsorption, electropolymerisation, electrodeposition, electrografting and click chemistry. The different methods were employed in this work due to nature of the electrocatalyst which were used to modify the electrode surface. NiPc is difficult to polymerize in solution while NiNPs are difficult to electrodeposit in solution hence adsorption was used to immobilise them on the electrode. However, adsorption has limitations in terms of reproducibility so other methods were employed. The best was to immobilise metal nanoparticles is through electrodeposition. Since Au and Pd can easily be electrodeposited, they were employed in this work. Having seen the challenges with unsubstituted NiPc, substituted MPc were employed namely NiTSPc, CoTAPc and FeTCPc. NiTSPc can polymerize easily in solution compared to NiPc. Both NiTSPc and CoTAPc were immobilised onto the electrode surface through electropolymerization, since the former forms O-Ni-O on polymerization and the latter has polymerizable NH_2 groups. Electrografting was used for aryl diazonium compound and click chemistry was employed for coupling azide and alkyne groups. FeTCPc was immobilised onto the electrode surface possessing pyridinic nitrogen through axial ligation, since nitrogen containing ligands co-ordinates with with FePc derivative axially and not with NiPc or CoPc derivatives. Table 4.1 shows the different methods employed to modifying the glassy carbon substrate.

Table 4.1. The different methods employed to modifying the glassy carbon electrode (GCE).

Material	**Electrode presentation**	**Modification method**
NiNPs	NiNP-GCE	Adsorption
AuNPs	Au-GCE	Eletrodeposition
PdNPs	Pd-GCE	Eletrodeposition
AuNPs & PdNPs	Au/Pd-GCE	Eletrodeposition of PdNPs followed by AuNPs
PdNPs & AuNPs	Pd/Au-GCE	Eletrodeposition of AuNPs followed by PdNPs
AuNPs-PdNPs	Au-Pd (co-deposited)-GCE	Co-eletrodeposition
NiPc	NiPc-GCE	Adsorption
NiTSPc	poly-NiTSPc-GCE	Electropolymerization
CoTAPc	poly-CoTAPc-GCE	Electropolymerization
NiNPs & NiPc	NiNP/NiPc mix-GCE	Adsorption
NiTSPc & AuNPs	poly-NiTSPc/Au-GCE	Eletrodeposition followed by electropolymerization
AuNPs & CoTAPc	Au/poly-CoTAPc-GCE	Electropolymerization followed by electrodeposition
CoTAPc & AuNPs	poly-CoTAPc/Au-GCE	Eletrodeposition followed by electropolymerization
PdNPs & CoTAPc	Pd/poly-CoTAPc–GCE	Electropolymerization followed by electrodeposition
AuNPs, PdNPs & CoTAPc	Au/Pd-poly-CoTAPc-GCE	Electropolymerization followed by electrodeposition
PdNPs, AuNPs & CoTAPc	Pd/Au-poly-CoTAPc-GCE	Electropolymerization followed by electrodeposition
AuNPs-PdNPs, CoTAPc	Au-Pd (co-deposited)/poly-CoTAPc-GCE	Electropolymerization followed by electrodeposition

4.1. NiPc and NiNPs

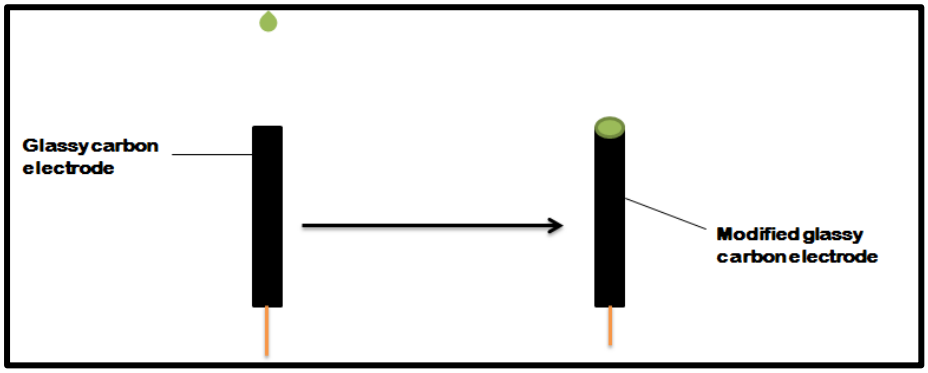

Scheme 4.1. Drop and dry of NiPc or NiNPs or the mixture of NiPc and NiNPs on to the glassy carbon electrode.

Scheme 4.1 shows the modification of GCE using the drop and dry method. NiPc, NiNPs, mixture of NiPc and NiNPs were used to modify the GCE and the electrodes are denoted as NiPc-GCE, NiNP-GCE and NiNP/NiPc mix-GCE, respectively. NiPc was studied in the presence of NiNPs since they both form O-Ni-O bridges hence the effect of combined bridges was tested. The characterization of the bare and modified electrodes was done electrochemically in ferricyanide and pH 9.2 buffer solutions.

4.1.1. Behaviour of electrodes in ferricyanide

The surface roughness factor for NiNP-GCE and NiPc-GCE were determined using the $[Fe(CN)_6]^{3-/4-}$ redox system (figure not shown but similar figure to that is shown below for NiTSPc system) and applying the Randles–Sevcik Eq. 4.1 [40].

$$I_p = 2.69 \times 10^5 n^{\frac{3}{2}} A_{eff} D^{\frac{1}{2}} C v^{\frac{1}{2}} \qquad (4.1)$$

where *D* and *C* are the diffusion coefficient and the bulk concentration of the redox probe (1 mM $K_3[Fe(CN)_6]$ in 1 M KCl), respectively, n is the number of electrons transferred (n = 1), υ is the scan rate (0.1 V s^{-1}) and A_{eff} is the effective surface area. *D* value for $K_3[Fe(CN)_6]$ = 7.6 × 10^{-6} cm^2 s^{-1} [41]. The surface roughnesses of the electrodes (ratio of I_{pa} experimental/I_{pa} theoretical) are found to be 1.4 for NiNP-GCE and 1.1 for NiPc-GCE corresponding to a real electrode areas (roughness factor × theoretical surface area, = 0.071 cm^2) of 0.0978 cm^2 for NiNP-GCE and 0.079 cm^2 for NiPc-GCE. There is increased roughness for NiNP compared to NiPc. Thus the NiNP-GCE is expected to perform better than NiPc-GCE based on the effective electrode area. The cathodic to anodic peak potential separation (ΔE) of the bare, NiPc-GCE, NiNP-GCE and NiNP/NiPc mix-GCE were 74, 135, 120 and 140 (versus Ag|AgCl), respectively, at a scan rate of 100 mV/s, Table 4.2. Of the modified electrodes, NiNP-GCE showed the lowest ΔE value confirming its better electron transfer kinetic compared to the rest of the modified electrodes.

Table 4.2. The different electrocatalysts employed and electrochemical parameters for the modification of electrode.

Electrode	**ΔE/mV (ferricyanide)**	**Γ (mol cm^{-2})**	**Medium**
Bare GCE	74	-	
NiNP-GCE	120	6.59×10^{-10}	pH 9.2
Au-GCE	83	2.44×10^{-10}	pH 4 & 8
Pd-GCE	88	1.82×10^{-9}	pH 8
Au/Pd-GCE	113	2.95×10^{-10}	pH 8
Pd/Au-GCE	103	1.94×10^{-9}	pH 8
Au-Pd (co-deposited)-GCE	83	3.30×10^{-10}	pH 8
NiPc-GCE	135	1.12×10^{-10}	pH 9.2
Poly-NiTSPc-GCE	126	1.79×10^{-10}	pH 8
Poly-CoTAPc-GCE	78	3.10×10^{-10}	pH 4 & 8
NiNP/NiPc mix-GCE	140	1.04×10^{-10}	pH 9.2
Poly-NiTSPc/Au-GCE	110	1.89×10^{-10}	pH 8
Au/poly-CoTAPc-GCE	78	3.40×10^{-10}	pH 4 & 8
Poly-CoTAPc/Au-GCE	83	3.15×10^{-10}	pH 4
Pd/poly-CoTAPc–GCE	88	1.90×10^{-9}	pH 8
Au/Pd-poly-CoTAPc-GCE	98	4.80×10^{-10}	pH 8
Pd/Au-poly-CoTAPc-GCE	98	1.30×10^{-9}	pH 8
Au-Pd (co-deposited)/poly-CoTAPc-GCE	103	4.3×10^{-10}	pH 8

4.1.2. Polymerization and surface coverage

Fig. 4.1 shows comparative cyclic voltammetric studies (2nd cycles) for the different electrodes in pH 9.2 buffer. All the electrodes (NiNP-GCE, NiPc-GCE, NiNP/NiPc mix-GCE) with the exception of the bare GCE (as expected)

showed the Ni^{3+}/Ni^{2+} couple. The half wave potentials were 0.76 V, 0.78 V and 0.79 V for the NiNP-GCE, NiPc-GCE and NiNP/NiPc mix-GCE, respectively. There was no anodic peak observed for the Ni^{3+}/Ni^{2+} couple during the first scan, though it has been observed during the first scan in other studies using different electrode materials [137]. However during successive scans the Ni^{3+}/Ni^{2+} couple began to be observed and continued to increase until it stabilises at scan number 15.

It is known that upon immersing Ni electrode in aqueous alkaline solution, a film of the hydrous Ni(II) oxide species, α-$Ni(OH)_2$, is spontaneously formed [68]. It is expected that the NiNPs on the surface of the GCE will also form the α-$Ni(OH)_2$ [138]. The α structure consists of $Ni(OH)_2$ layers with intercalated water molecules occupying the space between layers. With ageing or cyclic voltammetry cycling in alkaline medium, the α-$Ni(OH)_2$ dehydrates to form β-$Ni(OH)_2$.

The redox peaks after cycling in Fig. 4.1d are due to the reaction shown in Eq. 4.2 [138].

$$Ni(OH)_2 + OH^- \leftrightarrow NiOOH + H_2O + e^- \qquad (4.2)$$

Thus the couple at half wave potential ($E_{½}$) = 0.76 V (for NiNPs) is due to Ni^{3+}/Ni^{2+} redox process. The large increase in oxidation peaks beyond +0.8 V have been attributed to the electro-oxidation of OH^- ions to O_2 with OH· radicals as intermediates. For NiPc, the peaks are due to Ni^{3+}/Ni^{2+} redox couple after the formation of the O-Ni-O bridge.

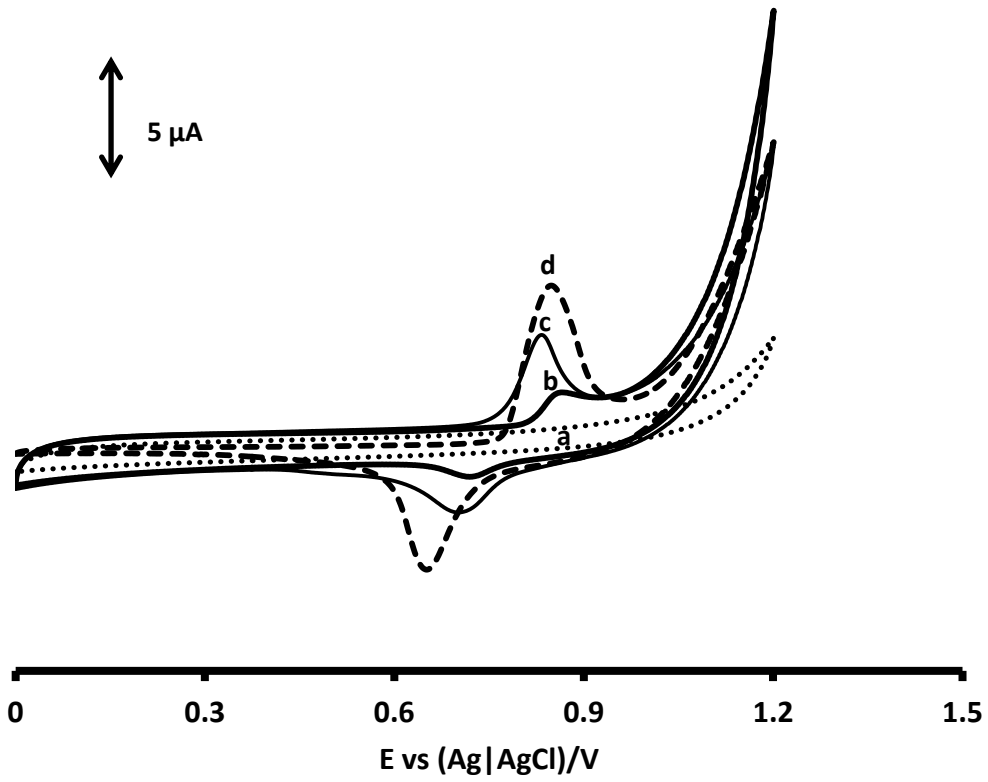

Fig. 4.1. Second cycle cyclic voltammograms in pH 9.2 for (a) bare GCE, (b) NiPc-GCE, (c) NiPc/NiNP mix-GCE and (d) NiNP-GCE. Scan rate = 100 mV/s.

Fig. 4.2 shows the increase in the cathodic and anodic peaks as the scan rate is increased from 50 mV/s to 500 mV/s (for NiNPs). Fig. 4.2 inset shows a plot of peak current versus sweep rate for the NiNP-GCE in pH 9.2. The linear relationship of the plot is characteristic of a surface-immobilized redox species. The surface coverage of NiNP or NiPc on GCE was estimated from the plot of background corrected peak current versus scan rate, according to Eq. 4.3 [42, 139]

$$I_p = \frac{n^2F^2\,vA_{eff}\Gamma}{4RT} \qquad (4.3)$$

where I_p is the background corrected peak current, n is the number of transferred electrons, F is the Faraday constant, Γ is the surface coverage by NiNPs film, A_{eff} (0.0978 cm^2 obtained above), R is the universal gas constant and T is the temperature (298 K). The Γ value of 6.59 $\times10^{-10}$ mol cm^{-2} was obtained for the NiNP film. The Γ values for NiPc-GCE and NiNP/NiPc mix-GCE were 1.12 $\times10^{-10}$ mol cm^{-2} and 1.04 $\times10^{-10}$ mol cm^{-2}, respectively which are much smaller compared to NiNP-GCE, explaining the lower catalytic activity observed in the next chapter for the NiPc-GCE and NiNP/NiPc mix-GCE.

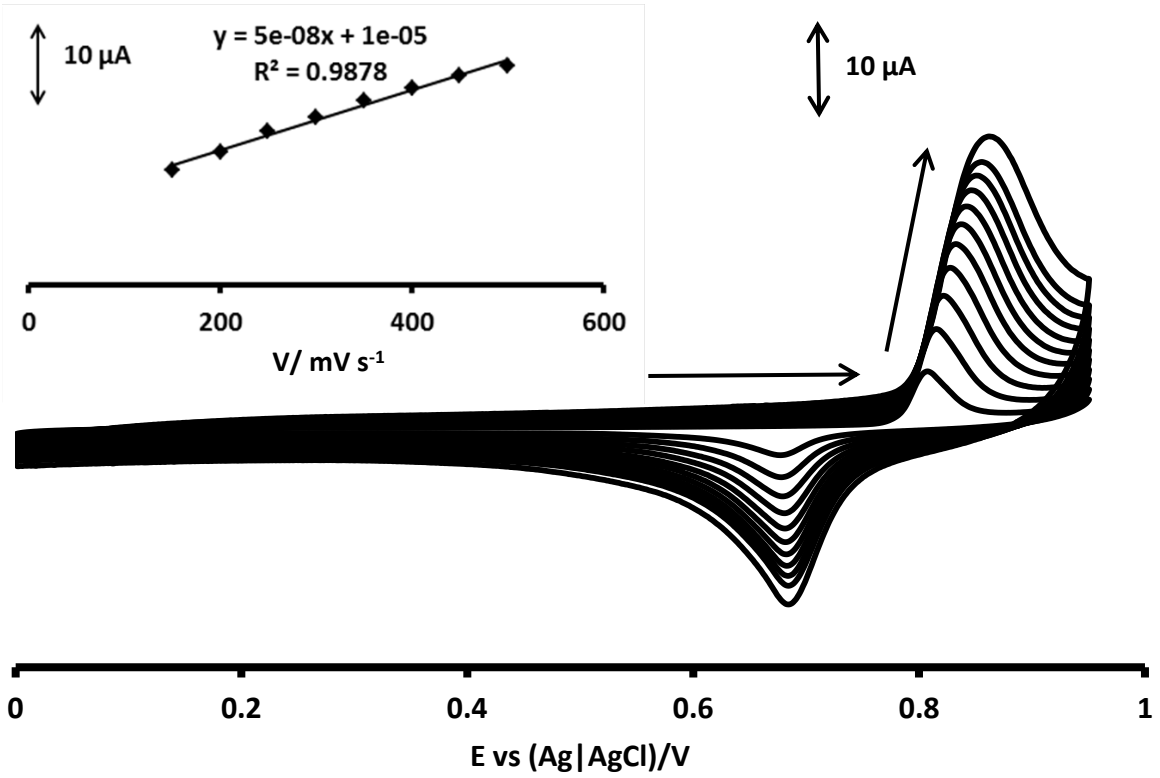

Fig. 4.2. Second cycle cyclic voltammograms of NiNP-GCE in pH 9.2 buffer with increasing scan rate (50 mV/s to 500 mV/s). Inset: Plot of peak current versus sweep rate for NiNP-GCE in pH 9.2 buffer.

4.2. NiTSPc and AuNPs

A combination of electrodeposition and electropolymerization was used to modify the electrode surface. Scheme 4.2 shows the summary of the modification of the GCE.

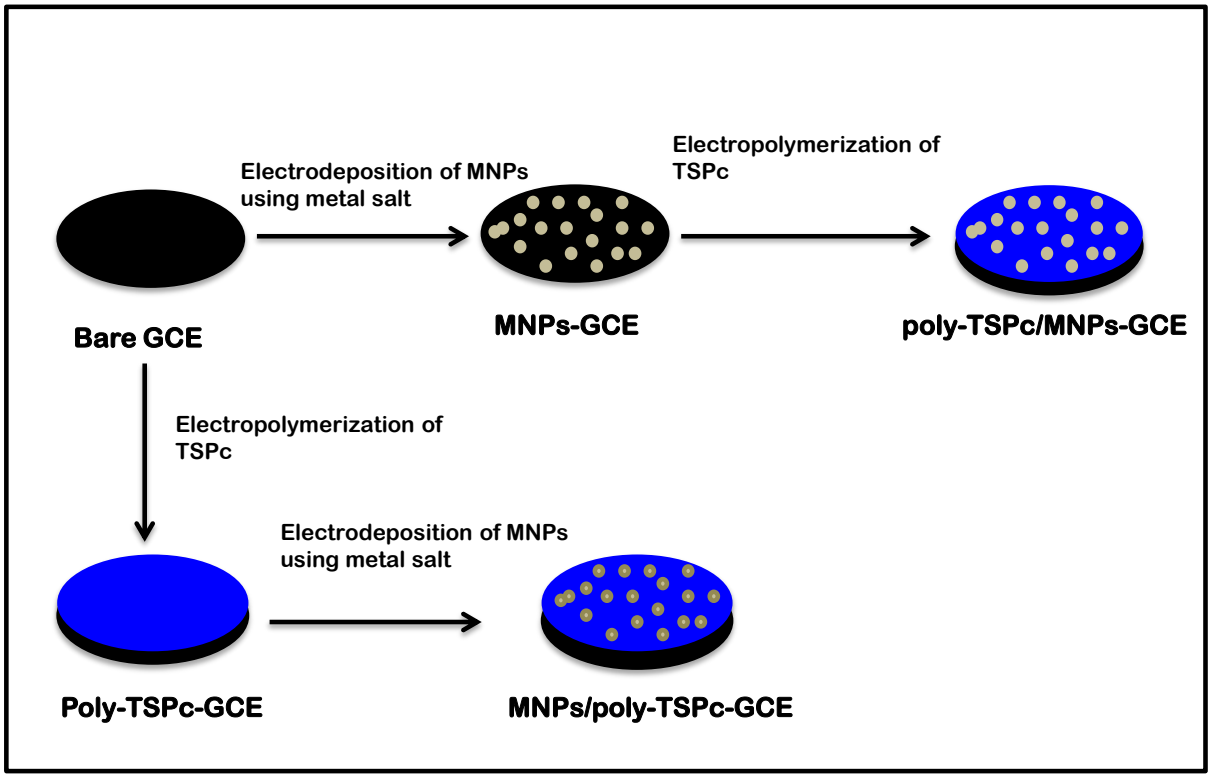

Scheme 4.2. Modification of the glassy carbon electrode (GCE). MNPs: metal nanoparticles, TSPc: tetrasubstituted phthalocyanine.

NiTSPc is water soluble unlike NiPc in the last section hence could be electrodeposited directly from its solution in basic medium. AuNPs were employed together with NiTSPc since AuNPs can be electrodeposited easily onto the electrode, unlike NiNPs.

4.2.1. Electrodeposition and activation of AuNPs

Fig. 4.3A shows the first and the last cyclic voltammogram of the electroreduction of 1 mM $HAuCl_4$ solution in 0.1 M $NaNO_3$. By cycling the potential from 1 V to 0 V, golden coloured deposits were observed. The forward scan shows the reduction of Au(III) to Au(0) with a cathodic peak at 0.53 V, inducing the deposition of AuNPs onto the GCE surface. This value is very close the one obtained by Hezard and co-workers [52] which was 0.48 V for the reduction of Au(III) on GCE. It can be observed from the cyclic voltammograms that the peak position has shifted to more positive values from 0.53 V to 0.70 V after the 10^{th} scan. This behaviour has been reported before for the formation of AuNPs on GCE [52]. This shift of the reduction peak indicates that on the subsequent scans, the Au deposition occurred on the NPs created during the first scan. Liu and co-workers suggested that the presence of Au nuclei make the deposition of Au easier [140].

The Au-GCE was activated (following literature methods [141]) using 0.5 M H_2SO_4 by cyclising (10 scans) within a potential window from 0.2 V to 1.4 V. Fig. 4.3B shows the cyclic voltammogram of scan number 10. The anodic and cathodic peaks increased with the increase of the number of scans. The anodic peaks between 1.0 and 1.3 V correspond to Au oxidation. The presence of two peaks is indicative of the formation of different types of Au oxides, mainly AuO according to Eq. 4.4 [141].

$$Au + H_2O \rightarrow AuO + 2H^+ + 2e^- \qquad (4.4)$$

The cathodic peak was found at 0.80 V which corresponds to the reduction of oxides formed during the forward scan.

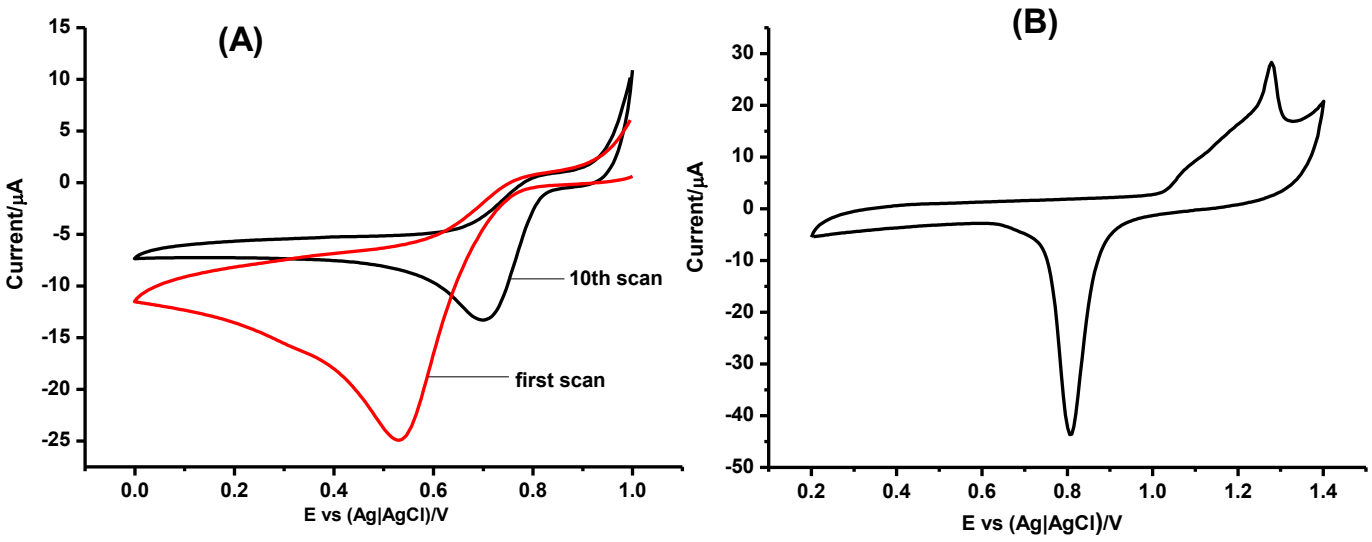

Fig. 4.3. Cyclic voltammograms (A) of the first and the last scan of 1 mM $HAuCl_4$ in 0.1 M $NaNO_3$. Number of scans: 10, scan rate: 50 mV/s, (B) on AuNPs-GCE recorded in 0.5 M H_2SO_4 solution, scan rate: 100 mV/s.

4.2.2. UV-Vis absorption spectrum of AuNPs

Fig. 4.4 shows the absorption spectra of gold nanoparticles in dimethyformamide (DMF). The AuNPs were removed from the GCE by sonicating the Au-GCE in DMF for 5 min. A colour in DMF was pale purple. The surface plasmon absorption resonance peak was obtained at 534 nm. The broad feature between 600 nm and 800 nm is associated with formation of aggregates. Hu and co-workers [142] found out that as the number of cycles increase for the electrodeposition, the peak between 600 nm and 800 nm become more pronounced and they attribute the peak to the formation of aggregates [142], due to the coalescence of adjacent AuNPs with increasing particle size.

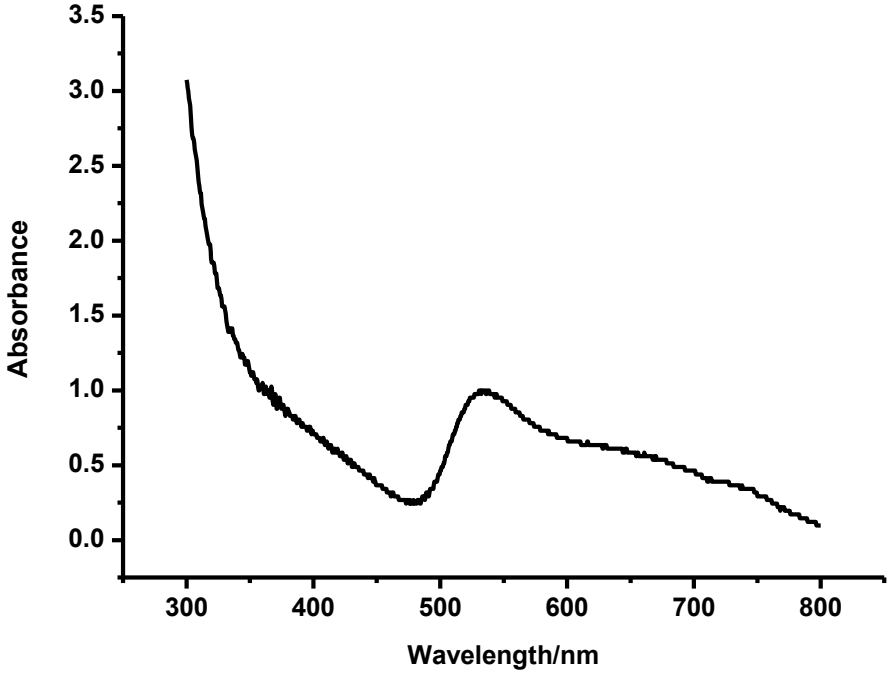

Fig. 4.4. Absorption spectrum of AuNPs in DMF.

4.2.3. Electrodeposition of poly-NiTSPc films

Poly-NiTSPc films were deposited onto the bare and Au-GCE using 1mM NiTSPc in 0.1 M NaOH. The intensity of currents for the Ni^{III}/Ni^{II} couple increased with increase in the number of cycles, Fig. 4.5A. Fig. 4.5B shows the typical cyclic voltammograms of the polymerized NiTSPc using 20 cycles on bare and Au-GCE. The peaks are similar to those in Fig 4.1 for the activation of NiPc in pH 9.2 buffer. The cyclic voltammograms shows that the current for the Ni^{III}/Ni^{II} couple was larger for Au-GCE than bare GCE for the same number of cycles. On the forward cycle, bare GCE had a current of 26 μA while Au-GCE had a current of 42 μA. This indicates that the AuNPs play an important role in promoting the deposition of NiTSPc. Similar cyclic

voltammograms were obtained for the electrodeposition of NiTSPc by Berrios and co-worker [143]. After the electropolymerization, the electrodes are denoted as poly-NiTSPc-GCE and poly-NiTSPc/Au-GCE for the bare and Au-GCE, respectively.

4.2.4. Microscopic characterization

Fig. 4.6a shows the transmission electron microscopy (TEM) image of the AuNPs evaporated from DMF solutions onto the copper grids. Some evidence of agglomeration can be seen on the image. This may be attributed to the number of cycle during electrodeposition as well as the concentration of $HAuCl_4$. The other probable cause of agglomeration is that, when the solvent evaporates from the TEM copper grids, it concentrates the AuNPs resulting in the formation of aggregates. The AuNPs are spherical in nature even though aggregated. Fig. 4.6 (b, c) shows a scanning electron microscope (SEM) AuNPs (b) and poly-NiTSPc/AuNPs (c) on a glassy carbon plate. Fig. 4.6b shows that the AuNPs well distributed across the glassy plate surface. Hezard et al [52] have observed similar results and they deduced that increasing the electrodeposition cycles would increase the average size of the particles. The SEM image of poly-NiTSPc/AuNPs (Fig. 4.6c) suggests that AuNPs have not been completely covered by the NiTSPc layer, since there are still some white spots (though reduced in number) compared to Fig. 4.6b. It is also possible that poly-NiTSPc occupies the empty area not covered by AuNPs in Fig. 4.6c. The morphological changes

that are observed on the glassy plates will in turn affect electrocatalytic activities.

To further confirm the presence of AuNPs, NiTSPc and NiTSPc on the carbon paste plate, energy dispersion spectroscopy (EDS) was used, Fig. 4.7. The carbon seen on the spectrum is obtained from the glassy carbon plate and is observed on all the substrates. Fig. 4.7a shows the presence of Ni on the NiTSPc modified glassy plate. Sodium is also observed as the phthalocyanine is a sodium salt (nickel tetrasulfonated phthalocyanine tetrasodium salt). Fig. 4.7b shows the presence of the AuNPs and no other element was observed apart from carbon. Fig. 4.7c shows the presence of both Ni (from NiTSPc) and Au (from AuNPs).

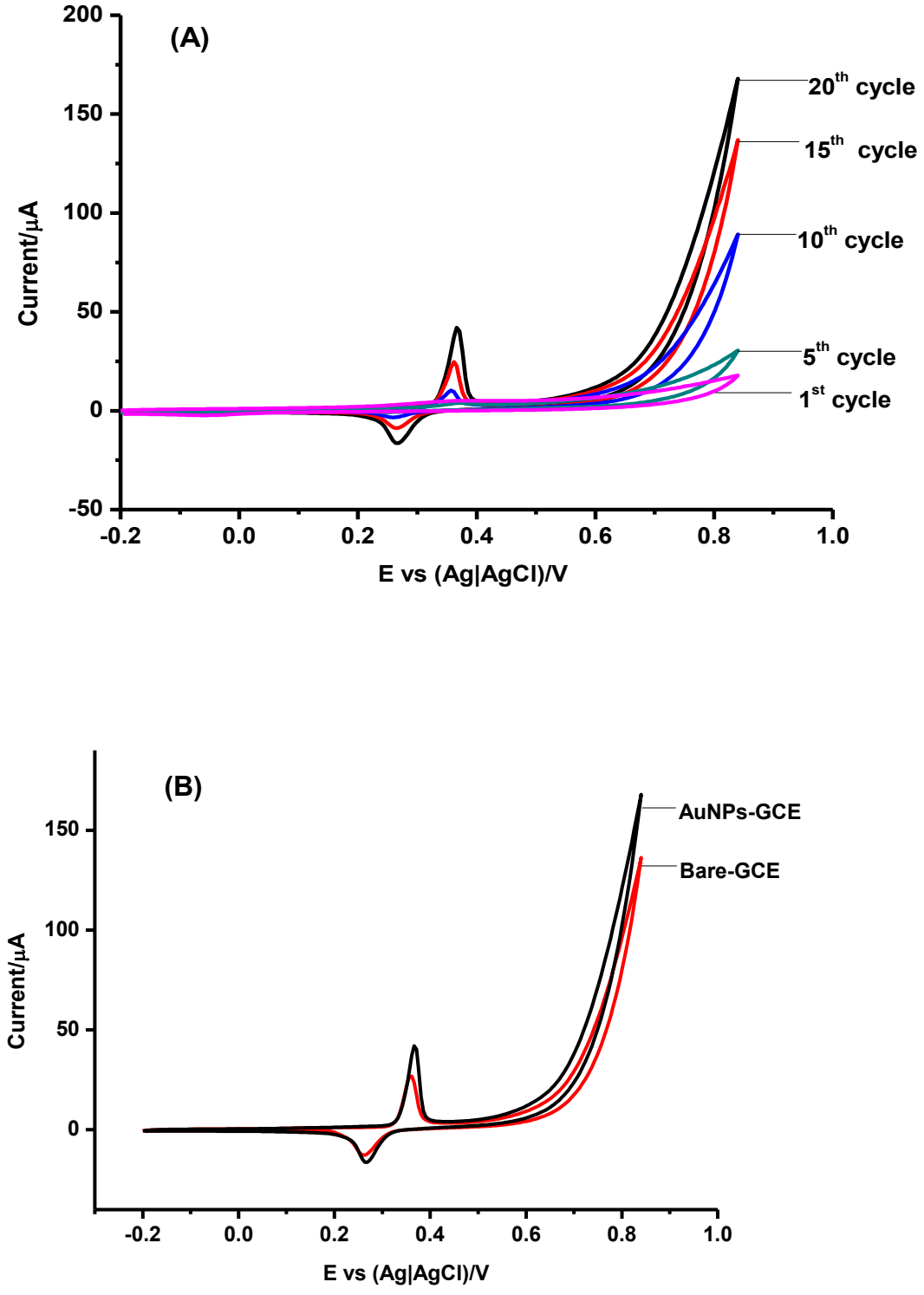

Fig. 4.5. (A) Continuous cyclic voltammograms for polymerization of NiTSPc (1 mM) on Au-GCE in 0.1 M NaOH and (B) and the comparison of the 20th cycle of bare GCE and Au-GCE in 1 mM NiTSPc. Scan rate: 10 mV/s.

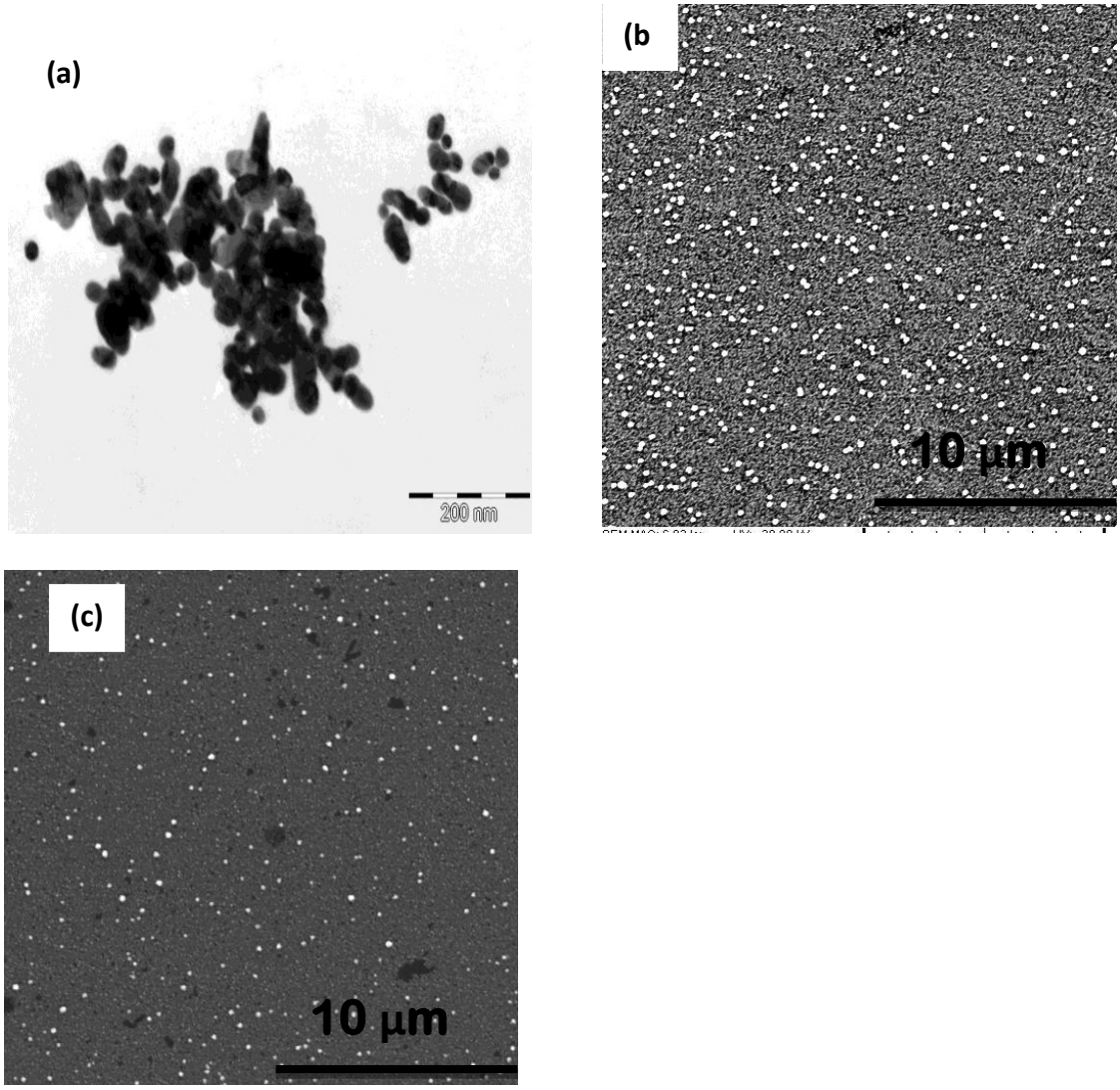

Fig. 4.6. TEM image of AuNPs evaporated from DMF solutions (a), and SEM image of AuNPs (b) and poly-NiTSPc/AuNPs (c) on a glassy carbon plate.

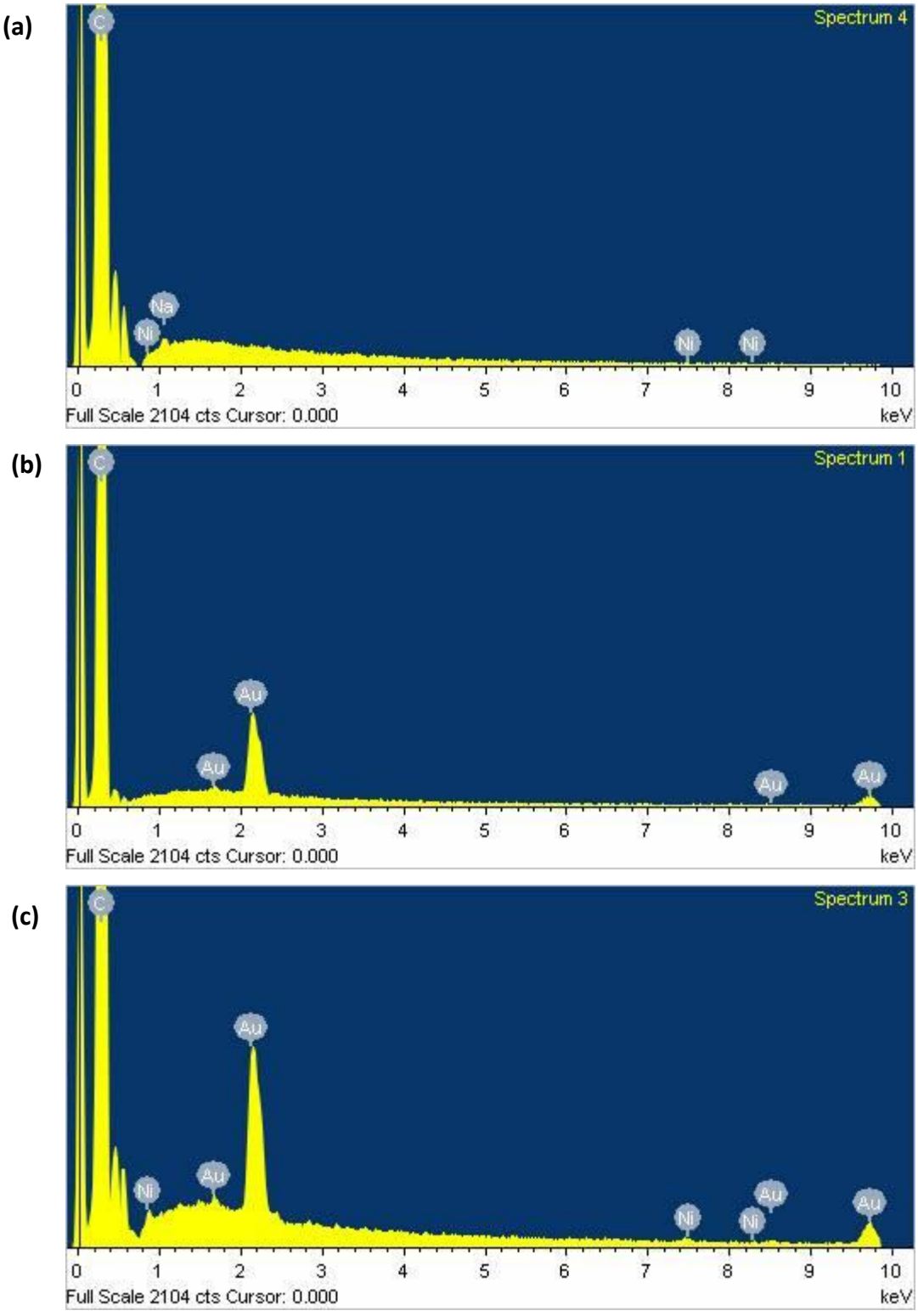

Fig. 4.7. EDS spectrum of poly-NiTSPc (a), AuNPs (b) and poly-NiTSPc/AuNPs (c) on glassy carbon plate.

4.2.5. Electrochemical characterization of the modified electrodes

Fig. 4.8 shows the cyclic voltammograms (CVs) of bare and modified electrodes in 2 mM ferricyanide dissolved in 0.1 M KCl. The anodic and cathodic peak separation (ΔE) for bare GCE, Au-GCE, poly-NiTSPc-GCE and poly-NiTSPc/Au-GCE are 74 mV, 83 mV, 126 mV and 110 mV respectively at a scan rate of 100 mV/s. In terms of electron transfer efficiency the order is bare GCE > Au-GCE > poly-NiTSPc/Au-GCE > poly-NiTSPc-GCE. ΔE is 126 mV for poly-NiTSPc-GCE and it decreases to 110 mV for poly-NiTSPc/Au-GCE. Thus the latter shows better electron transfer behaviour, confirming that the presence of AuNPs improves the electron transfer for NiTSPc. Au-GCE has a lower ΔE (compared to the rest of the modified electrodes) because AuNPs provide a high surface to volume ratio thus promoting good electron transfer between the redox probe and the electrode modifier much faster.

The surface roughness factor for the modified electrodes were determined using $[Fe(CN)_6]^{3-/4-}$ redox system (Fig. 4.8) and applying Randles–Sevcik Eq. (4.1) for reversible systems. The surface roughness factors (ratio of I_{pa} experimental/I_{pa} theoretical) of the electrodes were found to be 1.13, 1.02 and 1.04 for Au-GCE, poly-NiTSPc-GCE and poly-NiTSPc/Au-GCE, respectively, corresponding to a real electrode areas {(roughness factor × theoretical surface area (0.0707 cm^2)} of 0.072 cm^2 for poly-NiTSPc-GCE, 0.074 for poly-NiTSPc/Au-GCE and 0.080 cm^2 for AuNPs-GCE, thus showing a larger surface area for poly-NiTSPc/Au-GCE compared to poly-

NiTSPc, again showing the importance of the presence of both poly-NiTSPc and AuNPs.

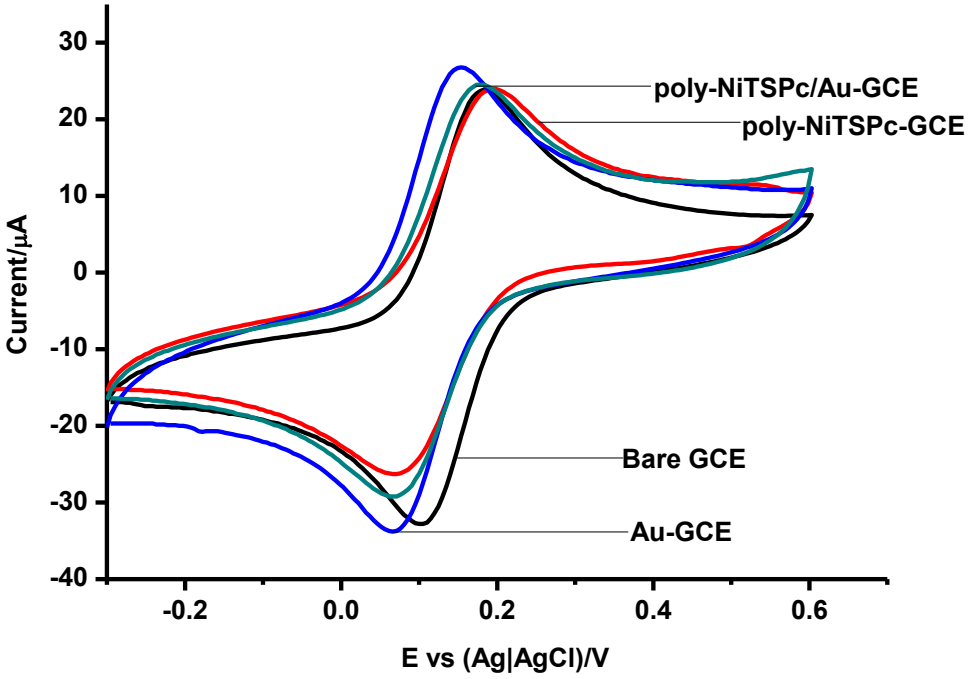

Fig. 4.8. Cyclic voltammograms of bare and modified GCE in 2 mM ferricyanide with 0.1 M KCl electrolyte. Scan rate: 100 mV/s.

The surface coverages of the modified GCE were determined using the CVs of modified electrodes in pH 8 buffer (to be used for nitrite detection). The CVs for poly-NiTSPc-GCE and poly-NiTSPc/Au-GCE are similar to those shown in Fig. 4.5B in 0.1 M NaOH. Surface coverage was calculated using Eq. 4.5.

$$\Gamma = \frac{Q}{nFA} \qquad (4.5)$$

where Γ is the surface coverage, Q was determined by integrating the area under the cathodic peak, n is the number of transferred electrons, F is the

Faraday constant and *A* is the real electrode area. The values of the surface coverage were found to be 1.79 × 10^{-10} mol cm^{-2} for poly-NiTSPc-GCE, 2.44 ×10^{-10} mol cm^{-2} for Au-GCE and 1.89 ×10^{-10} mol cm^{-2} for poly-NiTSPc/Au-GCE, Table 4.2. Thus higher surface coverages are obtained in the presence of both AuNPs and poly-NiTSPc.

4.3. CoTAPc with NPs

Repetitive cyclic voltammetry (CV) scanning of a solution containing CoTAPc in DMF results in a gradual increase in the oxidation currents, due to polymerization of this complex [121, 144]. Fig. 4.9 shows repetitive cyclic voltammograms for CoTAPc in DMF solutions in the presence of the 0.1 M $TBAFB_4$ as an electrolyte. A gradual increase in the faradaic current was observed for both the oxidation and reduction processes. As seen in Fig. 4.9, the first scan is different from the second and subsequent scans for CoTAPc, as has been observed before [121, 144]. Following polymerization, the poly-CoTAPc electrode was cycled in pH 8 buffer (pH to be used for electrocatalysis) and the CV is shown as an insert in Fig. 4.9. Process labelled **I** at $E_{½}$ = ~ -0.08 V is attributed to Co^{II}/Co^{I}. Similar peaks were observed in literature [10, 122].

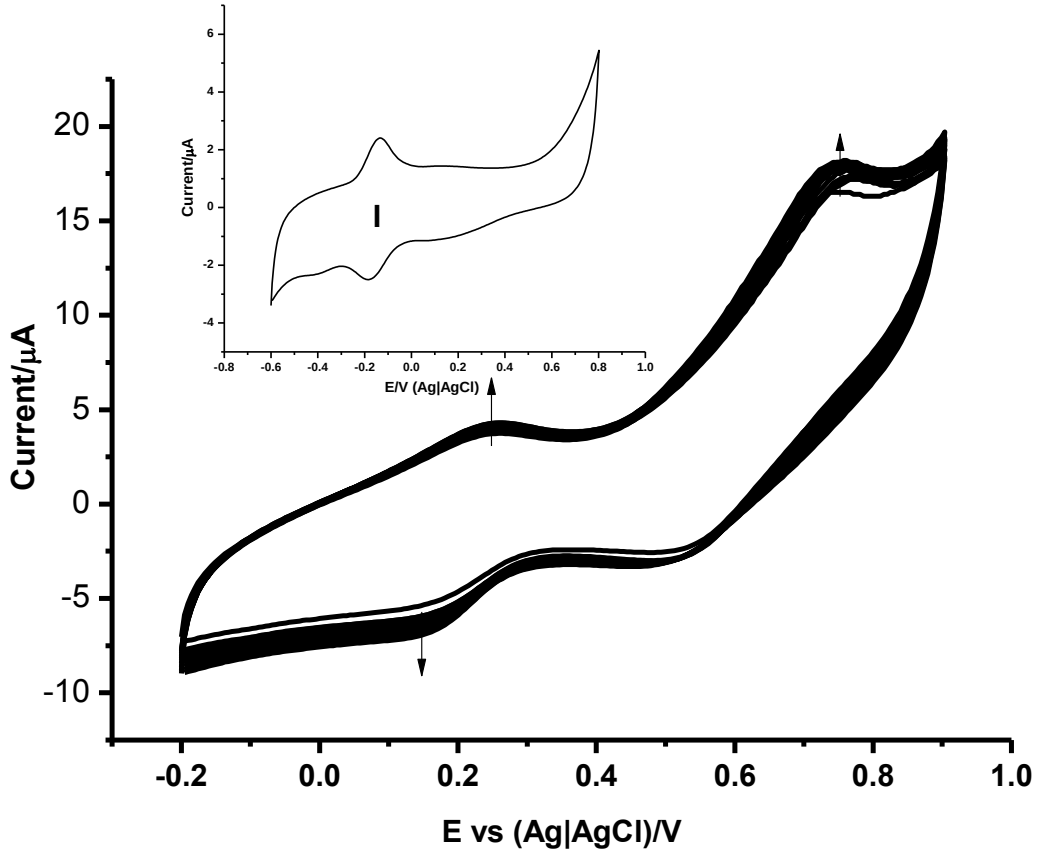

Fig. 4.9. Cyclic voltammetry of 1 mM CoTAPc in DMF containing 0.1 M $TBABF_4$ (electrolyte). Scan rate 200 mV/s. Inset: CV of poly-CoTAPc in pH 8 buffer.

4.3.1. CoTAPc and AuNPs

The electrodeposition and activation of AuNPs has been described in section 4.2.1.

4.3.1.1. SEM images and EDS

Fig. 4.10 shows a scanning electron microscope (SEM) image of AuNPs/poly-CoTAPc (a) and poly-CoTAPc/AuNPs (b) on a glassy carbon plate. SEM of

AuNPs are shown in Fig. 4.6b. When AuNPs are deposited on top of poly-CoTAPc, Fig. 4.10a the nanoparticles were evenly distributed, compared to poly-CoTAPc on top of AuNPs, Fig. 4.10b, and this will in turn affect electrocatalytic activities.

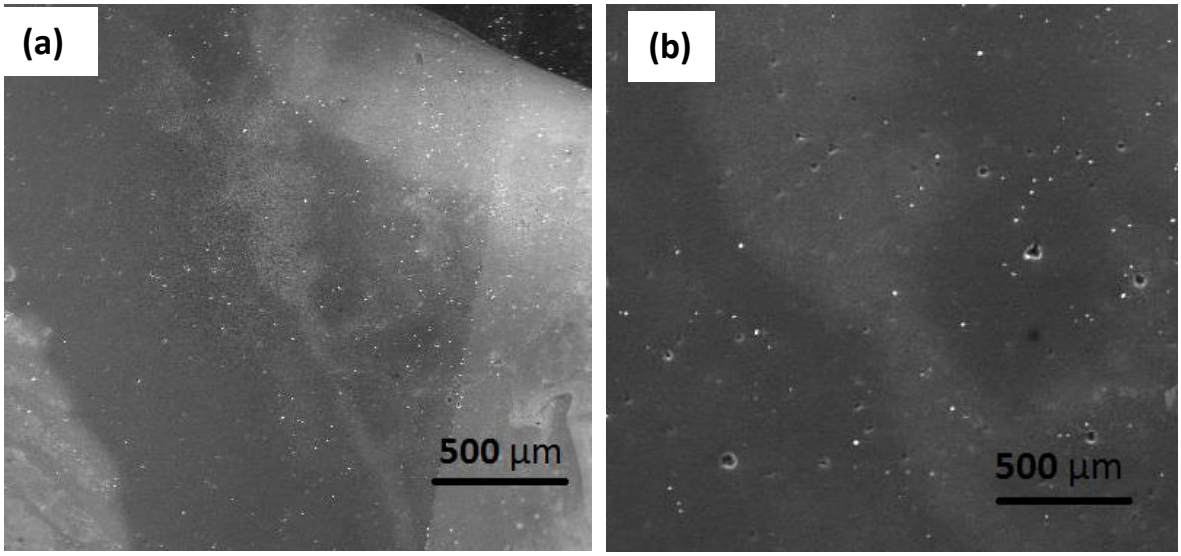

Fig. 4.10. SEM image of AuNPs/poly-CoTAPc (a) and poly-CoTAPc/AuNPs (b) on a glassy carbon plate.

4.3.1.2. X-ray photoelectron spectroscopy (XPS)

X-ray photoelectron spectroscopy was used to study the surface of unmodified and modified glassy carbon electrodes. Fig. 4.11 shows the X-ray photoelectron survey spectra of bare glassy carbon plate (GCP), Au-GCP, poly-CoTAPc-GCP, Au/poly-CoTAPc-GCP and poly-CoTAPc/Au-GCP. The wide scan shows the presence of C (1s) at around 282 eV. The intensity of the peak varies depending on the nature of modification of the GCP. Au/poly-CoTAPc-GCP has the lowest C (1s) peak. The gold peaks are

observed at 84 eV (4f), 88 eV (4f), 335 eV (4d), 355 eV (4d), 547 eV (4p). They are prominent for Au-GCP and Au/poly-CoTAPc-GCP, where the AuNPs are exposed. In poly-CoTAPc/Au-GCP, the peaks are weak indicating that the top layer is the one that dominates. Cobalt peaks are observed at 781 eV (2p) and 795 eV (2p). The nitrogen peaks are clearly seen on poly-CoTAPc and poly-CoTAPc/Au-GCP at 400 eV (1s). There were no observable peaks of Co on the Au/poly-CoTAPc-GCE this is due to the fact that the AuNPs completely cover the surface containing poly-CoTAPc. The samples were all exposed to atmospheric oxygen as a result we observed the presence of oxygen peak at 533 eV (1s).

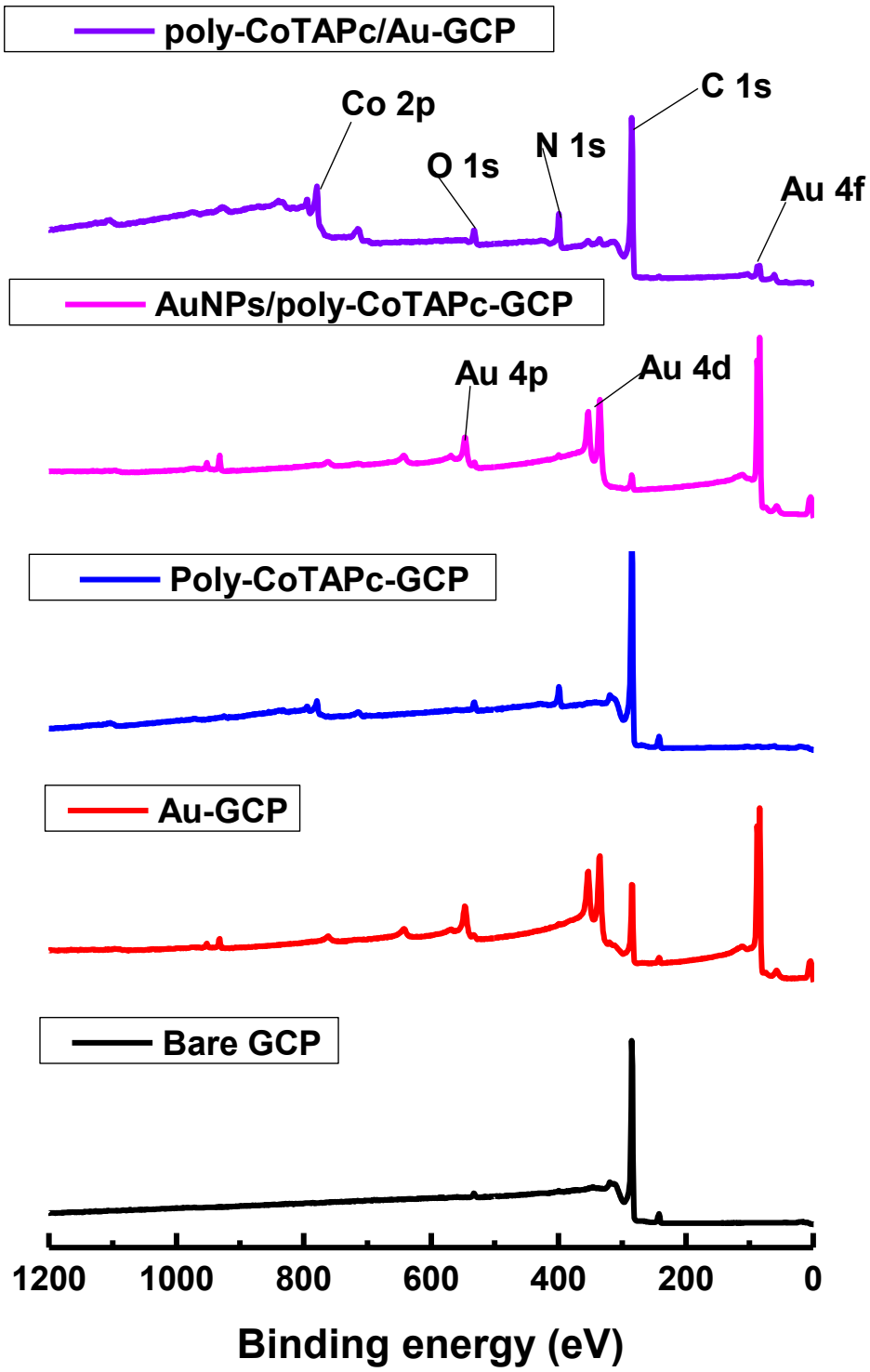

Fig. 4.11. X-ray photoelectron spectra for bare GCP, Au-GCP, poly-CoTAPc-GCP, Au/poly-CoTAPc-GCP and poly-CoTAPc/Au-GCP.

4.3.1.3. Electrochemical characterization

The CVs of ferricyanide for bare GCE, Au-GCE, poly-CoTAPc-GCE, poly-CoTAPc/Au-GCE and Au/poly-CoTAPc-GCE have similar peaks to Fig. 4.8. The anodic and cathodic peak separation (ΔE_p) for bare GCE, Au-GCE, poly-CoTAPc-GCE, poly-CoTAPc/Au-GCE and Au/poly-CoTAPc-GCE are 74 mV, 83 mV, 78 mV, 83 mV and 78 mV, respectively, at a scan rate of 100 mV/s. In terms of electron transfer efficiency the order is bare GCE > Au/poly-CoTAPc-GCE = poly-CoTAPc-GCE > Au-GCE = poly-CoTAPc/Au-GCE. This confirms good electron transfer kinetics of the bare GCE. Au/poly-CoTAPc-GCE has a lower ΔE (compared to the rest of the modified electrodes) suggesting fast electron transfer between the redox probe and the electrode modifier.

The surface roughness factor for the modified electrodes were determined using $[Fe(CN)_6]^{3-/4-}$ redox system and applying Randles–Sevcik Eq. (4.1) for reversible systems. A_{eff} was estimated to be 0.076 cm^2, 0.092 cm^2, 0.096 cm^2 and 0.10 cm^2 (higher than–geometric area = 0.071 cm^2 for a GCE) for Au-GCE, poly-CoTAPc-GCE, poly-CoTAPc/Au-GCE and Au/poly-CoTAPc-GCE respectively, giving roughness factor (= area of modified GCE/area of bare GCE) of 1.07, 1.30, 1.35 and 1.46, respectively. The roughness factors for the poly-CoTAPc/Au-GCE and Au/poly-CoTAPc-GCE are higher than for the rest of the electrodes due to heterogeneity caused by two different layers (AuNPs and poly-CoTAPc).

The values of the surface coverage was found to be 2.44 $\times 10^{-10}$ mol cm^{-2}, 3.10 $\times 10^{-10}$ mol cm^{-2}, 3.15 $\times$ 10^{-10} mol cm^{-2} and 3.40 $\times$ 10^{-10} mol cm^{-2}, for Au-GCE, poly-CoTAPc-GCE, poly-CoTAPc/Au-GCE and Au/poly-CoTAPc-GCE, respectively, Table 4.2. These values are higher than a monolayer surface coverage for a phthalocyanine molecule lying flat [123]. For CoTAPc, surface coverage is known to increase with the number of scans [144].

Fig. 4.12 shows the cyclic voltammograms of bare GCE, Au-GCE, poly-CoTAPc-GCE, poly-CoTAPc/Au-GCE and Au/poly-CoTAPc-GCE recorded in pH 4 buffer at a scan rate of 100 mV/s. pH 4 buffer was chosen since nitrite analysis will be carried out at this pH. Au/poly-CoTAPc-GCE showed no peak. Since the poly-CoTAPc layer is under the AuNPs for Au/poly-CoTAPc-GCE, no peaks due to the CoTAPc were observed, Fig. 4.12. Au-GCE showed a small anodic peak at 0.89 V this was attributed to the oxidation of AuNPs. The cyclic voltammogram for Au-GCE (in pH 4) differs from one in Fig. 4.3B due to the conditioning in Fig. 4.3B and also differences in media. Three processes are observed for poly-CoTAPc/Au-GCE and two for poly-CoTAPc-GCE. The process labelled **II** at $E_{½}$ = 0.37 V and 0.35 V (for poly-CoTAPc-GCE and poly-CoTAPc/Au-GCE, respectively) is attributed to Co^{III}/Co^{II} and process **III** at $E_{½}$ =0.55 V and 0.52 V (poly-CoTAPc-GCE and poly-CoTAPc/Au-GCE respectively) is attributed to the ring based process [145-147]. Process **I** ($E_{½}$ = 0.16 V) is observed for poly-CoTAPc/Au-GCE (and not for poly-CoTAPc-GCE because it occurs at a negative potential window). This process may be attributed to the Co^{II}/Co^{I} in comparison with literature [122] but shifted to more positive potentials in acid media used in this work.

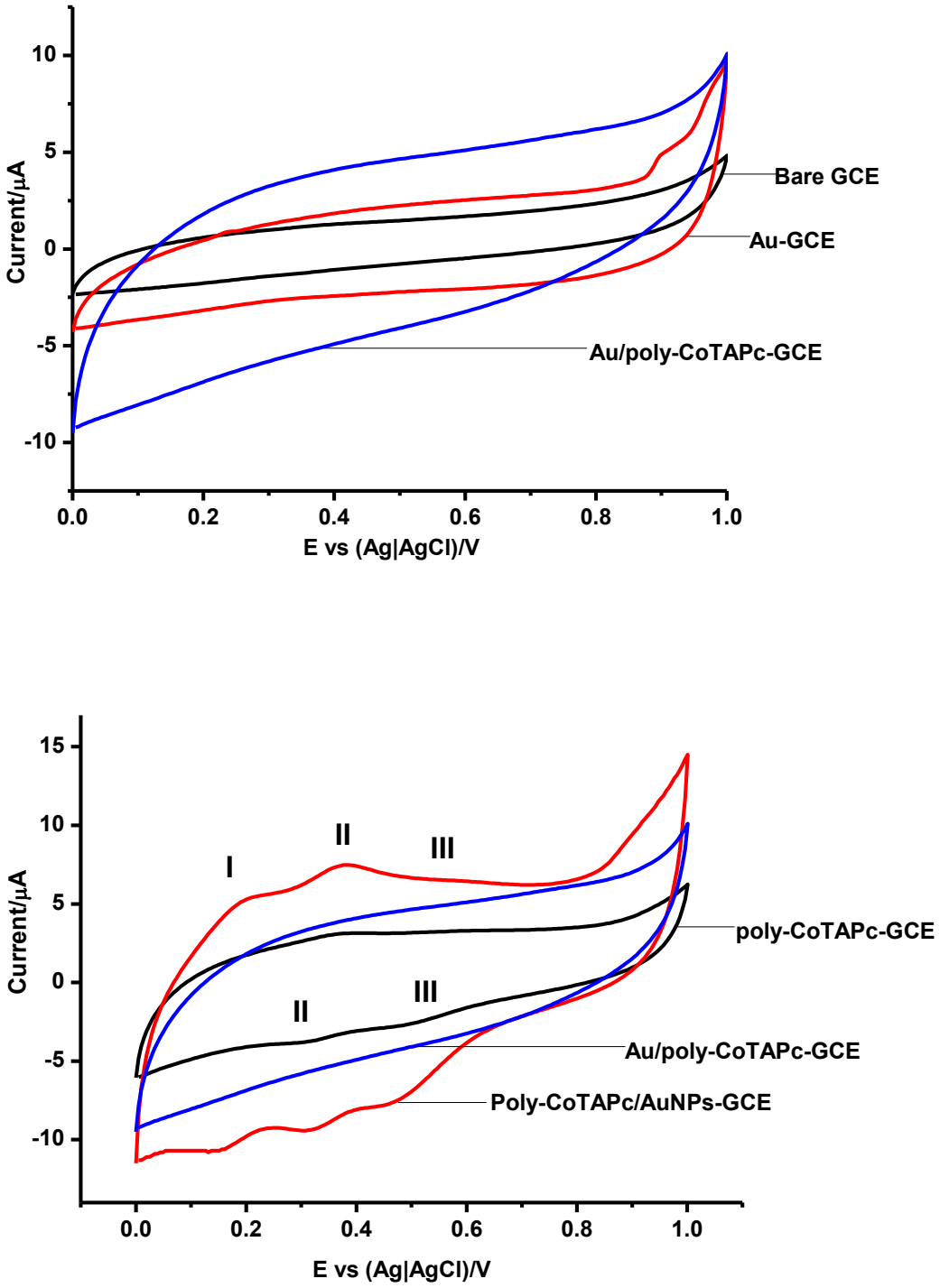

Fig. 4.12. Cyclic voltammograms of bare and modified GCE recorded in pH 4 buffer. Scan rate: 100 mV/s.

4.3.1.4. Scanning electrochemical microscopy (SECM)

Fig. 4.13 shows the 3 D images of unmodified and modified glassy carbon plates (GCP) surfaces. The plates were immersed in an aqueous solution of 2 mM ferricyanide and 0.1 M KCl. The ultramicroelectrode (UME) 15 μm radius Pt, was held at -0.1 V vs Ag|AgCl and brought 10 μm close to the GCP. This resulted in a reduction current corresponding to $[Fe^{III}(CN)_6]^{3-} + e^- \rightarrow [Fe^{II}(CN)_6]^{4-}$. Then, the tip was scanned in the x,y plane (200 μm × 200 μm), ≈ 10 μm above the substrate. From the image in Fig. 4.13a, it can be seen that the surface of the unmodified plate is smooth and low current was detected. When GCP was modified (Fig. 4.13b-e), the surface becomes rougher and shows higher currents as compared to the unmodified GCP. Au/poly-CoTAPc-GCP (Fig. 4.13e) had the roughest surface and highest currents were detected. The results are well supported by the cyclic voltammetry ferricyanide studies in which Au/poly-CoTAPc-GCP had the lowest ΔE for the modified GCEs.

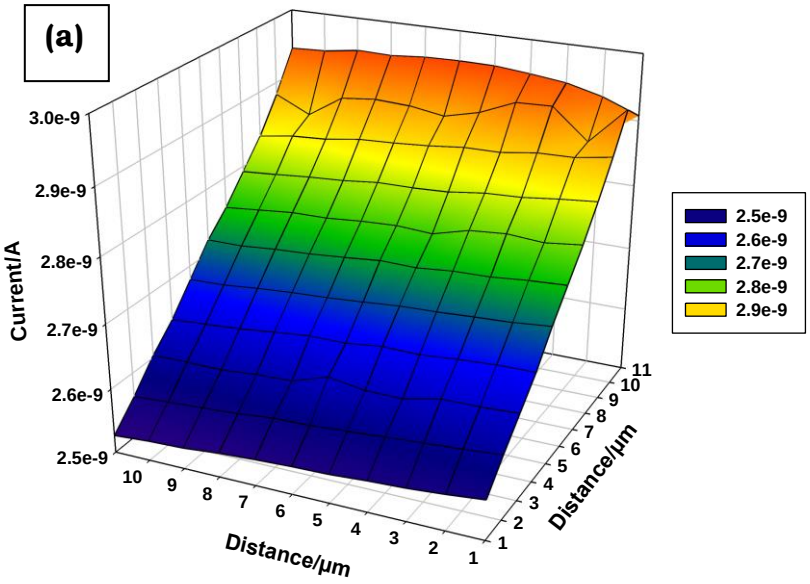
(a)
Current/A
3.0e-9
2.9e-9
2.8e-9
2.7e-9
2.6e-9
2.5e-9
Distance/µm
Distance/µm
2.5e-9
2.6e-9
2.7e-9
2.8e-9
2.9e-9

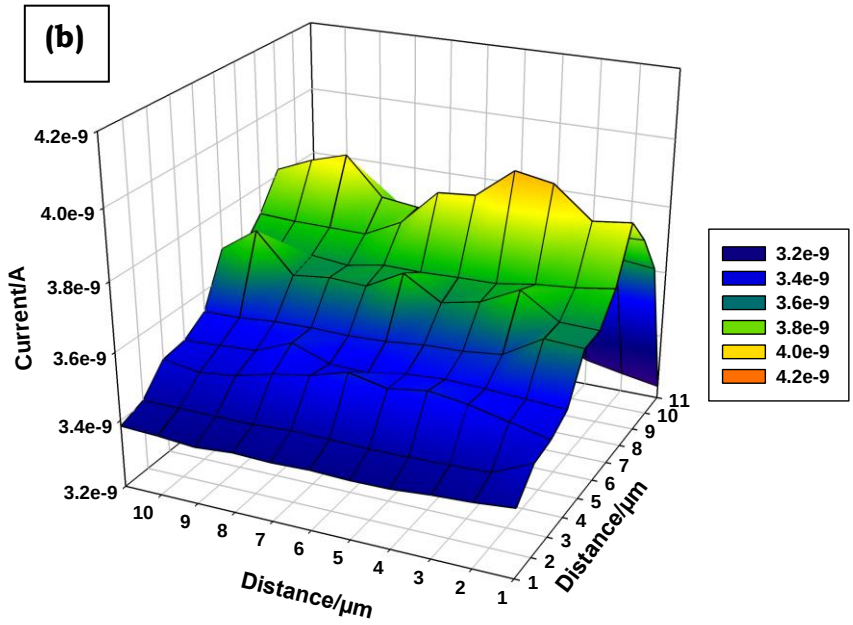
(b)
Current/A
4.2e-9
4.0e-9
3.8e-9
3.6e-9
3.4e-9
3.2e-9
Distance/µm
Distance/µm
3.2e-9
3.4e-9
3.6e-9
3.8e-9
4.0e-9
4.2e-9

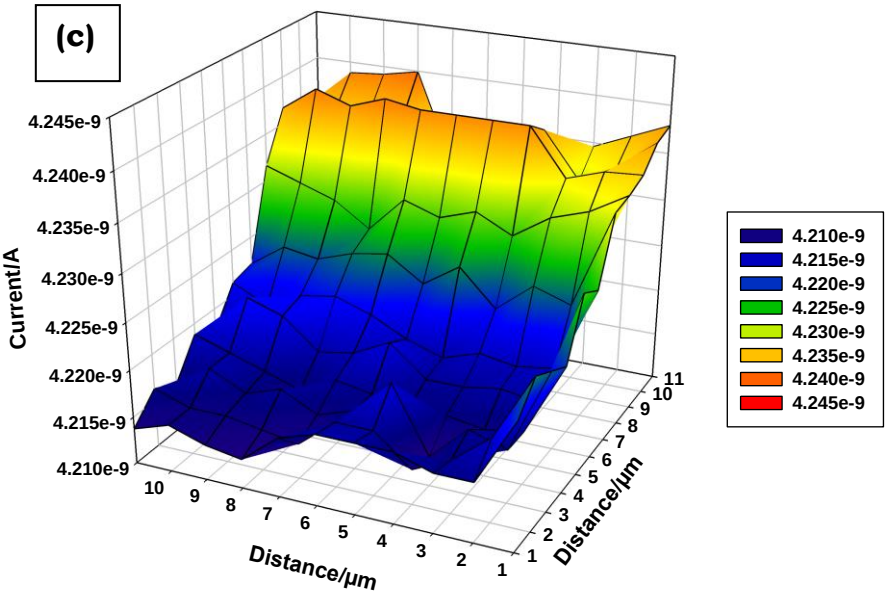
(c)
Current/A
4.245e-9
4.240e-9
4.235e-9
4.230e-9
4.225e-9
4.220e-9
4.215e-9
4.210e-9
Distance/µm
Distance/µm
4.210e-9
4.215e-9
4.220e-9
4.225e-9
4.230e-9
4.235e-9
4.240e-9
4.245e-9

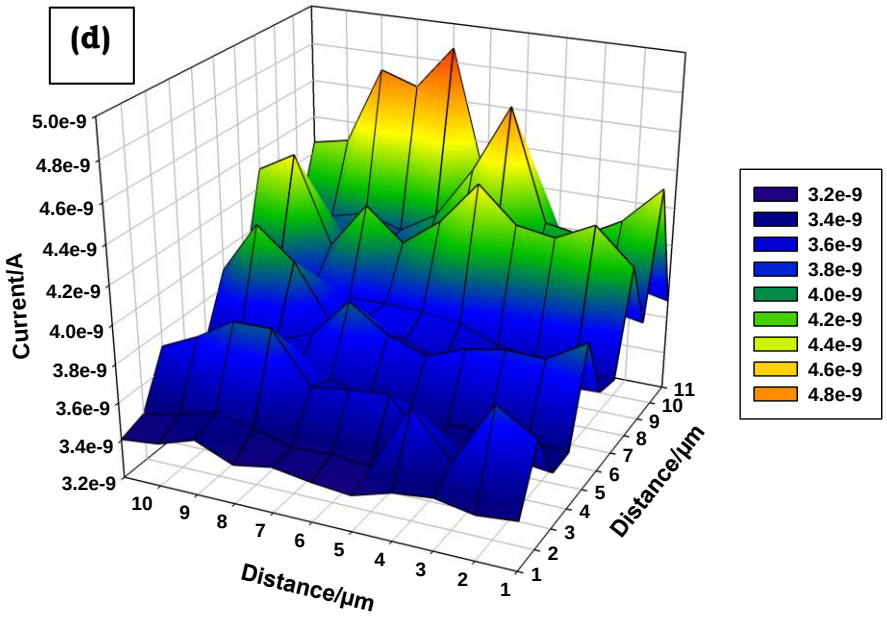
(d)
Current/A
5.0e-9
4.8e-9
4.6e-9
4.4e-9
4.2e-9
4.0e-9
3.8e-9
3.6e-9
3.4e-9
3.2e-9
Distance/µm
Distance/µm
3.2e-9
3.4e-9
3.6e-9
3.8e-9
4.0e-9
4.2e-9
4.4e-9
4.6e-9
4.8e-9

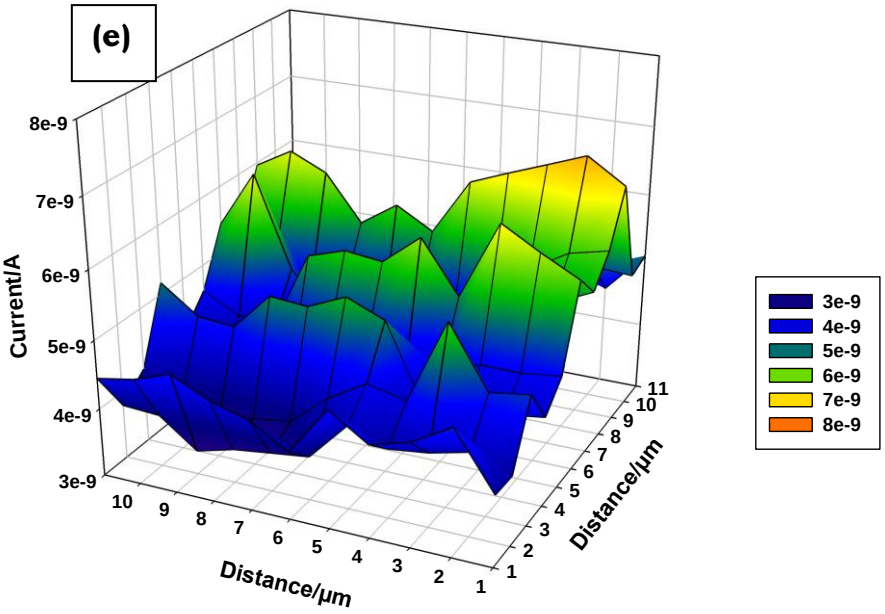

Fig. 4.13. SECM image of (a) bare GCP, (b) Au-GCP, (c) poly-CoTAPc-GCP, (d) poly-CoTAPc/Au-GCP (e) Au/poly-CoTAPc-GCP in 0.1 M KCl containing 2 mM ferricyanide solution. Imaging conditions: Pt UME (15 µm diameter) placed 10 µm above the substrate, poised at a potential of − 0.1 V vs Ag/AgCl.

4.3.2. CoTAPc and PdNPs

Since it was shown that attaching poly-CoTAPc first followed by AuNPs gave the best ΔE values for ferricyanide, the subsequent studies involving CoTAPc were all performed by attaching CoTAPc first followed by nanoparticles.

4.3.2.1. Microscopic characterization

Fig. 4.14 shows the SEM images of PdNPs and PdNPs/poly-CoTAPc, PdNPs can be clearly seen on Fig. 4.14a, showing that they are not well dispersed and they have agglomerated. When the PdNPs are deposited on top of the poly-CoTAPc (Fig. 4.14b), there is more evidence of more isolated nanoparticles compared to agglomerated ones. Fig. 4.14b (inset) shows isolated PdNPs.

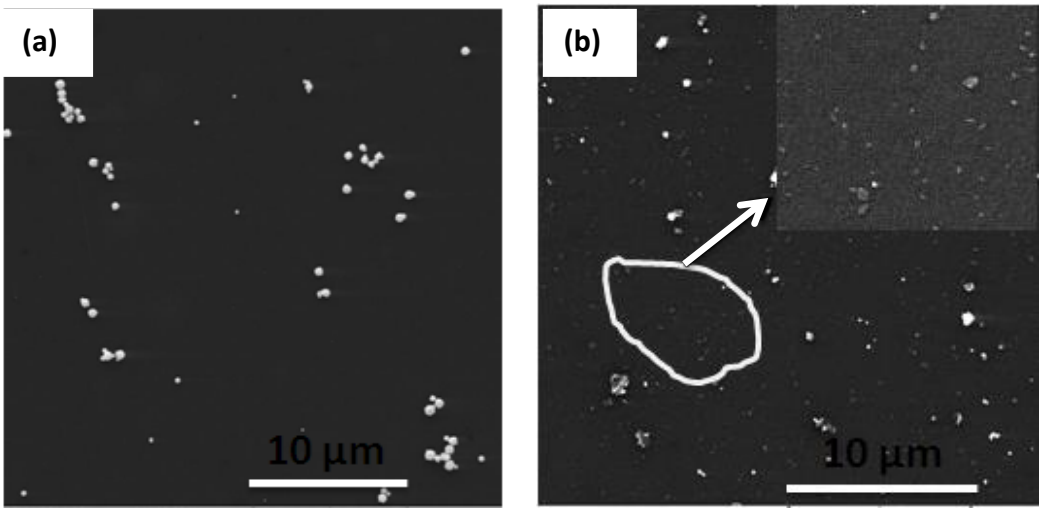

Fig. 4.14. SEM images of PdNPs (a) and PdNPs/poly-CoTAPc (b) on a glassy carbon plate. Inset in (b) individual nanoparticles.

4.3.2.2. XPS

XPS was also used to confirm the existence of poly-CoTAPc and PdNPs on the glassy carbon plate. Fig. 4.15a shows the wide scan XPS spectra of poly-CoTAPc, PdNPs and PdNPs/poly-CoTAPc. All the spectra have C (1s) peak

from the glassy carbon plates. Main peaks for XPS spectra for poly-CoTAPc are Co (2p) and N (1s) which confirms that the electropolymerization of CoTAPc was achieved. The oxygen peak at 532 eV is also visible on the poly-CoTAPc. The peak originates from the oxygen adsorbed on the surface of poly-CoTAPc. PdNPs and PdNPs/poly-CoTAPc do not show the oxygen peaks as the Pd (3p) has dominant peaks in the region where the oxygen peaks are located. Co (2p) and N (1s) peaks were also observed on the PdNPs/poly-CoTAPc. XPS spectra of PdNPs and PdNPs/poly-CoTAPc showed the characteristic features of palladium at 1159 eV (Pd MNNa), 672 eV (Pd 3s), 560 eV (Pd 3p), 533 eV (Pd 3p), 336 eV (Pd 3d), 88 eV (Pd 4s) and 52 eV (Pd 4p). The chloride peak is from the $PdCl_2$ used for the formation of PdNPs.

High resolution XPS spectra were carried out at Pd 3d peak for PdNPs and PdNPs/poly-CoTAPc. Fig. 4.15b shows peaks at 335.4 eV and 340.6 corresponding to Pd $3d_{5/2}$ and Pd $3d_{3/2}$ respectively for both PdNPs and PdNPs/poly-CoTAPc. This indicates that most of the Pd ions have been reduced to Pd^0 as reported in literature [148, 149]. However, there are some noticeable peaks at the binding energies of 337.8 eV and 343.0 eV. They correspond to the Pd^{2+} ions which have not been reduced. In the case of PdNPs/poly-CoTAPc it is possible that nitrogen atoms (from the peripheral amino groups on the Pc) are coordinatively bonded to palladium ions [37], hence contributing to the intensity of the peaks. To prove if there are any bonds formed between nitrogen atoms and palladium ions, a high resolution XPS was carried out at the N 1s energy levels. Fig. 4.15c and 4.15d show the N 1s spectra of poly-CoTAPc and PdNPs/poly-CoTAPc. The peaks at

binding energy of around 398 eV and 400 eV are observed and are attributed to imine (=N–) and amine (–NH–), respectively [148, 149]. The latter has shifted to higher energies for PdNPs/poly-CoTAPc due to the presence of Pd. The peak at binding energy of 402.5 eV is attributed to charged nitrogen species [148, 149] and it is not observed on the PdNPs/poly-CoTAPc. This may suggest that it have been involved in forming a bond with palladium ions.

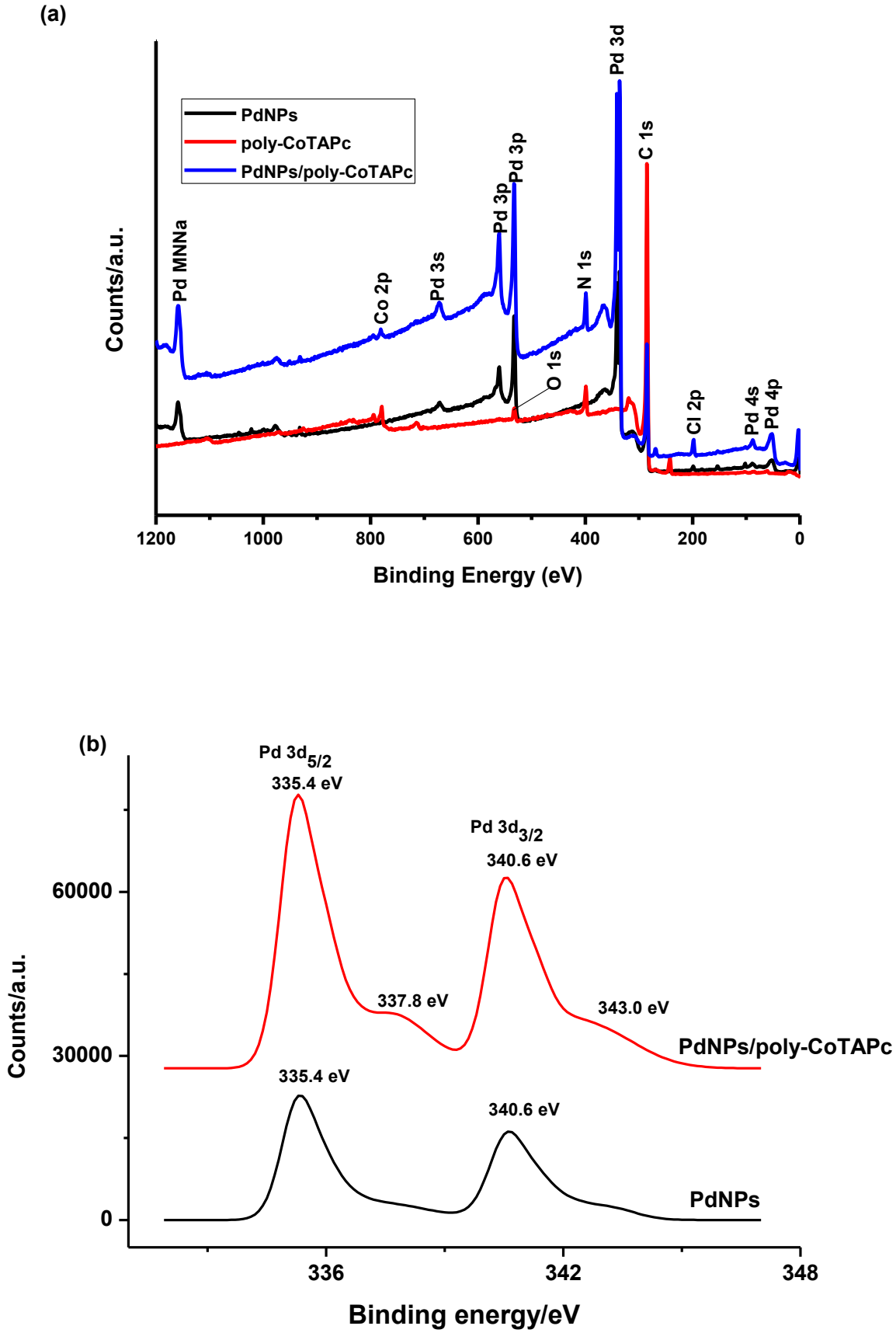
(a)
PdNPs
poly-CoTAPc
PdNPs/poly-CoTAPc
Pd MNNa
Co 2p
Pd 3s
Pd 3p
Pd 3p
O 1s
N 1s
Pd 3d
C 1s
Cl 2p
Pd 4s
Pd 4p
Counts/a.u.
1200
1000
800
600
400
200
0
Binding Energy (eV)
(b)
Pd 3d5/2
335.4 eV
Pd 3d3/2
340.6 eV
337.8 eV
343.0 eV
PdNPs/poly-CoTAPc
335.4 eV
340.6 eV
PdNPs
60000
30000
0
Counts/a.u.
336
342
348
Binding energy/eV

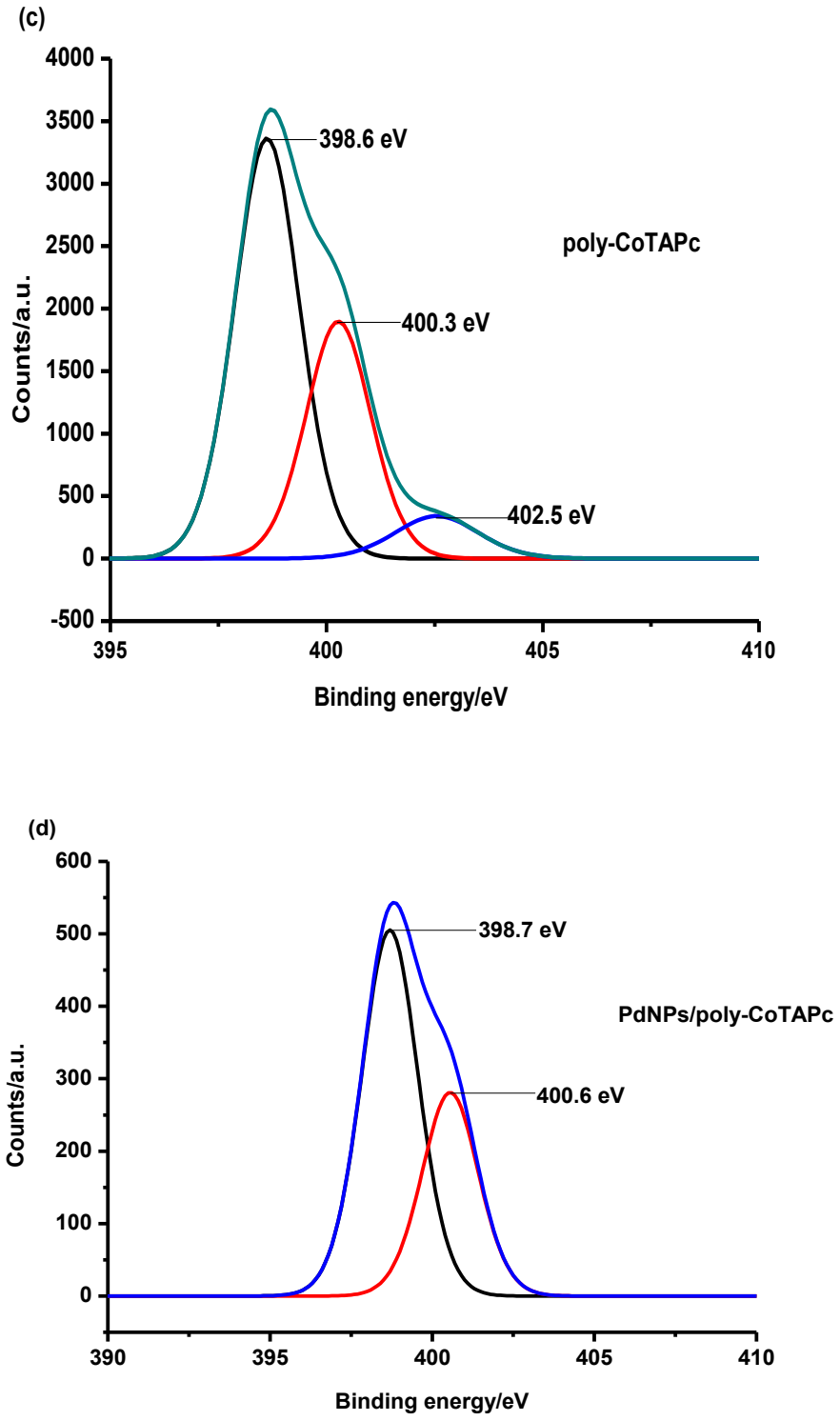

Fig. 4.15. Wide scan XPS spectra of poly-CoTAPc, PdNPs and PdNPs/poly-CoTAPc (a). High resolution Pd 3d XPS spectra for PdNPs and PdNPs/poly-CoTAPc (b). High resolution N 1s XPS spectra for poly-CoTAPc (c) and PdNPs/poly-CoTAPc (d).

4.3.2.3. Electrochemical characterization of the modified electrodes

The anodic and cathodic peak separation (ΔE) for modified electrodes (in 2 mM ferricyanide in 0.1 M KCl) for bare GCE, Pd-GCE, poly-CoTAPc-GCE and Pd/poly-CoTAPc-GCE are 74 mV, 88 mV, 78 mV and 88 mV, respectively at a scan rate of 100 mV/s, Table 4.2. In terms of electron transfer efficiency the order is bare GCE > poly-CoTAPc-GCE > Pd/poly-CoTAPc-GCE = Pd-GCE.

The surface roughness factor for the modified electrodes were determined using $[Fe(CN)_6]^{3-/4-}$ redox system and applying Randles–Sevcik Eq. 4.1 for reversible systems. The surface roughness factors (ratio of I_{pa} experimental/I_{pa} theoretical) of the electrode were found to be 1.08, 1.33 and 1.46 for Pd-GCE, poly-CoTAPc-GCE and Pd/poly-CoTAPc-GCE, respectively. Corresponding to real electrode areas {(roughness factor × theoretical surface area (0.071 cm^2)} of 0.077 cm^2 for Pd-GCE, 0.094 for poly-CoTAPc-GCE and 0.10 cm^2 for Pd/poly-CoTAPc-GCE. Using the effective area of the electrode, the surface coverage was calculated using Eq. 4.5. The values of the surface coverages were found to be 1.82×10^{-9} mol cm^{-2} for Pd-GCE, 3.10×10^{-10} mol cm^{-2} for poly-CoTAPc-GCE and 1.90×10^{-9} mol cm^{-2} Pd/poly-CoTAPc-GCE, Table 4.2. Thus, higher surface coverages are obtained in the presence of both poly-CoTAPc and PdNPs.

Fig. 4.16 shows the cyclic voltammograms of bare GCE, poly-CoTAPc-GCE, Pd-GCE and Pd/poly-CoTAPc-GCE recorded in pH 8 buffer at a scan rate of 50 mV/s. pH 8 buffer was used since hydrazine analysis will be carried out at this pH. The bare GCE showed no peak and this was expected. Poly-CoTAPc-GCE showed peaks though they were not well pronounced. The inset on Fig. 4.16 shows that there are two processes occurring at the electrode. Process labelled **I** at $E_{½}$ = -0.20 V is attributed to Co^{II}/Co^{I} (though the assignment is still controversial [144]). Process **II** at $E_{½}$ = 0.15 V is attributed to the Co^{III}/Co^{II} [144-147]. Both peaks are not well resolved as has been observed before [144]. Increasing the number of scan for polymer formation was reported not to improve resolution of these peaks [144]. The peak near 0.8 V (Fig. 4.16, inset) is associated with the oxidation of the amino group [150]. Palladium nanoparticles undergo oxidation to give different types of oxides, processes **2a** and **3a** (Fig. 4.16) [151-153] which are reduced at **3c.** The redox couples labelled **1a** and **1c** are also associated with PdNPs redox processes [151, 152].

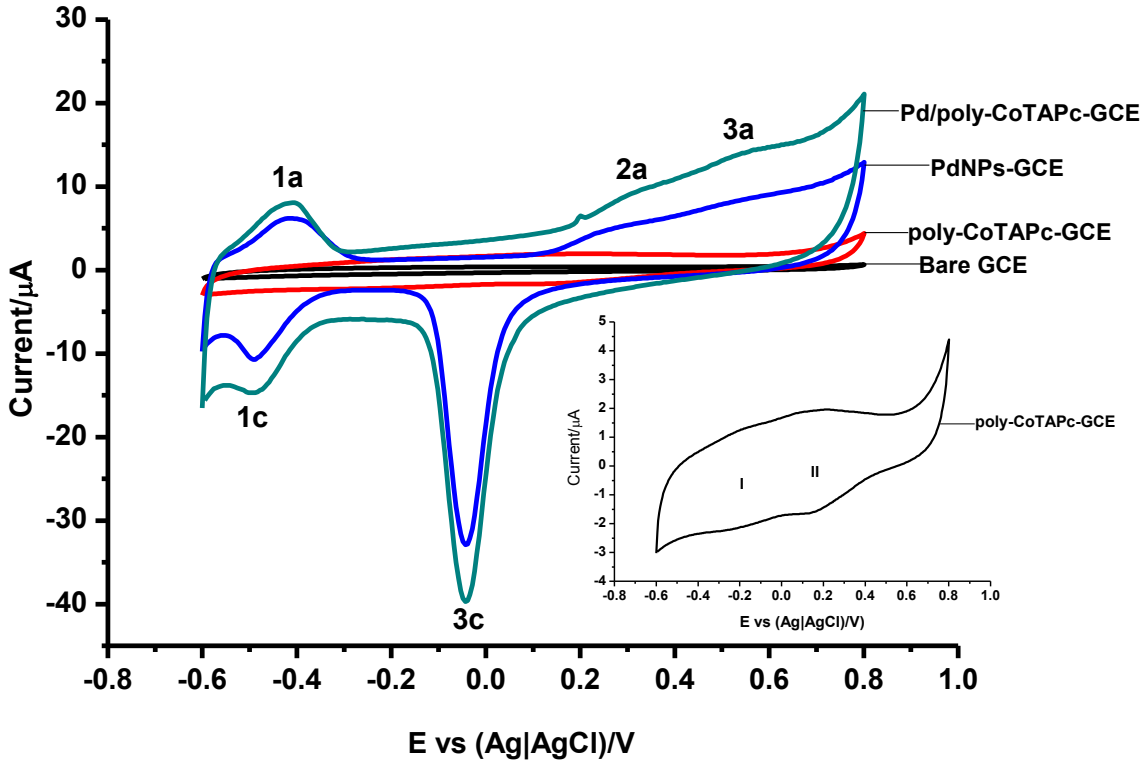

Fig. 4.16. Cyclic voltammograms of poly-CoTAPc-GCE, Pd-GCE and Pd/poly-CoTAPc-GCE in pH 8 buffer. Inset of the cyclic voltammograms of poly-CoTAPc-GCE in pH 8 buffer. Scan rate = 50 mV/s.

4.2.3.4. Electrochemical impedance spectroscopy (EIS)

The analysis was done as a representative of all electrodes. The bare and the modified electrodes were examined by electrochemical impedance spectroscopy (EIS) in 2 mM ferricyanide containing 0.1 M KCl and the results are shown in Fig. 4.17a and b. Fig. 4.17a shows the Nyquist plot for the various electrodes that were used in this section. The plots are composed of semi-circles and straight line portions, representing charge transfer (R_{ct}) and diffusion controlled processes, respectively. The Randles

equivalent circuit for this process is shown as an inset in Fig. 4.17a. The equivalent circuit is composed of R_s (the resistance of the electrolyte), in series connection with parallel elements of C_{dl} (double layer capacitance), R_{ct} (resistance to charge transfer) and Z_w (Warburg impedance). Such circuits have been observed in other studies [154]. The R_{ct} values as determined by the diameter of the semi-circle were found to be 202.4 Ω, 251.0 Ω, 9.6 Ω and 17.4 Ω, for bare GCE, Pd-GCE, poly-CoTAPc-GCE and Pd/poly-CoTAPc-GCE respectively, Table 4.3. The bare electrode and Pd-GCE have larger semi-circles than for the rest of the electrodes, showing that poly-CoTAPc-GCE and Pd/poly-CoTAPc-GCE have better conductivity. This has been observed before for carbon nanotubes/FePc composite electrode [155]. Also Pd/poly-CoTAPc-GCE offers limited resistance to charge transfer (compared to Pd-GCE) hence promoting very fast electron exchange rate.

The Bode plot (phase angle (θ) versus log frequency) for the various electrodes in this section is shown in Fig. 4.17b. On a Bode plot, the Warburg impedance exhibits a phase angle below 45^0. The Bode plots confirm the structural differences between the modified and the bare GCE. The slight changes in the phase angle and frequencies confirmed that oxidation processes were taking place at the modified surfaces rather than on the bare GCE.

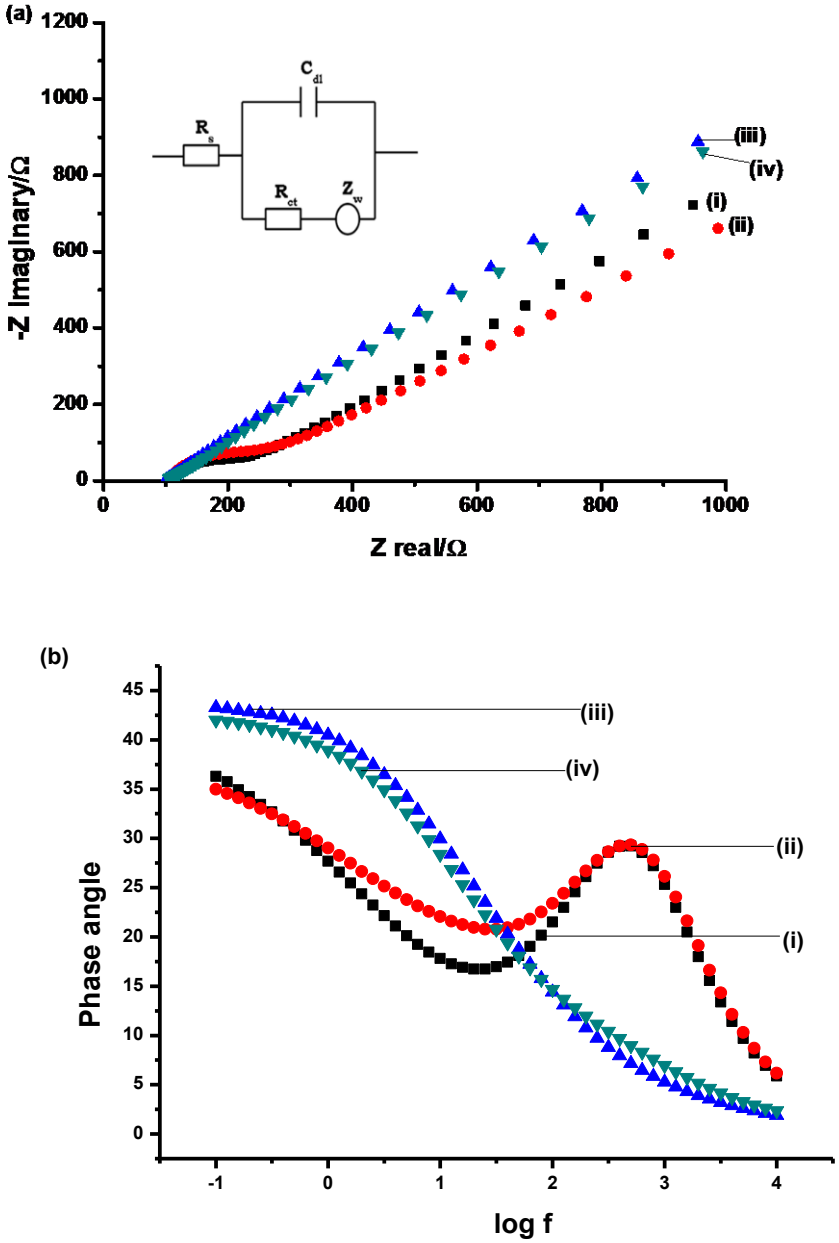

Fig. 4.17. (a) Nyquist and (b) Bode plots obtained for (i) Bare GCE, (ii) Pd-GCE, (iii) poly-CoTAPc-GCE, (iv) Pd/poly-CoTAPc-GCE in 2 mM ferricyanide containing 0.1 M KCl (electrolyte). Inset in (a) is the Randles equivalent circuit employed.

Table 4.3. Electrochemical parameters for the impedance data

Electrode	**R_{ct} /Ω**	**k_{app} /cm s^{-1}**
Bare GCE	202.4	9.26×10^{-6}
Pd-GCE	251.0	6.9×10^{-6}
poly-CoTAPc-GCE	9.6	1.5×10^{-4}
Pd/poly-CoTAPc-GCE	17.4	7.7×10^{-5}

4.3.3. CoTAPc and Bimetallic nanoparticles

4.3.3.1. Electrodeposition of NPs

Fig. 4.18A shows the electrodeposition of Au (Au-GCE), Pd followed by Au (Au/Pd-GCE), and Au-Pd co-deposited (Au-Pd (co-deposited)-GCE). Au-GCE has two peaks occurring at 1.04 V and 0.40 V corresponding to gold oxidation and gold reduction respectively, Fig. 4.18A. Similar peaks were obtained with Au/Pd-GCE. Au-Pd (co-deposited)-GCE has peaks at 0.94 V and 0.35 V, Fig. 4.18A. They correspond to the oxidation and reduction of gold, shifted to less positive values in the bimetallic nanoparticle. Thus the AuNPs dominate the CV when on top. At the end of the cathodic reaction, there is hydrogen evolution. The oxidation of the hydrogen on the bimetallic nanoparticles occurs at -0.26 V.

In the presence of poly-CoTAPc (for Au-poly-CoTAPc, Au-Pd (co-deposited)-poly-CoTAPc-GCE and Au/Pd-poly-CoTAPc), the gold peaks did not shift significantly, Fig. 4.18B, compared to electrodes in the absence of CoTAPc, Fig. 4.18A. Wang et al [83] observed Pd/Au NPs exhibits the same electrochemical behaviours as compared with PdNPs in region of hydrogen adsorption/desorption. Fig. 4.18C compares electrodeposition for Pd (Pd-GCE), Au followed by Pd (Pd/Au-GCE), and Au-Pd co-deposited (Au-Pd (co-deposited)-GCE). Pd-GCE shows the oxidation peaks at -0.25 V, -0.17 V and 0.46 V. They are attributed to oxidation of hydrogen on the surface of Pd, oxidation of absorbed hydrogen and oxidation of palladium respectively. Similar peaks are observed for Pd/Au-GCE though there is an additional oxidation peak at 0.58 V which may be attributed to gold oxidation. The peaks do not change significantly when poly-CoTAPc in underneath the NPs, Fig. 4.18D. These variations in the peaks obtained during electrodeposition will in turn affect the electrocatalytic activity of the electrocatalyst.

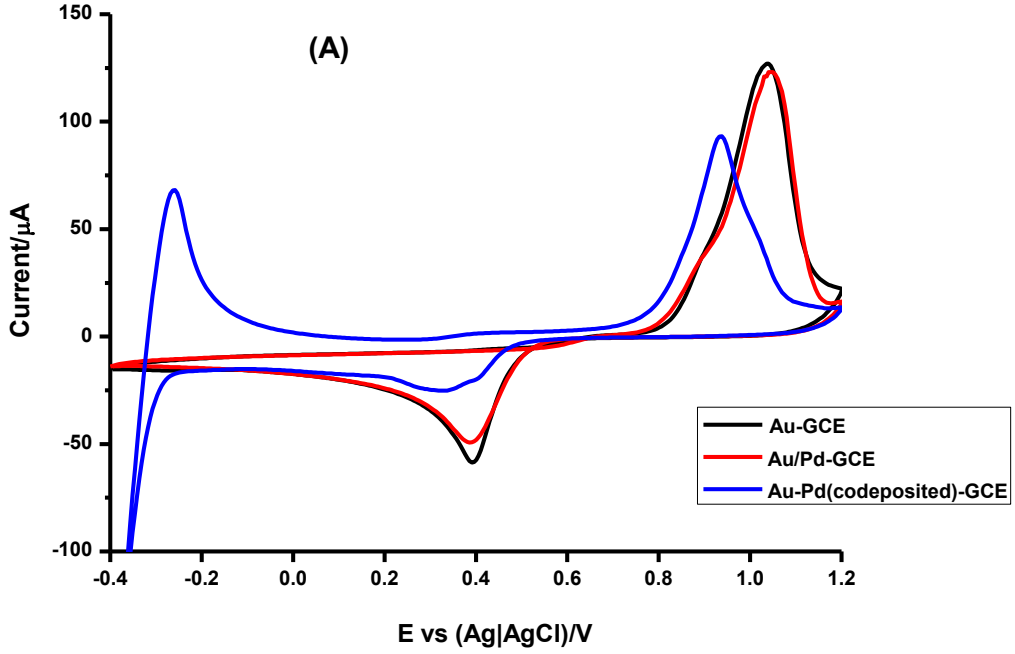
(A)
Current/μA
E vs (Ag|AgCl)/V
Au-GCE
Au/Pd-GCE
Au-Pd(codeposited)-GCE

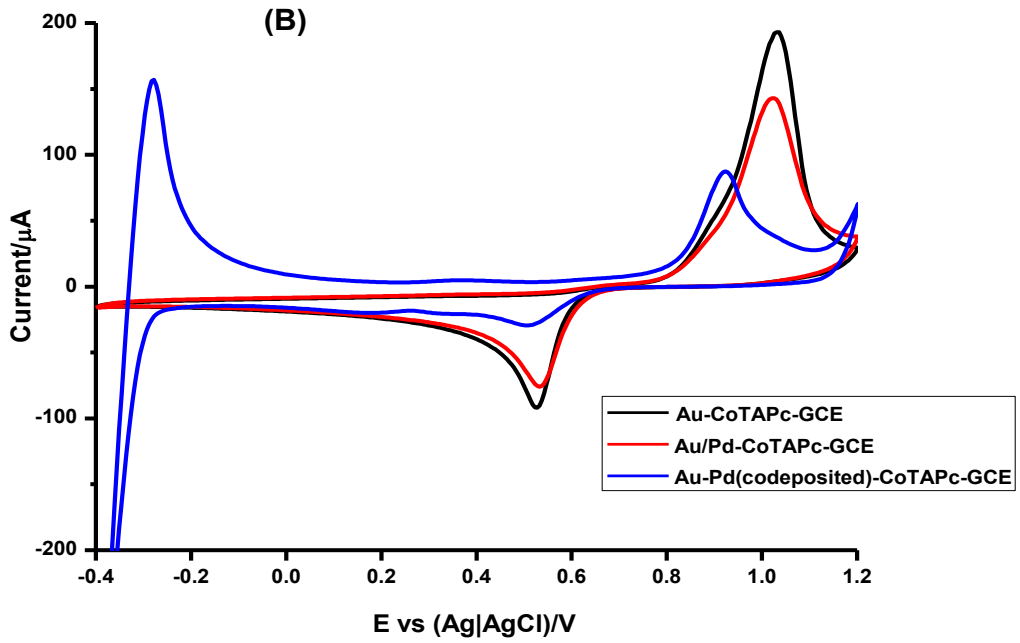
(B)
Current/μA
E vs (Ag|AgCl)/V
Au-CoTAPc-GCE
Au/Pd-CoTAPc-GCE
Au-Pd(codeposited)-CoTAPc-GCE

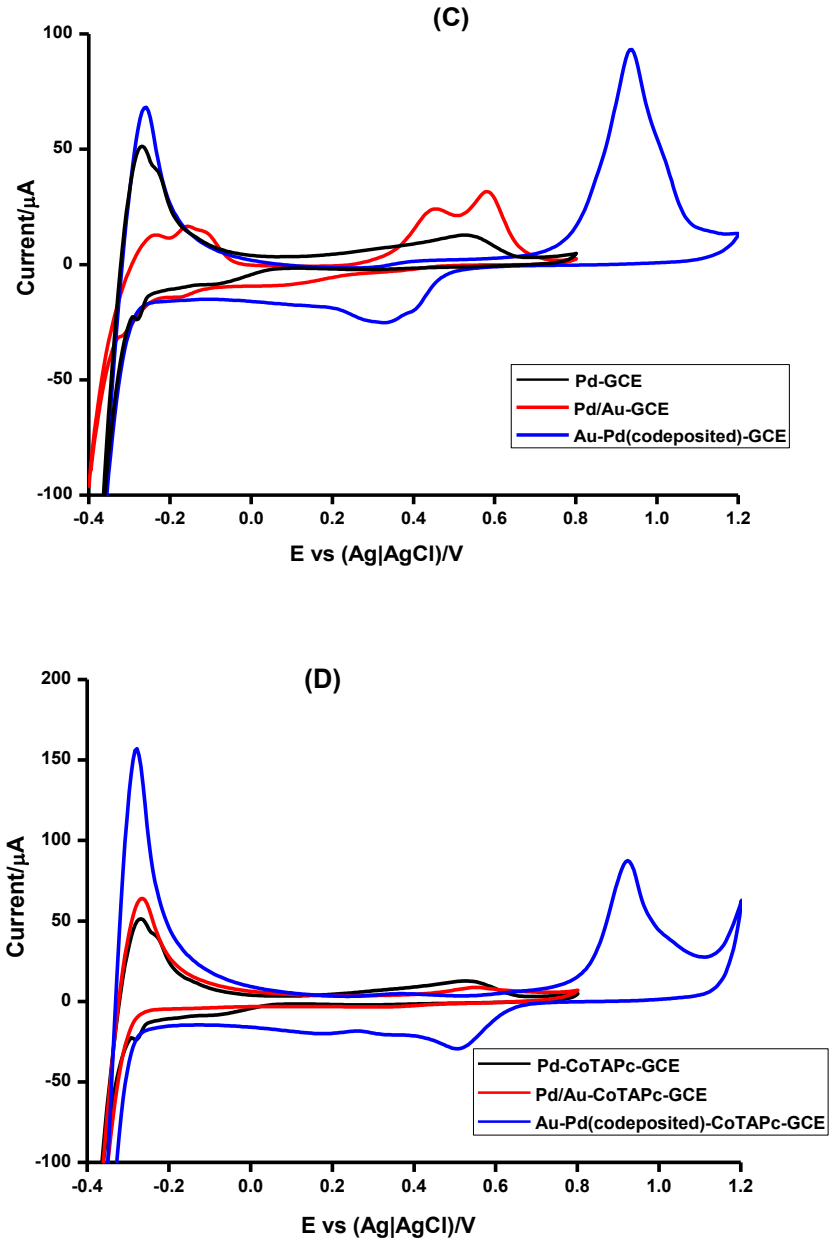

Fig. 4.18. Cyclic voltammetry for the deposition on GCE of (A) AuNPs to form Au-GCE, AuNPs on PdNPs to form Au/Pd-GCE) and co-deposition of AuNPs and PdNPs to form Au-Pd (co-deposited), (B) NPs from (A) electrodeposited on polymerized CoTAPc; (C) PdNPs to form Pd-GCE, PdNPs on AuNPs to form Pd/Au-GCE) and co-deposition of AuNPs and PdNPs to form Au-Pd (co-deposited) and (D), NPs from (C) electrodeposited on polymerized CoTAPc. Concentrations: 1 mM $PdCl_2$ or 1 mM $HAuCl_4$ dissolved in 0.1 M HCl. Scan rate 50 mV/s.

4.3.3.2. Microscopic and spectroscopic characterisation

Fig. 4.19 shows the SEM image of Au-Pd (co-deposited)/poly-CoTAPc that shows evenly distributed nanoparticles. Further characterization was carried out using the energy dispersion spectroscopy (EDS). Fig. 4.20 shows the EDS spectra of Au-Pd (co-deposited)/poly-CoTAPc. The EDS spectrum was taken by selecting a nanoparticle and then zooming on it. The spectrum shows the presence of both gold and palladium nanoparticles. This indicates that the electrodeposition of Au-Pd (co-deposited) nanoparticles formed an alloy onto the carbon plate. The spectra have carbon, as the glassy plates are made from carbon.

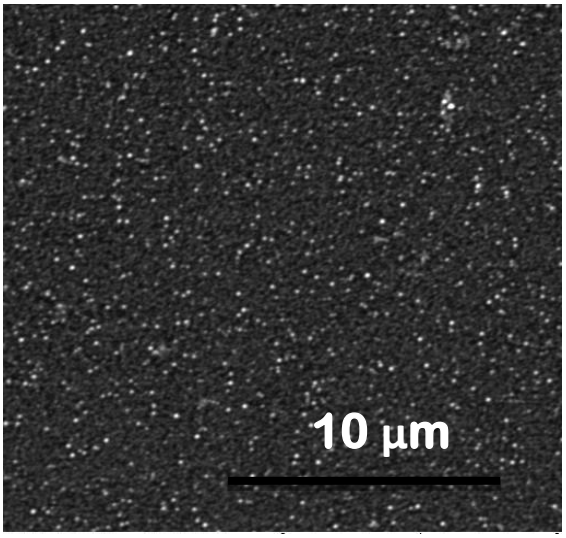

Fig. 4.19. SEM image of Au-Pd (co-deposited)/poly-CoTAPc on a glassy carbon plate.

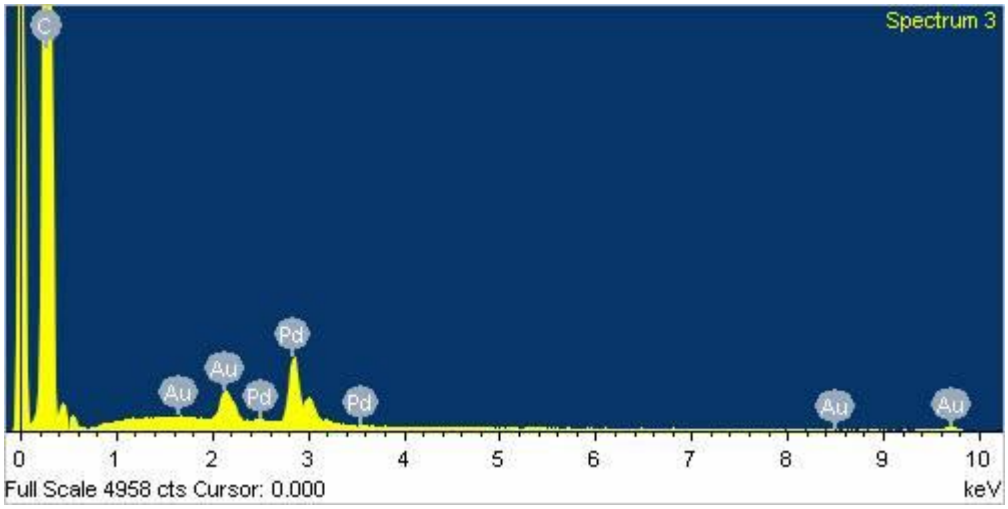

Fig. 4.20. EDS spectrum of Au-Pd (co-deposited)/poly-CoTAPc on a glassy carbon plate.

4.3.3.3. XPS

XPS was also used to confirm the existence of AuNPs, PdNPs and Au-Pd co-deposited on the glassy carbon plate. Fig. 4.21a shows the wide scan XPS spectra of AuNPs, PdNPs and Au-Pd co-deposited. All the spectra have C (1s) peak (283.4 eV) as it is obtained from the glassy carbon plates. Main peaks for XPS spectra for Pd in Au-Pd co-deposited are 1157.6 eV (Pd MNNa), 670.1 eV (Pd 3s), 560.4 eV (Pd 3p), 532.7 eV (Pd 3p) and 335.3 eV (Pd 3d) and for Au in Au-Pd co-deposited the XPS peaks are 763.2 eV (Au 4s), 642.4 eV (Au 4p), 547.6 eV (Au 4p), 354.1 eV (Au 4d) and 84.3 eV (Au 4f). AuNPs and PdNPs XPS peaks are all seen in Au-Pd co-deposited. This may suggest that the alloy has been formed during the co-electrodeposition from $HAuCl_4.3H_2O$ and $PdCl_2$ solution. Upon further analysis, the elemental composition (atomic percentage) was obtained to be (3:2/Pd:Au) which was

equivalent to 1:1 weight percent distribution. High resolution XPS spectra were carried to further confirm that an alloy has been formed.

Fig 4.21b shows high resolution spectra of Au 4f in AuNPs and Au-Pd co-deposited. Bond energies of 84.0 eV and 87.7 eV (AuNPs) correspond to pure Au^0 [156]. Any deviation from these bond energies imply that the gold nanoparticles are interacting with other elements. In this case with Au-Pd co-deposited 83.7 eV and 87.4 eV bond energies were obtained. This may suggest that the alloy have been formed with characteristic bond energy differing from the AuNPs alone. Similar observations were found in literature, that the presence of Pd causes such a shift in the bond energy of Au in the alloy (Au-Pd/SiO_2) [157, 158]. Fig 4.21c shows the high resolution of Pd 3d bond energies in PdNPs and Au-Pd co-deposited. Peaks at 335.4 eV and 340.6 eV corresponding to Pd $3d_{5/2}$ and Pd $3d_{3/2}$ for PdNPs. This indicates that most of the Pd ions have been reduced to Pd^0 as reported in literature [148]. Slight deviation is found on Au-Pd co-deposited with peaks at 335.0 eV and 340.3 eV. This shows that the alloy will have characteristics different from the individual nanoparticles. Other peaks were also observed at 335.8 eV and 341.2 eV which may correspond to the occurrence of the Pd^{2+} species [148]. This may be attributed to the presence $PdCl_2$ obtained from solution.

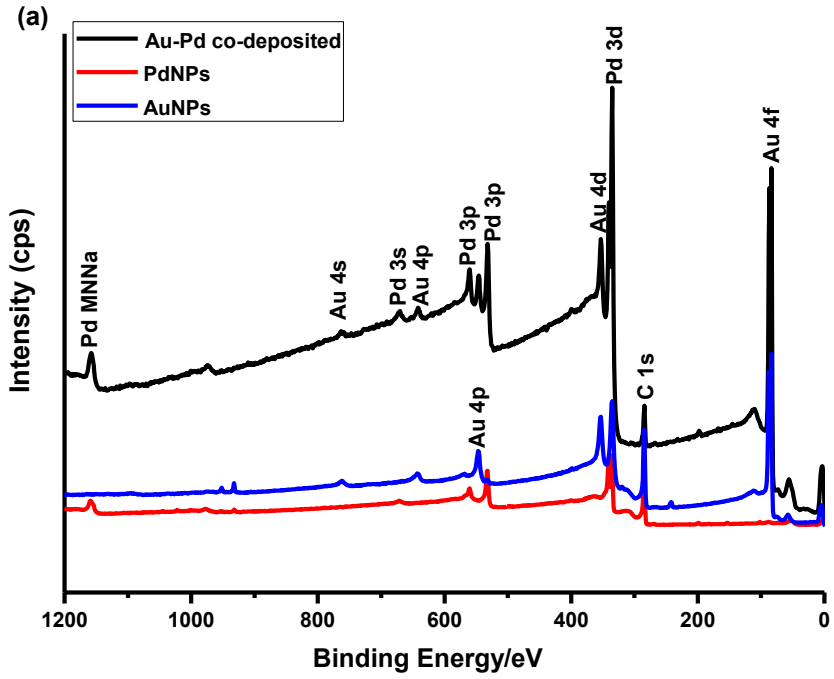
(a)
Au-Pd co-deposited
PdNPs
AuNPs
Intensity (cps)
Pd MNNa
Au 4s
Pd 3s
Au 4p
Pd 3p
Pd 3p
Au 4d
Pd 3d
Au 4f
C 1s
Au 4p
1200
1000
800
600
400
200
0
Binding Energy/eV

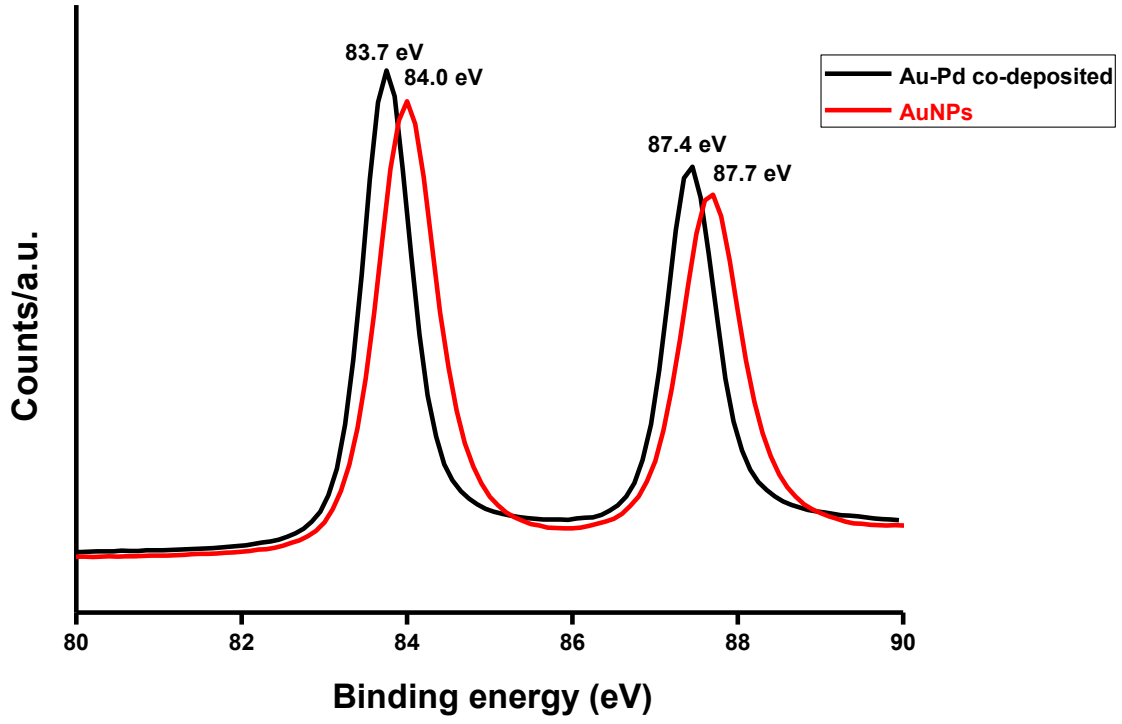
83.7 eV
84.0 eV
87.4 eV
87.7 eV
Au-Pd co-deposited
AuNPs
Counts/a.u.
80
82
84
86
88
90
Binding energy (eV)

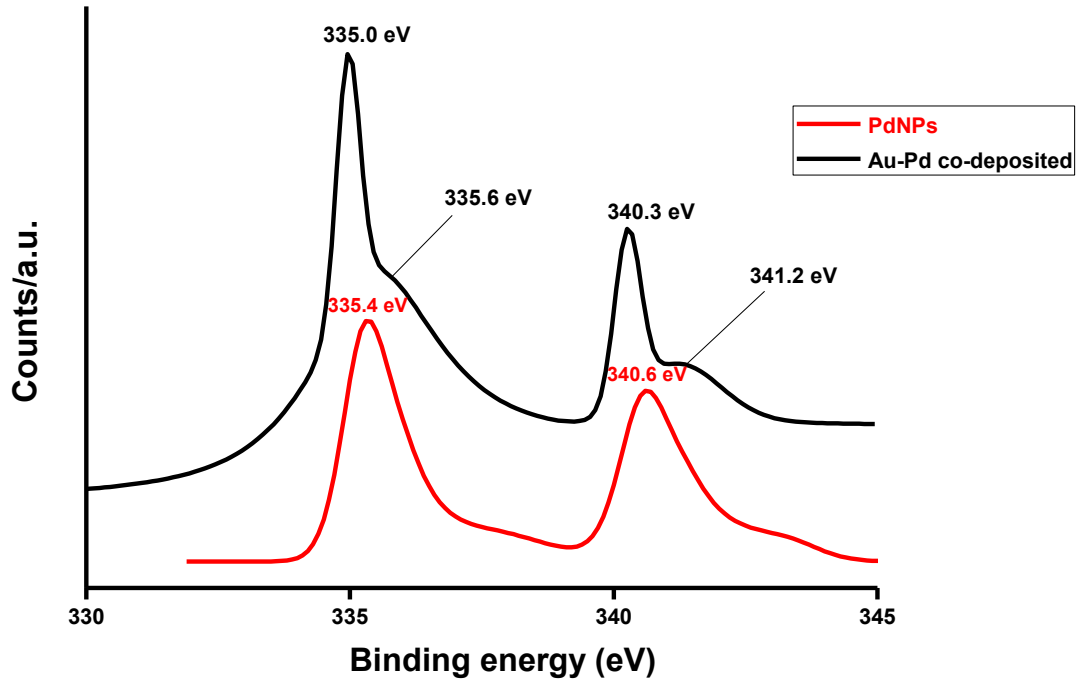

Fig. 4.21. (a) Wide scan XPS spectra of Au-Pd co-deposited, PdNPs and AuNPs. (b) High resolution Au 4f XPS spectra for Au-Pd co-deposited and AuNPs. (c) High resolution Pd 3d XPS spectra for Au-Pd co-deposited and PdNPs.

4.3.3.4. Electrochemical characterization

The anodic and cathodic peak separation (ΔE) values are shown in Table 4.2. Comparing the electrodes in the presence of CoTAPc, the lowest ΔE value of electrodes in ferricyanide is obtained for poly-CoTAPc-GCE (showing good electron transfer) and Au-Pd (co-deposited)/poly-CoTAPc-GCE the highest ΔE value, Table 4.2.

The surface roughness factor for the modified electrodes were determined using $[Fe(CN)_6]^{3-/4-}$ redox system and applying Randles–Sevcik Eq. 4.1 for

reversible systems. The surface roughness factors (ratio of I_{pa} experimental/I_{pa} theoretical) of the electrode were found to be 1.06, 1.02, 1.03, 1.06, 1.08, 1.05, 1.07, 1.05 and 1.07 for Au-GCE, Au/Pd-GCE, Pd/Au-GCE, Au-Pd (co-deposited)-GCE, poly-CoTAPc-GCE, Pd-poly-CoTAPc, Au-poly-CoTAPc, Au/Pd-poly-CoTAPc Pd/Au-poly-CoTAPc and Au-Pd (co-deposited)/poly-CoTAPc-GCE, respectively. Corresponding to a real electrode areas {(roughness factor × theoretical surface area (= 0.071 cm^2)} of 0.075, 0.068, 0.070, 0.075, 0.077, 0.075, 0.076, 0.075 and 0.076 cm^2 for Au-GCE, Au/Pd-GCE, Pd/Au-GCE, Au-Pd (co-deposited)-GCE, poly-CoTAPc-GCE, Au-poly-CoTAPc, Au/Pd-poly-CoTAPc-GCE Pd/Au-poly-CoTAPc-GCE and Au-Pd (co-deposited)/poly-CoTAPc-GCE, respectively.

Fig. 4.22 shows the cyclic voltammograms of bare and modified GCE recorded in pH 8 buffer at a scan rate of 50 mV/s. pH 8 buffer was used since hydrazine analysis will be carried out at this pH. Fig. 4.22a shows that the bare GCE had no peak and this was expected. Both Au-GCE and Au-poly-CoTAPc have a peak at 0.43 V which can be attributed to reduction of gold oxides. The Au-Poly-CoTAPc-GCE had an extra peak at -0.16 V. This may be attributed to the reduction of the central atom on the phthalocyanine, Co^{II} to Co^{I} (as shown above, Fig. 4.9 inset), suggesting that some CoTAPc is exposed and hence will be involved in catalysis. Fig. 4.22b shows that Au/Pd-GCE has a peak at 0.43 V which is attributed to reduction of gold oxide. Pd/Au-GCE shows the oxidation of palladium at 0.59 V and its reduction at -0.085 V, shifted compared to Fig. 4.18 due to differences in media. Au-Pd (co-deposited)-GCE has peaks at 0.42 V and

0.13 V corresponding to reduction of gold and palladium oxides respectively. Fig. 4.22c shows the Co^{II} to Co^{I} couple in poly-CoTAPc-GCE at ~ -0.2 V. Au/Pd-poly-CoTAPc-GCE has a gold reduction peak at 0.42 V. Pd/Au-poly-CoTAPc-GCE has a palladium reduction peak at -0.077 V. Au-Pd (co-deposited)-poly-CoTAPc-GCE has peaks at 0.39 V and 0.11 V corresponding to reduction of gold and palladium oxides respectively. Similar voltammograms were observed by Chen et al, though the peak position differs since the medium used were different [36]. The CVs show the presence of both Pd and Au in the presence of CoTAPc, Fig. 4.22c.

Using the effective area of the electrode determined above, the surface coverage was calculated using Eq. 4.5, for CV of modified electrodes in pH 8 buffer, Fig. 4.22. Modified GCE with palladium as the outer layer have the highest surface coverage, Table 4.2. Pd/Au-poly-CoTAPc-GCE has the least surface coverage among the electrodes with palladium as the outer layer. The electrodes modified GCE with gold as the outer layer has the lowest surface coverage. Even though for Au-Pd (co-deposited)-GCE, the Pd:Au ratio is 3:2, the electrode shows a surface coverage that is in the range for when Au is on top, suggesting that Au dominates in terms of its position. Au/Pd-poly-CoTAPc-GCE has the highest Γ value among those with gold as the outer layer. This may suggest that the order of depositing the nanoparticles is very important at it can influence some electrochemical properties. Au-Pd (co-deposited)/poly-CoTAPc-GCE shows a surface coverage in the range of Au on top, showing that AuNPs dominate.

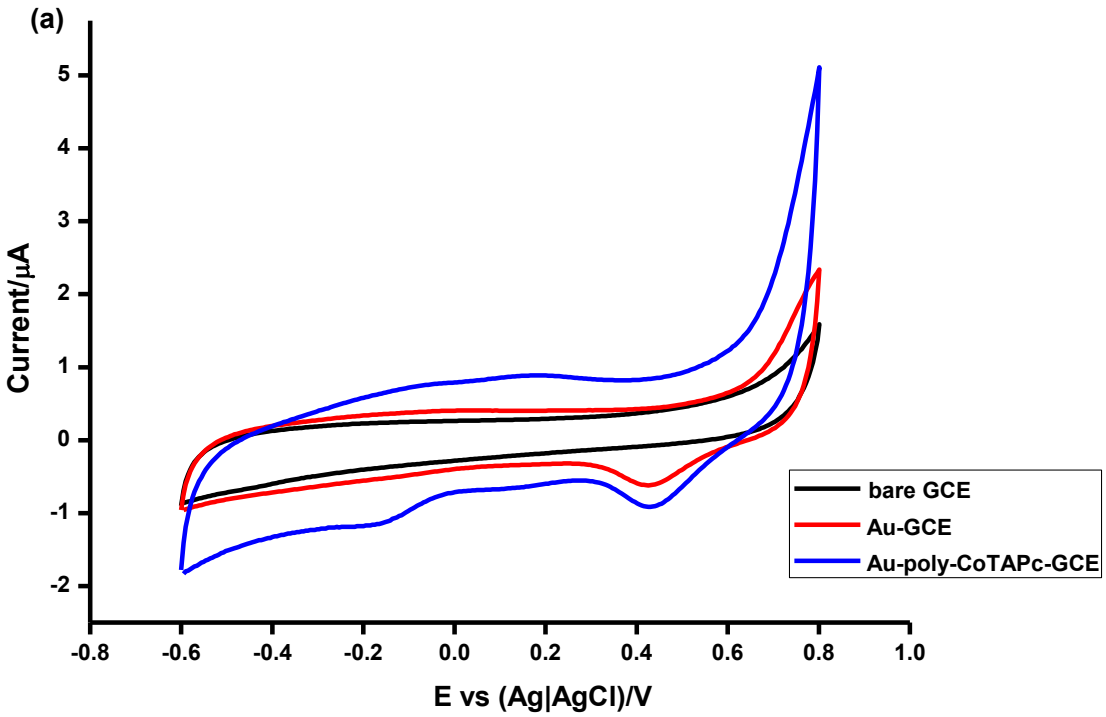
(a)
Current/μA
E vs (Ag|AgCl)/V
bare GCE
Au-GCE
Au-poly-CoTAPc-GCE

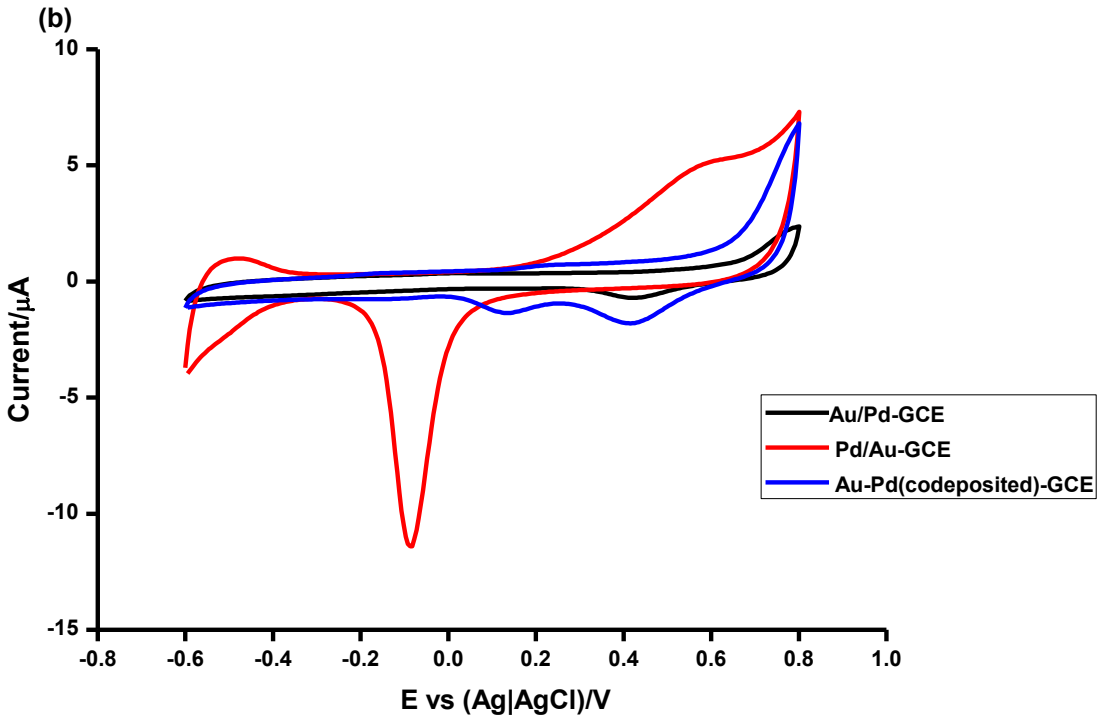
(b)
Current/μA
E vs (Ag|AgCl)/V
Au/Pd-GCE
Pd/Au-GCE
Au-Pd(codeposited)-GCE

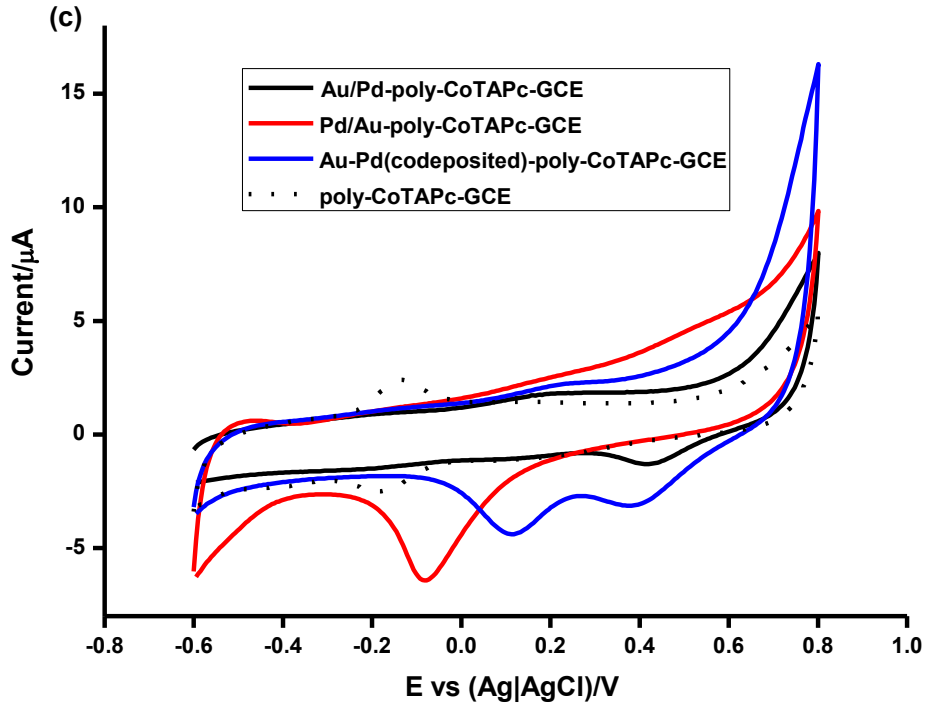

Fig. 4.22. Cyclic voltammograms of (a) bare GCE, Au-GCE and Au-poly-CoTAPc, (b) Au/Pd-GCE, Pd/Au-GCE and Au-Pd (co-deposited) and (c) Au/Pd-poly-CoTAPc-GCE, Pd/Au-polyCoTAPc-GCE, Au-Pd (co-deposited)/poly-CoTAPc-GCE and poly-CoTAPc in pH 8 buffer. Scan rate = 50 mV/s.

4.3.3.5. SECM

Fig. 4.23 shows the 3 D images of unmodified and modified glassy carbon plate (GCP) surfaces. The plates were immersed in an aqueous solution of 2 mM ferricyanide and 0.1 M KCl. When GCP was modified (Fig. 4.23a, 4.23b) compared to bare GCP, Fig. 4.13a, the surface becomes rougher and results in increase in current range of 8 nA to 12 nA and 9.5 nA to 13.5 nA for Au-Pd (co-deposited)-GCP and Au-Pd (co-deposited)/poly-CoTAPc-GCP,

respectively, compared to 2-3 nA for the bare (Fig. 4.13a). Thus the combination of poly-CoTAPc and Au-Pd (co-deposited) nanoparticles resulted in higher currents in SECM images than Au-Pd (co-deposited) nanoparticles alone.

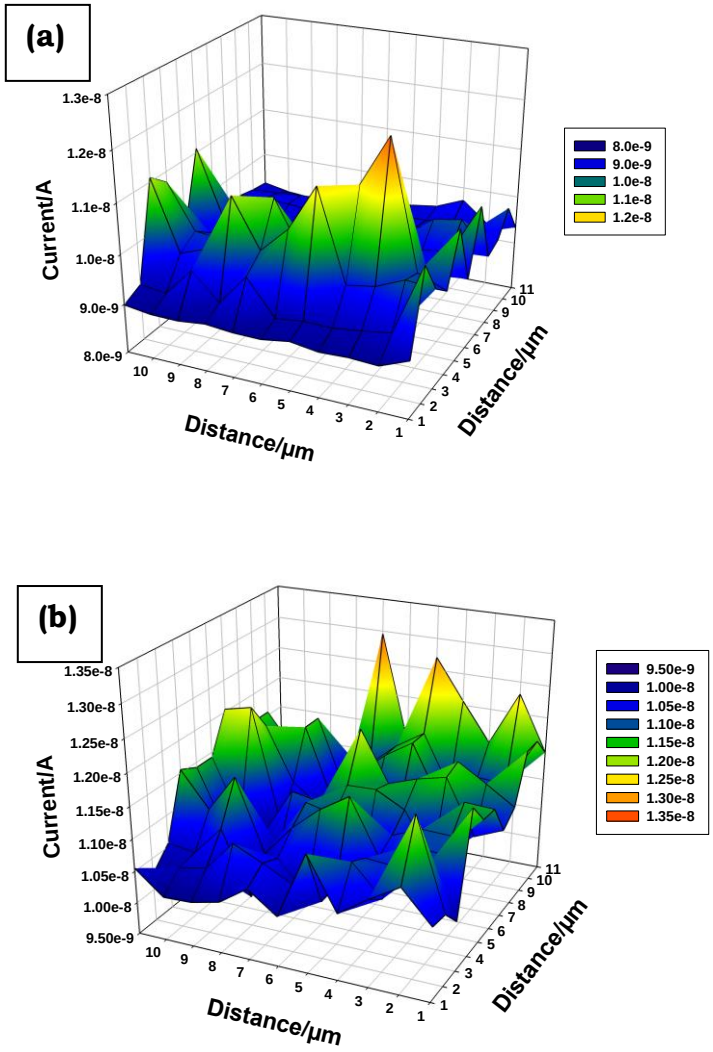

Fig. 4.23. SECM image of Au-Pd (co-deposited)-GCP (a) and Au-Pd (co-deposited)/poly-CoTAPc-GCE (b) in 0.1 M KCl containing 2 mM ferricyanide solution. Imaging conditions: Pt UME (25 µm diameter) placed 10 µm above the substrate, poised at a potential of − 0.1 V vs Ag/AgCl.

4.4. Electrografting and click chemistry

The GCE was modified by electrografting of 4-azidobenzenediazonium tetrafluoroborate followed by click chemistry with ethynylferrocene. The modified electrodes were characterized in ferricyanide solution. When the click chemistry reaction was achieved by applying a potential at the tip of the SECM, the process is called micropatterning.

4.4.1. Electrografting of 4-azidobenzenediazonium salt

Scheme 4.3 shows the grafting of the 4-azidobenzenediazonium tetrafluoroborate onto the electrode. The cyclic voltammograms (Fig. 4.24) recorded at a GC electrode in aqueous solution containing 1 mM 4-azidobenzenediazonium tetrafluoroborate 0.1 M sulphuric acid, exhibits broad irreversible cathodic peak at approximately -0.75 V. During the second scan, the peak disappeared. This behaviour is consistent with the formation of a grafted layer on the electrode surface.

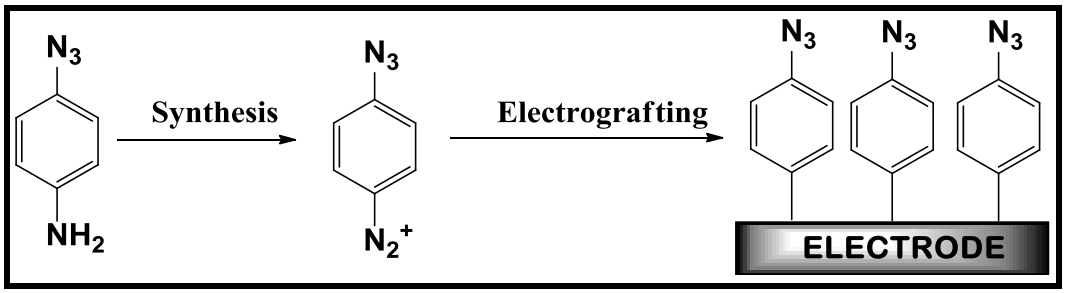

Scheme 4.3. Proposed electrografting of the 4-azidobenzenediazonium tetrafluoroborate onto the electrode.

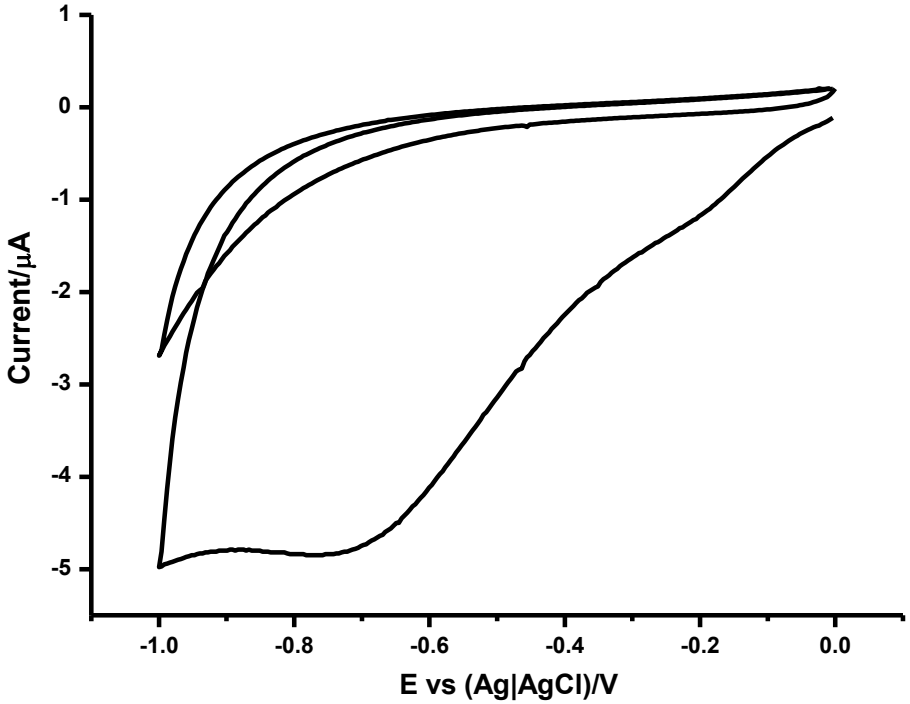

Fig. 4.24. Cyclic voltammograms of 5 mM 4-azidobenzenediazonium salt in 0.1 M H_2SO_4 at a GC electrode. 2 cycles were at 50 mV/s.

4.4.2. Global click chemistry with ethynylferrocene

The global click chemistry was done as a proof of concept. The azide grafted GC electrode was placed in a click solution (1 mM $CuSO_4$, 5 mM Na ascorbate and 10 μM ethynylferrocene in ethanol) for 30 minutes. This was done to couple the azide and ethynylferrocene. Fig. 4.25 shows behavior of the bare GC, grafted GC and clicked GC in 2 mM ferricyanide. The bare GC shows the characteristic Fe^{3+} and Fe^{2+} couple and the grafted showed no peak. The clicked GC shows that ferrocene is facilitating the reduction of Fe^{3+} to Fe^{2+} but the reduction peak has decreased.

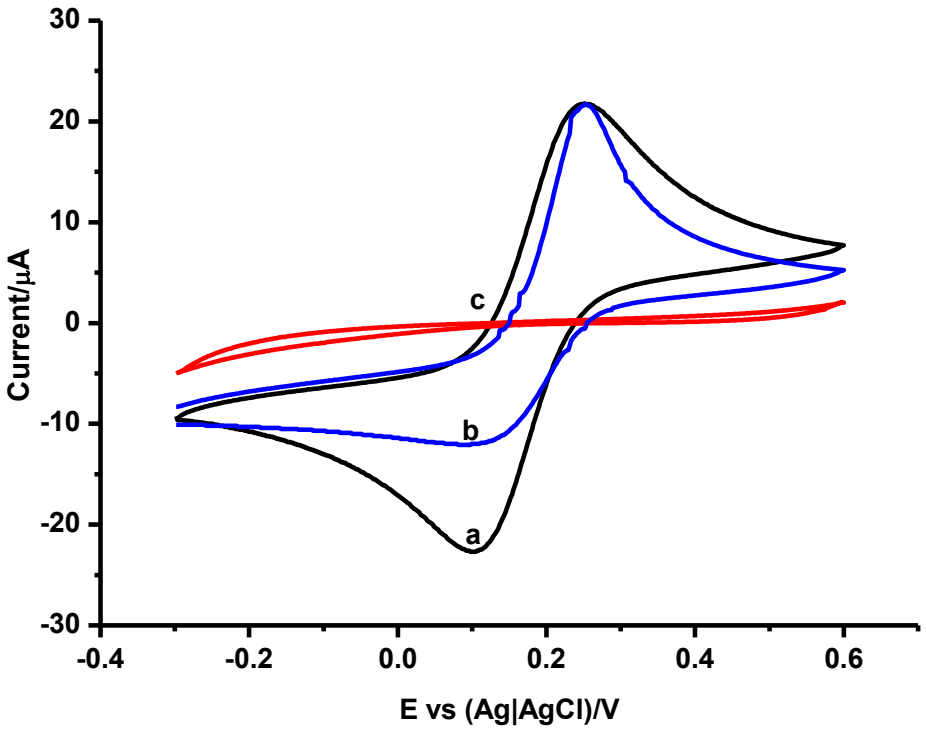

Fig. 4.25. Cyclic voltammetry of bare GCE (a), GCE after grafting plus click chemistry (b) and grafted GCE (c) in 2 mM ferricyanide solution in 0.1 M KCl. Scan rate 100 mV/s.

4.4.3. Local click chemistry with ethynylferrocene using SECM (micropatterning)

The SECM tip was positioned ≈10 μm above the surface of the azido-modified substrate, and Cu^{+} ions were produced at the tip. This is aimed at locally triggering the CuAAC reaction between azido moieties on the surface and ethynylferrocene in solution. A potential of −0.3 V was applied on the tip for the local click procedure. Although this process probably corresponds to the reduction of Cu^{2+} to Cu^{0}, a small amount of Cu^{+} is also present and this

small amount can be enough to catalyze the click chemistry reaction [159]. Scheme 4.4 shows the locally electroassisted click reaction of azide and ethynylferrocene.

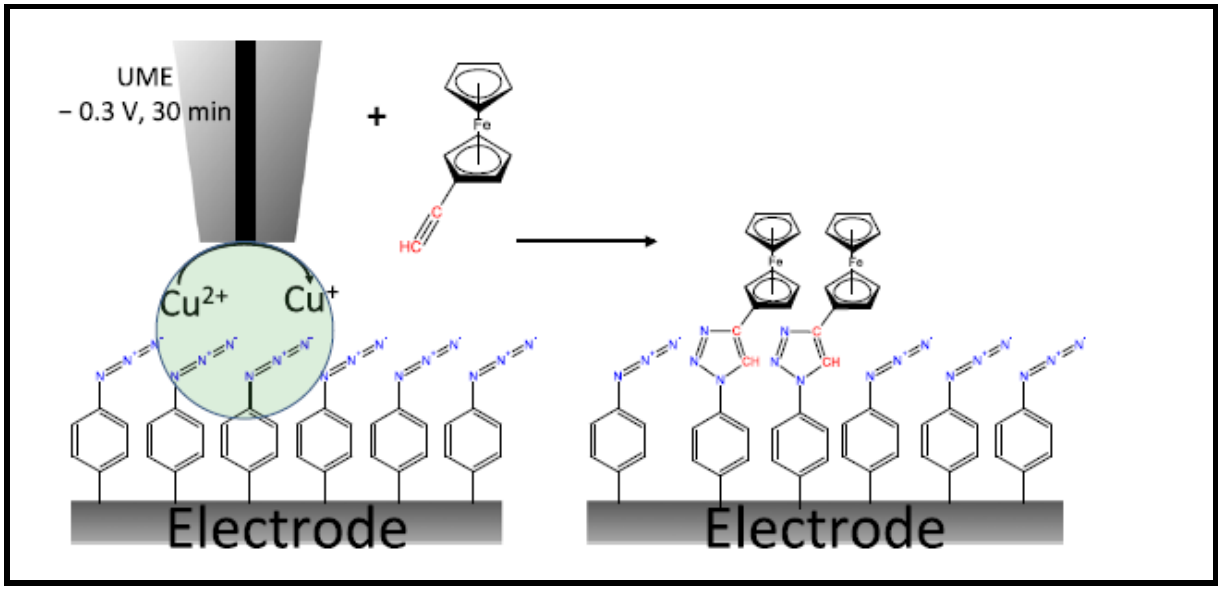

Scheme 4.4. Locally electroassisted click reaction of azide and ethynylferrocene

4.4.4. SECM

In order to show the successful patterning of the glassy carbon substrate, SECM was performed. Fig. 4.26 shows (a) SECM approach curves at the spot and -250 µm in x direction from the spot using 2 mM $K_3Fe^{III}(CN)_6$ solution in 0.1 M KCl, (b and c) SECM images (contour and 3 D plots) of an azido-modified glassy carbon electrode locally "clicked" by applying a potential of −0.3 V vs Ag/AgCl wire for 30 min to a Pt UME (12.5 µm diameter). An example of negative feedback is at -250 µm in x direction from the spot where current is decreasing, indicating that $[Fe^{III}(CN)_6]^{3-}$ redox

probe is not regenerated by the grafted substrate after its reduction at the tip. At the clicked spot, the current increases meaning that $[Fe^{II}(CN)_6]^{4-}$ is reoxidized by the substrate. This tends to indicate that the clicked ferrocene moieties act as a redox catalyst to assist the oxidation of $Fe^{II}(CN)_6^{4-}$. The images, Fig 4.26 b and c clearly show that the position where the localized click reaction occurred had high currents as ferrocene moieties have good redox properties, thus supporting the information from the SECM approach curves.

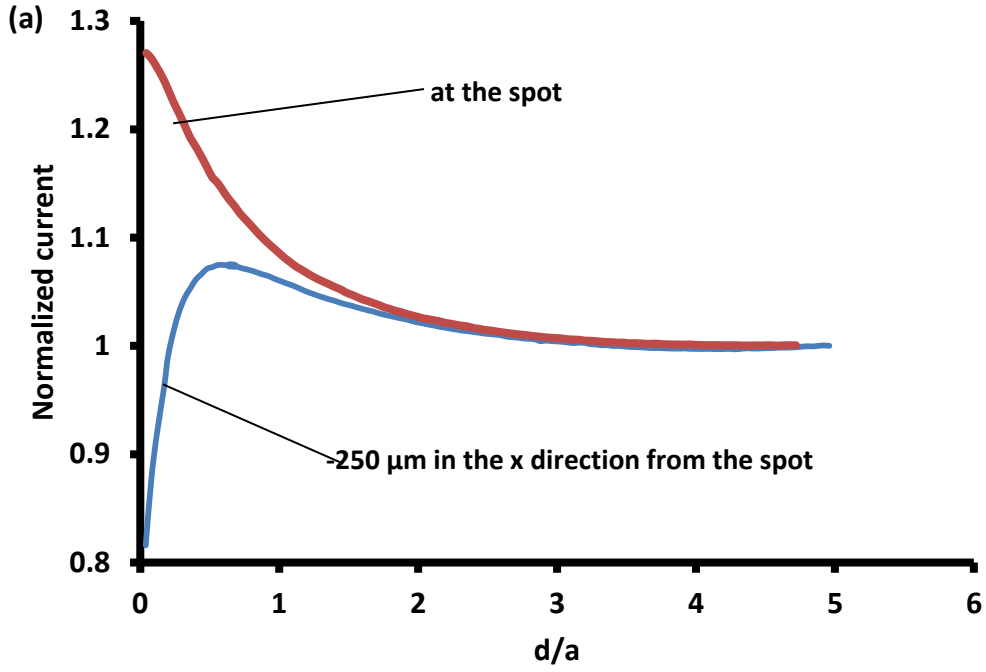
(a)
1.3
1.2
1.1
1
0.9
0.8
Normalized current
at the spot
250 µm in the x direction from the spot
0
1
2
3
4
5
6
d/a

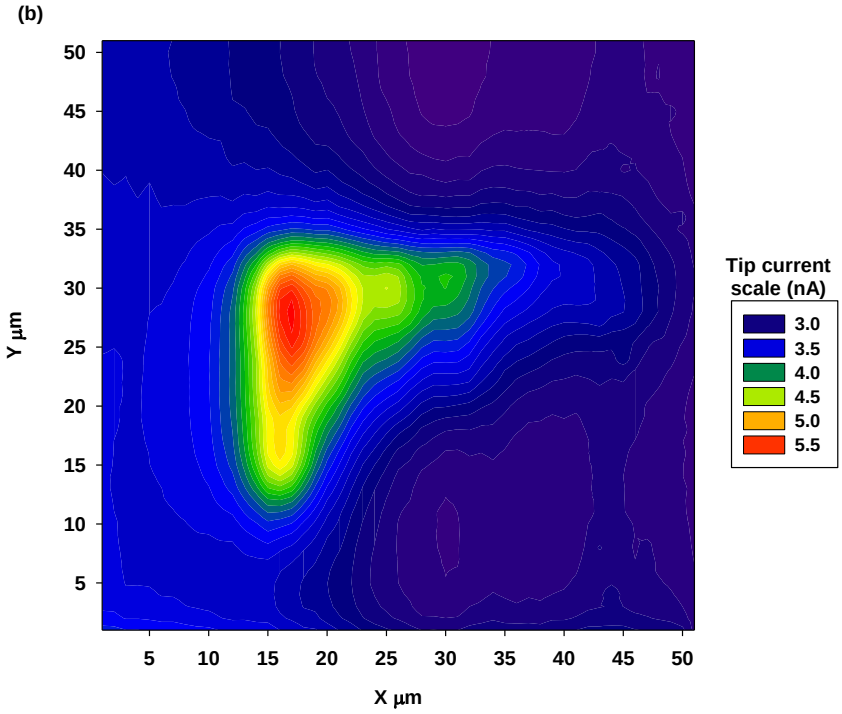
(b)
50
45
40
35
30
25
20
15
10
5
Y µm
5
10
15
20
25
30
35
40
45
50
X µm
Tip current scale (nA)
3.0
3.5
4.0
4.5
5.0
5.5

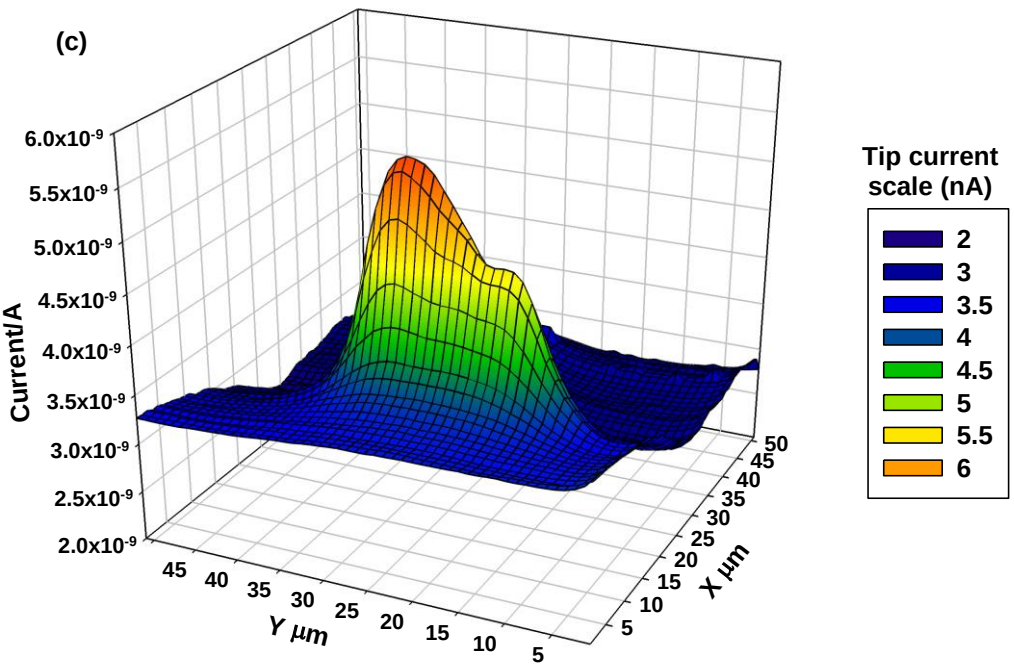

Fig. 4.26. SECM approach curves at the spot and -250 µm in x direction from the spot using 2 mM $K_3Fe^{III}(CN)_6$ solution in 0.1 M KCl (a), SECM images contour (b) and 3 D (c) plots) of an azido-modified glassy carbon electrode locally "clicked" by applying a potential of −0.3 V vs Ag/AgCl wire for 30 min to a Pt UME (12.5 µm diameter).

4.4.5. Attachment of Pc following click chemistry

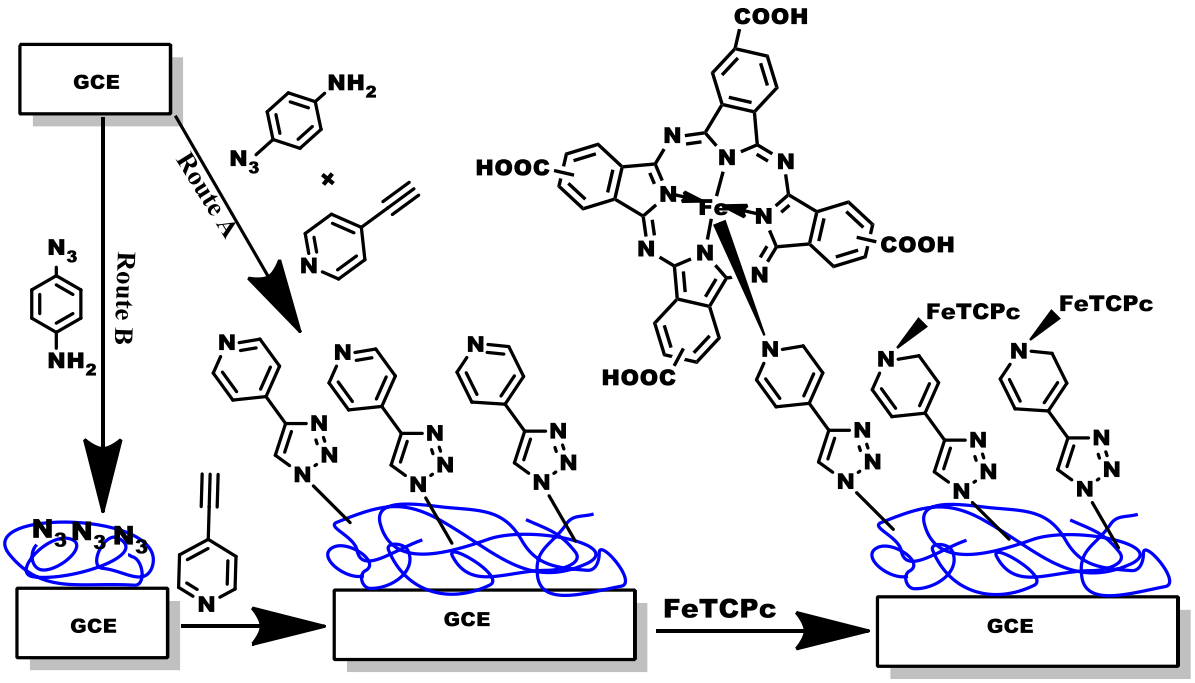

Scheme 4.5. Modification of the glassy carbon electrode (GCE) by simultaneous electropolymerization and electo-click (SEEC) reaction (Route A) or step by step (Route B).

Scheme 4.5 shows the summary of how the electrodes were modified. Route A involves simultaneous electropolymerization and electo-click (SEEC) reaction followed by axial ligation with FeTCPc. Route B involve electropolymerization (step 1), electro-click (step 2) and axial ligation with FeTCPc.

4.4.5.1. Microscopic characterization

Fig. 4.27 shows the SEM images of the film formed after SEEC. The image shows that the polymer has been deposited on the glassy carbon plate. From

literature, mostly polyaniline have been electropolymerized onto the electrode and the SEM image is very comparable with those obtained with polymers of azidoaniline [160, 161]. Rydzek et al obtained similar images of polymers for electropolymerization of azidoaniline and ethynylferrocene in the presence of copper catalyst [126]. When the film obtained during SEEC was immersed in a solution of DMF containing FeTCPc, there was no change in the morphology of the film. This may be due to the fact that the FeTCPc would be too small to be seen on the SEM.

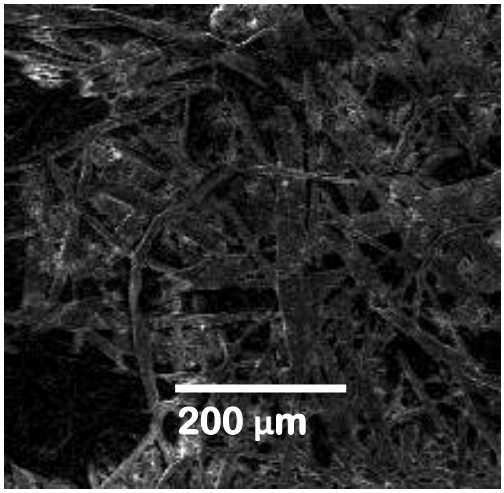

Fig. 4.27. SEM image after simultaneous electropolymerization and electro-click (SEEC) reaction.

4.4.5.2. XPS

Fig. 4.28 shows XPS spectra of the film formed by SEEC and after immersion in a solution of DMF containing FeTCPc. The wide XPS spectra show all the elements present on the film surfaces, Fig 4.28a. The elements present are C 1s (284 eV), N 1s (399 eV), O 1s (531 eV) and C (KLL, 977 eV

and 998 eV) [79] for both the films, with higher intensity peaks being observed for the film which has FeTCPc. Oxygen is obtained from the adsorbed oxygen from the atmosphere. For the film containing FeTCPc, the oxygen is also from the carboxylic groups on the FeTCPc. The spectrum with FeTCPc has iron peaks (711 eV and 725 eV). Fig 4.28b shows the high resolution XPS spectra for C 1s of the film formed after SEEC. The C1s spectrum has four peaks 284.2 eV, 285.3 eV, 286.5 eV and 288.5 eV. The first peak is attributed to C-H aromatic, second peak correspond to C-C and C=C, the third peak is attributed to carbon bonded to nitrogen in the triazole ring, C-N and C=N and the fourth peak may be ascribed to $C=N^+$ in the triazole structure [162-164]. Fig 4.28c shows the C 1s spectrum for SEEC followed by immersion in DMF containing FeTCPc. The C 1s spectrum gives three peaks with binding energies of 284.3 eV, 285.4 eV and 288.2 eV. The peak with binding energy around 286 eV (due to C-N and C=N) has disappeared. This may be ascribed to the strain on the C-N and C=N bonds forming more $C=N^+$. This suggestion is supported by the fact that the intensity of the peak at 288 eV increased for the film with FeTCPc. Fig 4.28d shows the high resolution XPS spectra for N 1s of the film for SEEC. The peaks at binding energies of 399.2 eV, 400.5 eV and 402.0 eV were obtained. The first peak corresponds to C-N and unprotonated N atoms (=N- structure) in the triazole ring, the second peak is attributed to the pyridinic nitrogen as well as the triazole ring [29], the third peak at higher binding energy is attributed to the positively charged N in the triazole ring. The presence of =N- confirms the success of the click reaction. Fig 4.28e shows the N 1s spectrum for SEEC followed by immersion in DMF containing

FeTCPc. When the FeTCPc was added, the binding energies shifted to 398.5 eV, 399. 8 eV and 401.5 eV. The first shows the presence of the pyrrole and aza-nitrogen groups of the FeTCPc ring [29], the second peak correspond to C-N and unprotonated N atoms (=N- structure) in the triazole ring, and third peak is attributed to the positively charged N in the triazole [162-164]. It is important to note that both Fig 4.28d and 4.28e did not show N 1s at the binding energy of 404 eV. This means that all the azide groups from azidoaniline were converted to the triazole. Fig 4.28f shows the high resolution XPS spectrum of Fe 2p. The prominent binding energy are 711 eV and 725 eV corresponding to Fe $2p_{3/2}$ and Fe $2p_{1/2}$ respectively [162-164]. The result shows that axial ligation of FeTCPc was a success.

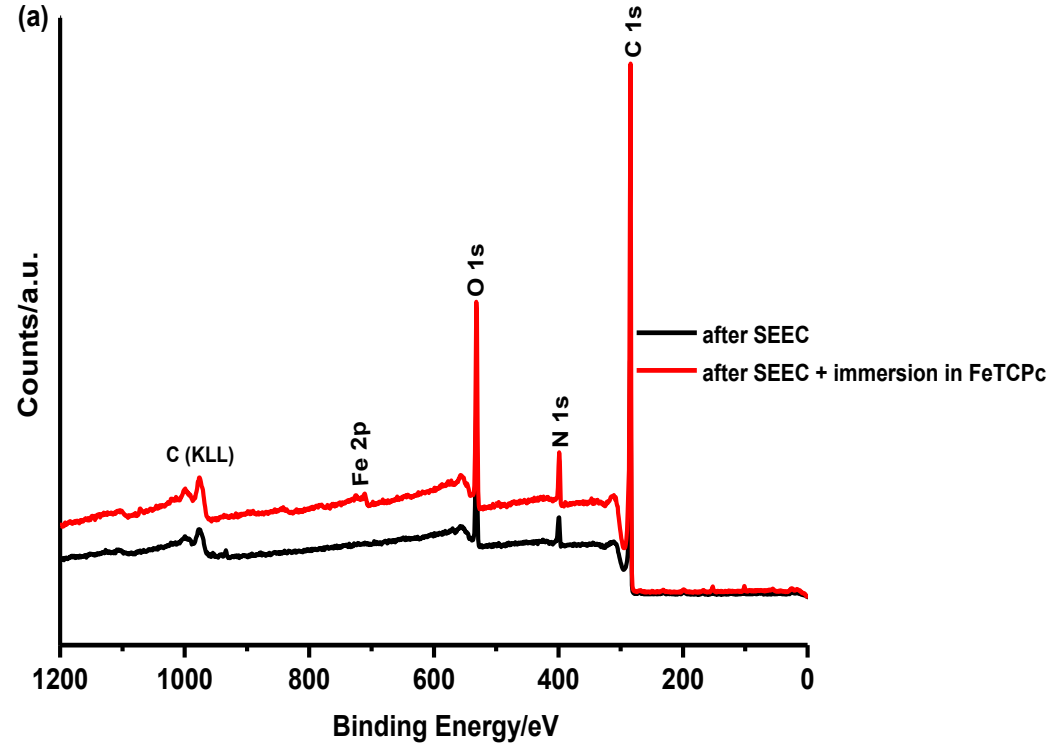
(a)
Counts/a.u.
C 1s
O 1s
N 1s
Fe 2p
C (KLL)
after SEEC
after SEEC + immersion in FeTCPc
1200
1000
800
600
400
200
0
Binding Energy/eV

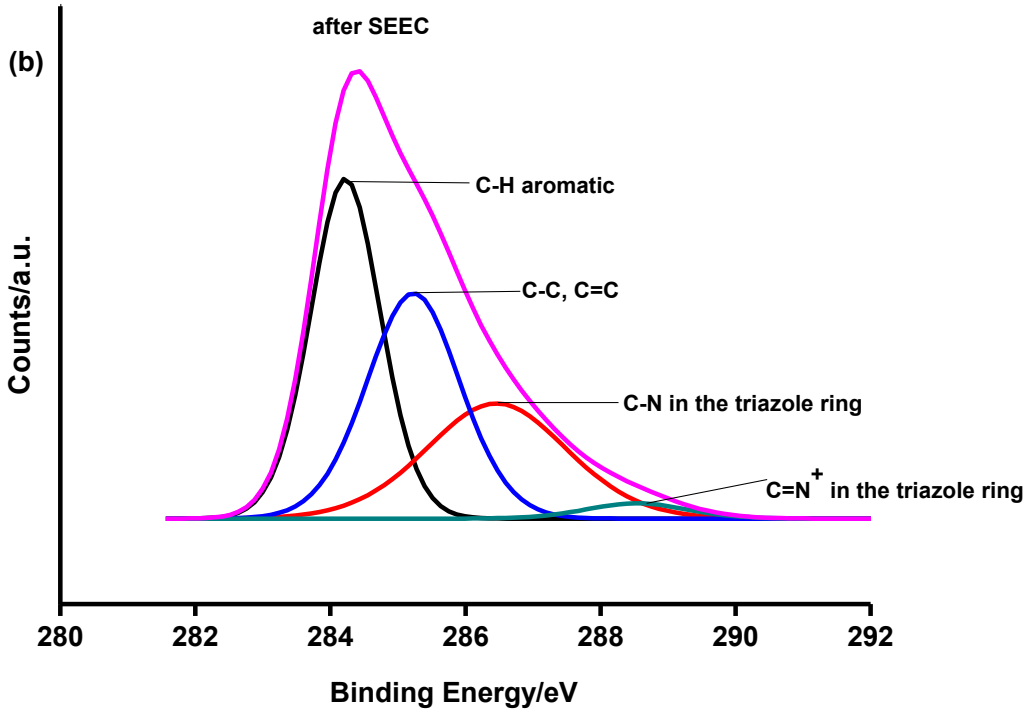
(b)
after SEEC
Counts/a.u.
C-H aromatic
C-C, C=C
C-N in the triazole ring
C=N+ in the triazole ring
280
282
284
286
288
290
292
Binding Energy/eV

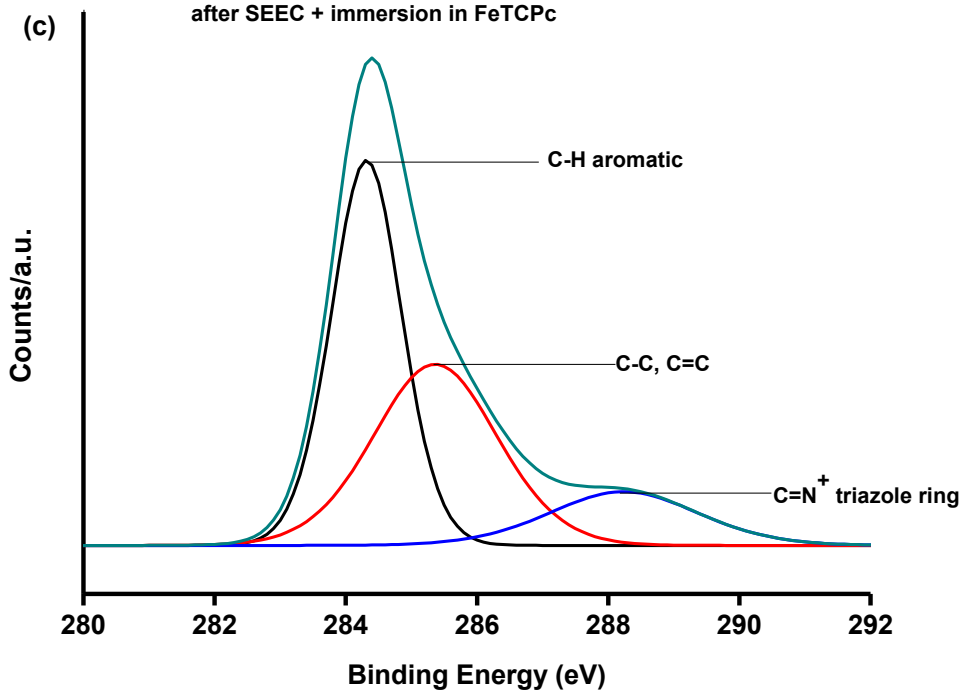
(c)
after SEEC + immersion in FeTCPc
C-H aromatic
C-C, C=C
C=N+ triazole ring
Counts/a.u.
280
282
284
286
288
290
292
Binding Energy (eV)

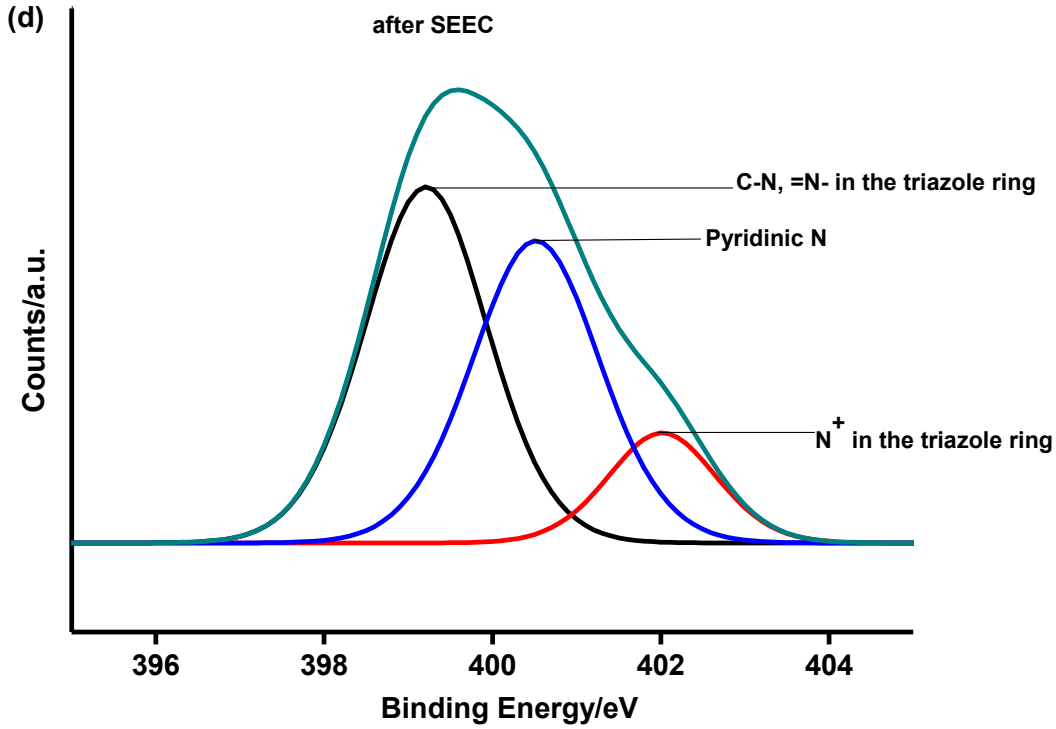
(d)
after SEEC
C-N, =N- in the triazole ring
Pyridinic N
N+ in the triazole ring
Counts/a.u.
396
398
400
402
404
Binding Energy/eV

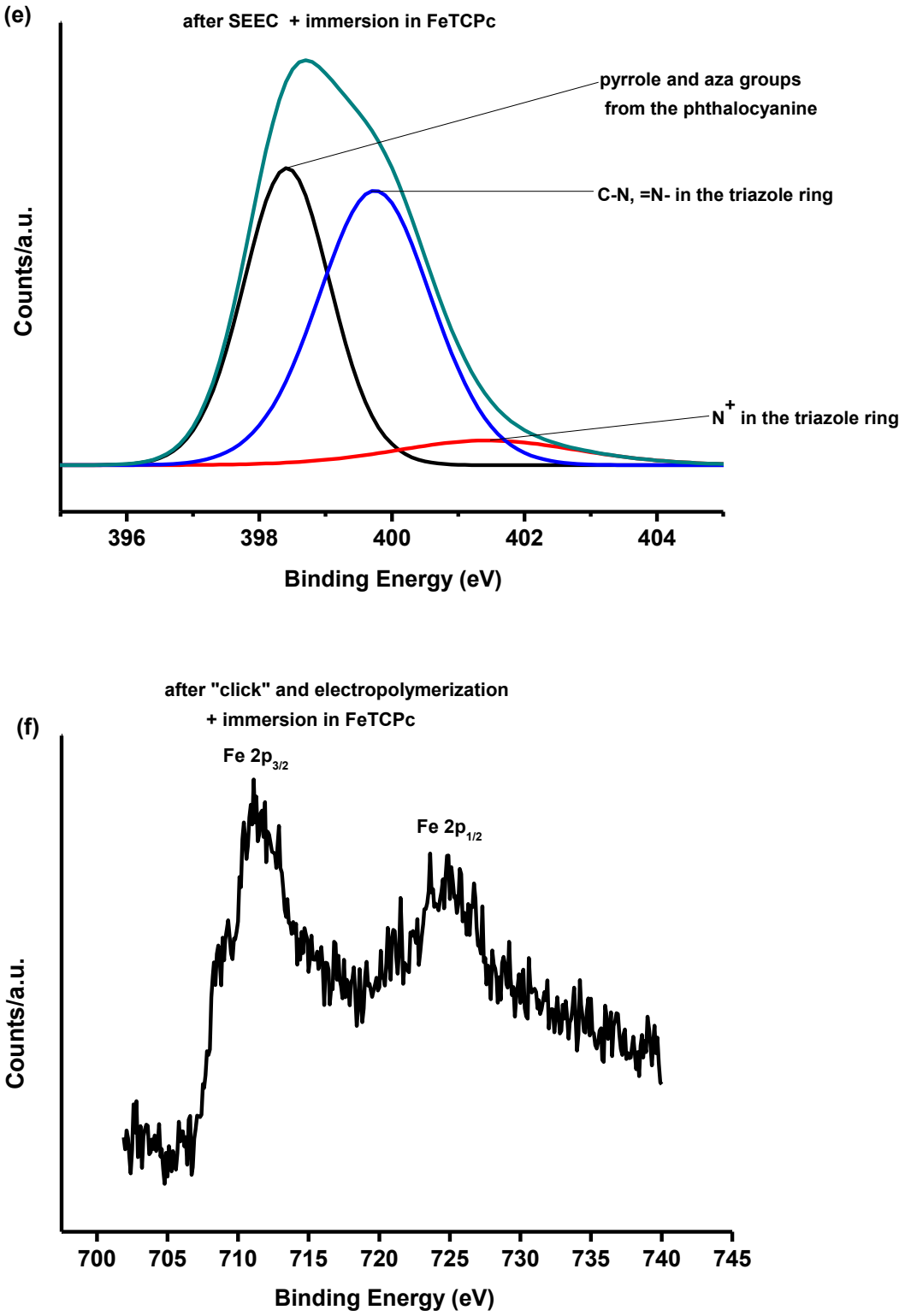

Fig. 4.28. Wide XPS spectra (a), high resolution spectra of C 1s (b and c), N 1s (d and e), and Fe 2p (f).

4.4.5.3. Electrochemical characterization

Fig. 4.29 shows the CVs of bare and modified electrodes in 2 mM ferricyanide dissolved in 0.1 M KCl. The anodic and cathodic peak separation (ΔE) the electrodes at a scan rate of 100 mV/s are shown in Table 4.4. The bare and the SEEC electrodes (without FeTCPc) had the same ΔE. This may suggest that the electrode is not passivated after SEEC. However the addition of FeTCPc caused the ΔE to increase, Table 4.4. This may be attributed to complexity of the modified electrode, which causes slow electron transfer. For the electrode modified by step by step followed by immersion in FeTCPc, the ΔE was 83 mV, hence was lower than that of the SEEC (93 mV), Table 4.4. The possible reason for the difference is that in the SEEC route, the formation of two polymers may cause the steric hindrance hence less FeTCPc on the surface.

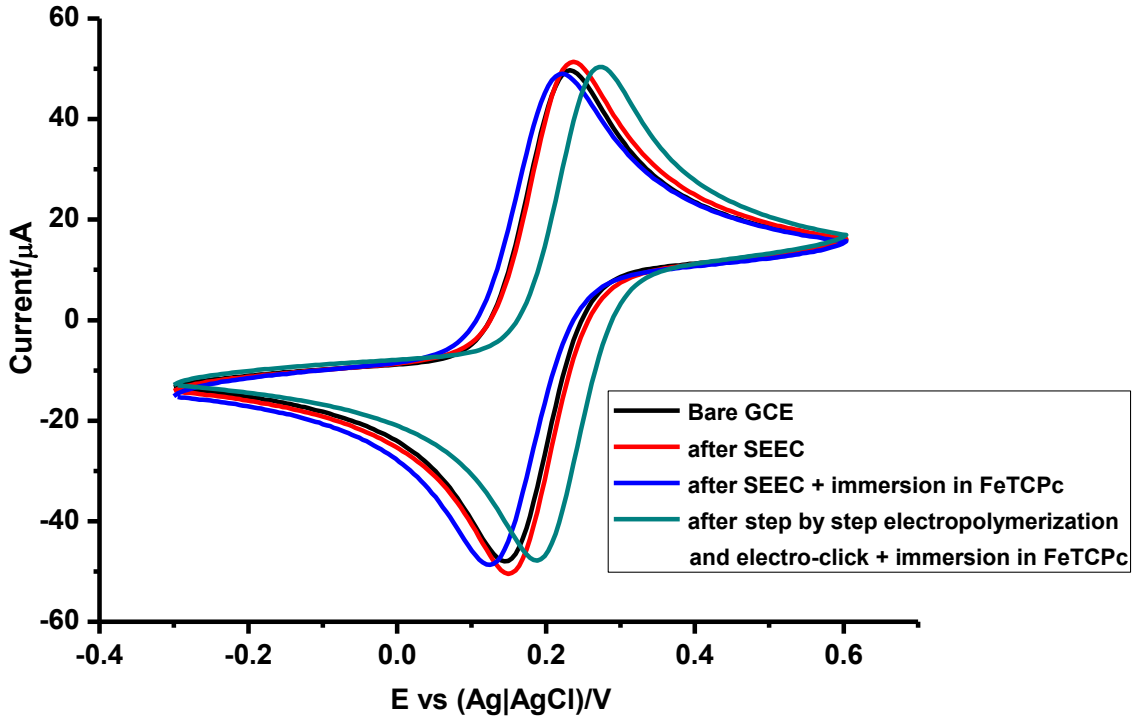

Fig. 4.29. Cyclic voltammograms of bare and modified GCE in 2 mM ferricyanide with 0.1 M KCl electrolyte. Scan rate: 100 mV/s.

Table 4.4. Electrochemical parameters for the electrode modification.

Electrode	**ΔE/mV**
Bare GCE	78
GCE after SEEC	78
GCE after SEEC + immersion in FeTCPc	93
GCE after step by step electropolymerization and electro-click + immersion in FeTCPc	83

Fig. 4.30 shows the cyclic voltammograms of bare and modified GCE recorded in pH 8 buffer at a scan rate of 100 mV/s. pH 8 buffer was used since hydrazine analysis will be carried out at this pH. Fig. 4.30 shows that the bare GCE had no peak and this was expected. The modified electrode after SEEC without FeTCPc shows a redox couple with $E_{1/2}$ of 0.011 V. This may be attributed to the polyaniline redox formed as the electropolymerization was taking place. Inset on Fig. 4.30 shows the cyclic voltammogram of GCE after electropolymerization of azidoaniline alone. It has a redox couple with $E_{1/2}$ of 0.038 V. Similar redox behaviour was obtained for electrochemical activity of polyaniline [31]. The modified electrode after SEEC plus immersion in a solution of DMF containing FeTCPc did not show any pronounced peaks but there was increase in the faradaic currents. The modified electrode after step by step electropolymerization and electro-click plus immersion in a solution of DMF containing FeTCPc showed peaks similar to the ones after SEEC only. The decrease in intensity may suggest interactions between the amine and FeTCPc.

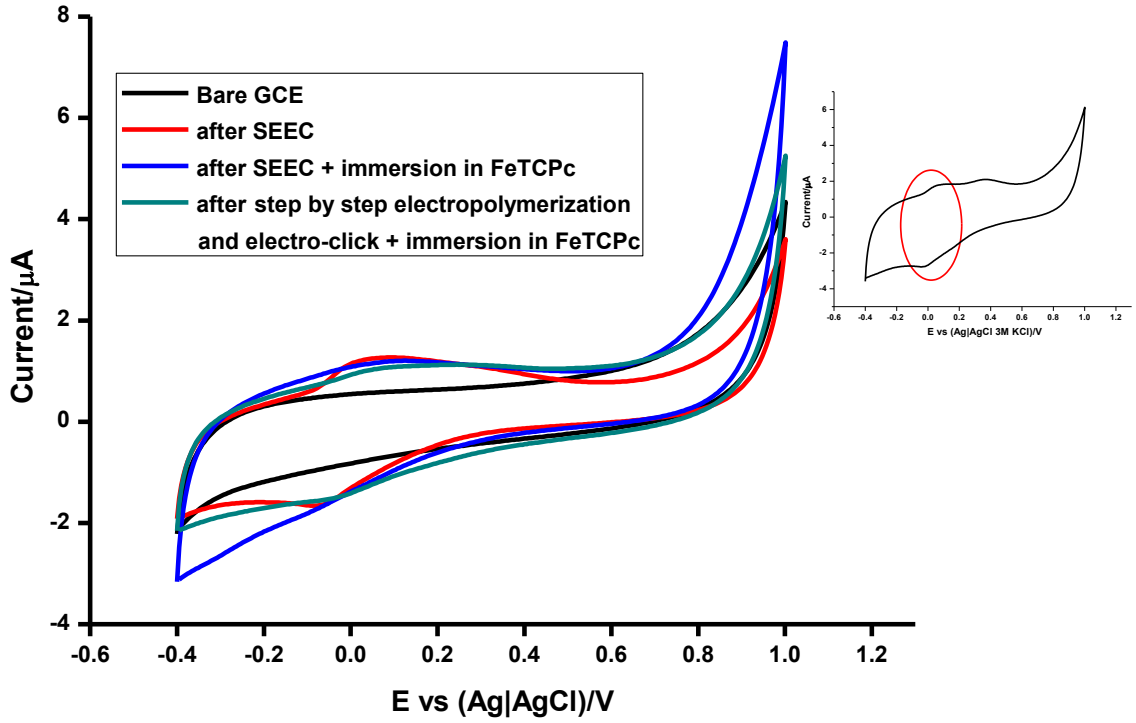

Fig. 4.30. Cyclic voltammograms of bare and modified GCE in pH 8 buffer. Scan rate = 100 mV/s.

4.4.5.4. SECM

Fig. 4.31 shows the 3 D images of unmodified and modified glassy carbon plates (GCP) surfaces. From the image in Fig. 4.31a, it can be seen that the surface of the unmodified plate has a lower current range of 2 nA to 3 nA. When GCP was modified with SEEC in the absence of FeTCPc (Fig. 4.31b), the surface becomes rougher and results in increase in current range of 8 nA to 12 nA. There is a drop in the current range (2.5 nA to 5.0 nA) for the modified electrode after SEEC followed by immersion in a solution of DMF containing FeTCPc (Fig. 4.31c), showing that the interaction of the triazole

and the FeTCPc causes passivation of the electrode. This observation was also seen in the ΔE values, Table 4.4. However, Fig. 4.31d the modified electrode after step by step (electropolymerization followed by electro-click) plus immersion in a solution of DMF containing FeTCPc had a current range of 7.8 nA to 8.8 nA. This shows the superiority of the step by step method compared to SEEC followed by attachment of FeTCPc.

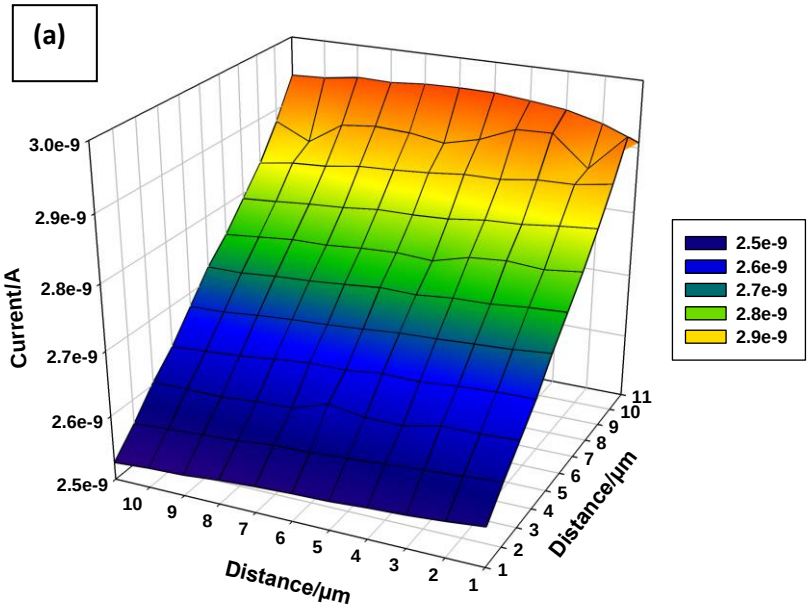
(a)
Current/A
3.0e-9
2.9e-9
2.8e-9
2.7e-9
2.6e-9
2.5e-9
Distance/μm
Distance/μm
2.5e-9
2.6e-9
2.7e-9
2.8e-9
2.9e-9

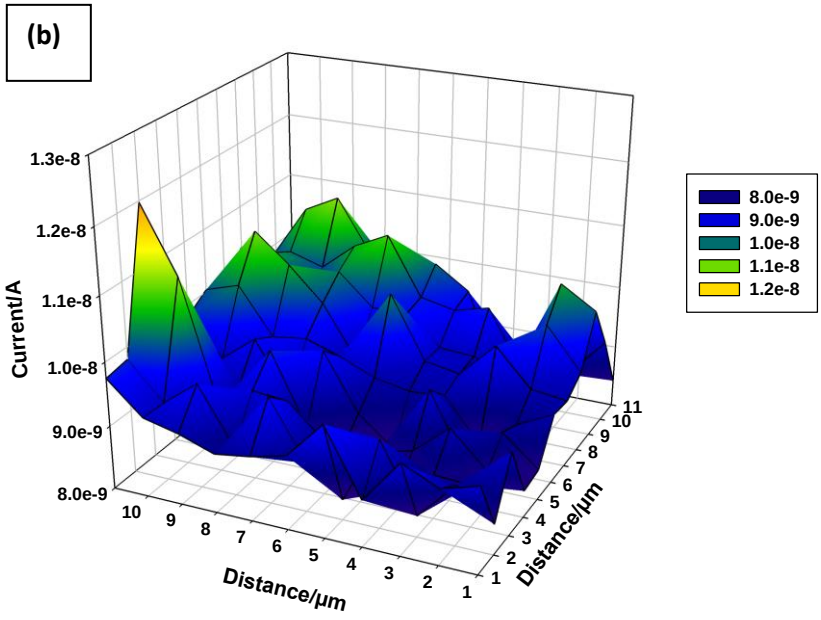
(b)
Current/A
1.3e-8
1.2e-8
1.1e-8
1.0e-8
9.0e-9
8.0e-9
Distance/μm
Distance/μm
8.0e-9
9.0e-9
1.0e-8
1.1e-8
1.2e-8

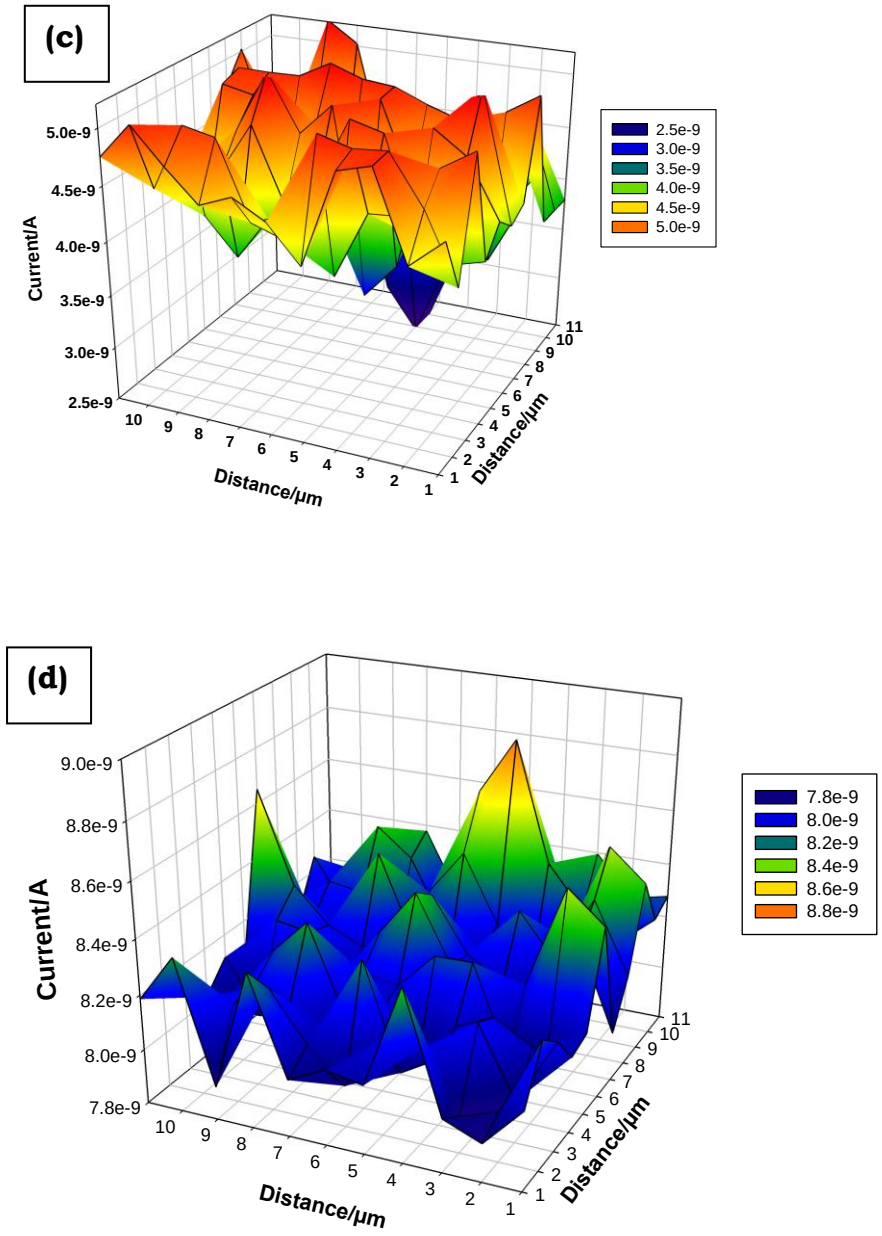

Fig. 4.31. SECM image of (a) bare GCP, (b) GCP after SEEC (c) GCP after SEEC + immersion in FeTCPc (d) GCP after step by step electropolymerization and electro-click + immersion in FeTCPc , in 0.1 M KCl containing 2 mM ferricyanide solution. Imaging conditions: Pt UME (25 µm diameter) placed 10 µm above the substrate, poised at a potential of − 0.1 V vs Ag/AgCl.

4.5. Conclusion

Microscopic (SEM) and spectroscopic (EDS and XPS) characterization have shown that the electrode surfaces were successful immobilised with MPcs and NPs. Electrochemical characterization showed the different responds of the modified electrodes to ferricyanide and buffer solutions. From the behaviour of modified electrodes in ferricyanide, ΔE values were determined to check the electron transfer abilities of the modified electrodes. Amongst the NPs, AuNPs and Au-Pd were the best with the lowest ΔE value of 83 mV, while on MPcs, CoTAPc was the best with ΔE value of 78 mV. Based on ΔE values, the best combination was Au/poly-CoTAPc. CV showed the response of modified electrodes in pH 4, 8 and 9.2. The peaks obtained in the buffer soulution enabled the estimation of the surface coverages. Based on the surface coverage, the best results were from Pd/Au (1.94×10^{-9} mol cm^{-2}), CoTAPc (3.10×10^{-10} mol cm^{-2}) and Pd/poly-CoTAPc (1.90×10^{-9} mol cm^{-2}) for NPs, MPcs and the best combination of NPs and MPcs, respectively.

CHAPTER 5

ELECTROCATALYTIC STUDIES

Modification of electrode surface has been achieved by adsorption, electropolymerization, electrodeposition, electrografting and click chemistry as discussed in Chapter 4. The modified surface are then employed for the detection of analytes namely amitrole, nitrite and hydrazine.

5.1. Amitrole

The NiPc/NiNP was employed in this study using amitrole as a test analyte. The effects of NiNPs on NiPc will be evaluated.

5.1.1. Cyclic voltammetric detection of amitrole

Figure 5.1 shows the comparative cyclic voltammetric responses of the various electrodes in the presence of amitrole. The amitrole oxidation peaks were observed in the potential range 0.93-1.0 V and this is in agreement with other studies [165] done in pH 4 buffer. The oxidation potential of amitrole on NiNP-GCE was 0.93 V, a value 60 mV less positive than that of the bare GCE, Table 5.1. The NiNP-GCE (Fig. 5.1e) shows better electrocatalytic activity relative to the NiPc-GCE (Fig. 5.1d) as judged by the huge catalytic current observed for the former. The current for amitrole oxidation on NiNPs is a factor of 10 higher than the current obtained on unmodified GCE or NiPc-GCE showing the effects of effective electrode area and surface coverage, Table 5.1. In Fig. 5.1a, the cathodic peak is due to Ni^{2+}/Ni^{3+}, and the return peak is due to Ni^{3+}/Ni^{2+}. The preoxidation peak at around 0.76 V for the detection of amitrole on NiNPs, Fig. 5.1, might be due

to the oxidation of Ni^{2+} to Ni^{3+} ions. The drastic decrease of the cathodic peak of the Ni^{3+}/Ni^{2+} process on the return scan suggests that Ni^{3+} species are being consumed during the oxidation of amitrole, Fig. 5.1e and Ni^{2+} regenerated. At higher amitrole concentrations (10 mM), the reduction peak completely disappears (Fig. 5.1 inset), an indication that it is the Ni^{3+} ions that are involved in the catalysis of amitrole. The NiNP/NiPc(mix)-GCE (Fig. 5.1c) is not very electrocatalytic when compared to the bare electrode, Fig. 5.1 (b). Even though methanol may be electrocatalysed by NiNPs [13], at the low amounts of methanol in amitrole solutions, no peak was observed for methanol. This was confirmed by recording the spectra of the same volume (as used for amitrole analysis) of methanol in pH 9.2 buffer in the absence of amitrole. No peak was obtained. Having established that NiNPs offer good electrocatalytic properties relative to the other electrodes, NiNP-GCE was used in kinetic studies. This electrode is very stable and has a shelf life of approximately 3 months if stored in pH 9.2 buffer. Its regeneration is through voltammetric cyclisation in pH 9.2 buffer after use.

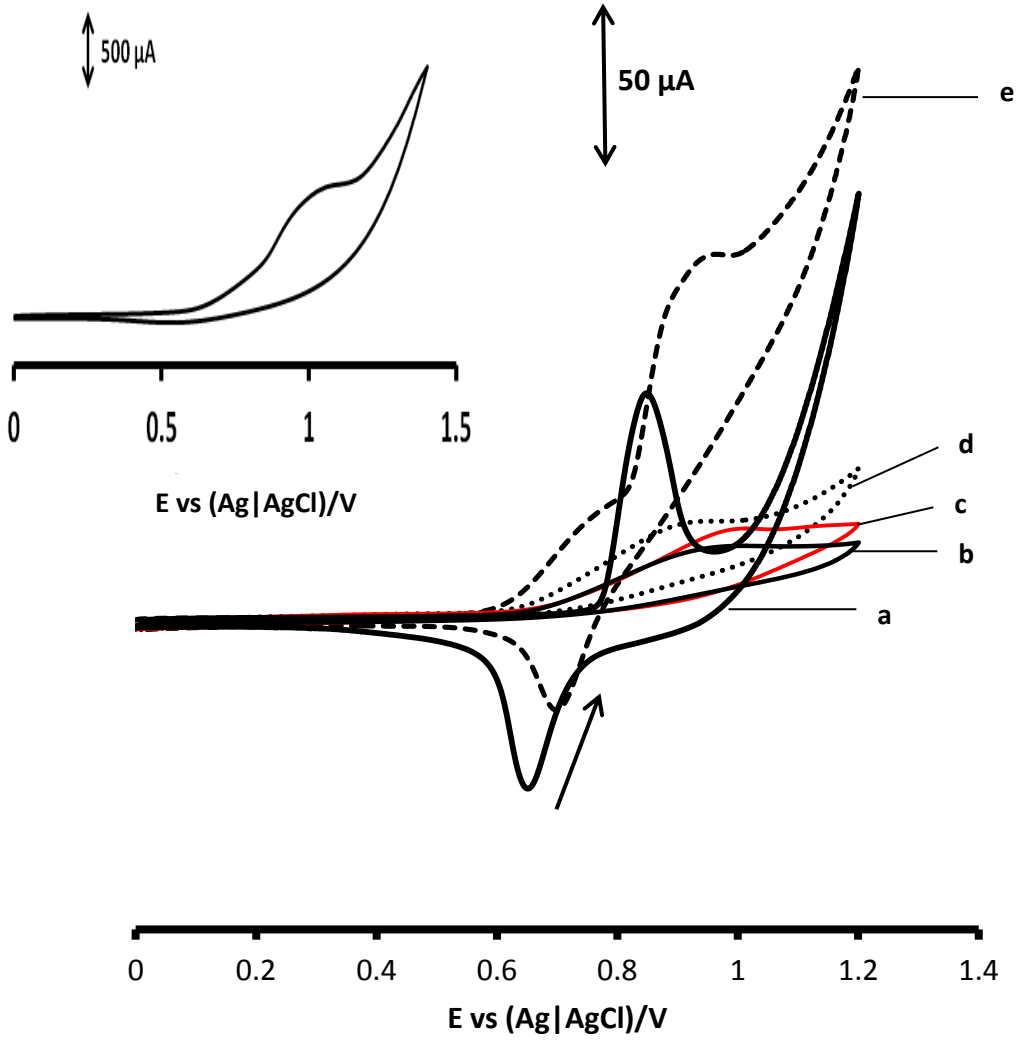

Fig. 5.1. Comparative cyclic voltammograms (Second cycle) for 1 mM amitrole on (b) bare GCE, (c) NiNP/NiPc mix-GCE, (d) NiPc-GCE and (e) NiNP-GCE, b-e done in 1 mM amitrole (pH 9.2). Scan rate = 100 mV/s. Inset: 10 mM amitrole voltammogram on NiNP-GCE. (a) NiNP-GCE (in pH 9.2 buffer) with no amitrole.

5.1.2. Kinetic studies of amitrole on NiNP–GCE

Fig. 5.2 shows a linear plot of peak potential, E_p, versus log v. Increases in scan rates (from 50 mV/s to 600 mV/s) resulted in the amitrole oxidation peak shifting towards more positive potentials, an indication of irreversibility

of the redox reaction. A linear plot of current versus root of scan rate (not shown) confirmed that the irreversible catalytic oxidation of amitrole is diffusion controlled.

The relationship between peak potential and scan rate for an irreversible diffusion-controlled process is given by Eq. 5.1 [42].

$$E_p = \frac{2.3RT}{2(1-\alpha)n_\alpha}\log v + K \qquad (5.1)$$

where α is the transfer coefficient, n is the number of electrons involved in the rate determining step, υ is the scan rate, K is a constant, R is the universal gas constant and T is the temperature (298 K). From the plot of *Ep* versus log υ (Fig. 5.2) a linear relationship represented by Eq. 5.2 and a Tafel slope (2 x the slope of the plot E_p versus log υ) of 210 mV decade^{-1} was obtained.

$$E_p = \frac{b}{2}logv + K \qquad (5.2)$$

where E_p is the peak potential, υ is the scan rate, K is a constant, and b indicates the Tafel slope.

Such high Tafel slopes have no kinetic meaning and are consistent with substrate-catalyst interactions in a reaction intermediate [166] or simply passivation of the electrode surface. Very high Tafel slopes, much greater than the normal 30–120 mV decade^{-1} for one electron rate determining steps are known [167] and have been also been linked to chemical reactions coupled to electrochemical steps [167]. Similar Tafel values have been observed in systems involving species with very high surface to volume ratio, like MPcs and carbon nanotubes [165, 168]. In this study it is not surprising

to have such high Tafel slopes since the NiNP have an average size of 14 nm and a very high surface coverage of 6.59 $\times 10^{-10}$ mol cm^{-2}. As a result there is bound to be very strong interactions between the amitrole and the nickel nanoparticles.

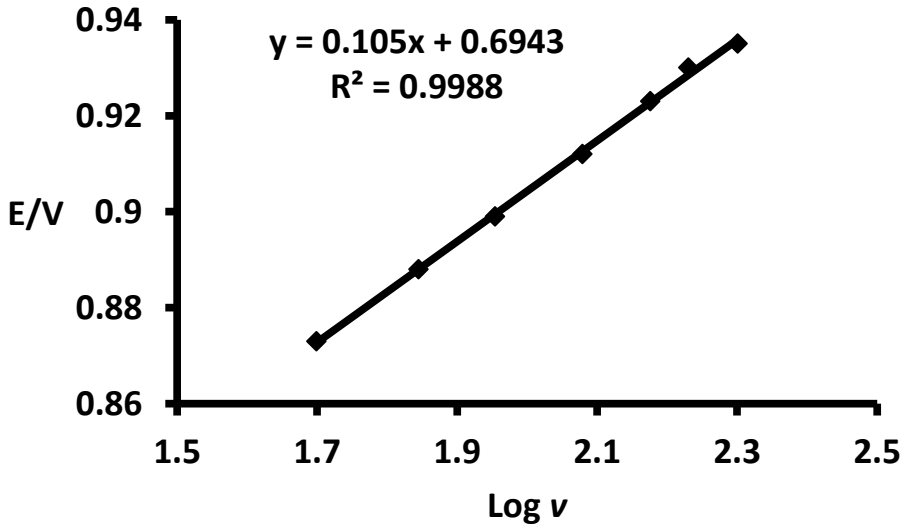

Fig. 5.2. Plot of potential versus log scan rate for 1 mM amitrole.

5.1.3. Electrochemical impedance spectroscopy (EIS)

The electrochemical behaviour of the different electrodes were further investigated by electrochemical impedance spectroscopy (EIS) in 1 mM amitrole and the results are shown in Figure 5.3a and b. Figure 5.3a shows the Nyquist plot for the various electrodes that were used in this study. The plots are composed of semi-circles and straight line portions, representing charge transfer (R_{ct}) and diffusion controlled processes, respectively. The Randles equivalent circuit for this process is shown as an inset in Fig. 5.3a. The equivalent circuit is composed of R_s (the resistance of the electrolyte), in

series connection with parallel elements of C_{dl} (double layer capacitance), R_{ct} (resistance to charge transfer and Z_w (Warburg impedance). Such circuits have been observed in other studies [169, 170]. The R_{ct} as determined by the diameter of the semi-circle was found to be 10.3 kΩ for NiNP-GCE and is much smaller than that of bare GCE, NiPc-GCE and NiNP/NiPc(mix)-GCE which are 35.5 kΩ, 17.0 kΩ and 26.5 kΩ, respectively, see Table 5.1. This shows that the NiNP modified electrode offer limited resistance to charge transfer, hence promoting very fast electron exchange rate, results already confirmed through cyclic voltammetric studies, Fig. 5.1.

The n-values are in the range 0.64 – 0.86 (n<1) confirming the non-capacitative nature of the electrodes. Eq. 5.3 was used to calculate the apparent electron-transfer rate constant (k_{app}) and the results are shown in Table 5.1.

$$k_{app} = \frac{RT}{F^2 R_{ct} C} \qquad (5.3)$$

where R is the universal gas constant, T is the temperature (298 K), F is the Faraday constant, R_{ct} is the resistance to charge transfer and C is the concentration of amitrole (1 mM). The k_{app} also confirm that the transfer of electrons was faster on the NiNP-GCE relative to the other electrodes, as shown in Table 1. The order in terms of magnitude of k_{app} is as follows: NiNP > NiPc > NiNP/NiPc(mix) > bare GCE.

The Bode plot (phase angle (θ) versus log frequency) for the various electrodes is shown in Figure 5.3b. Such plots give information which is not easily provided by the Nyquist plot and their nature confirms the structural differences between the modified and the bare GCE. The bare GCE had a

phase angle at ~60^{o} corresponding to the GCE|amitrole interface. NiNP-GCE, NiPc-GCE and NiNP/NiPc(mix)-GCE had their peaks shifted towards lower frequencies (compared to bare GCE) with NiNP/NiPc(mix)-GCE showing the largest shift. However, NiNP/NiPc(mix)-GCE showed two peaks and this confirms the presence of both NiNP and NiPc species on the electrode surface, with the higher frequency value being attributed to the NiNP species as already confirmed by the Nyquist plots (Figure 5.3a). The changes in the phase angle and frequencies confirmed that oxidation processes were taking place at the modified surfaces rather than on the bare GCE.

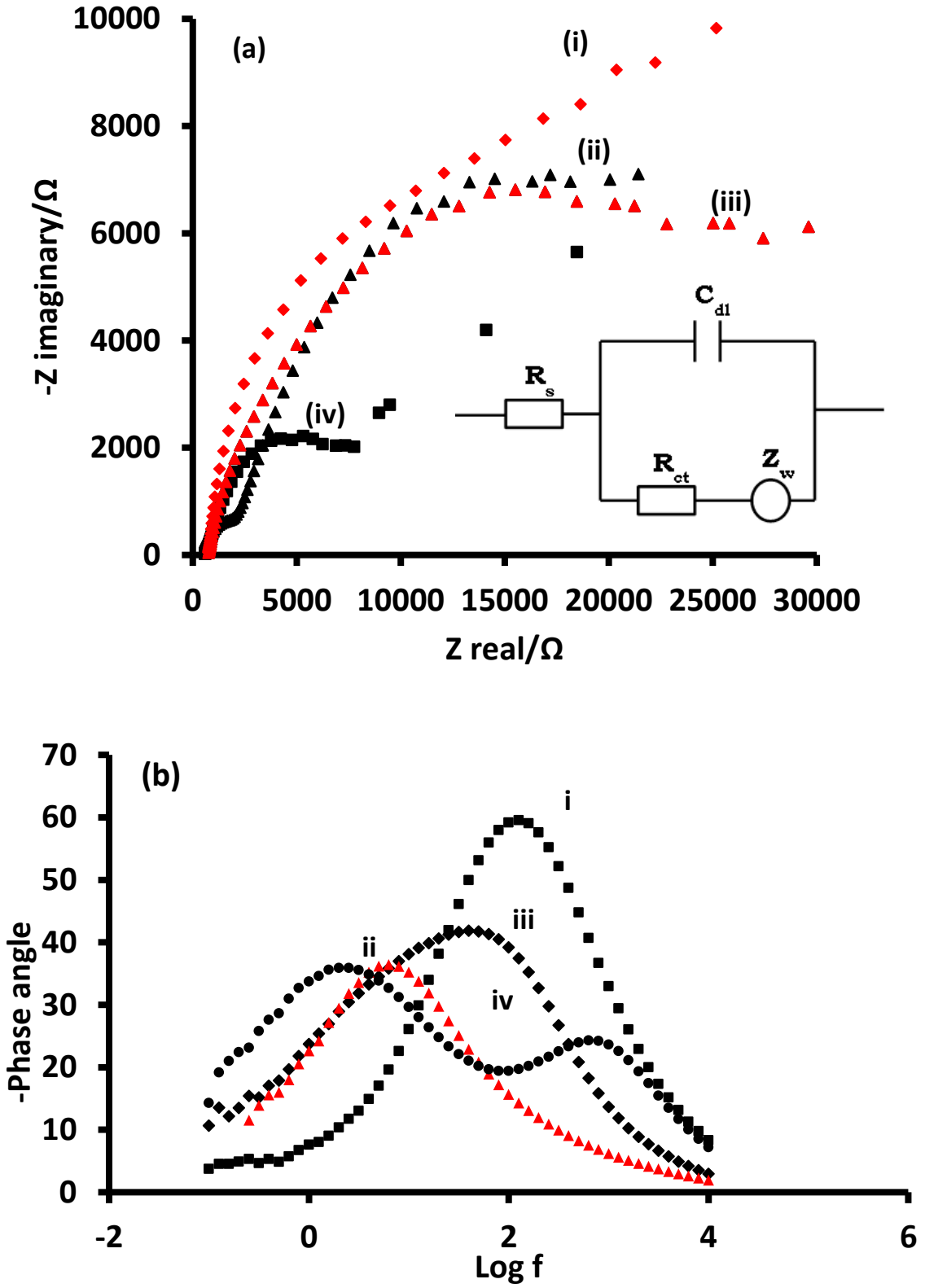

Fig. 5.3. Nyquist (a) and Bode (b) plots obtained for (i) Bare GCE, (ii) NiPc/NiNP (mix)-GCE, (iii) NiPc-GCE and (iv) NiNP-GCE in 1 mM amitrole (pH 9.2 buffer). Inset in (a): Randles equivalent circuit for this process.

Table 5.1. Electrochemical parameters for the impedance data and detection of amitrole.

Electrode	**R_{ct}/kΩ**	**n**	**k_{app}/cm s^{-1}**	**E/V**	**Γ (mol cm^{-2})**
Bare GCE	35.5	0.86	7.50×10^{-6}	0.99	-
NiNP-GCE	10.3	0.68	2.58×10^{-5}	0.93	6.59×10^{-10}
NiPc-GCE	17.0	0.72	1.56×10^{-5}	0.96	1.12×10^{-10}
NiPc-NiNP mix-GCE	25.6	0.64	1.00×10^{-5}	1.00	1.04×10^{-10}

5.1.4. Chronoamperometric studies

Chronoamperometry data was used to determine catalytic rate constant for the oxidation of amitrole. Catalytic rate constants are a measure of how fast redox processes takes place at the electrode/analyte interface. Fig. 5.4a shows the chronoamperometric evolutions on polarized NiNP-GCE for pH 9.2 buffer (i) and amitrole (in pH 9.2 buffer): (ii) 200 μM, (iii) 400 μM, (iv) 600 μM, (v) 800 μM, (vi) 1000 μM. The inset shows a linear relationship between current and concentration and the slope of this plot represent the sensitivity of electrode towards the analyte. Fig 5.4b is the plot of (I_{cat}/I_{buf}) versus $t^{1/2}$ (Eq. 5.4) for amitrole. The catalytic current (I_{cat}) is dominated by the rate at which amitrole is oxidized on the NiNP-GCE surface. The slopes of the plot of (I_{cat}/I_{buf}) versus $t^{1/2}$ were used to calculate the rate constant according to Eq. 5.4 [154].

$$\frac{I_{cat}}{I_{buf}} = \gamma^{1/2}\pi^{1/2} = \pi^{1/2}(kCt)^{1/2} \qquad (5.4)$$

where I_{cat} and I_{buf} are currents in the presence and absence of amitrole, respectively, k is the catalytic rate constant, C is the concentration of amitrole and t is the time elapsed in seconds. The plots of the square of slopes obtained from plot of (I_{cat}/I_{buf}) versus $t^{1/2}$, Fig. 5.4b) versus concentration of amitrole were done (figure not shown). A linear relationship was observed and represented by Eq. 5.5.

$$y = 3.4885\,[amitrole]\left(\frac{s^{-1}}{mM}\right) - 0.1035\,s^{-1},\ R^2 = 0.9956 \quad (5.5)$$

where the slope of this plot is equal to πk and the value of k was found to be 1.11 x 10^3 M^{-1} s^{-1}, Table 5.2. This rate constant is lower but with the same order of magnitude to that which was obtained for amitrole on FeTAPc–SWCNT (single walled carbon nanotubes)–GCE (4.55 × 10^3 M^{-1} s^{-1}) [171]. An almost equal value of 1.2 × 10^3 M^{-1} s^{-1} was obtained on CoTCPc-EA-SWCNT(linked)-GCE (TCPc = tetracarboxy phthalocyanine, EA = ethylene amine) [165]. This indicates that NiNPs are very effective electrocatalysts for the oxidation of amitrole. The mechanism for the oxidation of amitrole may be represented by Eqs. 5.6 and 5.7, similar to the one reported before for other phthalocyanines [165], Table 5.2.

$$Ni^{II} \rightarrow Ni^{III} + e^- \quad (5.6)$$

$$Ni^{III} + amitrole \rightarrow Ni^{II}\ amitrole\ oxidation\ products \quad (5.7)$$

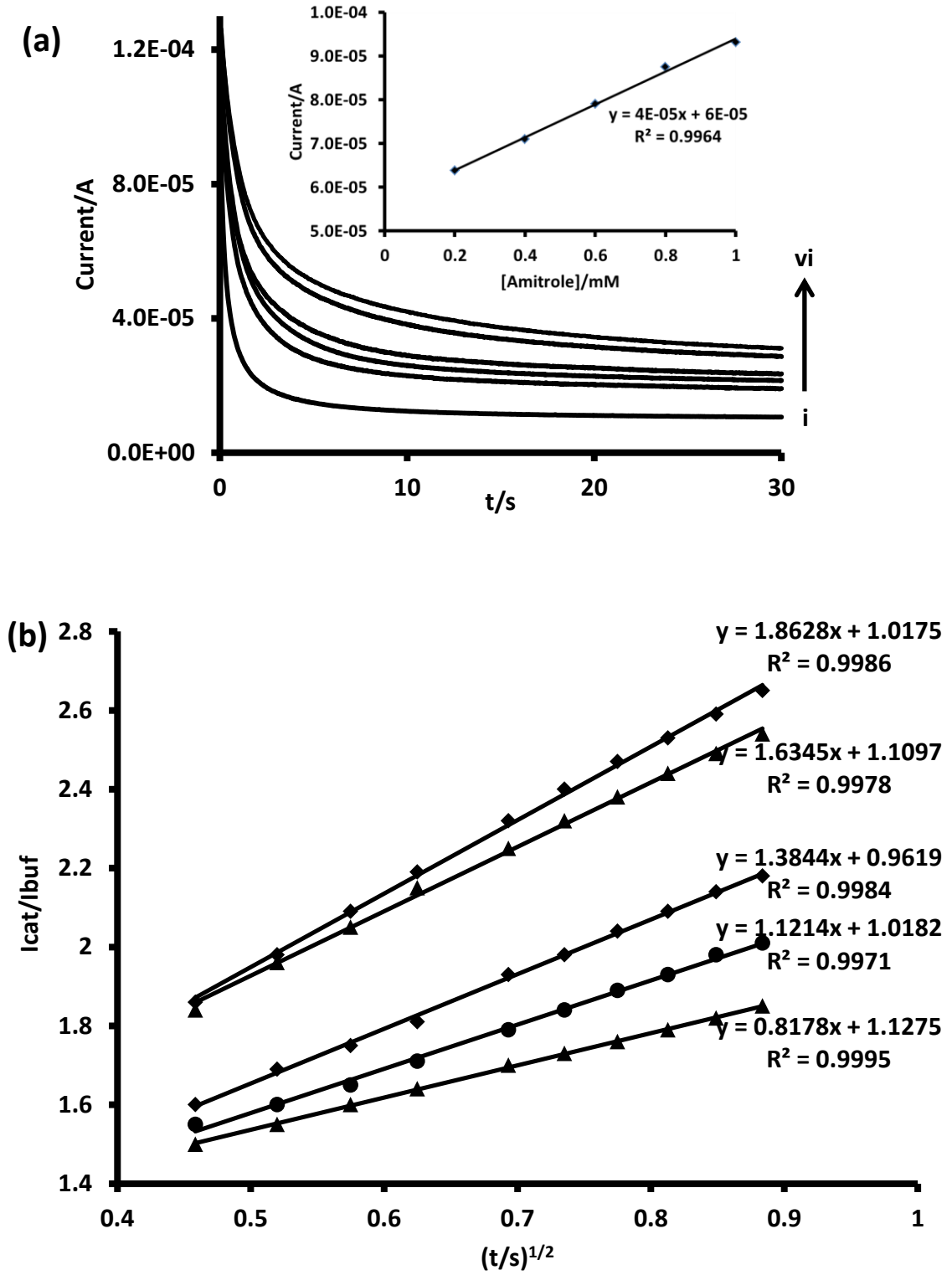

Fig. 5.4. (a) Chronoamperograms for (i) pH 9.2 buffer, (ii) 200, (iii) 400, (iv) 600, (v) 800, (vi) 1000 μM amitrole produced on polarized NiNP-GCE. Inset: current-concentration plot for amitrole. (b) Plot of (I_{cat}/I_{buf}) versus $t^{1/2}$ for (i) 200, (ii) 400, (iii) 600, (iv) 800, (v) 1000 μM amitrole, respectively.

Table 5.2. Catalytic rate constant (*k*)

Electrode	***k*/ cm^3 mol^{-1} s^{-1}**	**Ref**
Amitrole		
NiNP-GCE	1.11 x 10^6	TW
CoTCPc-EA-SWCNT-GCE	1.12 x 10^6	165
FeTAPc-SWCNT-GCE	1.55 x 10^6	171
Nitrite		
Au-GCE	7.84 × 10^6	TW
poly-NiTSPc-GCE	2.24 × 10^6	TW
poly-NiTSPc/Au-GCE	1.23× 10^7	TW
Au/poly-CoTAPc-GCE	3.96 x 10^7	TW
prussian blue NPs-EPPG	4.37 x 10^6	174
Hydrazine		
Pd-GCE	5.54 x 10^8	TW
poly-CoTAPc-GCE	2.86 x 10^8	TW
Pd/poly-CoTAPc-GCE	6.12 x 10^8	TW
GCE after step by step (electropolymerization followed by electro-click and immersion in FeTCPc)	2.1 x 10^9	TW
Au/Ch-GCE	4.7 x 10^7	178
Au/PPy-GCE	4.1 x 10^7	179

where GCE: glassy carbon electrode, CoTCPc-EA-SWCNT(linked)-GCE: Co tetracarboxy phthalocyanine-ethylene amine-single wall carbon nanotubes, NPs: nanoparticles, EPPG: edge plane pyrrolytic graphite, Ch: choline, PPy: poly-pyrrole and TW: this work

In conclusion, NiNPs showed better electrocatalytic activity than NiPc alone or the mixed. This could be due to the high surface coverage of NiNPs compared to NiPc and the mixed.

5.2. Nitrite

5.2.1. AuNPs and NiTSPc

5.2.1.1. Cyclic voltammetric detection of nitrite

Fig. 5.5 shows the cyclic voltammograms of bare and modified GCE in 1 mM nitrite in pH 8 buffer. The bare GCE had an oxidation peak at 0.78 V, Table 5.3. Relative to the bare GCE, the modified electrodes shift the oxidation peak to lower values, Table 5.3. The peak potential obtained with the modified electrodes were 0.62 V, 0.62 V and 0.61 V for Au-GCE, poly-NiTSPc-GCE and poly-NiTSPc/Au-GCE respectively, Table 5.3. The Au-GCE showed two reduction peaks at 0.14 V and 0.85 V. They are attributed to the reduction of gold oxides that would have been formed during the forward scan. Poly-NiTSPc/Au-GCE did not show the reduction peaks implying that the oxidation of AuNPs had been suppressed. Huang and co-workers found out that the gold nanoparticles play an important role in the oxidation of nitrite by accelerating the rate of electron transfer [172]. Nitrite oxidation on Au-GCE, poly-NiTSPc-GCE and poly-NiTSPc/Au-GCE occurred at similar potentials. However, higher currents were observed for poly-NiTSPc/Au-GCE, corresponding to the higher surface coverage, Table 5.3. This was attributed to the synergistic effect of AuNPs and NiTSPc.

Table 5.4 compares the potentials for the electrocatalytic oxidation of nitrite reported in this work with literature values. It has been documented that

gold nanoparticles attached glassy carbon electrode show improved catalytic ability when compared to bulk gold electrode alone [107], Table 5.4. Also when gold electrodes are modified with phthalocyanine complexes [173], nitrite oxidation occurs at higher potential than when phthalocyanines are combined with AuNPs as is the case in this work, Table 5.4.

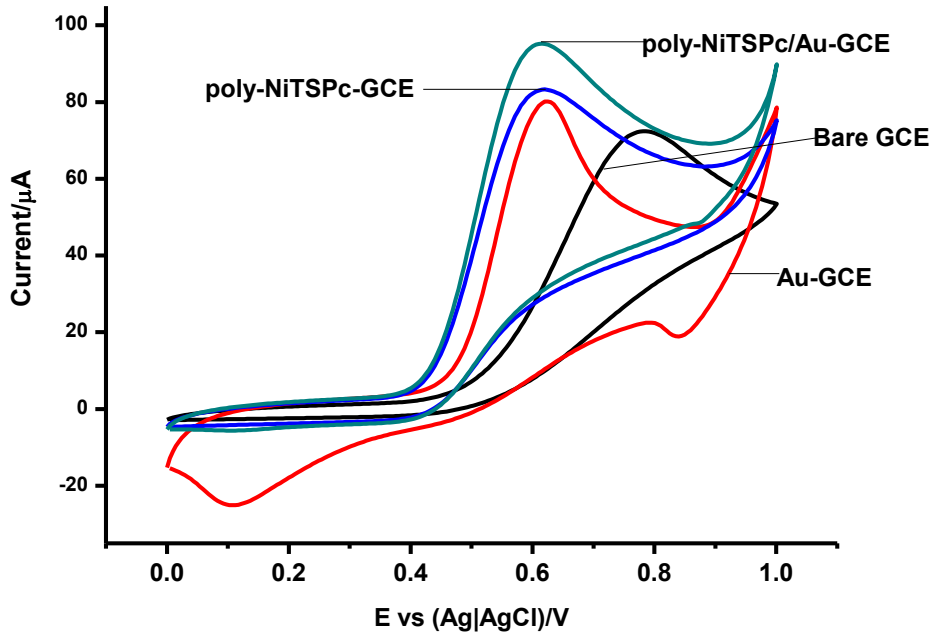

Fig. 5.5. Cyclic voltammograms of bare and modified GCE recorded in 1 mM nitrite in pH 8 buffer solution. Scan rate: 100 mV/s.

Table 5.3. Electrochemical parameters for the electrode modification and detection of nitrite.

Electrode	***E*/V, (nitrite)**	**Tafel slopes (mV/decade)**	**Γ (mol cm^{-2})**
pH 8			
Bare GCE	0.78	-	-
Au-GCE	0.62	186	2.44×10^{-10}
Poly-NiTSPc-GCE	0.62	153	1.79×10^{-10}
Poly-NiTSPc/Au-GCE	0.61	130	1.89×10^{-10}
pH 4			
Bare GCE	0.92	-	-
Au-GCE	0.83	-	2.44×10^{-10}
poly-CoTAPc-GCE	0.88	-	3.10×10^{-10}
poly-CoTAPc/Au-GCE	0.79	-	3.15×10^{-10}
Au/poly-CoTAPc-GCE	0.76	-	3.40×10^{-10}

Table 5.4. Electrochemical detection of nitrite using various electrodes.

Electrode	**E_p/V**	**Medium**	**Reference**
Au/GCE	0.76	pH 4.6	107
Bare Au	0.85	pH 7.4	107
NiTBMPc-Au	0.76	pH 7.4	173
FeTBMPc-Au	0.66	pH 7.4	173
Au-GCE	0.62	pH 8.0	This work
Poly-NiTSPc-GCE	0.62	pH 8.0	This work
Poly-NiTSPc/Au-GCE	0.61	pH 8.0	This work

where NiTBMPc: nickel(II) tetrakis (benzylmercapto)phthalocyanines, FeTBMPc: iron(II) tetrakis (benzylmercapto) phthalocyanines, p-NiTAPc-polymeric nickel tetraaminothphalocyanine and SWCNT: Single wall carbon nanotubes.

5.2.1.2. Kinetic studies of nitrite

Kinetics studies were done in this section for NiTSPc/AuNPs as a representative of both CoTAPc/AuNPs (to be described in the next section) and NiTSPc/AuNPs. When the scan rate was increased from 50 mV/s to 300 mV/s, the nitrite oxidation peak shifted towards positive potentials. This is an indication of irreversibility of the redox reaction. Fig. 5.6 shows linear plots (using poly-NiTSPc/Au-GCE as an example) of current versus root of scan rate and the plot of peak potential versus log scan rate for nitrite oxidation. Linear plots shown in Fig. 5.6a and b were observed on all three electrodes: Au-GCE, poly-NiTSPc-GCE and poly-NiTSPc/Au-GCE. The plots

in Fig. 5.6a confirm that the catalytic oxidation of nitrite is diffusion controlled. The relationship between peak potential and scan rate for an irreversible diffusion-controlled process is given by Eq. 5.1. The plot of E_p versus log υ (Fig. 5.6b) gave a linear relationship and the Tafel slopes were 186 mV decade^{-1}, 153 mV decade^{-1} and 130 mV decade^{-1}, Table 5.3, for nitrite oxidation on Au-GCE, poly-NiTSPc-GCE and poly-NiTSPc/Au–GCE respectively. As stated above, Tafel slopes larger than 30–120 mV decade^{-1} have been associated with chemical reactions coupled to electrochemical steps [167] or to substrate–catalyst interactions in a reaction intermediate [166]. Similar Tafel values have been observed for MPcs and carbon nanotubes [165].

Using the slopes of the plots of *E*p versus log υ (Fig. 5.6b), the electron transfer coefficient (α) for nitrite was found to be 0.68, 0.61 and 0.55 for Au-GCE, poly-NiTSPc-GCE and poly-NiTSPc/Au-GCE respectively, indicating a higher probability of the activated complex being converted to the product for all electrodes. The proposed mechanism for the oxidation of nitrite on NiTSPc modified electrode is given by Eqs. 5.8-5.10.

$$\mathrm{Ni(II)TSPc} \rightarrow [\mathrm{Ni(III)TSPc}]^{+} + \mathrm{e}^{-} \qquad (5.8)$$

$$[\mathrm{Ni(III)TSPc}]^{+} + \mathrm{NO_2^-} \rightarrow [[\mathrm{Ni(III)TSPc}]^{+} - \mathrm{NO_2^-}] \qquad (5.9)$$

$$[[\mathrm{Ni(III)TSPc}]^{+} - \mathrm{NO_2^-}] \rightarrow \mathrm{Ni(II)TSPc} + \mathrm{NO_2} \qquad (5.10)$$

Nitrite oxidation is in the range of the Ni^{III}/Ni^{II} couple in NiTSPc, hence this couple is implicated in the electrocatalytic oxidation, Eq. 5.8. High Tafel slopes suggest substrate-catalyst interaction, Eq. 5.9, followed by nitrite

oxidation, Eq. 5.10. And the NO_2 species may then disproportionate to give nitrite and nitrate.

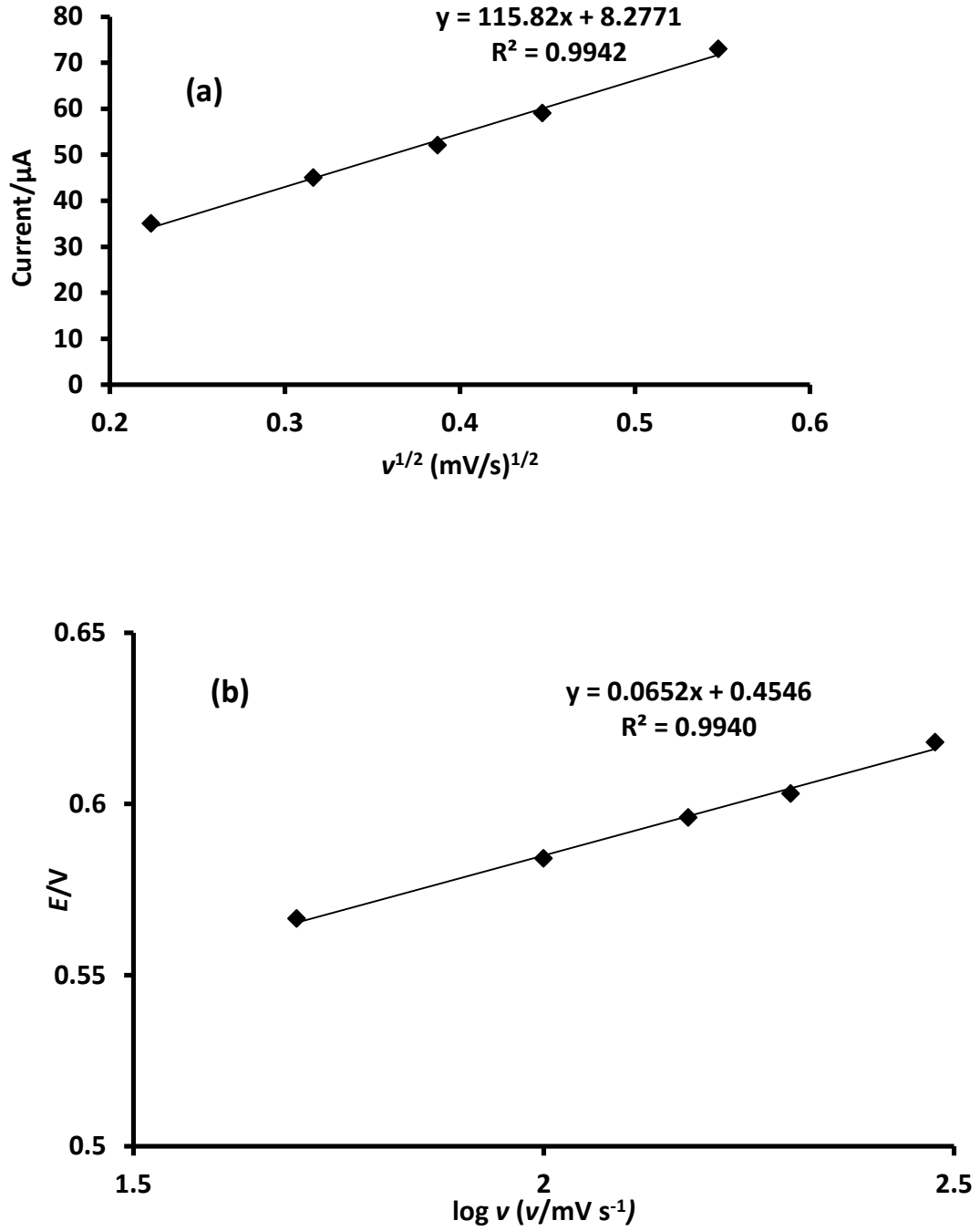

Fig. 5.6. Plots of (a) peak current versus root of the scan rate and (b) peak potential versus log υ for 1 mM nitrite (pH 8 buffer) detection on poly-NiTSPc/Au-GCE.

5.2.1.3. Electrochemical impedance spectroscopy (EIS)

The bare and the modified electrodes were examined by electrochemical impedance spectroscopy (EIS) in 1 mM nitrite and the results are shown in Fig. 5.7a and b. Fig. 5.7a shows the Nyquist plot for the various electrodes that were used in this study. The circuit is as described in section 5.1.3. The R_{ct} values as determined by the diameter of the semi-circle were found to be 4.59 kΩ, 4.01 kΩ, 5.28 kΩ and 3.95 kΩ, for bare GCE, Au-GCE, poly-NiTSPc-GCE and poly-NiTSPc/Au-GCE respectively, Table 5.5. This shows that poly-NiTSPc/Au-GCE offer limited resistance to charge transfer in the presence of nitrite (compared to Au-GCE, poly-NiTSPc-GCE) hence promoting very fast electron exchange rate, results already confirmed by larger catalytic currents in cyclic voltammetric studies, Fig. 5.5. The n-values are in the range 0.87 – 0.90 (n<1) confirming the non-ideal capacitative nature of the electrodes. Eq. 5.3 was used to calculate the apparent electron-transfer rate constant (k_{app}) and the results are shown in Table 5.5. The k_{app} also confirm that the transfer of electrons for nitrite oxidation was faster on the poly-NiTSPc/Au-GCE relative to the other electrodes, as shown in Table 5.4. The order in terms of magnitude of k_{app} is as follows: poly-NiTSPc/Au-GCE > Au-GCE > bare GCE > poly-NiTSPc-GCE.

The Bodes plot (phase angle (θ) versus log frequency) for the various electrodes are shown in Figure 5.7b. The Bode plots confirm the structural differences between the modified and the bare GCE. The slight changes in

the phase angle and frequencies confirmed that oxidation processes were taking place at the modified surfaces rather than on the bare GCE.

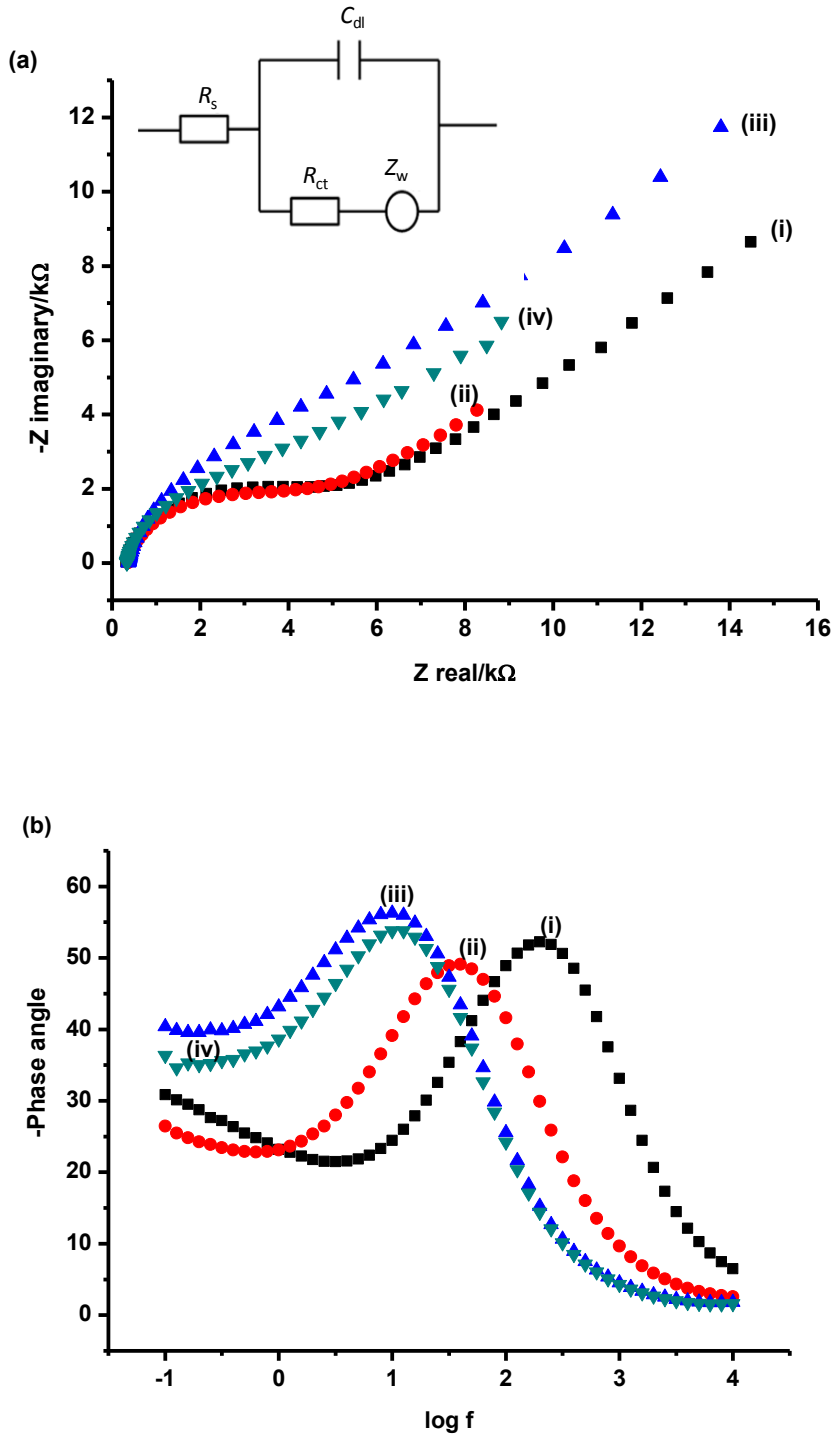

Fig. 5.7. (a) Nyquist and (b) Bode plots obtained for (i) Bare GCE, (ii) Au-GCE, (iii) poly-NiTSPc-GCE, (iv) Au/poly-NiTSPc-GCE in 1 mM nitrite (pH 8 buffer). Inset in (a) is the Randles equivalent circuit employed.

Table 5.5. EIS data and detection of nitrite.

Electrode	R_{ct} **/kΩ**	n	k_{app} **/cm s^{-1}**	E_p**/V, (nitrite)**
pH 8				
Bare GCE	4.59	0.88	5.80×10^{-5}	0.78
Au-GCE	4.01	0.87	6.59×10^{-5}	0.62
poly-NiTSPc-GCE	5.28	0.90	5.00×10^{-5}	0.62
poly-NiTSPc/Au-GCE	3.95	0.90	6.69×10^{-5}	0.61
pH 4				
Bare GCE	16.6	0.87	1.61×10^{-5}	0.92
Au-GCE	12.6	0.84	2.11×10^{-5}	0.83
poly-CoTAPc-GCE	13.8	0.86	1.93×10^{-5}	0.88
poly-CoTAPc/Au-GCE	11.1	0.81	2.40×10^{-5}	0.79
Au/poly-CoTAPc-GCE	9.9	0.82	2.69×10^{-5}	0.76

5.2.1.4. Chronoamperometric studies

The modified electrodes Au-GCE, poly-NiTSPc-GCE and poly-NiTSPc/Au-GCE were employed for chronoamperometric studies. Chronoamperometry data was used to determine catalytic rate constant for the oxidation of nitrite. Fig. 5.8a shows the chronoamperometric evolutions on polarized poly-NiTSPc/Au-GCE (as an example) for pH 8 buffer (i) and nitrite (in pH 8 buffer): (ii) 200 μM, (iii) 400 μM, (iv) 600 μM, (v) 800 μM, (vi) 1000 μM. Similar chronoamperograms were observed for the other modified electrodes. As described above, the slopes of this plot represent the sensitivity of

electrode towards the analyte. Fig. 5.8b shows the plots of (I_{cat}/I_{buf}) versus $t^{1/2}$ (Eq. 5.4) for nitrite. The catalytic current (I_{cat}) is dominated by the rate at which nitrite is oxidized on Au-GCE, poly-NiTSPc-GCE and poly-NiTSPc/Au-GCE surfaces. The slopes of the plot of (I_{cat}/I_{buf}) versus $t^{1/2}$ were used to calculate the rate constant according to Eq. 5.4. Linear relationships (derived in a manner similar to eq. 5.5) were observed and represented by Eqs. 5.11 to 5.14 for, poly-NiTSPc-GCE, Au-GCE and poly-NiTSPc/Au-GCE, respectively.

$$y = 7.03\ [\text{nitrite}]\left(\frac{s^{-1}}{mM}\right) - 1.91\ s^{-1},\ R^2 = 0.9954 \qquad (5.11)$$

$$y = 24.65\ [\text{nitrite}]\left(\frac{s^{-1}}{mM}\right) - 6.37\ s^{-1},\ R^2 = 0.9945 \qquad (5.12)$$

$$y = 38.64\ [\text{nitrite}]\left(\frac{s^{-1}}{mM}\right) - 9.36\ s^{-1},\ R^2 = 0.9960 \qquad (5.13)$$

where the slopes of this plots are equal to πk and the values of k were found to be 2.24×10^6 cm^3 mol^{-1} s^{-1}, 7.84×10^6 cm^3 mol^{-1} s^{-1} and 1.23×10^7 cm^3 mol^{-1} s^{-1}, for poly-NiTSPc-GCE, Au-GCE and poly-NiTSPc/Au-GCE, respectively, Table 5.2. The high catalytic rate constant for poly-NiTSPc/Au-GCE shows the effectiveness of this electode for the oxidation of nitrite compared to poly-NiTSPc-GCE and Au-GCE. The catalytic rate constants obtained for poly-NiTSPc-GCE and poly-NiTSPc/Au-GCE are higher than 4.37×10^6 cm^3 mol^{-1} s^{-1} which was reported for nitrite detection on prussian blue nanoparticles modified edge plane pyrolytic graphite [174], Table 5.2.

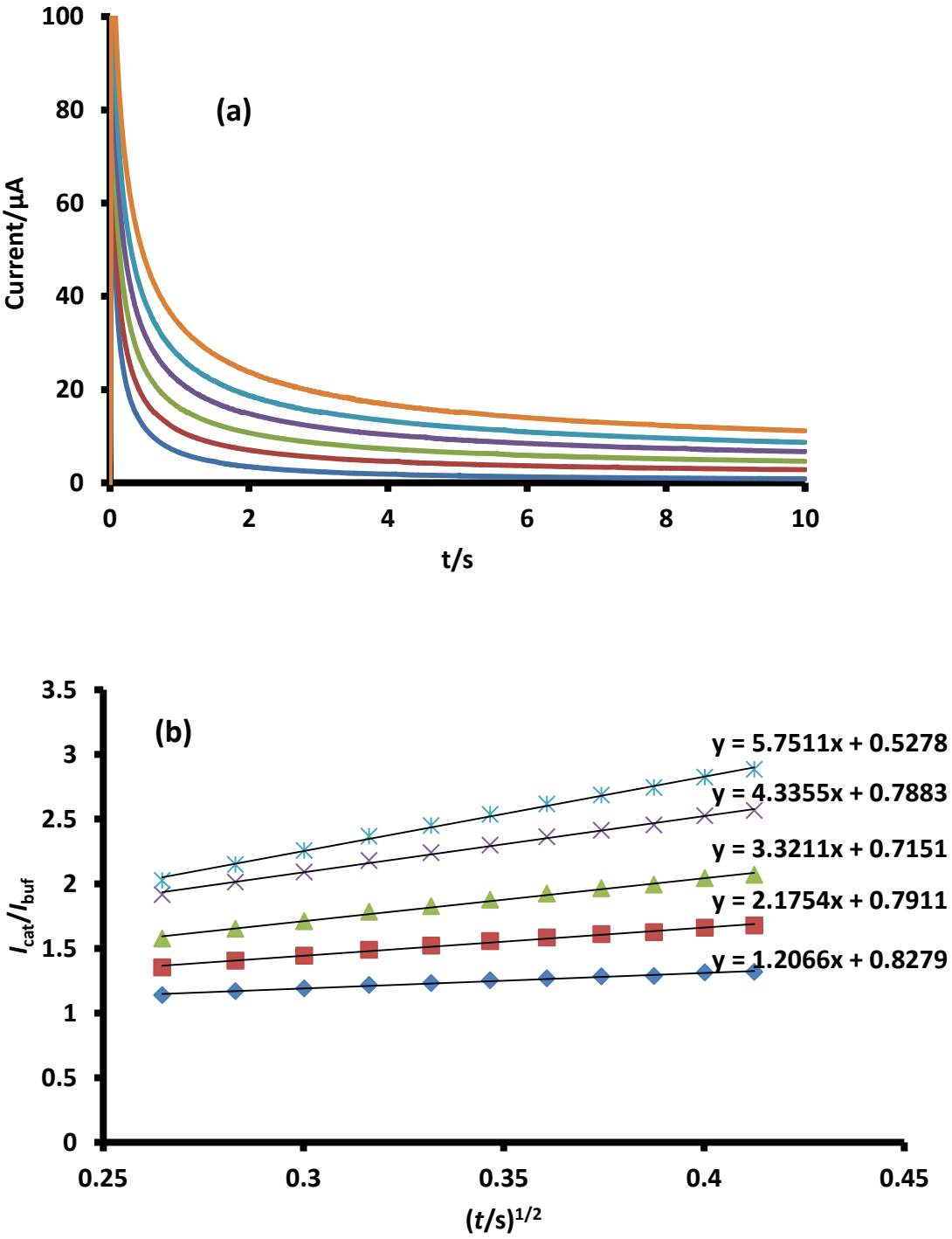

Fig. 5.8. Chronoamperograms (a) for (i) pH 8 buffer, (ii) 200, (iii) 400, (iv) 600, (v) 800, (vi) 1000 µM nitrite produced on polarized poly-NiTSPc/Au-GCE. (b) Plots of (I_{cat}/I_{buf}) versus $t^{1/2}$ from (a). With R^2 values ranging from 0.9934 to 0.9972.

5.2.2. AuNPs and CoTAPc

5.2.2.1. Cyclic voltammetric detection of nitrite

Fig. 5.9 shows the cyclic voltammograms of bare and modified GCE in 1 mM nitrite in pH 4 buffer. The bare GCE had an oxidation peak at 0.92 V, Table 5.3. Relative to the bare GCE, the oxidation peak is shifted to lower values for the modified electrodes. The peak potential for nitrite oxidation on modified electrodes were 0.83 V, 0.88 V, 0.79 V and 0.76 V for Au-GCE, poly-CoTAPc-GCE, poly-CoTAPc/Au-GCE and Au/poly-CoTAPc-GCE respectively, Table 5.3. Nitrite oxidation on Au/poly-CoTAPc-GCE occurred at a much lower potential of 0.76 V. Higher currents were observed for both Au/poly-CoTAPc-GCE and poly-CoTAPc/Au-GCE compared to Au-GCE or poly-CoTAPc-GCE, showing the advantage of combining the two electrocatalysts (AuNPs and poly-CoTAPc). The observation may be supported by relatively higher surface coverage on the combined electrocatalyst compared to the individual electrocatalyst. Poly-CoTAPc-GCE on its own showed electrocatalysis in terms of peak potential compared to bare GCE, but worse than for the rest of the modified electrodes. Thus the presence of AuNPs enhanced the electrocatalytic oxidation of nitrite. Huang and co-workers found out that the gold nanoparticles play an important role in the oxidation of nitrite by accelerating the rate of electron transfer [172].

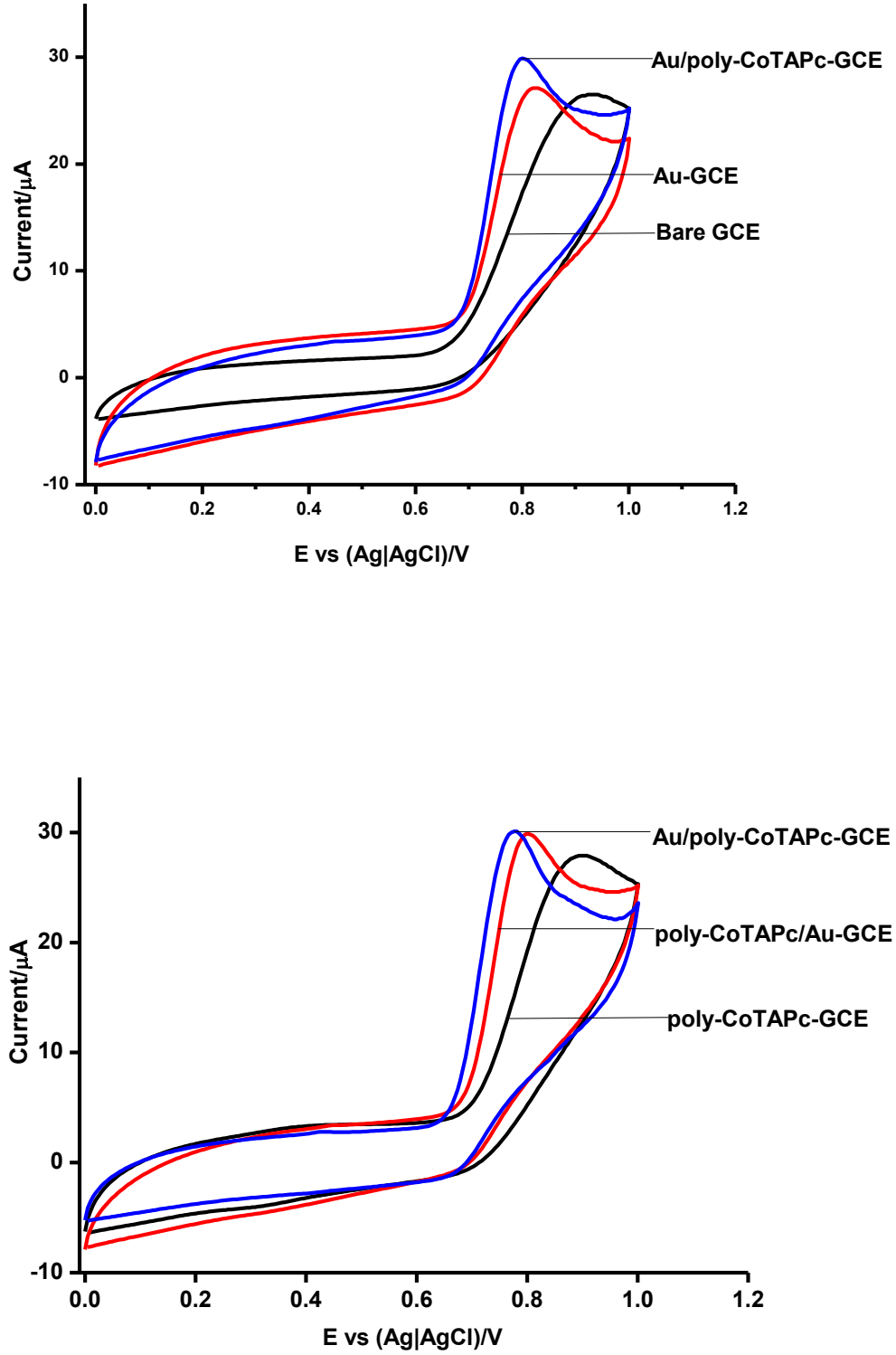

Fig. 5.9. Cyclic voltammograms of bare and modified GCE recorded in 1 mM nitrite in pH 4 buffer solution. Scan rate: 100 mV/s.

5.2.2.2. Electrochemical impedance spectroscopy (EIS)

The electrochemical behaviour of the different electrodes were further investigated by electrochemical impedance spectroscopy (EIS) in 1 mM nitrite and the results are shown in Fig. 5.10. Fig. 5.10a shows the Nyquist plots. The R_{ct} as determined by the diameter of the semi-circle was found to be 9.9 kΩ for Au/poly-CoTAPc-GCE and is much smaller than that of bare GCE, Au-GCE, poly-CoTAPc-GCE and poly-CoTAPc/Au-GCE which are 16.6 kΩ, 12.6 kΩ, 13.8 kΩ and 11.1 kΩ respectively, Table 5.5. This shows that Au/poly-CoTAPc-GCE offer limited resistance to charge transfer in the presence of nitrite, hence promoting very fast electron exchange rate, results already confirmed by lower potentials in cyclic voltammetric studies, Fig. 5.9. The n-values are in the range 0.82-0.87 (n<1) confirming the non-capacitative nature of the electrodes. Eq. 5.3 was used to calculate the apparent electron-transfer rate constant (k_{app}) and the results are shown in Table 5.5.

The k_{app} also confirm that the transfer of electrons for nitrite oxidation was faster on the Au/poly-CoTAPc-GCE relative to the other electrodes, Table 5.5. The order in terms of magnitude of k_{app} is as follows: Au/poly-CoTAPc-GCE > poly-CoTAPc/Au-GCE > Au-GCE > poly-CoTAPc-GCE > bare GCE.

The Bode plot (phase angle (θ) versus log frequency) for the various electrodes is shown in Fig. 5.10b. The slight changes in the phase angle and frequencies, compared to bare GCE confirmed that oxidation processes were taking place at the modified surfaces.

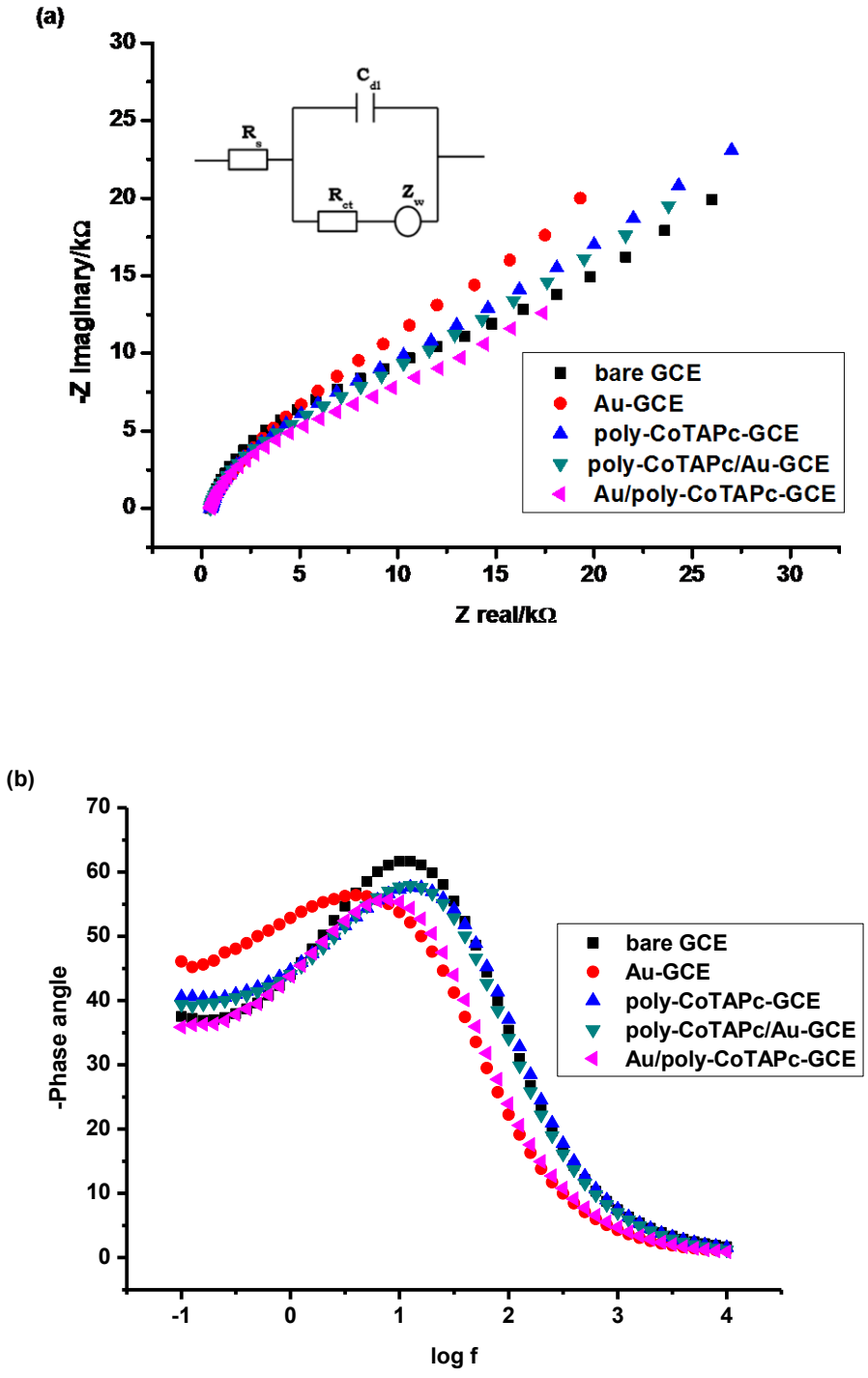

Fig. 5.10. Nyquist (a) and Bode (b) plots obtained for (i) Bare GCE, (ii) Au-GCE, (iii) poly-CoTAPc-GCE, (iv) poly-CoTAPc-Au-GCE and (v) Au/poly-CoTAPc-GCE in 1 mM nitrite (pH 4 buffer). Inset in (a): Randles equivalent circuit for this process.

5.2.2.3. Chronoamperometric studies

Au/poly-CoTAPc-GCE was employed for these studies due to its superior catalytic activity discussed above. Chronoamperograms similar to those shown in Fig. 5.8 were constructed. The slopes of the plot of (I_{cat}/I_{buf}) versus $t^{1/2}$ were used to calculate the rate constant according to Eq. 5.4. The plots of the square of slopes from figure similar to Fig. 5.8 b versus concentration of nitrite were done. A linear relationship was observed and represented by Eq. 5.14.

$$y = 124.63\,[nitrite]\left(\frac{s^{-1}}{mM}\right) - 30.63\,s^{-1},\ R^2 = 0.9944 \quad (5.14)$$

where the slope of this plot is equal to πk and the value of k was found to be 3.96 x 10^7 cm^3 mol^{-1} s^{-1}, Table 5.2. The rate constant of Au/poly-CoTAPc-GCE is also higher than that of NiTSPc/Au-GCE, showing that CoTAPc is superior, Table 5.2. The rate constant indicates that Au/poly-CoTAPc-GCE was very effective electrocatalysts for the oxidation of nitrite since the value is higher that the reported (4.37 x 10^6 cm^3 mol^{-1} s^{-1}) for nitrite detection on prussian blue nanoparticles modified edge plane pyrolytic graphite [174]. The mechanism for the detection of nitrite would be similar to eq. 5.8 to 5.10.

In conclusion, AuNPs and CoTAPc alone were not as effective as to when combined unlike NiNPs and NiPc, where NiNPs gave better results for the electrooxidation of amitrole. NiNPs were the best for amitrole detection but did not work for nitrite detection. CoTAPc better than NiTSPc in terms of the rate constant.

5.3. Hydrazine

Hydrazine was detected on poly-CoTAPc in the presence of AuNPs or PdNPs individual or when in bimetallic form. Hydrazine was also detected on FeTCPc. The discussion will start with the detailed detection on CoTAPc and PdNPs.

5.3.1. CoTAPc and PdNPs

5.3.1.1. Cyclic voltammetric detection of hydrazine

Fig. 5.11A shows the cyclic voltammograms of bare and modified GCE recorded in 1 mM hydrazine. The bare had a broad peak for hydrazine at 0.77 V, Table 5.6. Modifying the electrode with CoTAPc caused a shift of potential to lower values. The hydrazine peak potential was found at 0.15 V, Table 5.6, with current of 16 μA for poly-CoTAPc. Ivanov et al obtained hydrazine detection at -0.28 V using PdNPs and polyaniline [175]. In this work we observed the hydrazine oxidation peak at -0.20 V and -0.28 V for Pd-GCE (Fig. 5.11B) and Pd/poly-CoTAPc-GCE (Fig. 5.11C), Table 5.6, with background corrected currents of 36 μA and 60 μA, respectively, Fig. 5.11C. Both show larger currents than poly-CoTAPc-GCE alone at 16 μA, hence Pd/poly-CoTAPc-GCE shows the largest currents for hydrazine oxidation at 60 μA. Oxidation of PdNPs was observed at 0.54 V and 0.50 V for Pd-GCE and Pd/poly-CoTAPc-GCE respectively. The oxides of palladium were reduced near 0 V, Fig. 5.11. Peaks due to hydrazine oxidation (at -0.20 V

and -0.28 V for Pd-GCE and Pd/poly-CoTAPc-GCE, respectively) increased with increase in concentration in Fig. 5.11B and C confirming that they are due to the analyte. Increasing the concentration of hydrazine resulted in the shift of its oxidation potential to more positive values, Fig. 5.11C. The hydrazine peak is observed at -0.28 for Pd/poly-CoTAPc-GCE in this work which much more negative than PdNPs and Pc alone, but also more negative than reported on similar electrodes in the literature [176], Table 5.7. Thus combining Pc with PdNPs offers an advantage for the detection of hydrazine as a test molecule.

The overall reaction for hydrazine is represented by Eq. 5.15.

$$N_2H_4 \longrightarrow N_2 + H^+ + 4e^- \quad (5.15)$$

This mechanism has been proposed for the oxidation of hydrazine on PdNPs [76]. The oxidation of hydrazine on CoTAPc is in the range of Co^{II}/Co^{I} couple of CoTAPc, hence this couple is involved in the catalysis mechanism. The mechanism for oxidation of hydrazine has been reported in literature for FePc [177]. Thus following literature [177] and the fact the Co^{II}/Co^{I} couple is involved, we propose the following mechanism (Eqs 5.16-5.19) for CoTAPc catalysed hydrazine oxidation in basic media.

$$[Co^{I}TAPc]^- \rightarrow Co^{II}TAPc + e^- \quad (5.16)$$

$$Co^{II}TAPc + N_2H_4 + OH^- \rightarrow [Co^{I}TAPc]^-(N_2H_3)^+ + H_2O + e^- \quad (5.17)$$

$$[Co^{I}TAPc]^-(N_2H_3)^+ + OH^- \rightarrow Co^{II}TAPc + (N_2H_2)^{\cdot} + H_2O + e^- \quad (5.18)\ (\text{rds})$$

$$(N_2H_2)^{\cdot} + 2OH^- \rightarrow N_2 + 2H_2O + 2e^- \quad (5.19)$$

The overall mechanism involves the four electron oxidation of hydrazine.

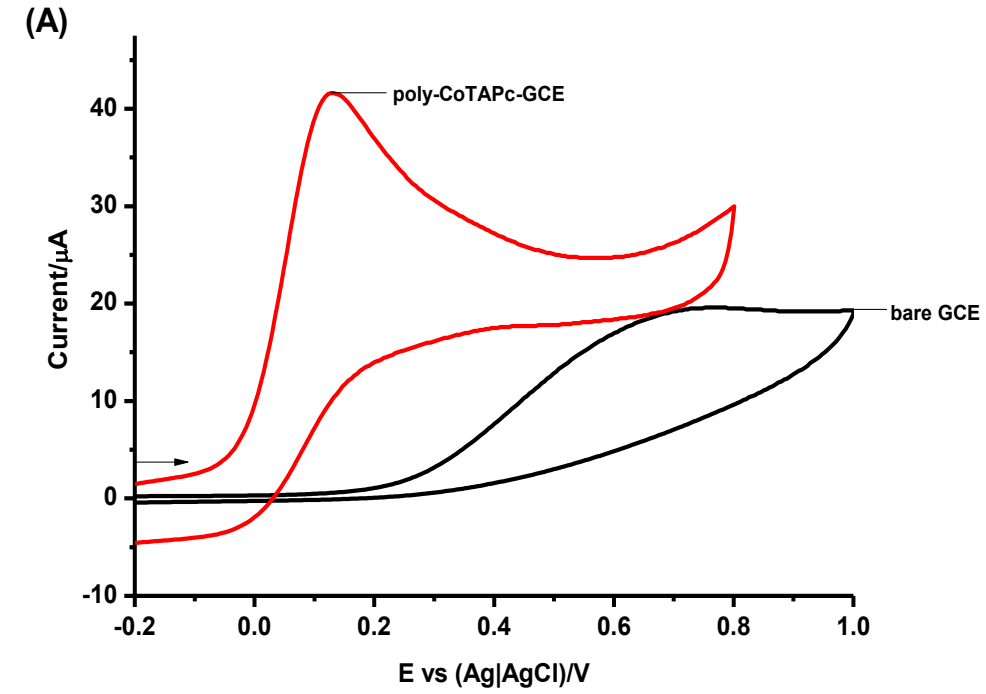
(A)
poly-CoTAPc-GCE
bare GCE
Current/μA
E vs (Ag|AgCl)/V
40
30
20
10
0
-10
-0.2
0.0
0.2
0.4
0.6
0.8
1.0

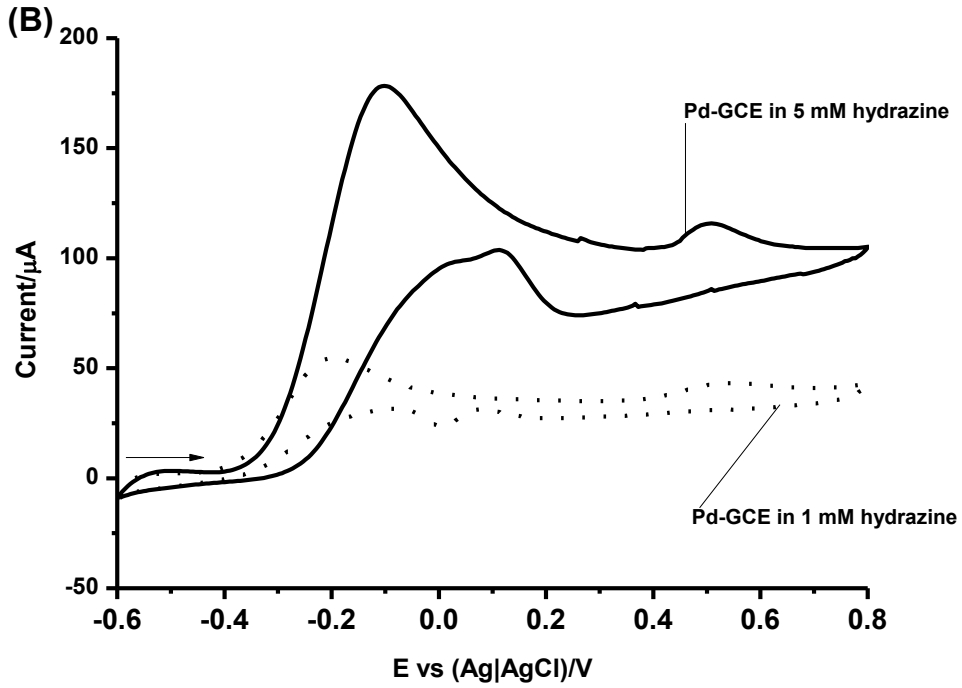
(B)
Pd-GCE in 5 mM hydrazine
Pd-GCE in 1 mM hydrazine
Current/μA
E vs (Ag|AgCl)/V
200
150
100
50
0
-50
-0.6
-0.4
-0.2
0.0
0.2
0.4
0.6
0.8

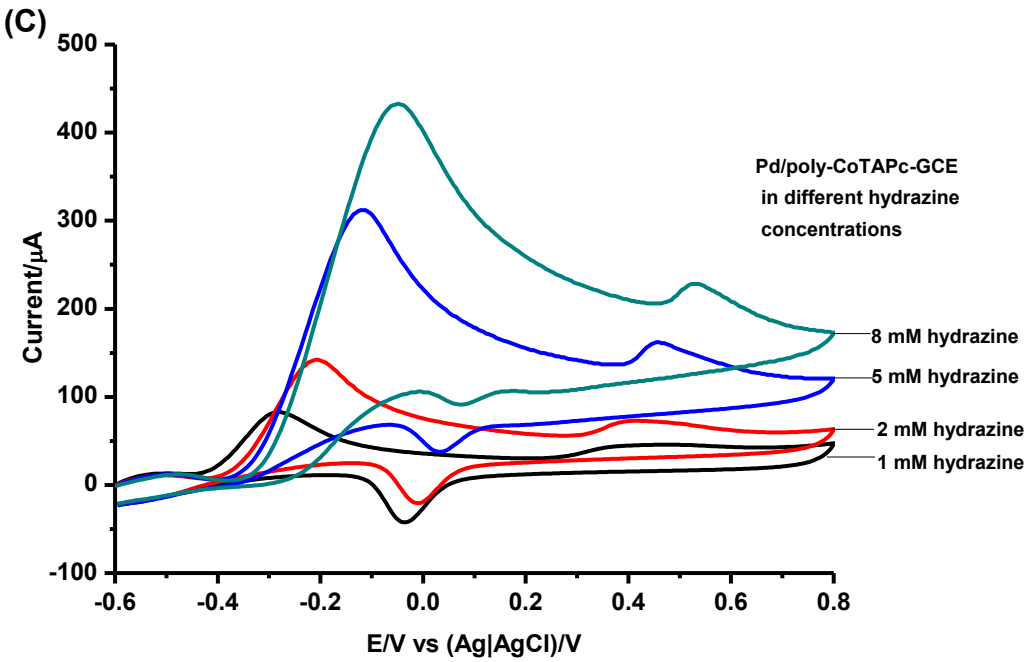

Fig. 5.11. Cyclic voltammograms of hydrazine on (A) bare and poly-CoTAPc-GCE (1 mM hydrazine), (B) Pd-GCE (1 and 5 mM hydrazine), (C) Pd/poly-CoTAPc-GCE (1, 2, 5 and 8 mM hydrazine). Scan rate: 50 mV/s.

Table 5.6. Electrochemical parameters for the impedance data for hydrazine.

Electrode	**Γ/mol cm^{-2}**	**R_{ct} /kΩ**	**n**	**k_{app} /cm s^{-1}**	***E*/V, (hydrazine)**
Bare GCE	-	23.7	0.95	1.6 x 10^{-4}	0.77
Pd-GCE	1.82 × 10^{-9}	6.9	0.93	5.4 x 10^{-4}	-0.20
Au-GCE	2.44 × 10^{-10}	10.8	0.90	3.5 x 10^{-4}	0.22
Au/Pd-GCE	2.95 × 10^{-10}	9.6	0.90	3.9 x 10^{-4}	0.05
Pd/Au-GCE	1.90 × 10^{-9}	8.1	0.91	4.6 x 10^{-4}	-0.19
Au-Pd (co-deposited)-GCE	3.30 × 10^{-10}	6.2	0.91	6.0 x 10^{-4}	-0.02
Poly-CoTAPc-GCE	3.10 × 10^{-10}	15.3	0.82	2.4 x 10^{-4}	0.15
Pd/Poly-CoTAPc -GCE	1.94 × 10^{-9}	6.6	0.86	5.7 x 10^{-4}	-0.28
Au/poly-CoTAPc-GCE	3.40 × 10^{-10}	9.7	0.85	3.9 x 10^{-4}	0.11
Au/Pd-poly-CoTAPc-GCE	4.80 × 10^{-10}	9.5	0.85	3.9 x 10^{-4}	0.04
Pd/Au-poly-CoTAPc-GCE	1.30 × 10^{-9}	8.4	0.85	4.5 x 10^{-4}	-0.21
Au-Pd (co-deposited)/poly-CoTAPc-GCE	4.30 × 10^{-10}	6.1	0.86	6.1 x 10^{-4}	-0.12
GCE after SEEC		68.1	0.94	5.5 x 10^{-5}	No peak
GCE after SEEC + immersion in FeTCPc		68.6	0.91	5.5 x 10^{-5}	0.30
GCE after step by step (electropolymerization followed by electro-click and immersion in FeTCPc)		30.9	0.91	1.2 x 10^{-4}	0.26

Table 5.7. Oxidation potentials and limits of detection for hydrazine on various electrodes

Electrode	Medium	Potential (V)	LoD (μM)	Reference
Pd/BDD	pH 7	0.16	2.6	176
Pd/CB/GCE	pH 9	-0.1	8.8	111
FePc-SAM-Au	pH 7	0.35	5	114
CoPc/CPE	pH 6.5	0.5	0.5	116
Poly-CoTAPc-GCE	pH 8	0.15	5.7	This work
Pd-GCE	pH 8	-0.20	9.6	This work
Pd/Poly-CoTAPc-GCE	pH 8	-0.28	1.3	This work

GCE: glassy carbon electrode, MWCNT: multi-walled carbon nanotubes, BDD: boron dopped diamond electrode, CB: carbon black, SAM: self-assembled monolayer, LoD: limit of detection and CPE: carbon paste electrode.

5.3.1.2. Kinetic studies of hydrazine oxidation

Pd/poly-CoTAPc-GCE was employed in this section due to its high electrocatalytic activity for hydrazine detection compared to the individual compounds. When the scan rate was increased from 50 mV/s to 300 mV/s, the hydrazine oxidation peak shifted towards positive potentials as shown in Fig 5.12a. This is an indication of irreversibility of the redox reaction. Fig. 5.12b shows linear plots of current versus root of scan rate and the plot of peak potential versus log scan rate for hydrazine oxidation. The plots in Fig. 5.12b confirm that the catalytic oxidation of hydrazine is diffusion controlled. The relationship between peak potential and scan rate for an

irreversible diffusion-controlled process is given by Eq. 5.1. The plot of E_p versus log υ (Fig. 5.12c) gave a linear relationship and the Tafel slope was 204 mV decade^{-1}. As stated above such large Tafel slopes have been associated with chemical reactions coupled to electrochemical steps [166] or to substrate–catalyst interactions in a reaction intermediate [167].

Using the slope of the plot of E_p versus log υ (Fig. 5.12c), the electron transfer coefficient (α) for hydrazine oxidation was found to be 0.71 indicating a high probability of the activated complex being converted to the product.

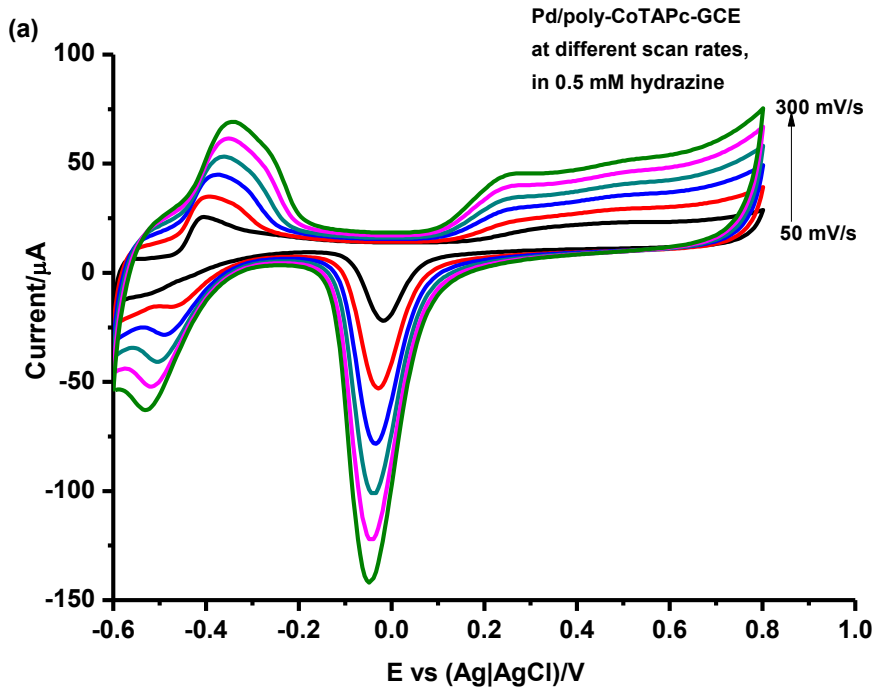
(a)
Pd/poly-CoTAPc-GCE
at different scan rates,
in 0.5 mM hydrazine
300 mV/s
50 mV/s
Current/µA
E vs (Ag|AgCl)/V

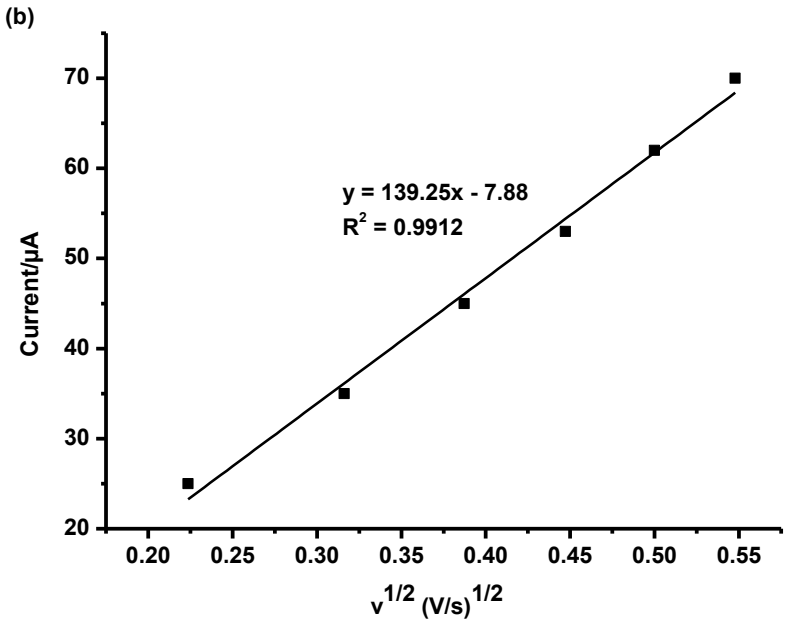
(b)
y = 139.25x - 7.88
R2 = 0.9912
Current/µA
v1/2 (V/s)1/2

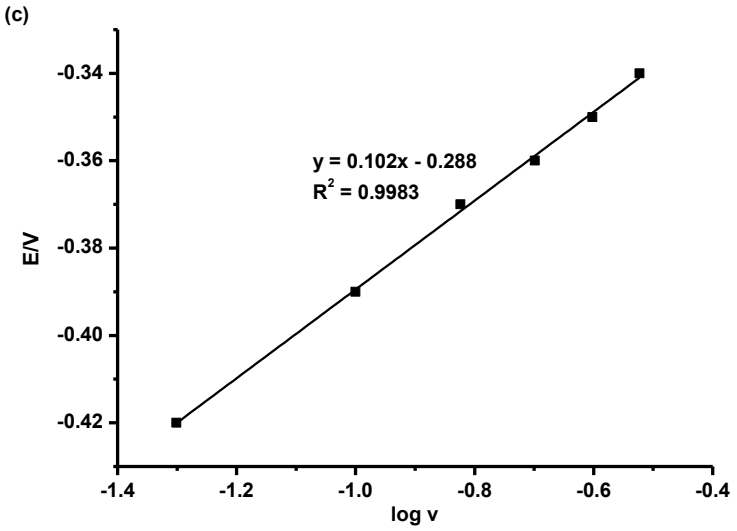

Fig. 5.12. Plots of (a) scan rate from 50 mV/s to 300 mV/s (b) peak current versus root of the scan rate and (c) peak potential versus log υ for 0.5 mM hydrazine (pH 8 buffer) detection on Pd/poly-CoTAPc-GCE.

5.3.1.3. Chronoamperometric studies

Chronoamperograms similar to those shown for nitrite Fig. 5.8 were obtained. A linear relationship was observed similar to eqs. 5.11 to 5.13 and represented by Eq. 5.20, for Pd/poly-CoTAPc-GCE.

$$y = 1926.1\,[hydrazine]\left(\frac{s^{-1}}{mM}\right) - 743.54\,s^{-1},\ R^2 = 0.9924 \qquad (5.20)$$

where the slope of this plot is equal to πk and the value of k was found to be 6.12 x 10^8 cm^3 mol^{-1} s^{-1}. The catalytic rate constant for poly-CoTAPc-GCE and Pd-GCE were found to be 5.54 x 10^8 cm^3 mol^{-1} s^{-1} and 2.86 x 10^8 cm^3 mol^{-1} s^{-1} respectively. This shows the superiority of the combining poly-CoTAPc and PdNPs. The catalytic rate constants obtained for hydrazine detection in literature are 4.7 x 10^7 cm^3 mol^{-1} s^{-1} and 4.1 x 10^7 cm^3 mol^{-1} s^{-1}

for gold nanoparticles-choline film and gold nanoparticles-polypyrrole nanowire respectively [178, 179], Table 5.2. The high catalytic rate constant for Pd/poly-CoTAPc-GCE shows the effectiveness of the electrocatalyst for the oxidation of hydrazine.

The detection limit (LoD) of 5.7 x 10^{-6} mol L^{-1} for poly-CoTAPc, 9.6 x 10^{-6} mol L^{-1} for Pd-GCE and 1.3 x 10^{-6} mol L^{-1} for Pd/poly-CoTAPc-GCE, using the 3δ/slope ratio notation (where δ is the standard deviation of the plot) were obtained. The values obtained for LoD are comparable to the ones obtained in literature as showed in Table 5.7, therefore they can serve as a good electrocatalysts for detecting hydrazine.

5.3.2. CoTAPc and bimetallic nanoparticles

5.3.2.1. Cyclic voltammetric detection of hydrazine

Fig. 5.13 shows the cyclic voltammograms of bare and modified GCE recorded in 1 mM hydrazine. Fig 5.13a shows that the bare GCE had a broad peak for hydrazine at 0.77 V. When the bare GCE is modified with Au and Au/poly-CoTAPc, Fig. 5.13a, the overpotential is lowered to 0.22 V and 0.11 V respectively. The influence of the poly-CoTAPc is very significant as a lower potential for hydrazine electrooxidation is obtained for Au/poly-CoTAPc compared to Au-GCE alone. Fig 5.13b shows the hydrazine peak at 0.05 V (Au/Pd-GCE), -0.19 V (Pd/Au-GCE) and -0.02 V (Au-Pd co-deposited-GCE). Fig 5.13c shows the behaviour of these electrodes in the presence of

the poly-CoTAPc. The poly-CoTAPc-GCE itself has a potential of 0.15 V. Upon adding the nanoparticles, there is a shift in peak potential for the electrooxidation of hydrazine to 0.04 V, -0.21 V and -0.12 V for Au/Pd-poly-CoTAPc-GCE, Pd/Au-poly-CoTAPc-GCE and Au-Pd (co-deposited)/poly-CoTAPc-GCE, respectively. There is significant improvement in the oxidation potential in the presence of poly-CoTAPc-GCE for Au-GCE, Pd-GCE and Au-Pd (co-deposited), showing that CoTAPc enhances the catalytic acitivity. In general when PdNPs are alone or electrodeposited on top of AuNPs, the oxidation of hydrazine occurs at a lower potential and as discussed above and shown in Table 5.6, these electrodes also have the largest surface coverage.

Using Au-Pd (co-deposited)/poly-CoTAPc-GCE as an example, the reaction occurs at the outer layer that is the Au-Pd surface. The role of poly-CoTAPc is to promote electron transfer between the reaction site and GCE. The mechanism for oxidation of hydrazine on Au-Pd (co-deposited)/poly-CoTAPc-GCE (Eqs 5.21 to 5.23) has been reported in literature [180].

$$N_2H_{4ad} + OH^- \rightarrow N_2H_{3ad} + H_2O + e^- \quad (5.21)$$

$$N_2H_{3ad} \rightarrow N_2 + 3H_{ad} \quad (5.22)$$

$$3H_{ad} + 3OH^- \rightarrow 3H_2O + 3e^- \quad (5.23)$$

The overall reaction for hydrazine is represented by Eq. 5.24 [181].

$$N_2H_4 + 4OH^- \rightarrow N_2 + 4H_2O + 4e^- \quad (5.24)$$

The mechanism of how the Au-Pd surface is not yet understood. However it is generally accepted that Au promotes the electrocatalytic activity, selectivity and stability of Pd [182].

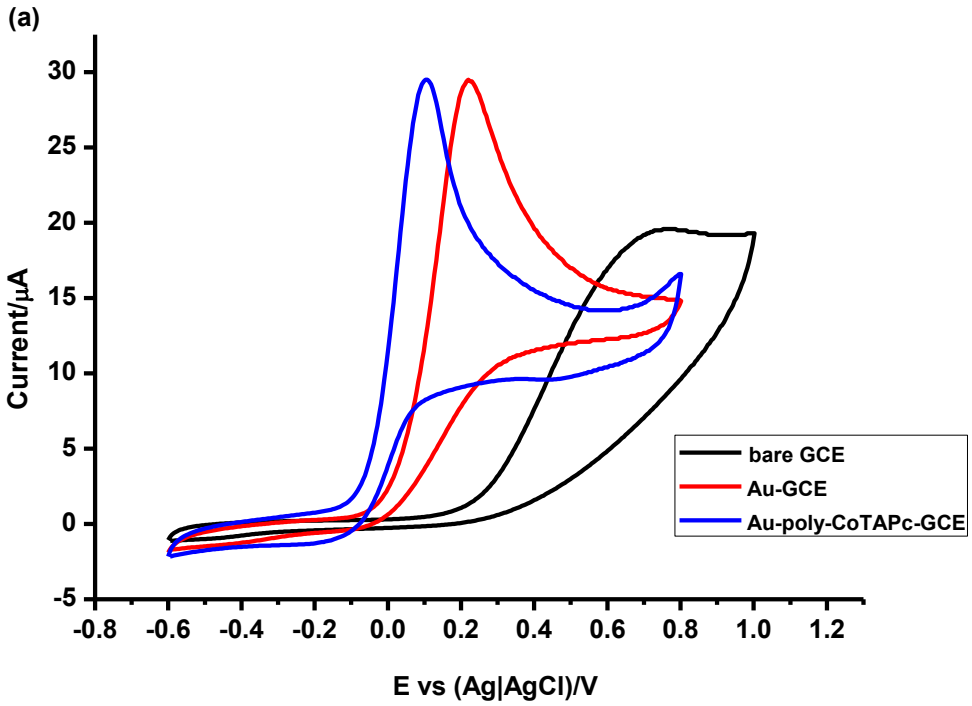
(a)
Current/μA
E vs (Ag|AgCl)/V
bare GCE
Au-GCE
Au-poly-CoTAPc-GCE

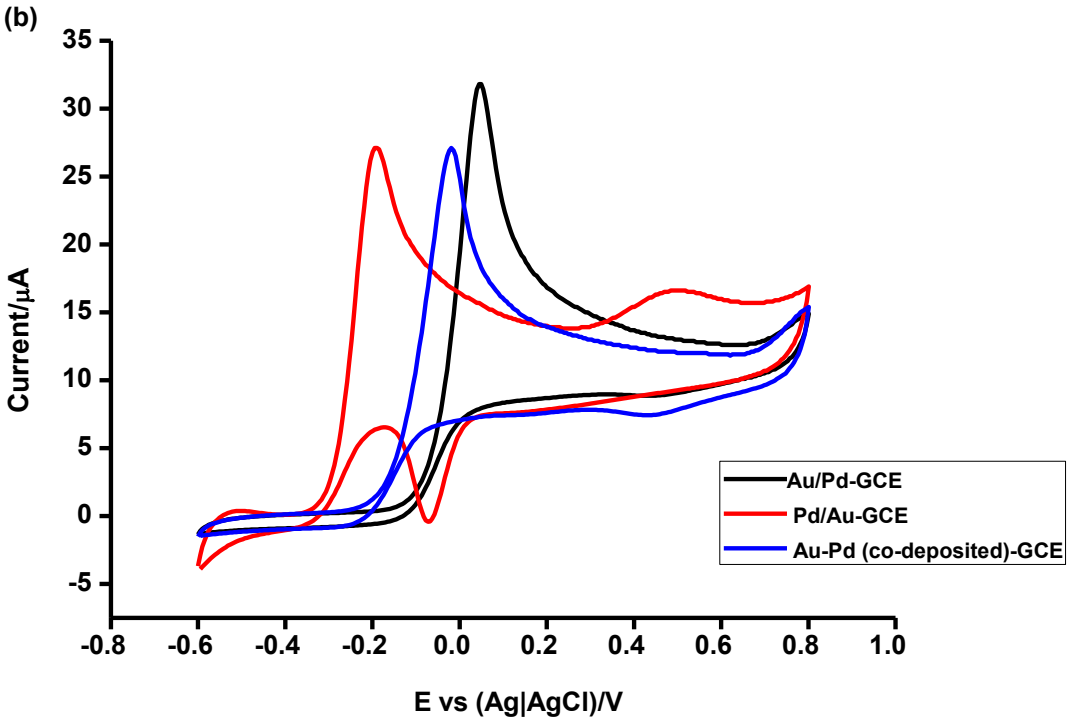
(b)
Current/μA
E vs (Ag|AgCl)/V
Au/Pd-GCE
Pd/Au-GCE
Au-Pd (co-deposited)-GCE

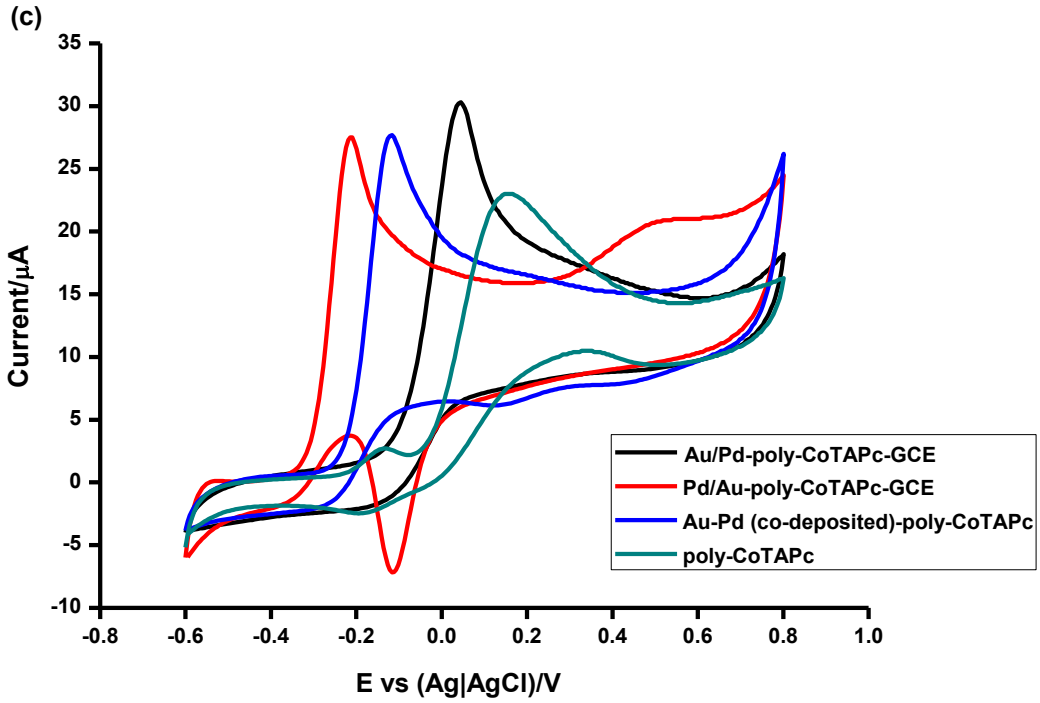

Fig. 5.13. Cyclic voltammograms of (a) bare GCE, Au-GCE and Au-poly-CoTAPc, (b) Au/Pd-GCE, Pd/Au-GCE and Au-Pd (co-deposited)-GCE and (c) Au/Pd-poly-CoTAPc-GCE, Pd/Au-poly-CoTAPc-GCE, Au-Pd (co-deposited)/poly-CoTAPc-GCE and poly-CoTAPc-GCE in 1 mM hydrazine dissolved in pH 8 buffer solution. Scan rate = 50 mV/s.

5.3.2.2. Electrochemical impedance spectroscopy (EIS)

The bare and the modified electrodes were examined by electrochemical impedance spectroscopy (EIS) in 1 mM hydrazine dissolved in pH 8 buffer. Fig. 5.14 shows the Nyquist plots for the various electrodes that were used in this study. The Randles equivalent circuit for this process is as described above. The R_{ct} values as determined by the diameter of the semi-circle are listed in Table 5.6. The bare electrode has the largest diameter of the semi-circle imply that there is high resistance to the flow of current for hydrazine

electrooxidation. The fact that Au-Pd (co-deposited)/poly-CoTAPc-GCE has a smallest diameter of the semi-circle than the rest of the electrodes shows that it offers limited resistance to charge transfer in the presence of hydrazine hence promoting very fast electron exchange rate. Thus even though this electrode did not give the lowest hydrazine oxidation potential, Table 5.6, it gives the best result for hydrazine electrooxidation in terms of low charge transfer resistance hence was employed for kinetic studies below. In general, there is a slight improvement in R_{ct} value in the presence of CoTAPc, with a few exceptions. The n-values are in the range 0.82 – 0.95 (n<1) confirming the non-ideal capacitative nature of the electrodes. Eq. 5.3 was used to calculate the apparent electron-transfer rate constant (k_{app}) and the results are shown in Table 5.6. The k_{app} also confirm that the transfer of electrons for hydrazine oxidation was fastest on Au-Pd (co-deposited)/poly-CoTAPc-GCE than the rest of electrodes, Table 5.6.

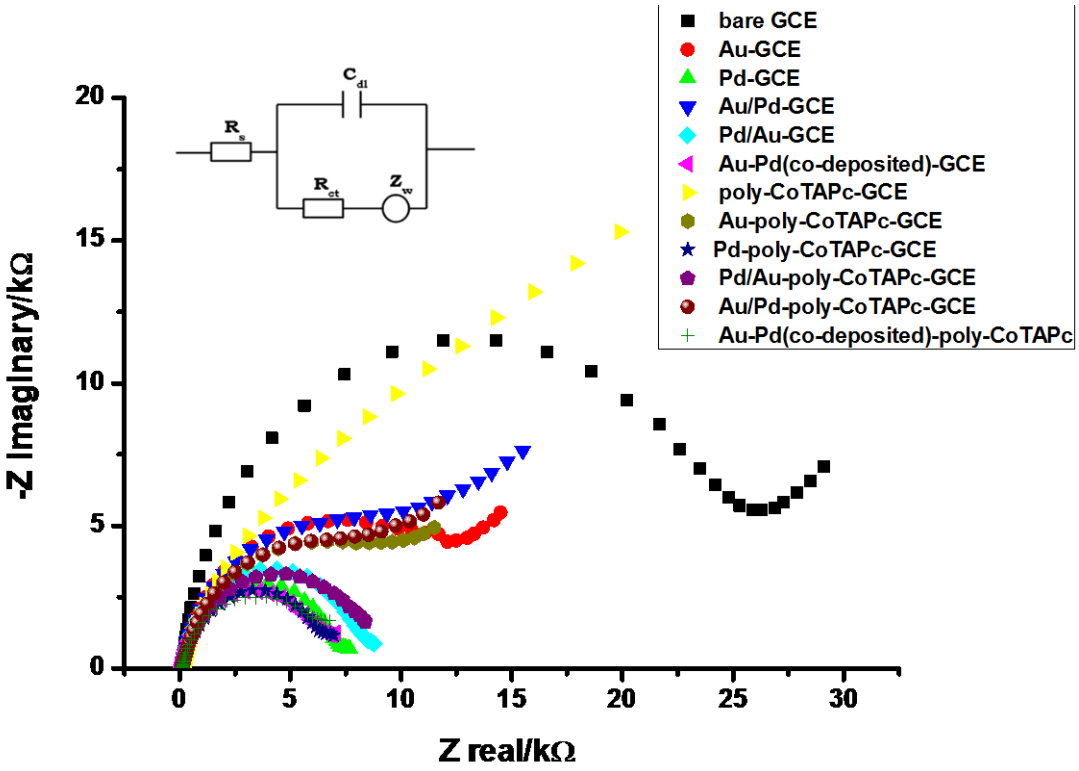

Fig. 5.14. Nyquist plots obtained for bare GCE and modified GCE in 1 mM hydrazine dissolved in pH 8 buffer solution. Inset: The Randles equivalent circuit employed.

5.3.2.3. Kinetic studies of hydrazine oxidation

Au-Pd (co-deposited)/poly-CoTAPc-GCE was employed in this section due to its superior electrocatalytic activity for hydrazine oxidation compared to the rest of the electrodes in terms of the R_{ct} and K_{app}. When the scan rate was increased from 50 mV/s to 300 mV/s, the hydrazine oxidation peak shifted towards positive potentials as shown in Fig 5.15a. This is an indication of irreversibility of the redox reaction. Fig. 5.15b and 5.15c shows linear plots of current versus root of scan rate and the plot of peak potential versus log scan rate for hydrazine electrooxidation, respectively. The plots in Fig.

5.15b confirm that the catalytic electrooxidation of hydrazine is diffusion controlled. The plot of E_p versus log υ (Fig. 5.15c) gave a linear relationship and the Tafel slope was 190 mV decade^{-1}. The Tafel slope is b = 0.059/(1−α)nα, (where α, the transfer coefficient; n, the number of electrons involved in the rate-determining), assuming the number of electrons is 1, and the transfer coefficient (α) is estimated to be 0.69.

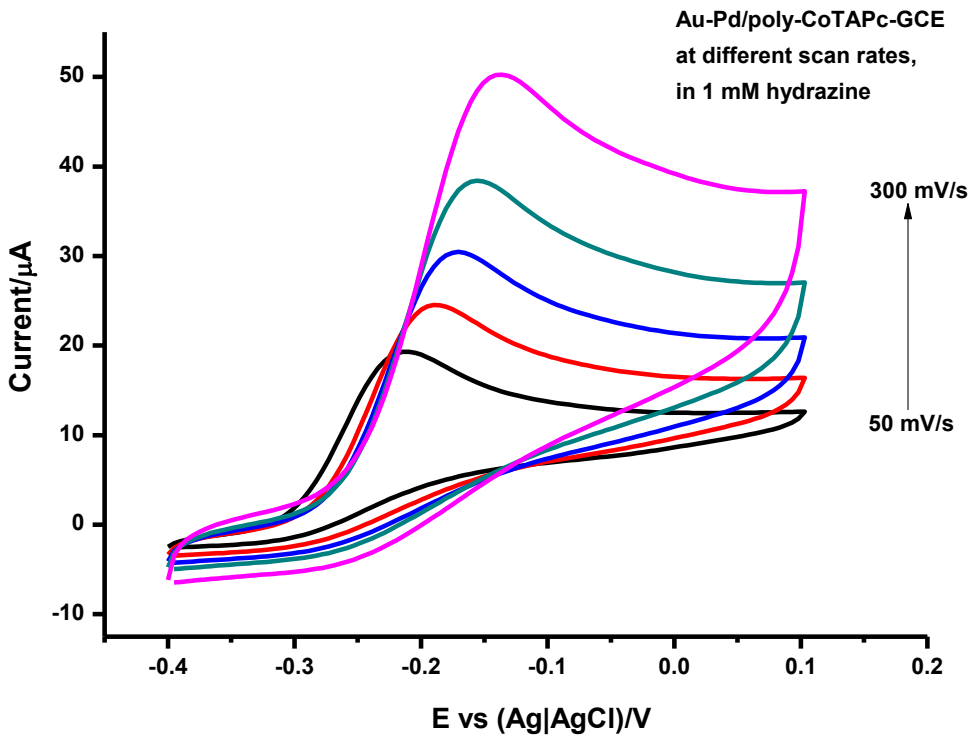
Au-Pd/poly-CoTAPc-GCE
at different scan rates,
in 1 mM hydrazine
300 mV/s
50 mV/s
Current/μA
E vs (Ag|AgCl)/V

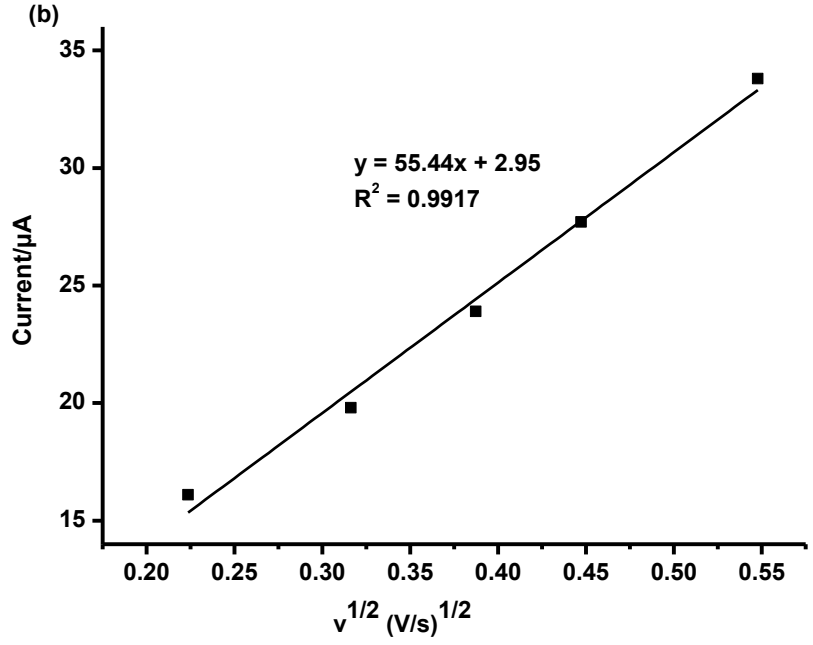
(b)
y = 55.44x + 2.95
R2 = 0.9917
Current/μA
v1/2 (V/s)1/2

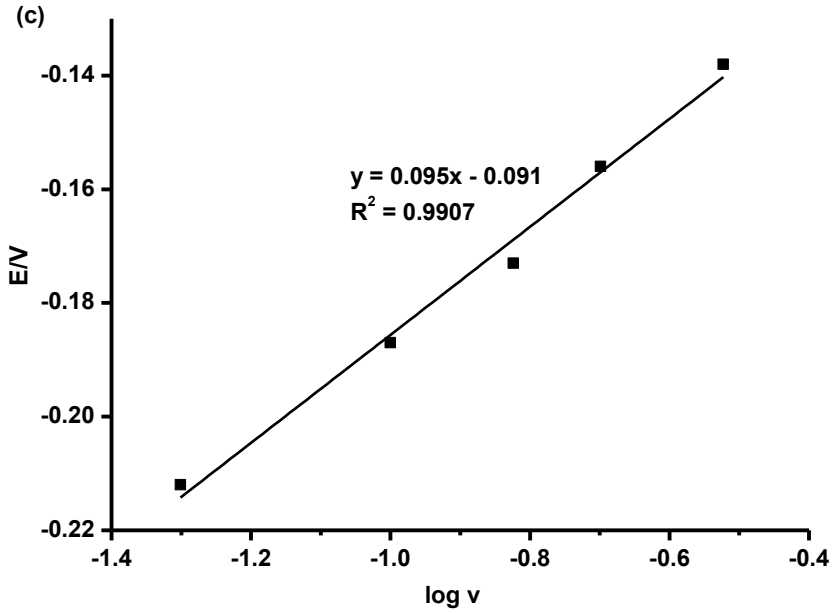

Fig. 5.15. Plots of (a) scan rate from 50 mV/s to 300 mV/s (b) peak current versus root of the scan rate and (c) peak potential versus log υ for 1 mM hydrazine (pH 8 buffer) detection on Au-Pd (co-deposited)/poly-CoTAPc-GCE.

5.3.2.4. Square wave voltammetry (SWV) detection of hydrazine

Fig. 5.16 shows square wave voltammograms of Au-Pd (co-deposited)/poly-CoTAPc-GCE in different concentrations of hydrazine. The current increased with the increase in concentration. The corresponding calibration curve is shown as an inset in Fig. 5.16. The plot is linear over the concentration range from 0.05 mM to 1 mM. Using the 3δ notation, the limit of detection LoD was estimated to be 0.5 μM for Au-Pd (co-deposited)/poly-CoTAPc-GCE and 0.7 μM for Au-Pd (co-deposited)-GCE. Table 5.8 shows a comparison of

LoD with those in literature [111, 176, 183, 184]. It shows most of the hydrazine studies were done in pH 7 and their systems are comparable to the studies done in pH 8. There is a marked improvement for bimetallic nanoparticles in terms of LoD compared to monometallic nanoparticles. The LoD for Au-Pd (co-deposited)/poly-CoTAPc-GCE was lower than PdNPs/ poly-CoTAPc-GCE (1.3 μM), Table 5.8.

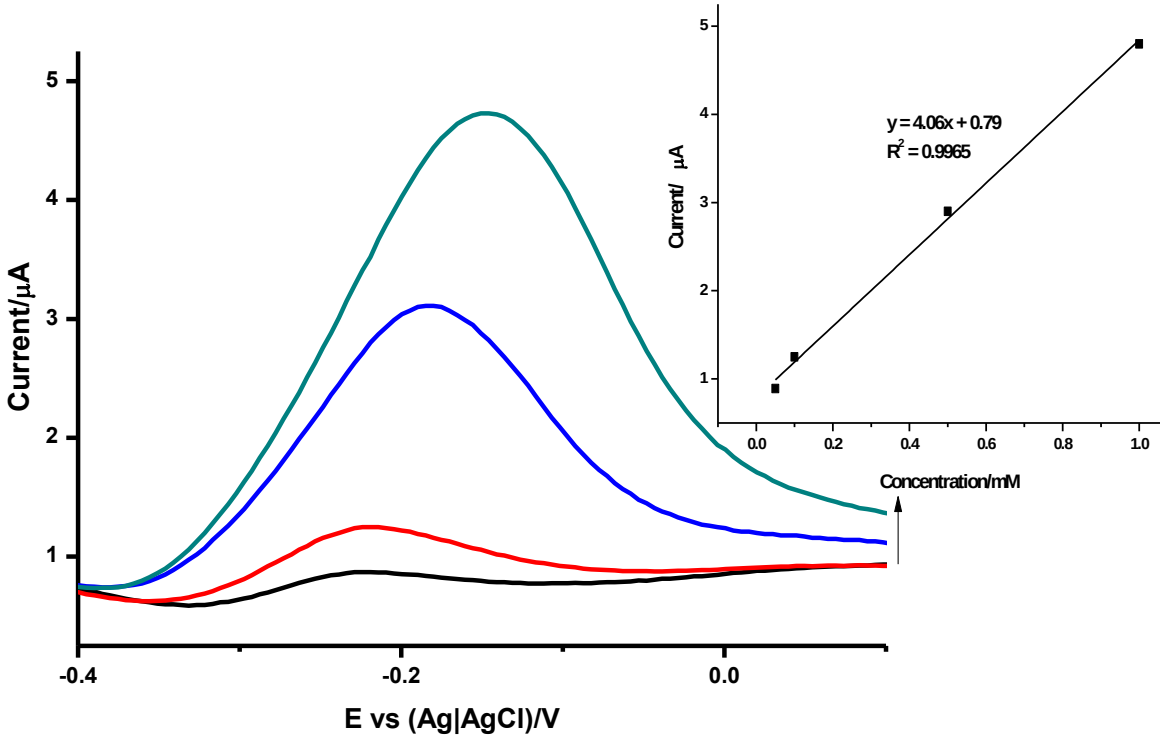

Fig. 5.16. Square wave voltammograms for (a) 0.05 mM, 0.1 mM, 0.5 mM and 1 mM hydrazine produced on polarized Au-Pd (co-deposited)/poly-CoTAPc-GCE. Inset: Corresponding calibration curve for hydrazine.

Table 5.8. Oxidation potentials and limits of detection for hydrazine on various electrodes.

Electrode	**Medium**	**E/V**	**LoD (μM)**	**Ref**
grafted GCE after click chemistry in ethynylpyridine and axial ligation with FePc	NaOH	-0.2	10	30
F-TiO_2NTs-Au@Pd	pH 7	0.02	0.012	82
Pd/CB/GCE	pH 9	-0.1	8.8	111
Pd/BDD	pH 7	0.16	2.6	176
Pd decorated bamboo MWCNTs	pH 7	0.04	10	183
PdHCFIAl	pH 7	0.95	4.6	184
Poly-CoTAPc-GCE	pH 8	0.14	9.6	This work
Pd-GCE	pH 8	-0.20	5.7	This work
Pd/Poly-CoTAPc-GCE	pH 8	-0.28	1.3	This work
Au-Pd (co-deposited)-GCE	pH 8	-0.02	0.7	This work
Au-Pd (co-deposited)/poly-CoTAPc-GCE	pH 8	-0.12	0.5	This work
GCE after step by step (electropolymerization followed by electro-click and immersion in FeTCPc)	pH 8	0.26	6.4	This work

GCE: glassy carbon electrode, BDD: boron doped diamond electrode, CB: carbon black, LoD: limit of detection, CPE: carbon paste electrode and PdHCFIAl: palladium hexacyanoferrate film-modified aluminium electrode.

5.3.3. FeTCPc

5.3.3.1. Cyclic voltammetric detection of hydrazine

Fig. 5.17 shows the cyclic voltammograms of bare and modified GCE recorded in 1 mM hydrazine in pH 8 buffer. Fig 5.17a shows that the bare GCE had a broad peak for hydrazine at 0.77 V, Table 5.6. When the bare GCE is modified by electropolymerization and electro-click, there was only a broad feature for hydrazine electrooxidation. This implies that the amines (from the polyaniline) are not responsible for the electrooxidation of hydrazine. When the bare GCE is modified by SEEC plus immersion in a solution of DMF containing FeTCPc, peaks were obtained in both the forward and reverse scans 0.30 V, Table 5.6. This behaviour is attributed to the regeneration of the species responsible for the electrooxidation of hydrazine [30]. The modified electrode after step by step (electropolymerization followed by electro-click) plus immersion in a solution of DMF containing FeTCPc shows an improvement in the peak potential. This is attributed to the fact the method does not have side products (like polymer from ethynylpyridine) which may affect the electrooxidation of hydrazine.

Ozoemena and Nyokong [114] have suggested the following mechanism for the oxidation of hydrazine on MPc modified electrodes (Eqs. 5.25-5.27).

$$Fe(II)Pc \rightarrow [Fe(III)Pc]^{+} + e^{-} \quad (5.25)$$

$$[Fe(III)Pc]^{+} + N_2H_4 \rightarrow [Fe(III)Pc.N_2H_4]^{+} \quad (5.26)\ (\text{rds})$$

$$[Fe(III)Pc.N_2H_4]^{+} + OH^{-} \rightarrow Fe(II)Pc + N_2H_3^{\cdot} + H_2O + e^{-} \quad (5.27)$$

However, Zagal and co-workers [185, 186] proposed that the electrooxidation of hydrazine proceeds via the M^{II}/M^{I} redox couple.

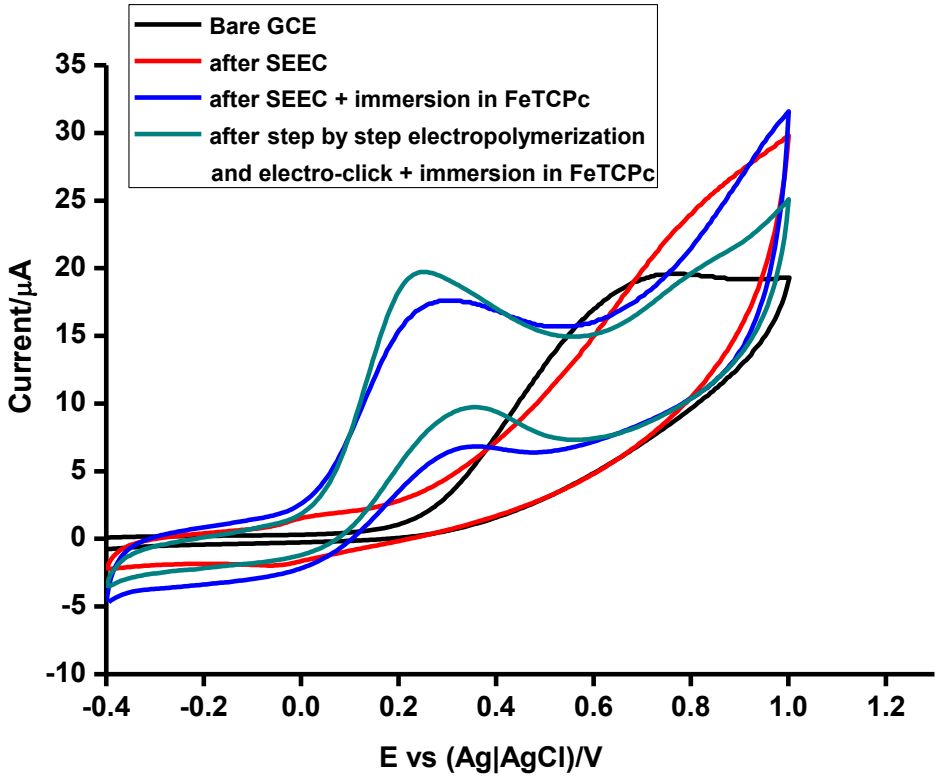

Fig. 5.17. Cyclic voltammograms of bare and modified GCE in 1 mM hydrazine dissolved in pH 8 buffer solution. Scan rate = 100 mV/s.

5.3.3.2. Electrochemical impedance spectroscopy (EIS)

The bare and the modified electrodes were examined by electrochemical impedance spectroscopy (EIS) in 1 mM hydrazine dissolved in pH 8 buffer. Fig. 5.18 shows the Nyquist plot for the various electrodes that were used in this study. The Randles equivalent circuit has been described above. The modified GCEs (after SEEC and after SEEC plus FeTCPc attachment) did

not have Warburg impedance. The modified electrode after step by step (electropolymerization followed by electro-click) plus immersion in a solution of DMF containing FeTCPc has Warburg impedance. This clearly shows that the method of modifying electrodes determines the effectiveness of the electrode in an electrocatalytic reaction. The R_{ct} values as determined by the diameter of the semi-circle are listed in Table 5.6. The bare electrode has the smallest diameter of the semi-circle implying that there is low resistance to the flow of current for hydrazine electrooxidation compared to the modified GCEs. For the modified electrodes, the step by step route had the lowest R_{ct} value signifying its superiority over the SEEC route. The n-values are in the range 0.91–0.95 (n<1) confirming the non-ideal capacitative nature of the electrodes. Eq. 5.3 was used to calculate the apparent electron-transfer rate constant (k_{app}) and the results are shown in Table 5.6. The k_{app} also confirm that the transfer of electrons for hydrazine oxidation was fastest on bare GCE than the rest of electrodes, Table 5.6. However, FeTCPc is catalytic in terms of potential towards electrooxidation of hydrazine. The step by step route gave the best k_{app} for the modified electrodes.

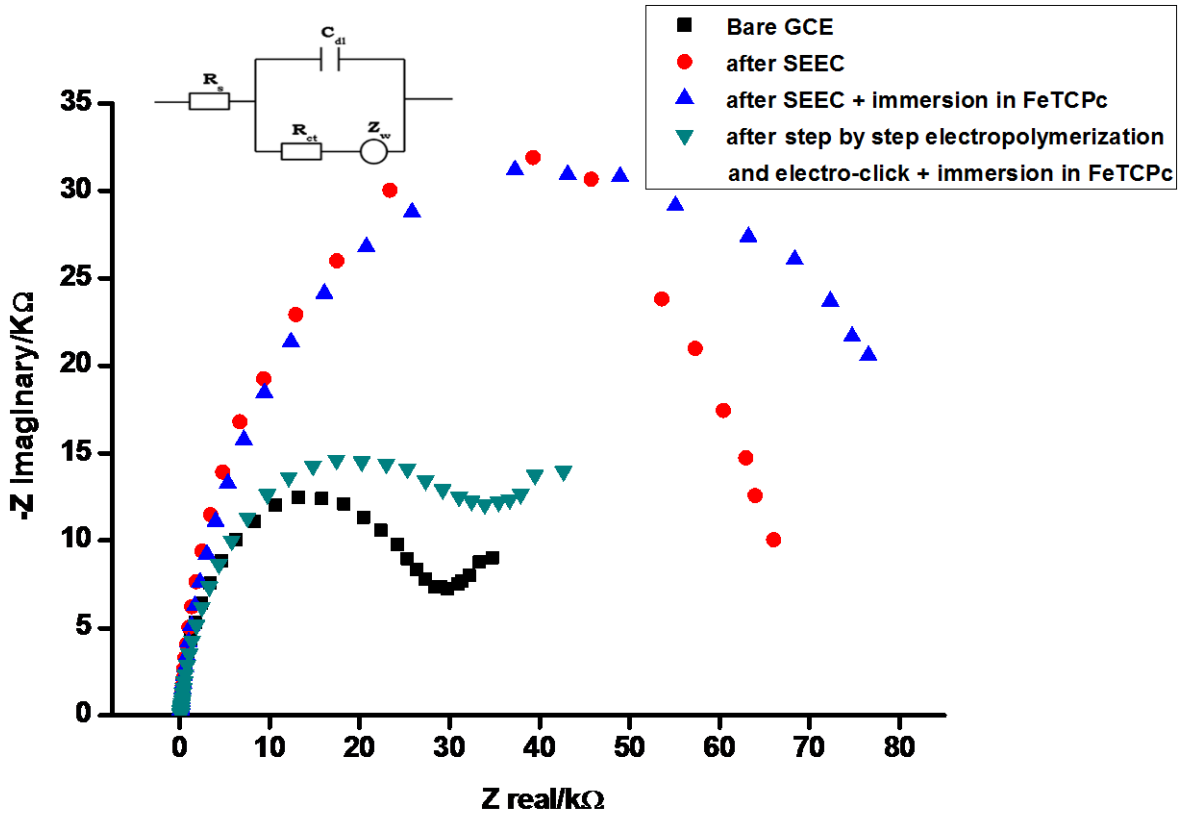

Fig. 5.18. Nyquist plots obtained for bare and modified GCE in 1 mM hydrazine dissolved in pH 8 buffer solution. Inset: The Randles equivalent circuit employed.

5.3.3.3. Chronoamperometric studies

Fig. 5.19a shows the chronoamperometric evolutions on polarized film formed after step by step (electropolymerization followed by electro-click) plus after immersion in a solution of DMF containing FeTCPc for pH 8 buffer (i) and hydrazine (in pH 8 buffer): (ii) 200 µM, (iii) 400 µM, (iv) 600 µM, (v) 800 µM, (vi) 1000 µM. The inset shows a linear relationship between current versus concentration and the slope of this plot represents the sensitivity of electrode towards the analyte. The detection limit (LoD) of 6.4 x 10^{-6} mol L^{-1}, using the 3δ/slope ratio notation (where δ is the standard deviation of the plot) was obtained. The value obtained for LoD is an improvement compared to when unsubstituted FePc was employed (using an electrode modified by grafting following click chemistry) at 10.0 µM [30] but poor compared to CoTAPc or PdNPs or CoTAPc + PdNPs, Table 5.7. Fig. 5.19b shows the plots of (I_{cat}/I_{buf}) versus $t^{1/2}$ (eq. 5.4) for hydrazine electrooxidation. The catalytic current (I_{cat}) is dominated by the rate at which hydrazine is oxidized on modified-GCE. The slopes of the plot of (I_{cat}/I_{buf}) versus $t^{1/2}$ were used to calculate the rate constant according to Eq. 5.4, in a similar manner as described above.

A linear relationships was observed and represented by Eq. 5.28.

$$y = 6624.9\,[hydrazine]\left(\frac{s^{-1}}{mM}\right) - 1992.1\,s^{-1},\ R^2 = 0.9915 \qquad (5.28)$$

where the slope of this plot is equal to πk and the value of k was found to be 2.1 x 10^9 cm^3 mol^{-1} s^{-1}, Table 5.2. The catalytic rate constants obtained for hydrazine detection in literature are 4.7 x 10^7 cm^3 mol^{-1} s^{-1} and 4.1 x 10^7

cm^3 mol^{-1} s^{-1} for gold nanoparticles-choline film and gold nanoparticles-polypyrrole nanowire, respectively [178, 179], Table 5.2. The high catalytic rate constant for step by step (electropolymerization followed by electro-click and immersion in FeTCPc) shows the effectiveness of the electrocatalyst for the electrooxidation of hydrazine.

In conclusion, based on the CVs, Pd/poly-CoTAPc was the best electrode for the detection of hydrazine with detection potential of -0.28 V, Table 5.6. This could be explained by the fact that Pd/poly-CoTAPc had the highest surface coverage. Analysis on the EIS data indicates that Au-Pd/poly-CoTAPc was the best electrode with the highest K_{app}, Table 5.6. Au-Pd/poly-CoTAPc also had the least LoD (0.5 μM, Table 5.8) for the detection of hydrazine. GCE modified by step by step (electropolymerization followed by electro-click) plus after immersion in a solution of DMF containing FeTCPc behaved much better in terms of the rate constant hence it is a superior method of electrode modification.

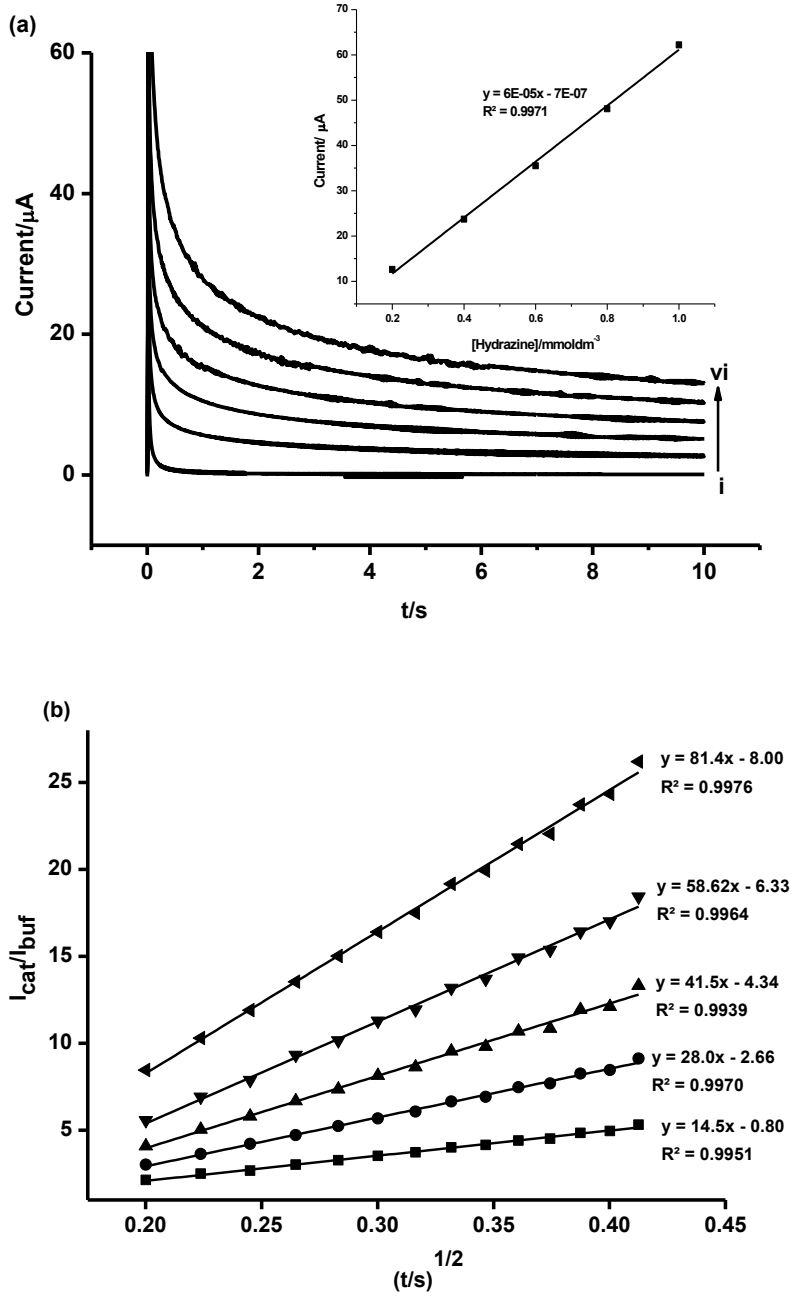

Fig. 5.19. Chronoamperograms (a) for (i) pH 8 buffer, (ii) 200, (iii) 400, (iv) 600, (v) 800, (vi) 1000 µM hydrazine produced on polarized modified electrode (GCE after electropolymerization and electro-click + immersion in FeTCPc). Inset: current-concentration plot for hydrazine. (b) Plots of (I_{cat}/I_{buf}) versus $t^{1/2}$ from (a).

CHAPTER 6

GENERAL CONCLUSIONS

6.1 General conclusions

The synthesis of metallophthalocyanines (NiPc, NiTSPc, CoTAPc and FeTCPc) and metal nanoparticles (NiNPs, AuNPs, PdNPs and bimetallic of Au and Pd) were successful. Microscopic, spectroscopic and electrochemical techniques were used to characterize the synthesized materials. These materials were used to modify the glass carbon substrates.

Various methods were used to modify the electrodes namely, adsorption, electropolymerization, electrodeposition, electrografting and click chemistry. Both NiPc and NiNPs were successfully deposited on the electrode surface and the results showed that the NiNPs exhibited better electrocatalytic activity for the electrooxidation of amitrole. The mixture of NiPc and NiNPs was the least as far as the electrooxidation of amitrole. Due to the shortcoming of adsorption, other methods were used to modify the electrodes.

Eletrodeposition and electropolymerization were employed to modify electrodes with metal nanoparticles and MPcs, respectively. This was the first time in which the combination was used. The results for AuNPs and NiTSPc showed that when AuNPs was deposited first on the electrode followed by attachment of NiTSPc through electropolymerization, there was higher electrocatalytic activity compared to individual AuNPs and NiTSPc.

The test analyte was nitrite in pH 8 buffer solution. However the results for AuNPs and CoTAPc showed that when CoTAPc was attached first followed by deposition of AuNPs, higher electrocatalytic performances were observed compared to the individual AuNPs and CoTAPc.

Having established that CoTAPc attachment first was the best, AuNPs, PdNPs, Au-Pd were deposited on top of the CoTAPc layer for the electrooxidation of hydrazine. Again the electrocatalytic activity of the combination of CoTAPc and metal nanoparticles was enhanced. The improvement in the electrocatalytic activities is attributed to synergistic effect. Metal nanoparticles providing a fast transfer of electrons and the MPc, offering accessibility of a wide range of oxidation states on the Pc ring and on the central metal.

This work shows the use of electropolymerization and electro-click chemistry for the modification of the electrode. This was followed by axial ligation of FeTCPc. This was the first time a tetrasubstituted MPc had been used. The electrode modification was monitored by XPS. XPS indicated that the azide bond at 404 eV (from azidoaniline) had disappeared following electro-click chemistry and also the appearance of Fe suggesting the success of axial ligation. We have proved that the electrodes modified step by step (electropolymerization followed by electro-click and immersion in FeTCPc)

was the better than the one after SEEC + immersion in FeTCPc for the electrooxidation of hydrazine.

Finally this work reports for the first time the micropatterning of the glassy carbon substrate, using the SECM tip. The glassy carbon substrate was electrografted with 4-azidobenzenediazonium salt. The SECM tip was positioned ≈10 μm above the surface of the azido-modified substrate, and Cu^{+} ions were produced at the tip. This was aimed at locally triggering the CuAAC reaction between azido moieties on the surface and ethynylferrocene in solution. The evidence of micropatterning was shown using the SECM images. The SECM images clearly show that the position where the localized electro-click reaction occurred had high currents as ferrocene moieties have good redox properties.

References

1. A. Braun, J. Tscherniac, Ber. Deut. Chem. Ges. 40 (1907) 2709-2714.
2. A. Dandridge, H. Drescher, J. Thomas, British Patent, 1927, 169.
3. R. Linstead, A. Lowe, J. Chem. Soc. (1934) 1017-1022.
4. P. Gregory, J. Porphyrins Phthalocyanines 4 (2000) 432–437.
5. K. Law, Chem. Rev. 93 (1993) 449-486.
6. J. Obirai, T. Nyokong, Electrochim. Acta 50 (2005) 3296-3304.
7. N. McKeown, J. Mater. Chem. 10 (2000) 1979-1995.
8. H. Uchida, P. Reddy, S. Nakamura, T. Toru, J. Org. Chem. 68 (2003) 8736-8738.
9. M. Hanack, J. Mertz, G. Pawlowski, Chem. Ber. 115 (1982) 2836-2853.
10. M. Somashekarappa, J. Keshavayya, S. Sampath, Pure Appl. Chem. 74 (2002) 1609-1620.
11. X. Song, Y. She, H. Ji, Y. Zhang, Organic Process Research & Development 9 (2005) 297-301.
12. P. Kissinger, W. Heineman, Laboratory Techniques in Electroanalytical Chemistry, Second Edition, Marcel Dekker, New York, 1996.
13. A. Malinauskas, Synthetic Metals 107 (1999) 75–83.

14. M. Situmorang, J. Gooding, D. Hibbert, Anal. Chim. Acta 394 (1999) 211-223.

15. V. Chauke, W. Chidawanyika, T. Nyokong, Electroanal. 23 (2011) 487-496.

16. V. Chauke, E. Antunes, T. Nyokong, J. Electroanal. Chem. 661 (2011) 1–7.

17. J. Leger, M. Berggren, S. Carter, Iontronics: Ionic Carriers in Organic Electronic Materials and Devices, CRC Press, Boca Raton, 2011.

18. K. Brown, H. Mottola, Langmuir 14 (1998) 3411-3417.

19. R. Durst, A. Bäumner, R. Murray, R. Buck, C. Andrieux, Pure Appl. Chem. 69 (1997) 1317-1323.

20. P. Mashazi, C. Togo, J. Limson, T. Nyokong, J. Porphyrins Phthalocyanines 14 (2010) 252-263.

21. S. Khene, K. Lobb, T. Nyokong, Electrochim. Acta 56 (2010) 706-716.

22. D. Belanger, J. Pinson, Chem. Soc. Rev. 40 (2011) 3995–4048.

23. S. Palacin, C. Bureau, J. Charlier, G. Deniau, B. Mouanda, P. Viel, Chem. Phys. Chem 5 (2004) 1468-1481.

24. F. Matemadombo, P. Westbroek, T. Nyokong, Electrochim. Acta 53 (2007) 480-486.

25. W. Zhao, B. Tong, Y. Pan, J. Shen, J. Zhi, J. Shi, Y. Dong, Langmuir 25 (2009) 11796-11801.

26. A. Gutierrez, S. Griveau, C. Richard, A. Pailleret, S. Granados, F. Bedioui, Electroanal. 21 (2009) 2303-2310.

27. P. Mashazi, N. Nombona, M. Muchindu, S. Vilakazi, J. Porphyrins Phthalocyanines 16 (2012) 742-753.

28. P. Mashazi, T. Mugadza, N. Sosibo, P. Mdlulia, S. Vilakazia, T. Nyokong, Talanta 85 (2011) 2202-2211.

29. M. Coates, T. Nyokong, Electrochim. Acta 91 (2013) 158-165.

30. M. Coates, T. Nyokong, J. Electroanal. Chem. 687 (2012) 111-116.

31. Y. Ipek, H. Dincer, A. Koca, Sensors and Actuators B 193 (2014) 830-837.

32. T. Menanteau, E. Levillain, T. Breton, Chem. Mater. 25 (2013) 2905-2909.

33. H. Kolb, M. Finn, K. Sharpless, Angew. Chem. Int. Ed. 40 (2001) 2004-2021.

34. R. Huisgen, Angew. Chem. 75 (1963) 604-637.

35. V. Rostovtsev, L. Green, V. Fokin, K. Sharpless, Angew. Chem. 114 (2002) 2708-2711.

36. A. Hayat, J. Marty, A. Radi, Electroanal. 24 (2012) 1446-1452.

37. H. Qi, M. Li, R. Zhang, M. Dong, C Ling, Anal. Chim. Acta 792 (2013) 28-34.

38. I. Choi, Y. Chi, Angew. Chem. Int. Ed. 45 (2006) 4894-4897.

39. G. Rydzek, J. Thomann, N. Ameur, L. Jierry, P. Mesini, A. Ponche, C. Contal, A. Haitami, J. Voegel, B. Senger, P. Schaaf, B. Frisch, F. Boulmedais, Langmuir 26 (2010) 2816-2824.

40. S. Dong, Z. Jin, Electrochim. Acta 34 (1989) 963-968.

41. J. Gooding, V. Praig, E. Hall, Anal. Chem. 70 (1998) 2396-2404.

42. A. Bard, L. Faulkner, Electrochemical Methods, John Wiley and Sons, New York, 2006.

43. B. Park, D. Yoon, D. Kim, J. Electroanal. Chem. 661 (2011) 329-335.

44. V. Lvovich, Impedance Spectroscopy: Applications to Electrochemical and Dielectric Phenomena, Wiley, New Jersey, 2012.

45. P. Gomadam, J. Weidner, Int. J. Energy Res. 29 (2005)1133-1151.

46. S. Ku, K. Wong, A. Bard, J. AM. Chem. Soc. 130 (2008) 2392-2393.

47. G. Sciutto, S. Prati, R. Mazzeo, M. Zangheri, A. Roda, L. Bardini, G. Valenti, S. Rapino, M. Marcaccio, Anal. Chim. Acta 831 (2014) 31–37.

48. A. Bard, M. Mirkin, Scanning Electrochemical Microscopy, 2nd edn, CRC Press, New York, 2012.

49. M. Coates, E. Cabet, S. Griveau, T. Nyokong, F. Bedioui, Electrochem. Commun. 13 (2011) 150-153.

50. S. Reed, Scanning Microprobe Analysis and Scanning Electron Microscopy, 2nd edn, Cambridge, New York, 2005.

51. A. Bogner, P. Jouneau, G. Thollet, D. Basset, C. Gauthier, Micron 38 (2007) 390-401.

52. T. Hezard, K. Fajerwerg, D. Evrard, V. Collière, P. Behra, P. Gros, J. Electroanal. Chem. 664 (2012) 46-52.

53. C. Wagner, W. Riggs, L. Davis, J. Moulder, Handbook of X-ray Photoelectron Spectroscopy, Perking-Elmer Corporation, Physical Electronics Division, USA, 1979.

54. J. Shwarz, C. Contescu, K. Putyera, Encyclopedia of Nanoscience and Nanotechnology, 2nd edn, Marcel-Dekker, New York, 2004.

55. R. White, R. Luque, V. Budarin, J. Clark, D. Macquarrie, Chem. Soc. Rev., 38 (2009) 481-494.

56. G. Schmid, D. Fenske, Phil. Trans. R. Soc. A 368 (2010) 1207-1210.

57. S. Senkan, M. Kahn, S. Duan, A. Ly, C. Ledholm, Catal. Today 117 (2006) 291-296.

58. H. Choi, S. Al-Abed, S. Agarwal, D. Dionysiou, Chem. Mater. 20 (2008) 3649-3655.

59. Y. Ma, J. Di, X. Yan, M. Zhao, Z. Lu, Y. Tu, Biosensors and Bioelectronics 24 (2009) 1480-1483.

60. C. Yen, K. Shimizu, Y. Lin, F. Bailey, I. Cheng, C. Wai, Energy & Fuels 21 (2007) 2268-2271.

61. R. Ferrando, J. Jellinek, R. Johnston, Chem. Rev. 108 (2008) 845-910.

62. P. Mashazi, P. Westbroek, K. Ozoemena, T. Nyokong, Electrochim. Acta 53 (2007) 1858-1869.

63. X. Qi, R. Baldwin, Electroanal. 5 (1993) 547-554.

64. L. Bai, F. Yuan, Q. Tang, Mater. Lett. 62 (2008) 2267-2270.

65. R. Alkasir, M. Ganesana, Y. Won, L. Stanciu, S. Andreescu, Biosensors and Bioelectronics 26 (2010) 43–49.

66. N. Stradiotto, K. Toghill, L. Xiao, A. Moshar, R. Compton, Electroanal. 21 (2009) 2627-2633.

67. L. Garcıa-Cruz, A. Saez, C. Ania, J. Solla-Gullon, T. Thiemann, J. Iniesta, V. Montiel, Carbon 73 (2014) 291-302.

68. M. Lyons, M. Brandon, Int. J. Electrochem. Sci. 3 (2008) 1386-1424.

69. A. Yagati, T. Lee, J. Min, J. Choi, Colloids and Surfaces B: Biointerfaces 92 (2012) 161-167.

70. S. Hebié, K. Kokoh, K. Servat, T. Napporn, Gold Bull. 46 (2013) 311-318.

71. J. Hernandez, J. Solla-Gullon, E. Herrero, A. Aldaz, J. Feliu, Electrochim. Acta 52 (2006) 1662-1669.

72. M. Etesami, F. Karoonian, N. Mohamed, J. Chinese Chem. Soc. 58 (2011) 688-693.

73. K. Kokoh, J. Leger, B. Beden, C. Lamy, Electrochim. Acta. 37 (1992) 1333-1342.

74. Q. Wang, Y. Wang, P. Guo, Q. Li, R. Ding, B. Wang, H. Li, J. Liu, X. Zhao, Langmuir 30 (2014) 440-446.

75. C. Bianchini, P. Shen, Chem. Rev. 109 (2009) 4183-4206.

76. S. Kim, Y. Jeong, M. Ahmed, J. You, H. Choi, S. Jeon, Sensors Actuators B, 153 (2011) 246-251.

77. M. Grden, M. Łukaszewski, G. Jerkiewicz, A. Czerwinski, Electrochim. Acta 53 (2008) 7583-7598.

78. C. Yen, K. Shimizu, Y. Lin, F. Bailey, I. Cheng, C. Wai, Energy & Fuels 21 (2007) 2268-2271.

79. A. Geraldes, D. da Silva, E. Pino, J. da Silva, R. de Souza, P. Hammer, E. Spinacé, A. Neto, M. Linardi, M. dos Santos, Electrochim. Acta 111 (2013) 455-465.

80. M. Ahn, J. Kim, J. Phys. Chem. C 117 (2013) 24438-24445.

81. G. Zhang, Y. Kuang, J. Liu, Y. Cui, J. Chen, H. Zhou, Electrochem. Commun. 12 (2010) 1233-1236.

82. X. Chen, W. Liu, L. Tang, J. Wang, H. Pan, M. Du, Materials Science and Engineering C 34 (2014) 304-310.

83. X. Wang, B. Tang, X. Huang, Y. Ma, Z. Zhang, J. Alloys and Compounds 565 (2013) 120-126.

84. X. Sun, F. Li, G. Shen, J. Huang, X. Wang, Analyst, 139 (2014) 299-308.

85. W. Alencar, F. Crespilho, M. Martins, V. Zucolotto, O. Oliveira, W. Silva, Phys. Chem. Chem. Phys. 11 (2009) 5086-5091.

86. J. Ahmed, Y. Yuan, L. Zhou, S. Kim, J. Power Sources 208 (2012) 170-175.

87. M. Pal, V. Ganesan, J. Electroanal. Chem. 672 (2012) 7–11.

88. J. Zeng, S. Sun, J. Zhong, X. Li, R. Wang, L. Wu, L. Wang, Y. Fan, Inte. J. Hydrogen Energy xxx (2014) 1-9.

89. A. Jeevagan, S. John, RSC Adv. 3 (2013) 2256-2264.

90. A. Jeevagan, M. Raj, S. John, RSC Adv. 3 (2013) 870-878.

91. K. Lokesh, Y. Shivaraj, B. Dayananda, S. Chandra, Bioelectrochem. 75 (2009) 104-109.

92. J. Guo, H. Li, H. He, D. Chu, R. Chen, J. Phys. Chem. C 115 (2011) 8494-8502.

93. J. Zhong, Y. Fan, H. Wang, R. Wang, L. Fan, X. Shen, Z. Shi, Electrochim. Acta 113 (2013) 653-660.

94. L. Sannegowda, K. Reddy, K. Shivaprasad, RSC Adv. 4 (2014) 11367–11374.

95. J. Zhong, Y. Fan, H. Wang, R. Wang, L. Fan, X. Shen, Z. Shi, J. Power Sources 242 (2013) 208-215.

96. K. Kaneko, K. Furuya, A. Hungria, J. Hernandez-Garrido, P. Midgley, T. Onodera, H. Kasai, Y. Yaguchi, H. Oikawa, Y. Nomura, H. Harada, T. Ishihara, N. Baba, J. Electron Microscopy 58 (2009) 289-294.

97. M. Pal, V. Ganesan, Langmuir 25 (2009) 13264-13272.

98. J. Wang, Analytical Electrochem. 2nd edn, Wile-VCH, New York, 2001.

99. F. Campbell, R. Compton, Anal. Bioanal. Chem. 396 (2010) 241-259.

100. Fontecha-Cámara, M. Álvarez-Merino, F. Carrasco-Marín, M. López-Ramón, C. Moreno-Castilla, Appl. Catal. B: Environmental 101 (2011) 425-430.

101. USA EPA, Washington D.C. 20460, Office of prevention, pesticides and toxic substances, amitrole reregistration, 1996.

102. M. Siswana, K. I. Ozoemena, T. Nyokong, Sensors 8 (2008) 5096-5105.

103. M. Hayyan, S. Sameh, A. Hayyan, I. AlNashef, Int. J. Electrochem. Sci. 7 (2012) 6941-6950.

104. E. Tosi, E. Re, M. Ortega, A. Cazzoli, Food Chemistry 104 (2007) 1025-1029.

105. Y. Huang, J. Ji, Q. Hou, Mutation Research 358 (1996) 7-14.

106. S. Mirvish Cancer Lett. 93 (1995) 17-48.

107. Y. Cui, C. Yang, W. Zeng, M. Oyama, W. Pu, J. Zhang, Analytical Sciences 23 (2007) 1421-1425.

108. B. Agboola, K. Ozoemena, T. Nyokong, Electrochim. Acta 51 (2006) 6470-6478.

109. U.S. Environmental Protection Agency. Health and Environmental Effects Profile for Hydrazine and Hydrazine Sulfate. Environmental Criteria and Assessment Office, Office of Health and Environmental Assessment, Office of Research and Development, Cincinnati, OH. 1984.

110. S. Golabi, H. Zare, J. Electroanal. Chem. 465 (1999) 168-176.

111. J. Panchompoo, L. Aldous, C. Downing, A. Crossley, R. Compton, Electroanal. 23 (2011) 1568-1578.

112. B. Haghighi, H. Hamidi, S. Bozorgzadeh, Anal. Bioanal. Chem. 398 (2010) 1411-1416.

113. C. Batchelor-McAuley, C. Banks, A. Simm, T. Jones, R. Compton, Analyst, 131 (2006) 106-110.

114. K. Ozoemena, T. Nyokong, Talanta, 67 (2005) 162-168.

115. V. Mani, A. Vilian, S. Chen, Int. J. Electrochem. Sci., 7 (2012) 12774-12785.

116. W. Siangproh, O. Chailapakul, R. Laocharoensuk, J. Wang, Talanta, 67 (2005) 903-907.

117. J. Chaves, A. Tanaka, J. Brazil Chem. Soc. 1 (2007) 35-40.

118. P. Borker, A. Salker, Indian J. Chem. Technol. 13 (2006) 341–346.

119. G. Couto, J. Klein, W. Schreiner, D. Mosca, A. de Oliveira, A. Zarbin, J. Colloid Interf. Sci. 311 (2007) 461-468.

120. D. Evrard, F. Lambert, C. Policar, V. Balland, B. Limoges, Chem. Eur. J. 14 (2008) 9286- 9291.

121. S. Maree, T. Nyokong, J. Electroanal. Chem. 492 (2000) 120-127.

122. Y. Tse, P. Janda, H. Lam, J. J. Zhang, W. J. Pietro, A.B.P. Lever, J. Porphyrins Phthalocyanines, 1 (1997) 3-16.

123. S. Griveau, V. Albin, T. Pauporté, J. Zagal, F. Bedioui, J. Mat. Chem. 12 (2002) 225-332.

124. C. Berrios, J. Marco, C. Gutierrez, M. Ureta-Zanartu, Electrochim. Acta. 54 (2009) 6417-6425.

125. T. Soreta, J. Strutwolf, C. O_Sullivan, Langmuir 23 (2007) 10823-10830.

126. G. Rydzek, T. Terentyeva, A. Pakdel, D. Golberg, J. Hill, K. Ariga, ACS Nano, 8 (2014) 5240-5248.

127. Y. Gok, H. Kantekin, M. Kılıcaslan, H. Alp, Dyes Pigments 74 (2007) 692-698.

128. M. Ureta-Zanartu, C. Berrıos, J. Pavez, J. Zagal, C. Gutierrez, J. Marco, J. Electroanal. Chem. 553 (2003) 147-156.

129. M. Stillman, T. Nyokong, C. Leznoff (eds), Phthalocyanines: properties and applications, VCH, New York, 1989.

130. H. Zhang, Y. Wang, Z. Fei, L. Wu, Q. Zhou, Dyes Pigments 78 (2008) 239-247.

131. D. Li, S. Komarneni, J. Am. Ceram. Soc. 89 (2006) 1510–1517.

132. Z. Libor, Q. Zhang, Mater. Chem. Phys. 114 (2009) 902-907.

133. M. Singh, M. Kumar, F. Štepanek, P. Ulbrich, P. Svoboda, E. Santava, M. Singla, Adv, Mat. Lett. 6 (2011) 409–414.

134. H. Wang, X. Kou, J. Zhang, J. Li, Bull. Mater. Sci. 31 (2008) 97-100.

135. H. Kavas, N. Kasapoğlu, A. Baykal, Y. Köseoğlu Chem. Papers 63 (2009) 450–455.

136. P. Voltairas, D. Fotiadis, C. Massalas, J. Magn. Magn. Mater. 217 (2000) L1-L4.

137. X. Wu, W. Xing, L. Zhang, S. Zhuo, J. Zhou, G. Wang, S. Qiao, Powder Techn. 224 (2012) 162–167.

138. M. Jayalakshmi, M. Mohan Rao, K. Kim, Int. J. Electrochem. Sci. 1(2006) 324-333.

139. D. Martel, N. Sojic, A. Kuhn, J. Chem. Educ. 79 (2002) 349-351.

140. A. Liu, J. Zhu, J. Han, H. Wu, C. Jiang, Electrochem. Commun. 10 (2008) 827-830.

141. T. Hezard, K. Fajerwerge, D. Evrard, V. Collièree, P. Behra, P. Gros, Electrochim. Acta 73 (2012) 15-22.

142. Y. Hu, Y. Song, Y. Wang, J. Di, Thin Solid Films 519 (2011) 6605-6609.

143. C. Berrios, M. Ureta-Zanartu, C. Gutierrez, Electrochim Acta. 53 (2007) 792-802.

144. S. Griveau, J. Pavez, J. H. Zagal, F. Bedioui, J. Electroanal. Chem. 497 (2001) 75-83.

145. A. Sivanesan, S. John, Langmuir 24 (2008) 2186-2190.

146. A. Sivanesan, S. John, Electrochim. Acta 54 (2009) 7458-7463.

147. J. Pillay, K. Ozoemena, Electrochim. Acta 52 (2007) 3630-3640.

148. J. Park, S. Park, A. Koukitu, O. Hatozaki, N. Oyama, Synthetic Metals, 141 (2004) 265-269.

149. A. Drelinkiewicz, M. Hasik, M. Choczynski, Materials Research Bulletin 33 (1998) 739-762.

150. G. Ramirez, E. Trollund, M. Isaacs, F. Armijo, J. Zagal, J. Costamagna, M. J. Aguirre, Electroanalysis 14 (2002) 540-545.

151. O. Corduneanu, V. C. Diculescu, A. M. Chiorcea-Paquim, A. M. Oliveira-Brett, J. Electroanal. Chem. 624 (2008) 97-108.

152. V. C. Diculescu, A. M. Chiorcea-Paquim, O. Corduneanu, A. M. Oliveira Brett, J. Solid State Electrochem. 11 (2007) 887-898.

153. S. Bastide, C. Zlotea, M. Laurent, M. Latroche, C. Cachet-Vivier, J. Electroanal. Chem. 706 (2013) 33-39.

154. M. Pournaghi-Azar, R. Sabzi, J. Electroanal. Chem. 543 (2003) 115-125.

155. V. Mani, A. T. E. Vilian, S. M. Chen, Int. J. Electrochem. Sci. 7 (2012) 12774-12785.

156. J. Sylvestre, S. Poulin, A. Kabashin, E. Sacher, M. Meunier, J. Luong, J. Phys. Chem. B 108 (2004) 16864-16869.

157. K. Qian, W. Huang, Catal. Today 164 (2011) 320-324.

158. A. Venezia, V. Parola, G. Deganello, B. Pawelec, J. Fierro, J. Catal. 215 (2003) 317–325.

159. A. El Haitami, J. Voegel, B. Senger, P. Schaaf, B. Frisch, F. Boulmedais, Langmuir 26 (2010) 2816-2824.

160. M. Pournaghi-Azar, B. Habibi, Electrochim. Acta 52 (2007) 4222-4230.

161. M. Guo, J. Chen, J. Li, B. Tao, S. Yao, Anal. Chim. Acta 532 (2005) 71-77.

162. F. Bentiss, C. Jama, B. Mernari, H. Attari, L. Kadi, M. Lebrini, M. Traisnel, M. Lagrenee, Corrosion Sci. 51 (2009) 1628-1635.

163. J. Watts, J. Wolstenholme, An Introduction to Surface Analysis by XPS and AES, John Wiley and Sons Inc., UK, 2003.

164. M. Tourabi, K. Nohair, M. Traisnel, C. Jama, F. Bentiss, Corrosion Sci. 75 (2013) 123-133.

165. T. Mugadza, T. Nyokong, Synthetic Metals 160 (2010) 2089-2098.

166. J. Zen, A. Kumar, M. Chang, Electrochim. Acta 45 (2000) 1691-1700.

167. C. Caro, F. Bedioui, J. Zagal, Electrochim. Acta 47 (2002) 1489-1494.

168. T. Mugadza, T. Nyokong, Polyhedron 30 (2011) 1820–1829.

169. W. Sun, C. Guo, Z. Zhu, C. Li, Electrochem. Commun. 11 (2009) 2105-2108.

170. C. Guo, F. Hu, X. Lou, C. Li, J. Power Sources 195 (2010) 4090-4097.

171. T. Mugadza, T. Nyokong, Electrochim. Acta 55 (2010) 2606-2613.

172. X. Huang, Y. Li, Y. Chen, L. Wang, Sensors and Actuators B: Chemical 134 (2008) 780-786.

173. B. Agboola, K. Ozoemena, T. Nyokong, Electrochim. Acta 51 (2006) 6470-6478.

174. A. Adekunle, B. Mamba, B. Agboola, K. Ozoemena, Inte. J. Electrochem. Sci. 6 (2011) 4388-4403.

175. S. Ivanov, U. Lange, V. Tsakova, V. Mirsky, Sensors Actuators B, 150 (2010) 271-278.

176. Q. Yi, F. Niu, W. Yu, Thin Solid Films 519 (2011) 3155-3161.

177. L. Dantas, A. dos Reis, S. Tanaka, J. Zagal, Y. Chen, A. Tanaka, J. Braz. Chem. Soc. 19 (2008) 720-726.

178. J. Li, H. Xie, L. Chen, Sensors Actuators B 153 (2011) 239-245.

179. J. Li, X. Lin, Sensors Actuators B 126 (2007) 527-535.

180. Y. Fukumoto, T. Matsunaga, T. Hayashi, Electrochim. Acta 26 (1981) 631-636.

181. Q. Yi, W. Yu, J. Electroanal. Chem. 633 (2009) 159-164.

182. M. Chen, D. Kumar, C. Yi, D. Goodman, Sci. 310 (2005) 291-293.

183. X. Ji, C. Banks, A. Holloway, K. Jurkschat, C. Thorogood, G. Wildgoose, R. Compton, Electroanal. 18 (2006) 2481-2485.

184. H. Razmi, A. Azadbakht, M. Sadr, Anal. Sci. 21 (2005) 1317-1323.

185. J. Zagal, S. Lira, S. Ureta-Zañartu, J. Electroanal. Chem. 210 (1986) 95–110.

186. J. Zagal, E. Muñoz, S. Ureta-Zañartu, Electrochim. Acta 27 (1982) 1373–1377.